Analysis of Compressive Ice Failure and Ice Crushing Dynamics during Medium-Scale Indentation Tests

by

© Pranav Rajshekhar Birajdar, B.E.

A thesis submitted to the School of Graduate Studies in partial fulfillment of the requirements for the degree of

Master of Engineering

Faculty of Engineering and Applied Science
Memorial University of Newfoundland

May 2017

St. John's Newfoundland

Abstract

Medium-scale laboratory tests have been carried out with an aim to improve the understanding of compressive ice failure phenomena and links between the formation of high-pressure zones and the occurrence of ice-induced structural vibrations under controlled conditions. The tests presented in this thesis focus on the indentation of ice using a single spherical indenter mounted on rigid and compliant indentation systems. Fifteen indentation tests were performed to investigate the effects of ice temperature, indenter size and structural feedback on ice failure processes associated with high-pressure zone formation and evolution during dynamic ice crushing tests.

It was observed that ice at warm temperatures was more prone to ductile type failure with lower, less dynamic pressures. By contrast, results from tests conducted at colder temperatures were characterized by a combination of spalling and crushing failure, which associate more with large-amplitude, sawtooth load cycles. In terms of scale effects, it was observed for the same indentation rate and temperature, smaller indenters produced higher amplitude, higher frequency sawtooth loading than was observed for larger diameter indenters. It was also observed that the structural compliance aids in the formation and development of cyclic loading patterns. Results presented in this thesis will be used to guide the remainder of the ice crushing dynamics research program.

Acknowledgments

I would like to express my sincere gratitude to my supervisor Dr. Rocky Taylor for his continued support and guidance throughout my graduate studies. His expert advice on ice mechanics, experimentation and thesis writing has been invaluable, for which I am truly grateful. I would also like to thank Dr. Charles Randell, Dr. Freeman Ralph, Centre for Arctic Resource Development (CARD) and C-CORE for providing me with financial support and an excellent environment to pursue my research. My sincerest gratitude to Mr. Andrew Macneil of C-CORE and Mr. Robert Pritchett of CARD for the design of the experimental setup and Ms. Kashfi Habib and Mr. Ridwan Hossain for their assistance and inputs during the setup, experimentation, data analysis and post-processing of the results. I am also thankful to Mr. Karl Kuehnemund at C-CORE and Mr. Jason Murphy at Memorial University of Newfoundland (MUN) for their help and assistance with the test setup and experiments.

I sincerely thank Memorial University for allowing the use of the Faculty of Engineering and Applied Science (FEAS) Strength Laboratory, Thermal Laboratory and associated cold room facilities, and Dr. Amgad Hussein in particular, for permitting me to modify and integrate elements of the existing structural test frame into my apparatus design. I gratefully acknowledge C-CORE for allowing the use of their equipment and cold room services, as well as MUN Technical Services for assisting with the fabrication and installation of the experimental equipment and apparatus.

I gratefully acknowledge core funding for the CARD program at C-CORE by Hibernia Management and Development Company, Ltd. (HMDC) and Terra Nova Development (Suncor Energy Inc. – Operator). Financial support from the Research and Development Corporation (RDC) of Newfoundland and Labrador for aspects of this work is highly acknowledged.

Finally, a special thanks to my parents who never stopped believing in me and always encouraged me to pursue my interests. I would not have been here without their unconditional love and support.

Table of Contents

List of Tables

List of Figures

List of Abbreviations and Symbols

E	Young's Modulus
σ	total stress
ε	total strain
λ	Lamé's first parameter
μ	Shear Modulus
v	Poisson's ratio
ε^c	delayed elastic strain
ε^d	viscous strain
ε^e	instantaneous strain
$\dot{\varepsilon}^d$	delayed-elastic strain rate
$\dot{\varepsilon}^c$	viscous creep strain rate
μ_k	viscosity coefficient for the Kelvin-Voigt model
μ_m	viscosity coefficient for the Maxwell model
T_m	melting temperature of ice in Kelvin
p	pressure
V_w	volume of water
V_i	volume of ice
S_w	entropy of water
S_i	entropy of ice
A	temperature dependent constant
$r(t)$	radius of the spherical indenter
r_c	radius of curvature for the spherical indenter
$d(t)$	depth of penetration
A_n	mean nominal area
t	time of penetration
v_p	velocity of penetration

hpz	high pressure zone
JOIA	Japan Ocean Industries Association
MTS	Material Testing System
LVDT	Linear Variable Differential Transformer
RTD	Resistance Temperature Detector
MUN	Memorial University of Newfoundland
CARD	Centre for Arctic Resource Development

List of Appendices

Chapter 1: Introduction

1.1 Overview

Arctic technology has come a long way since the first exploration in ice covered Cook Inlet, Alaska in the 1960s. Due to significant hydrocarbon potential in the Jeanne d'Arc Basin, Sakhalin Island, Beaufort Sea, Sverdrup Basin and other parts of the Arctic, the offshore industry will continue to expand over the new few decades. Harsh environmental conditions, poor infrastructure and uncertainty about ice conditions and ice load are still limiting the true potential of exploration, drilling and oil extraction efforts in these areas (Gudmestad et al., 2007). One of the key challenges identified by the offshore industry is reducing uncertainties in ice load estimation (Taylor et al., 2012).

To understand the physics and mechanics of ice-induced vibrations in structures, the industry has heavily invested in several research projects that had offshore structures susceptible to the action of moving ice. Both scale-model tests and full-scale measurements, as well as the theoretical models, have been developed to advance the countermeasures for structural design to avoid adverse ice-induced vibrations. Different, even contradicting models and explanations have been developed, but gradually a more coherent understanding of dynamic ice-structure interaction is emerging.

When ice sheets interact with fixed offshore structures, the ice-breaking process causes dynamic ice forces and may induce structural vibrations. These dynamic ice actions on

offshore structures are a highly important concern for engineering design. Ice-induced vibrations of vertical-faced structures in ice-covered waters have been a known challenge since the first observations of ice induced vibrations on the drilling platforms in Cook Inlet, Alaska by Peyton (1968) and Blenkarn (1970). Since then, ice loads and structural vibrations have been reported on lighthouses (Engelbrektson, 1977), bridge piers (Sodhi, 1988) and offshore jacket oil platforms (Yue et al., 2001). Ice-induced vibrations were also observed on multi-legged structures in the Bohai Sea (Xu et. al., 1986) that led to harmful resonant vibrations. Initially, it was believed that ice induced vibrations are a problem only for narrow and slender structures. In 1986, the Molikpaq, a massive low-rise caisson retained island in the Beaufort Sea, experienced heavy dynamic ice loads and steady-state vibrations in such range that the structure was close to its limit stability (Jeffries et al., 1988). The Molikpaq incident highlighted the need to study ice-structure interaction dynamics even for wide structures. The study of dynamic ice action is significant, and its knowledge is essential for economically sound and safe design of an offshore structure.

During the ice-structure interaction, ice failure may occur in many ways, including radial cracking, circumferential cracking, buckling, spalling, crushing, creep failure, flexural failure, compressive ice failure or a combination of any these (Sanderson, 1988). From an engineering point of view, compressive ice failure and crushing are considered as the primary failure mode of interest for vertical structures as they are associated with the highest ice action and significant dynamic loading. This phenomenon is quite complex as ice-induced vibrations are also associated with the compressive ice failure. These

vibrations have been observed on many full-scale fixed structures and it has been the cause of structural damage (Björk, 1981) and failure in some structures (Määttänen, 1975; Fransson and Danielsson, 1985). Ice-induced vibrations have also been observed on medium-scale testing structures (Frederking et al., 1990).

1.2 Objectives

The primary objective of this research program is to investigate and understand the compressive ice failure and crushing dynamics during ice-structure interaction and explore the effects of different parameters on ice loads and ice failure. This thesis investigates the following:

- The process responsible for the formation and evolution of high-pressure zones during the indentation tests.
- The effect of the temperature on failure mechanism.
- The effect of structural compliance on the compressive ice failure phenomenon.
- The influence of different indenter sizes on ice-structure interaction.
- The influence of the aforementioned parameters on the formation of cyclic loading patterns.
- The influence of the aforementioned factors on the microstructural behavior of ice.

1.3 Scope of Thesis

The research presented in this thesis focuses on medium-scale laboratory investigation of compressive ice failure and crushing dynamics during the interaction of ice samples with rigid and compliant structures. A series of tests were performed wherein ice samples produced using freshwater polycrystalline ice at different temperatures were crushed using spherical indenters of different sizes to study the effects of various parameters like sample temperature, indenter size and structural compliance on compressive ice failure, crushing dynamics, formation and evolution of high-pressure zone and cyclic loading phenomenon. The experimental program is divided into two phases: Phase 1A and Phase 1B respectively. The ice samples were produced in the Thermal Laboratory's reefer unit at the Memorial University of Newfoundland, and the cold room facility at C-CORE. All the tests were performed in the Strength Laboratory at Memorial University of Newfoundland. The effects of structural feedback on compressive ice failure and crushing dynamics during the formation of a single high-pressure zone were studied in Phase 1A, whereas in the case of Phase 1B, compressive ice failure and crushing dynamics during the formation of a single high-pressure zone were studied in the absence of structural feedback.

1.4 Outline of Thesis

The thesis is organized into six chapters. Chapter 1 deals with the introduction and overview of the research program. Chapter 2 covers a review of relevant literature on mechanical properties and behavior of ice, ice mechanics, damage and failure mechanics,

scale effects, compressive ice failure and crushing dynamics, formation and evolution of high-pressure zones, cyclic loading phenomenon and ice-induced vibrations. Chapter 3 provides a detailed description of the experimental methodology, test plan and design, test setup, ice sample preparation, test equipment and instrumentation, testing and post-experimental data collection. Chapter 4 consists of a sample of the data obtained from the tests with an exhaustive collection of results available in appendices. Detailed analysis of the experimental results that include ice failure observations and effects of sample temperature, structural compliance and indenter size are provided in Chapter 5. Chapter 6 discusses the major findings, conclusions and provides recommendations for future work.

Chapter 2: Literature Review

2.1 Overview

Ice is a unique material that behaves like a brittle, non-linear, viscoelastic solid. It is often encountered in a temperature range very close to its melting temperature. Ice fractures under high strain rate and creeps with very little stress. According to Sanderson (1988), ice is extremely brittle at high stresses and behaves like a creeping, ductile material at low stresses. The stress-strain relationship of loaded ice is time dependent in nature i.e. ice will experience time dependent strain under constant stress and stress relaxation under constant strain (Jordaan, 2001). It is difficult to describe its material behavior using a single mechanical property. The behavior of ice can be modeled using a combination of elasticity, viscoelasticity, damage or fracture mechanics (Timco and Weeks, 2010). As a geophysical material contains many flaws, ice failure behaviour is significantly influenced by random fractures. The uncertainty of ice behavior, the different properties associated with it and the complex physical and mechanical properties that are used to describe the ice behavior at different conditions makes ice a difficult material to understand.

2.2 The Mechanical Behavior of Ice

2.2.1 Elasticity

Young's Modulus (E) of the material is the ratio of stress (σ) to strain (ε) during elastic behavior. Ice responds elastically and linearly to low stresses applied for a short time. This elastic nature of ice is useful, but only in a highly restricted range of circumstances (Sanderson, 1988).

For the present research, freshwater granular ice is assumed to be isotropic in nature i.e. having same properties in all directions. The elastic response of ice, in this case, can be described by the Lamé's constants, λ (Lamé's first parameter) and μ (Shear Modulus), which can be related to the Young's modulus (E) and Poisson's ratio ν by,

$$\mu = \frac{E}{2(1+v)} \qquad \textbf{Equation 2.1}$$

$$\lambda = \frac{Ev}{(1+v)(1-2v)} \qquad \textbf{Equation 2.2}$$

Based on his study of the effects of temperature on the behavior of ice, Glen (1975) developed temperature dependent equations for *E* and *v* whereas Sinha (1979) argued that the temperature effects were insignificant and thus could be neglected. Subsequently, Sinha (1989) reported that the values of Young's modulus varied from 9 GPa to 10.16 GPa and Poisson's ratios varied from 0.308 to 0.365 for polycrystalline ice over a temperature range of 0°C to -50°C.

2.2.2 Viscoelasticity and Creep

Viscoelastic materials exhibit both viscous and elastic characteristics when undergoing deformation. It means that a material's response to deformation or force may change over time i.e. the relationship between stress and strain for viscoelastic materials is time dependent and the response of stress depends on both the strain applied and the strain rate at which it was applied.

Lockett (1972) documented some interesting properties about viscoelastic materials. Since ice is a viscoelastic material, it exhibits the following properties.

- Strain Rate Dependence: Viscoelastic materials are said to be strain rate-dependent as faster strain rates cause more elastic responses resulting in a stiff material, whereas slower strain rates cause more fluid-like behavior.
- Stress relaxation: If you apply a constant displacement to a viscoelastic material, the force required to hold the material in this configuration decreases over time.
- Creep: Viscoelastic materials show creep behavior. If you apply a constant force to a viscoelastic material, the displacement increases over time and on release, it takes time for the material to recover to its initial configuration.
- Hysteresis: When viscoelastic materials have a force applied to them, which is then removed, it consumes more energy to displace the material (loading phase) than it does to return the material to its original configuration (unloading phase).

Figures 2.1 and 2.2 illustrate the dependence of stress and strain behavior of ice on time. Constant strain rate creep curves are shown in Figure 2.1. It can be observed that for ice

deformed under constant strain rate, increasing strain rate increases the peak stress. For ice under low strain rates, the behavior is pure creep and ice behaves similarly under tensile and compressive loading, as evident from the tensile strain rate ($\dot{\varepsilon}_t$) and compressive strain rate ($\dot{\varepsilon}_c$). For intermediate strain rates, however, microstructural damage processes like microcracking and recrystallization cause pressure softening in the post-peak region. As the strain rates increase further, the failure mode changes to brittle fracture behavior.

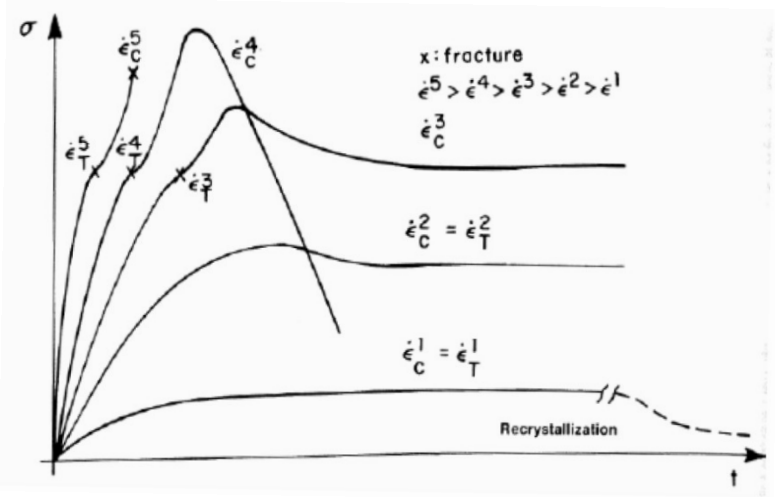

Figure 2.1: Typical constant strain rate creep curves for ice (Nadreau and Michel, 1984).

Deformation behavior of a polycrystalline ice sample under constant uniaxial load in tension and compression is illustrated in Figure 2.2. After elastic deformation, the creep deformation is divided into three stages: primary creep, secondary creep and tertiary creep. The delayed-elastic creep strain is also referred to as primary strain. Primary creep is recoverable i.e. if the compressive stresses are removed, the grains try to recover its original shape. Secondary creep, also known as viscous creep strain is non-recoverable

and the things that are highly non-linear and time dependant can still be recovered. Secondary creep occurs at all stresses and shows no yield point, resulting in a permanent deformation within ice. Tertiary creep is a complex deformation stage that is associated with the formation of microcracks, dynamic recrystallization, softening of ice, finally leading to a complete failure (Duval et al., 1983).

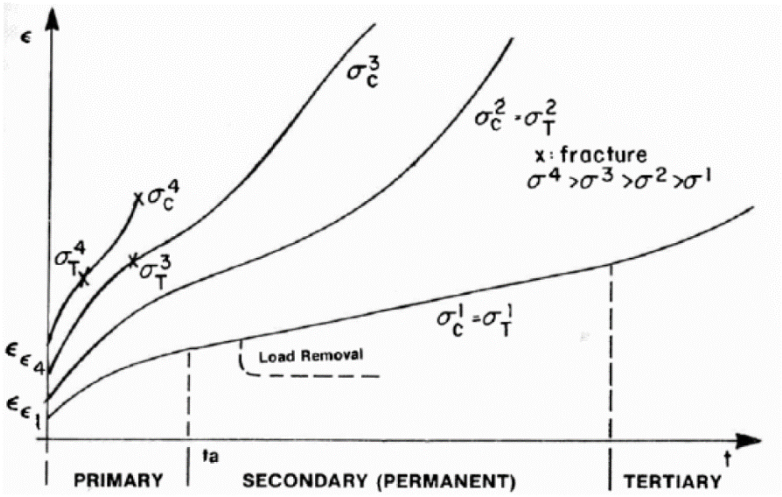

Figure 2.2: Typical creep curves for ice under constant stress (Nadreau and Michel, 1984).

The response of viscoelastic materials can be represented employing mechanical models. These models are obtained from different combinations of springs and dashpots. The behavior of viscoelastic materials can be represented using these combinations of the analogous responses of springs and dashpots, either in series or parallel. The Burgers system is the most commonly discussed mechanical model when it comes to modeling an idealized viscoelastic model of ice (Jordaan and McKenna, 1988). The Burgers mechanical model consists of a Kelvin-Voigt model (spring and dashpot in parallel) and a

Maxwell model (spring and dashpot in series) connected to each other in series. Figure 2.3 shows a schematic of Burgers model.

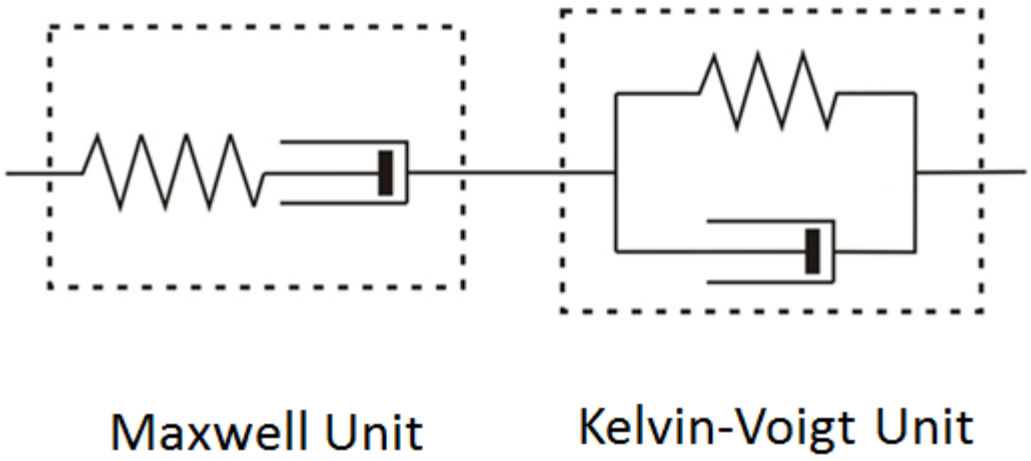

Figure 2.3: Burgers model: a Maxwell Unit and a Kelvin-Voigt Unit in series.

The Kelvin-Voigt unit in this system represents the delayed-elastic or primary creep strain whereas in the case of the Maxwell unit, the dashpot represents the viscous or secondary creep strain and the spring represents the instantaneous elastic strain in ice under load. The total strain ε in this model is the sum of delayed elastic strain ε^c, the viscous strain ε^d and the instantaneous strain ε^e.

$$\varepsilon = \varepsilon^c + \varepsilon^d + \varepsilon^e \qquad \textbf{Equation 2.3}$$

Where,

$$\varepsilon^e = \frac{\sigma}{E_m} \qquad \textbf{Equation 2.4}$$

For elastic strain, σ is the axial stress and E_m is the Young's modulus of ice. The delayed-elastic and viscous creep rates are given as,

$$\dot{\varepsilon}^d = \frac{\sigma}{\mu_k} \qquad \textbf{Equation 2.5}$$

$$\dot{\varepsilon}^c = \frac{\sigma}{\mu_m} \qquad \textbf{Equation 2.6}$$

Here, μ_k is the viscosity coefficient for the Kelvin-Voigt model and μ_m is the viscosity coefficient for the Maxwell model.

The Burgers model has been used by Jordan and Xiao (1992), Xiao (1997), Li (2007) and others to model ice behavior. Despite its application by various researchers, the model has encountered difficulties when paired with multiple Maxwell units in series to obtain a more accurate model. Taylor et al. (2010) discussed these shortcomings in further detail and also presented the improved methods to model the viscoelastic behavior of ice as suggested by Sinha (1979), Jordaan and McKenna (1988), Schapery (1997) and Meglis et al. (1999).

2.2.3 Fracture and Damage in Ice

2.2.3.1 Fracture

Ice, in its natural form, has many flaws, defects and irregularities. These defects play a significant role in determining the failure and fracture processes that lead to deformation in ice. When ice undergoes failure, the fracture processes are often associated with ice's transition from creep and ductile mode to brittle mode as the indentation rate increases.

Gold (1972) first recognized the importance of the brittle behaviour in this context. This transition is a result of temperature, underlying flaws, strain rate and load level (Sanderson, 1988).

Test ice grown in laboratories are often void of internal flaws or cracks. On applying load on ice, it deforms, causing internal dislocations and pile-up at grain boundaries that result in stress concentrations. To relieve these stress concentrations, grain boundaries grow apart, thus giving rise to microcracks (Schulson et al., 1984). Crack nucleation is that point in time when cracks appear where none were present earlier. Crack nucleation is the first point in the mechanical failure (Frost, 1995). It is associated with the transition of ice from ductile to brittle behavior. A propagation-controlled fracture is when the induced crack nucleation results in very small microcracks that do no propagate and extra load is applied until the propagation occurs. On the other hand, nucleation-controlled fractures are large enough to produce big microcracks that propagate on their own (Sanderson, 1988). A thorough study regarding the mechanism of crack nucleation is presented by Frost (2001). According to the author, the following mechanisms are responsible for local stress concentrations:

- Dislocation pile-ups.
- Grain-boundary sliding.
- Elastic stress concentrations due to elastic anisotropy and thermal effects.
- Elastic stress concentrations at interior flaws.

Thus, different nucleation mechanisms are observed for laboratory prepared ice under different conditions. According to Sanderson (1988), if natural ice contains many inherent flaws and defects, the fracture experienced will be more likely due to the existing flaws rather than crack nucleation.

2.2.3.2 Microstructural Damage in Ice

During an ice-structure interaction, ice that comes in contact with the structure undergoes modifications in its microstructure, physical and mechanical properties. Microstructural damage is referred to the stage in which ice undergoes microstructural changes and modifications that are irreversible i.e. the original grain boundaries and the mechanical properties of ice are permanently changed. Processes like microcracking, pressure melting and recrystallization are associated with microstructural damage.

Indentation rate plays a significant role in changing the failure mode of ice from creep and ductile to brittle behavior. At very slow indentation rates, ice undergoes ductile failure wherein the pressure is distributed uniformly across the indented ice surface. As the indentation rates increase, ice can no longer fail uniformly and undergoes various failure mechanisms such as dislocations, localized spalling, radial cracking, crushing and extrusion that will eventually lead to the formation of high-pressure zones (*hpz*s).

Frederking et al. (1990) performed medium-scale tests at the Hobson's Choice Ice Island. The indentation tests were performed using a rigid spherical indenter having a diameter of 1 m and a radius of curvature of 1.28 m, at an indentation rate of 0.3 mm/s. Results from these tests show that a permanent depression was formed at the indented area with

substantial damage observed near the area of the indentation. Neither extrusion nor localized spalling were observed, though radial cracks were observed surrounding the indented ice surface. Masterson et al. (1999) observed similar ductile failure during slow speed tests performed at Rae Point with an indentation speed of 0.3 mm/s. Figure 2.4 (a) presents a schematic of the indented area at low loading rates during the medium-scale field tests. Figure 2.4 (b) illustrates the formation of the permanent depression of the indented ice with little evidence of crushing and extrusion, though significant recrystallization was observed, indicating that a damaged region was formed.

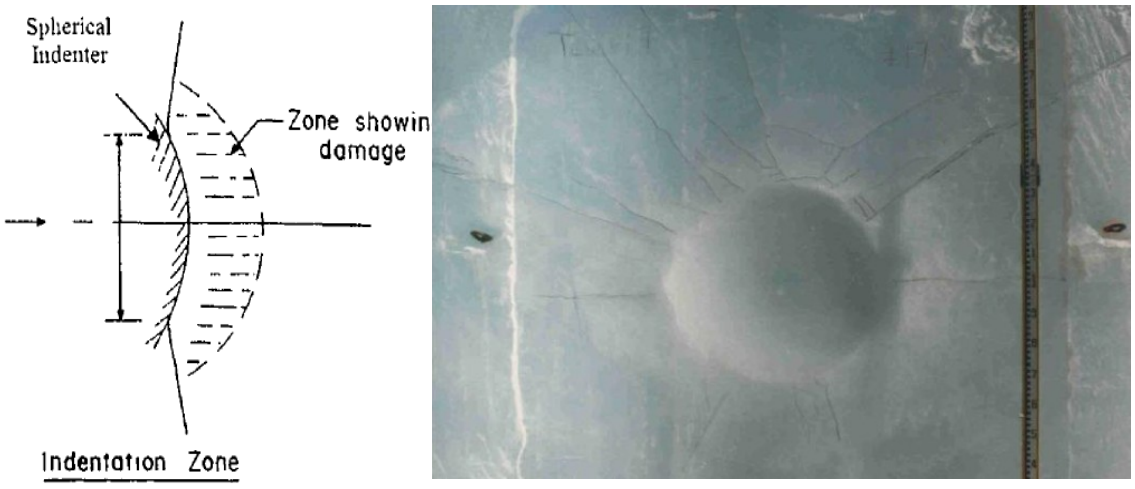

(a) (b)

Figure 2.4: (a) slow (0.03 mm/s) test results from Hobson's Choice Ice Island experiments (Frederking et al., 1990). (b) ductile failure observed for the Rae Point slow (0.03 mm/s) tests (Masterson et al., 1999).

As mentioned earlier, ice failure behavior changes from ductile to brittle mode with an increase in loading rate. Kheisin and Cherepanov (1973) and Kurdyumov and Kheisin (1976) first observed the formation of highly damaged layers while performing drop tests

using a 300 kg steel ball on the surface of an ice sheet. These damage zones resulted from crushing and extrusion of pulverized ice in addition to the evidence of microcracking.

Frederking et al. (1990) and Jordaan (2001) observed extensive crushed ice surrounded by recrystallized zones during the Hobson's Choice Ice Island medium-scale tests. A distinct boundary between the crushed ice and the parent ice suggested that lateral grain movement was also observed along the grain boundaries. Full-scale iceberg results reported by Muggeridge and Jordaan (1999) also reported highly crushed, fine-grained and microcracked ice at faster loading rates. Figure 2.5 (a) presents a schematic of the failure mode for high loading rates during the medium-scale field tests. Figure 2.5 (b) illustrates the results obtained from the Rae Point experiments as reported by Masterson et al. (1999).

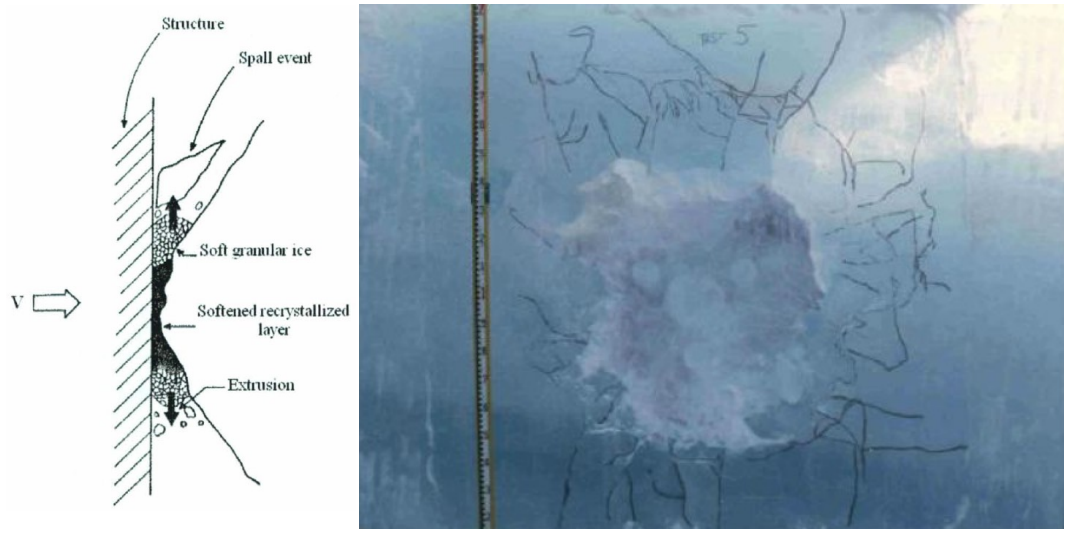

(a) (b)

Figure 2.5: (a) an illustration of ice failure mode observed at higher loading rates during medium-scale field tests (Jordaan and Xiao, 1992); (b) brittle failure observed for the Rae Point fast (10 mm/s) tests (Masterson et al., 1999).

For tests with higher loading rates, the damaged layer adjacent to the indenter became prominent in the area. As shown, the indented region is highly confined, recrystallized with evidence of microcracking and pressure softening whereas heavy spalling and microcracking has been observed in the areas surrounding the indented region. Further research on the brittle failure, fracture and damage processes has been carried out by Jordaan and Xiao (1992), Meglis et al. (1999), Xiao (1997) and Li (2007).

2.2.4 Dynamic recrystallization and Pressure Melting

When ice is subjected to high confining pressures, the deformation process is dominated by recrystallization and pressure melting. According to Meglis et al. (1999), recrystallization and pressure melting play a significant role in the enhancement of creep in ice under high pressures. Recrystallization is defined as the reorganization of material into different orientations, grains shapes and sizes (Vernon, 1981). Dynamic recrystallization is recrystallization associated with deformation processes. In the case of ice, recrystallization changes the grain size, grain boundary structure, sub-structure and the dislocation density. These changes result in ductility and softening of ice that eventually leads to the formation of strain localization and shear zones (Xiao, 1997). Jonas and Muller (1969) observed that dynamic recrystallization had varying effects with changes in the shear stress. For low shear stresses, dynamic recrystallization on ice could be avoided. For intermediate shear stresses, the dynamic recrystallization occurred periodically, whereas, for the higher shear stress states, continuous recrystallization is expected following a period of conventional creep flow. Wei and Dempsey (1991), Duval et al. (1983), Urai et al. (1986) and other authors have studied the effects of dynamic

recrystallization and its effects on creep enhancement, grain boundary formation and brittle crack propagation in greater detail.

For quasi-static pressure changes, Hobbs (1974) defined pressure melting in terms of a thermodynamic equation,

$$\frac{dT_m}{dp} = \frac{(V_w - V_i)}{(S_w - S_i)} \qquad \textbf{Equation 2.7}$$

Where T_m is the melting temperature of ice in Kelvin, p is the pressure, V_w, V_i, S_w and S_i are volume and entropy of water and ice respectively. On further simplification using the Clausius-Clapeyron's equation, an inverse relationship between the melting temperature and pressure was established.

$$dT_m = -Adp \qquad \textbf{Equation 2.8}$$

where A is a temperature dependent constant. For ice at -10°C, A= 0.0833 °C/MPa and at 0°C, A= 0.0743 °C/MPa. Tests performed by Nordell (1990) contains additional details about the relationship between temperature and pressure of ice and its association with the deformation processes observed on ice. According to Meglis et al. (1999) and Muggeridge and Jordaan (1999), ice tested under triaxial conditions and the damaged layer during full-scale indentation tests show clear evidence of pressure melting.

2.3 Compressive Ice Failure

From an engineering point of view, ice compressive failure loads due to spalling and crushing are a significant consideration for design scenarios involving the failure of ice

against vertical-walled structures, since such interactions are often associated with extreme ice loads and significant dynamic action (ISO 19906, 2010). This phenomenon is quite complex as ice-induced vibrations are also associated with the compressive ice failure as they are cyclic in nature (Jordaan et al., 2008).

Compressive ice failure is often linked to complex failure mechanisms such as spalling, splitting and crushing processes. These failure mechanisms play a crucial role in the formation of highly damaged ice under interaction with a structure and are responsible for the evolution of an important interaction process, the *hpz*s. During an ice-structure interaction, these *hpz*s transfer a majority of the force through a very small interaction area (Jordaan, 2001). According to the observations made by Taylor et al. (2008) during the medium-scale tests for the Japan Ocean Industries Association (JOIA), on average only 10% of the nominal area is actually loaded during crushing events. Thus, it is crucial that these *hpz*s should be thoroughly studied and understood. Failure mechanisms like macrofractures, recrystallization and pressure melting are often associated with spalling and crushing processes, which play a significant role in the formation, evolution and development of hpzs (Jordaan, 2001). Crushing is associated with the damage processes within hpzs, whereas spalling fracture is primarily associated with stress, geometry and flaws (Taylor et al., 2008). *Hpz*s are responsible for high local contact pressures and have been observed in various medium and small-scale indentation tests. Local pressures as high as 80 MPa (Frederking et al., 1990) and 50 MPa (Masterson et al., 1993) have been observed during medium-scale indentation tests and pressures reaching almost 100 MPa

have been recorded during small-scale indentation tests on freshwater polycrystalline ice samples (Mackey et al., 2007; Jordaan et al., 2008).

During an ice structure interaction, many high-pressure zones originate in the indented area and the failure of one high-pressure zone might trigger failure among adjacent *hpz*s. Thus, it is crucial that we study and analyze the formation of a single high-pressure zone. Figure 2.6 illustrates the formation of a high-pressure zone (Jordaan et al., 2008). According to Figure 2.6, extensive microcracking starts when ice comes into contact with the structure that leads to fragmentation of ice near the *hpz* (A). Ice near the edges of the contact zone undergo high shear and low confinement, resulting in spalling and microcracks while ice near the center of the *hpz*s undergo high confinement, thus leading to the formation of recrystallized, highly fine-grained ice. This results in pressure softening at the centre of the *hpz* (B) and an eventual low-pressure area, due to extrusion of softened and crushed ice (C). This constant crushing and extrusion phase results in continuous cycles of pressure softening and hardening leading to the formation of loading cycles. Localized spalls cause big load drops often causing an end to these cycles due to the reduction in contact area (E). Jordaan et al. (2008) discuss the formations, evolution and development of *hpz*s in further detail.

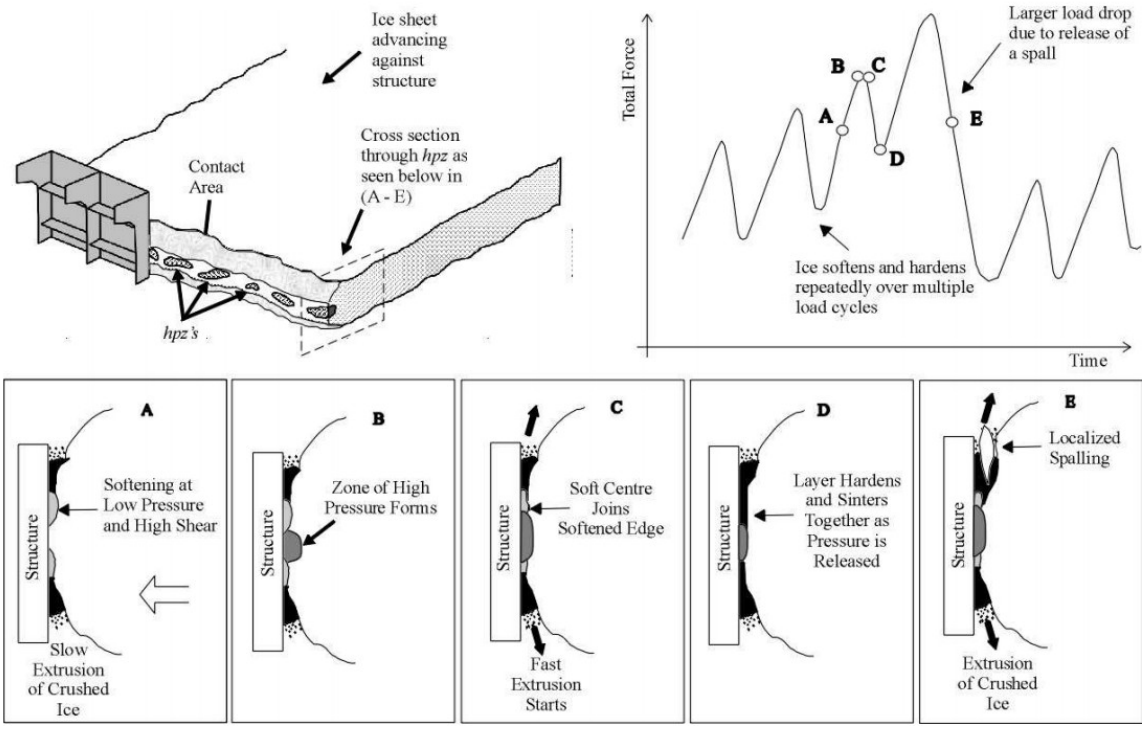

Figure 2.6: Illustration of an ice-structure interaction phenomenon (Jordaan et al., 2008).

The continuous loading and unloading cycle of ice under constant indentation results in ductile-brittle transition failure of ice that eventually leads to the self-excited vibrations under moderate indentation speeds. This feature of compressive ice failure is the effect of structural feedback. During the loading phase, kinetic energy is stored in the structure as ice advances and undergoes microcracking. When the density of microcracks reaches a critical level, they coalesce with each other, leading to the total failure of ice sheet thus causing the structure to spring back. The ice force drops down quickly during this process, which is called the "unloading phase". The frequency at which the load fluctuates is directly associated with the velocity of ice and the stiffness of the structure (Määttänen, 1988; Timco and Frederking, 1986; Yue et al., 2009).

2.4 High Pressure Zones

Compressive ice failure is a rate dependent process. Ice creeps at very slow loading rates and as the loading rates increase, there are changes in the microstructural behavior of ice and the rate of creep is enhanced. This microstructural change is known as damage. As the loading rates increase, the damage is more localized in regions adjacent to the indenter. This localized layer of heavily damaged ice is also called a 'high-pressure zone' (*hpz*). These localized *hpz*s are responsible for transmitting most of the total ice load onto the interacting structure. The formation of the *hpz*s is associated with two processes, concentration of stress resulting from spalling and fracture processes and the formation of the damaged layer (Jordaan, 2001).

Spalls frequently occur near the edges of the ice-structure contact zone. *Hpz*s are influential in the evolution of the ice-induced vibrations as they are associated with localized spalling, damage and softening processes. When *hpz*s occur, extensive spalling fractures are formed near the edge of an ice-sheet (Croasdale, 1975; Croasdale et al., 1977). This occurrence is particularly evident in the case of an ice sheet interacting with the structure, as *hpz*s tend to concentrate near the center of the ice sheet. These fractures, however, assist in reducing the load on structure significantly as illustrated in Figure 2.7. The fractures also end up destroying all or some part of these *hpz*s in the contact area. As the loading phase starts again, interaction occurs, thus resulting in the continuous birth, evolution and death of *hpz*s throughout the interaction zone.

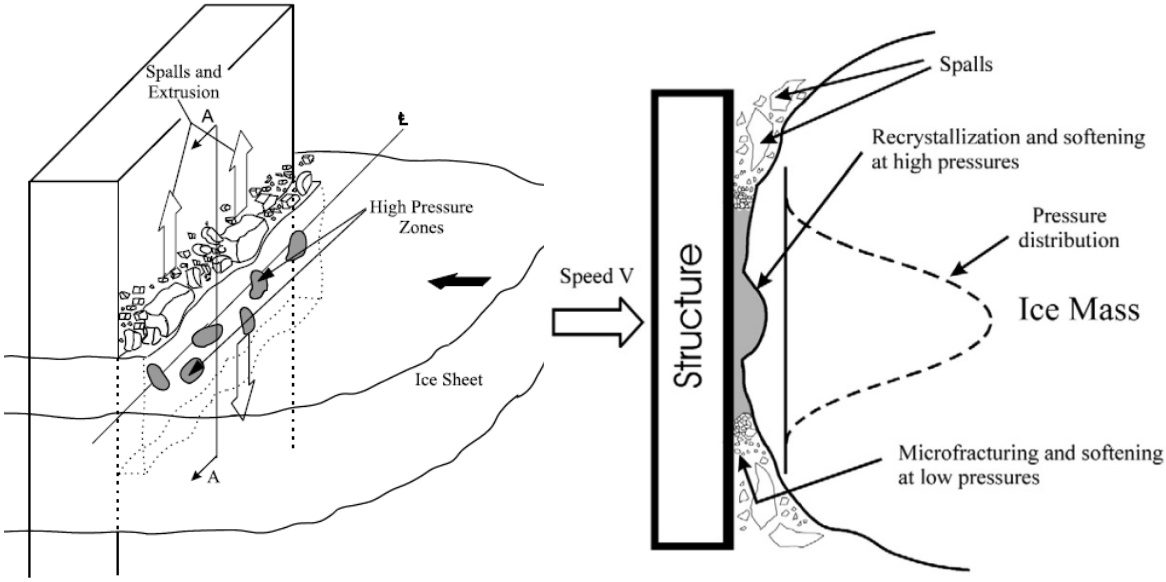

Figure 2.7: Schematic of the spalling, extrusion and high-pressure zone formation (Jordaan, 2001).

The stress states vary within the high-pressure zones ranging from low confinement near edges to high values, almost reaching 100 MPa near the center. These regions of intense shear permanently change the microstructural change in the indented ice. Damaged ice layers are formed in the vicinity of the *hpz*s. Microfracturing and recrystallization are observed near the edges of *hpz*s, whereas the central areas of *hpz*s are heavily dominated by highly recrystallized material, accompanied by pressure softening and ejection of crushed ice. Similar observations regarding the microstructural changes in the local *hpz*s were made by Sinha (1977), Sinha and Cai (1992), Jordaan and Singh (1994) and Barrette et al. (2002). The reader is referred to Jordaan (2001) for a detailed explanation of these microstructural changes and its study from the perspective of damage mechanics.

*Hpz*s vary in location and time, and their distribution is dependent upon the geometry of the contact zone. Thus, the *hpz*s present in large interaction areas are more random and

distributed over the entire area as compared to narrow interaction areas. Thus, the formation of *hpz*s during laboratory tests have a different effect on the overall failure behavior of ice as compared to the full-scale field tests. For a larger interaction area, the presence of multiple *hpz*s promotes non-simultaneous failure. The combination of localized extrusion of ice from the formation of several *hpz*s significantly reduces the total load during a full-scale interaction.

2.5 Local and Global Ice Loads

The design of an offshore structure against an ice crushing event requires estimates of global ice forces and local ice pressures. Global loads represent the maximum total force applied to the entire structure whereas the local loads represent the maximum force on a particular area of structural importance. The global interaction area and the local design area are required to calculate the global loads and local loads respectively.

Global interaction area: Nominal interaction area, also referred to as global interaction area is the area determined by the projection of the structure on the original shape of ice, without reducing the fractured or the spalled areas that occurred during the interaction. This area comprises areas with little to no pressure as well as high-pressure zones. A schematic of the global interaction area is shown in Figure 2.8 (a). Global interaction areas range from about ten square meters to hundreds of square meters.

Local design area: The smaller areas found within the global interaction area that are subjected to local high pressures are called local design areas. These areas are used to

design the panel, shell or the stiffening elements of a structure. Figure 2.8 (b) illustrates a local design area. For full-scale structures, local design areas typically range between 0.6 m^2 and 10 m^2.

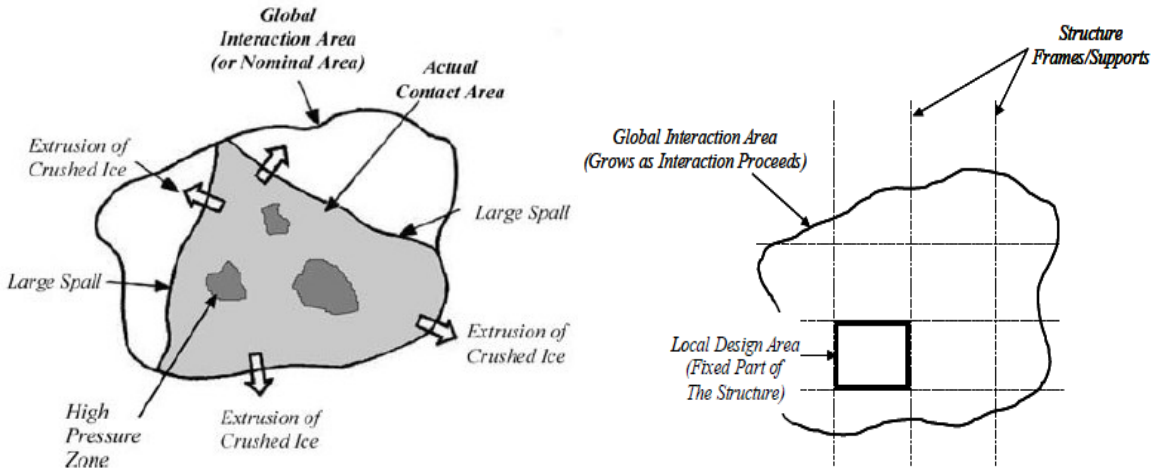

(a) (b)

Figure 2.8: Schematic of (a) global interaction area and (b) local design area (Jordaan et al., 2005 a).

2.6 Pressure-Area Scale Effect

Classical materials comprising of properties like elasticity, viscoelasticity or plasticity are independent of scale effects whereas fracturing materials like ice are fundamentally scale-dependent. According to Sanderson (1988), average pressure on a structure decreases with increasing contact area. The scale effects in ice-structure interaction are primarily attributed to two main reasons, (1) fracture of ice, that reduces the volume of ice to be crushed and assists in the formations of *hpz*s, and (2) probabilistic averaging, wherein the local pressures on local areas are averaged out to global pressures (Jordaan et al., 2006).

Flaw distribution in ice plays a significant role in the ice behavior when fractured. Figure 2.9 (a) illustrates that large ice samples have a higher probability of containing critical flaws, thus making the larger samples more prone to fractures at lower stress levels. Sanderson (1988) discussed the relationship between the statistical aspects of fractured ice and scale effects in further detail.

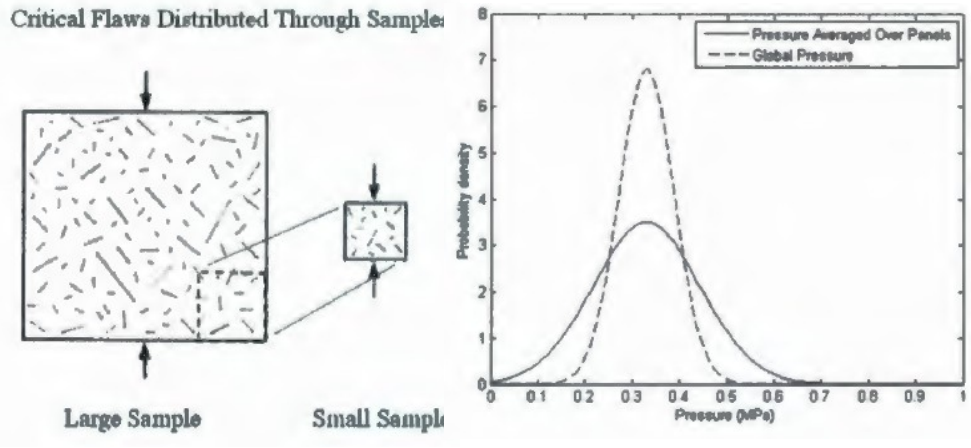

(a) (b)

Figure 2.9: (a) Statistical flaw distribution in large and small samples (Jordaan and Pond, 2001), (b) Variation in global pressure measurements using the probabilistic averaging approach (Li, 2007).

Pressure over small areas due to the formation of *hpz*s during ice compressive failure show large systematic and random fluctuations. Averaging ice loads across the width of a structure derives from the sum of all the *hpz*s averaged over the area of interest. Statistical averaging of *hpz*s leads to non-simultaneous failure of ice across a structure. Since this averaging of local pressures leads to a smaller global pressure standard deviation, probabilistic averaging has been found to reduce these variations significantly as illustrated in Figure 2.9 (b) (Li, 2007). Taylor et al. (2008) suggest further work on

probabilistic averaging methods can help identify the links between local and global pressure behavior that will ultimately contribute to the better understanding of the pressure-area scale effects.

2.7 Full Scale and Medium Scale Indentation Programs

Ice-induced vibrations (IIVs) of vertical-faced structures in ice-covered waters have presented designers with challenges since the first observations of such phenomenon on drilling platforms in Cook Inlet Alaska by Peyton (1968) and Blenkarn (1970). Since then, ice loads and structural vibrations have been reported on lighthouses and navigational aids (Määttänen, 1975; Engelbrektson, 1977; Fransson and Danielsson, 1985), bridge piers (Niell, 1975) and offshore jacket oil platforms (Yue et al., 2001). Ice-induced vibrations were also observed on multi-legged structures in the Bohai Sea (Xu et al., 1983) and even on Molikpaq, a massive caisson retained island in the Beaufort Sea, which experienced such heavy dynamic ice loads and associated vibrations that the structure was close to its limit stability (Jefferies and Wright, 1988). These observations highlight the importance of understanding and properly accounting for dynamic ice action to ensure the safe and economical design of full-scale offshore structures.

Data from past field programs, such as Pond Inlet (Masterson et al., 1992), Rea Point (Masterson et al., 1999), Hobson's Choice Ice Island (Frederking et al., 1990; Gagnon and Sinha, 1991; Masterson et al., 1993; Gagnon, 1998; Jordaan, 2001), as well as medium-scale field indentation tests (e.g. Takeuchi et al., 1997; Matsushita et al., 1997; Sodhi et al., 1998; Kaimo et al., 2000; Akagawa at al., 2000) carried out by the Japan

Ocean Industries Association (JOIA) have provided foundational insights into details of the compressive ice failure processes. Observations from these field tests suggest that during ice-structure interactions, the contact surface contains localized areas of intense pressure (*hpz*s), through which the majority of loads are transmitted. Tactile pressure sensor data from the JOIA data indicates that such *hpz*s comprise about 10% of the nominal interaction area (Taylor et al., 2008).

Oil and gas platforms in Cook Inlet, Alaska experienced unexpected vibrations during the late 1950s thus raising scientific interest to understand the dynamics of structures under ice loads. Cook Inlet platforms had monopod, as well as multi-legged foundations, and the ice sheet failed in crushing mode against the legs. Key findings indicated that the ice crushing strength is loading rate dependent and that the repeating ice failures occurred at certain frequencies. Two explanations were proposed: ice has a tendency to break at a frequency about 1 Hz (Peyton, 1968), and that the rise of ice-induced vibrations is a self-excited process originating from ice strength dependence on loading rate (Blenkarn, 1970). In both cases, the structure itself had a natural frequency close to 1 Hz.

Kemi and Norströmsgrund lighthouses have been one of the major contributors in capturing the ice-structure interaction data on full-scale structures. After reports of hard vibrations on the Norströmsgrund lighthouse during an ice crushing event were first reported, Engelbrektson (1977) captured data from 1973 to 1989 to study the dynamic ice crushing phenomena. The constant fluctuations in the ice loads during the failure of an ice sheet against the structure gave rise to resonant vibrations. The measurements and analysis of these severe vibrations by the author led to the conclusion that the forces

during ice crushing at certain velocities were sawtooth-shaped with a frequency close to the natural frequency of the lighthouse (Engelbrektson and Janson, 1985; Engelbrektson, 1989). Similar results were observed in the case of Kemi 1 lighthouse (Määttänen, 1977; Määttänen and Hoikkamen, 1990; Määttänen, 2008).

Ice problems related to the offshore structures in the Bohai Sea have been, for the most part, due to the vibrations in structures during ice crushing events. Yeu et al. (2000) conducted full-scale ice-structure interaction tests on three multi-leg jacket platforms in the Bohai Sea to understand the crushing process and the formation of steady-state vibrations on vertical structures. The authors observed that the steady-state vibrations have greater amplitude than random vibrations. Due to the higher ice speeds, the loading rate of ice fell within the ductile-brittle range. This ductile-brittle transition zone occurred during the unloading stage. Based on the above analysis, it was concluded that the failure process of ice depends on the relative speed and relative displacement of ice and structure.

Yeu et al. (2009) performed full-scale tests on a cylindrical monopod structure in Bohai Bay to generate dynamic ice forces and structural vibrations. The test data showed that the dynamic ice forces could be classified in three modes (quasi-static ice forces for ice speeds less than 2 cm/s, locked-in forces for ice speeds ranging between 2-4 cm/s and random and irregular forces for ice speeds greater than 4 cm/s). In the case of the quasi-static mode, ice fails abruptly r with a regular period that is much longer than the natural frequency of the structure. For the locked-in mode, the ice forces and the structure's natural period are similar, thus resulting in steady-state vibrations. It has been observed

that the steady-state vibrations can stay for long periods if the speed remains between 2-4 cm/s. When the speeds increase, the vibrations transform from stead-state to random vibrations. Since there are no correlations between local ice forces, the ice failure is asynchronous.

There was a belief that ice-induced vibrations pose a threat only to narrow and slender structures. In 1986, a thick multi-year floe crushed against the side of the Molikpaq, a massive low-rise caisson retained island in the Beaufort Sea. This event caused severe peak loads on the structure with large concurrent vibrations that led to severe dynamic ice loading. It was observed that the component of dynamic activity was higher than the mean load component. The loads were high enough to cause severe fatigue to the sand core. Had the cyclic ice loading continued, the platform likely would have reached its limiting stability. Figure 2.10 shows an occurrence of a phase locked cyclic event on the Molikpaq. It was clear that cyclic ice loading must be regarded as an ultimate limit state when assessing how much resistance is required. It was also confirmed that Molikpaq had similar loading conditions as any Arctic platform with vertical sides. Besides the dynamic platform response, the authors observed the simultaneity of ice crushing by comparing strain-gauge data. Although the ice failure pressure appeared different, a phenomenon of 'phase-lock' occurred to ensure simultaneity. The non-simultaneous crushing involved local ice-force fluctuations and induced a dynamic response in the platform, but had no discernable pattern.

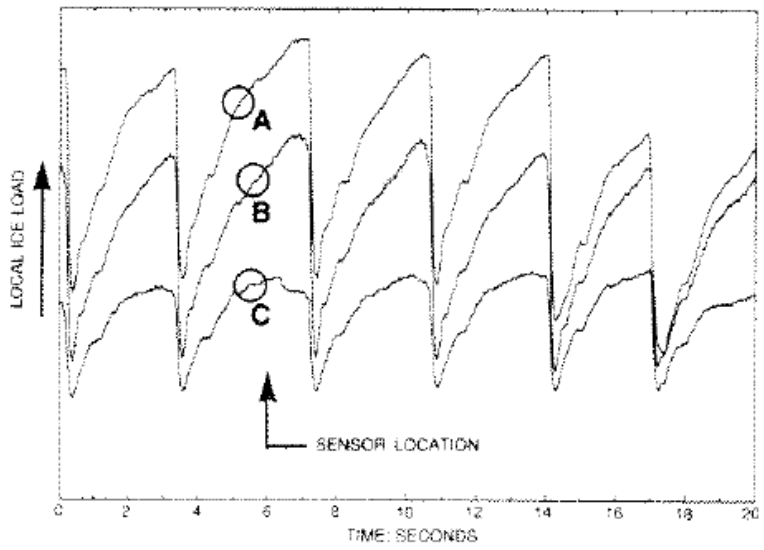

Figure 2.10: Phase locked loading event at Molikpaq (Jefferies and Wright, 1988).

During the medium-scale field tests carried out by Frederking et al. (1990), a total of 11 indentation tests were carried out using different indenters (spherical rigid, circular flat compliant, rectangular flat rigid) and different loading rates (ranging from 0.3 mm/s to 100 mm/s). During these tests, the maximum loading capacity was 3.8 MN at an indentation rate of 2.5 mm/s using a spherical indenter. Sawtooth failure was an essential characteristic of crushing ice failure, as shown in Figure 2.11. The results showed that the slow indentation rates led to creep deformation and micro-cracking to some depth in ice. Large flaking cracks were also observed at the surface. On the other hand, at higher indentation rates, most of the ice failure appeared to be localized near the indenter. Small flakes observed around the perimeter of the contact area formed a thin crushed layer of damaged ice. Thin-sections of ice near the indentation region revealed extensive evidence of recrystallization and localized pressure melting near the central region of the high-pressure zone, as well as extensive fracture and spalling near the periphery of the

indentation site (Frederking et al., 1990; Jordaan, 2001). It was also observed that the pressure near the center were about three times higher than the total pressure over an entire area. Pressures as high as 80 MPa (Frederking et al., 1990) and 50 MPa (Masterson et al., 1993) were reported from these medium-scale indentation tests.

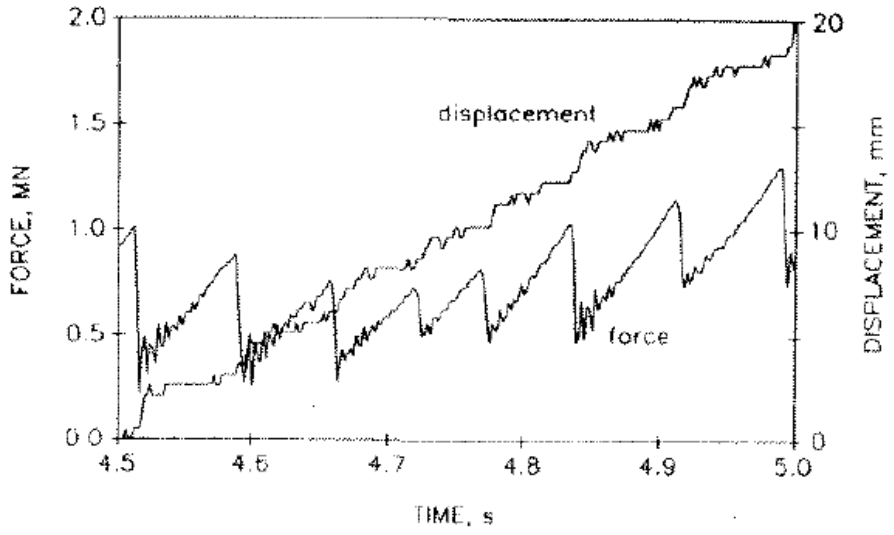

Figure 2.11: Force and Displacement vs Time plot for a test using a spherical indenter at 19mm/s (Jefferies and Wright, 1988).

2.8 Small Scale Indentation Programs

Small-scale laboratory tests are a cost-effective and efficient approach to analyze the complex phenomenon of compressive ice failure and the formation of high-pressure zones and ice crushing dynamics. Comparisons between the medium-scale and laboratory-scale tests performed by Jordaan (2001) and Barrette et al. (2002) respectively show that the mechanical phenomena within the damage layer and the characteristics of the *hpz*s remain relatively constant over different scales. Thus, results obtained from these

tests can be linked to the full-scale ice-structure interaction events. A selection of small-scale indentation tests recently conducted are discussed in this section.

Small-scale confined ice indentation tests were carried out by Barrette et al. (2002) using a spherical indenter (20 mm diameter, 25.6 mm radius of curvature) and freshwater polycrystalline cylindrical ice samples (150 mm diameter, 60-130 mm height). The small scale tests were scaled down by a reduction factor of 50 from the medium scale tests carried out by Frederking (1990) at Hobson's Choice Ice Island. A Materials Testing System (MTS) test frame located in a cold room was used to perform the indentation tests. Tests were carried out at various indentation rates (0.1 mm/s to 10 mm/s) and test temperatures (-2°C, -10°C, -20°C) to determine the effect of different parameters on the formation of high-pressure zones and ice failure behavior. The indented areas of the samples were used to prepare thin sections to study the microstructure of ice and the phenomenon of microcracking and recrystallization.

It was observed that the damage layer extended to a maximum depth of 5 mm below the indented surface. Cyclic loading patterns were observed in all the tests. Also, the indented surface appeared to be dark as compared to surrounding lighter areas due to the crushing of ice. Pulverized ice was observed in almost all of the tests, with radial cracks appearing in some of them. For the tests that were carried out at -2°C, uniform grain refinement was observed along the indented surface with almost no signs of microcracking, whereas, the damage layer for the tests carried out at -10°C consisted of a dense network of microcracks and with heavy recrystallization at the center. Ice samples at -20°C were heavily dominated by microcracking. On analyzing the thin sections, it was observed that

the recrystallized ice was present under all indented surfaces. It was observed that the results obtained from tests at -10°C were nearly identical to the medium-scale tests carried out by Frederking et al. (1990) at -14°C, thus concluding that the failure mechanisms are similar in nature at both scales.

Small scale indentation tests were carried out by Mackey (2005) and Mackey et al. (2007) to study the effects of indenter size, indentation rate and the location of the indentation on the ice failure behavior. Polycrystalline, freshwater ice of an average size of 4 mm and distilled, de-aerated and chilled water were used for the preparation of ice samples. The samples were frozen in a mold at -10°C for three days, after which there were removed and machined to obtain 200x200x100 mm rectangular ice samples. A total of 18 tests were performed by varying indenter sizes (10 mm radius and 12.8 mm radius of curvature; 20 mm radius and 25.6 mm radius of curvature), indenter speeds (slow: 0.1 mm/s, 0.2 mm/s; medium: 1 mm/s, 2 mm/s; fast: 5 mm/s, 10 mm/s) and indentation locations (20 mm, 50 mm and 100 mm from the edge). All the tests were conducted on a Materials Testing System at -10°C. Cameras were used to capture the complete indentation process. Thin sections were further carried out to study the microstructure of the ice and analyze the failure patterns.

On analyzing the results for the indentation tests, it was observed that the large-scale fractures occurred regularly, especially in the case of edge tests and some intermediate tests. The authors also observed some noteworthy similarities and differences due to change in indentation location. The initial slope for loads at same speeds and different locations were almost similar but these slopes change drastically when the distances to

the edge become significant. This led to large-scale fracture and massive load drops as shown in Figure 2.12. The authors suggested a link between some failure behaviors and its implications on the reduction of load. According to the visual records and the data obtained from the tests, the authors inferred that a significant load drop was noticed every time a large-scale fracture or significant spalls were observed. These fractures led to load drops by almost 60% to 80%.

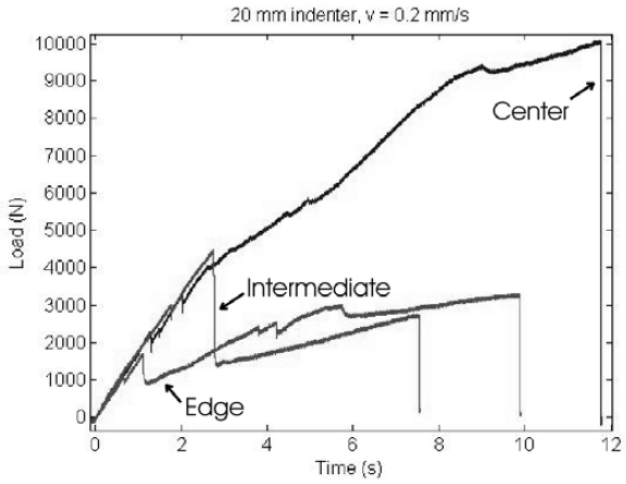

Figure 2.12: Comparison of indentation tests performed at different locations on an ice sample (Mackey et al., 2007).

The small-scale tests performed by Wells et al., (2010) builds on the work carried out by Barrette et al. (2002). A total of 46 indentation tests were performed using an identical 20 mm spherical indenter (25.6 mm radius of curvature) to test on 200x200x100 mm rectangular ice specimens made of polycrystalline ice grains of ~4 mm and distilled, de-aerated and chilled water at -10°C. The major difference between the tests carried out by Barrette et al. (2002) and Wells et al. (2010) was that Wells et al., (2010) used non-confined specimens. All the indentation tests were carried out using a Materials Testing

System at -10°C. The indentation rates ranged between 0.2 to 10 mm/s and the indentation depth ranged between 3 to 20 mm. A tactile pressure sensor was used to record the pressure distribution during the indentation of the unconfined ice sample. This sensor proved useful as it provided key data regarding the load drops associated with individual ice failure processes and dynamic high-pressure zone activity.

On observing the total force and the pressure distribution plots, it was observed that there was a substantial agreement between the two plots except for a few tests. It was also observed that the localized peak pressures were always greater than average pressures recorded at any point during the experiments. The localized pressures ranged anywhere from 2 to 8 times higher than average pressures, but were highly localized and did not remain stationary throughout the test.

The ice failure was categorized and studied in five categories. Figure 2.13 shows the different types of failure modes during an indentation test.

1) The ductile behavior was observed at slow rates (0.2 mm/s) and during this phase there was a steady rise in force and contact area that led to minimal localized spalling and crushing. This phenomenon became less frequent when the indentation rate was increased to 2 mm/s.
2) Wells et al. (2010) described localized spalling as an event in which big chunks of ice break away from the sample that results in a sudden drop in load, extrusion of ice and the loss of contact area. The severity and frequency of localized spalls are directly related to the increase in indentation rates.

3) Isolated crushing was an event in which a loss of total force and pressure was observed due to the extrusion of crushed ice without any negligible change in the contact area. These events were often observed at indentation rates of 2-5 mm/s.

4) According to the author, the cyclic loading events were very rare, making up for only 0.9% of the total duration of the tests. This type of crushing was observed at indentation rates of 2-5 mm/s and often followed the localized spalling failure. During the cyclic crushing, the load showed an increasing trend and were not interrupted by other types of failure events.

5) Mixed mode events were observed in all the tests performed above 2 mm/s indentation speed and were more regular with increasing speed. Mixed mode failure were the events that did not fit the description of the four cases mentioned above. The event was a combination of localized spalls and crushing and the pressure distribution was highly irregular with frequent load drops during crushing and spalling.

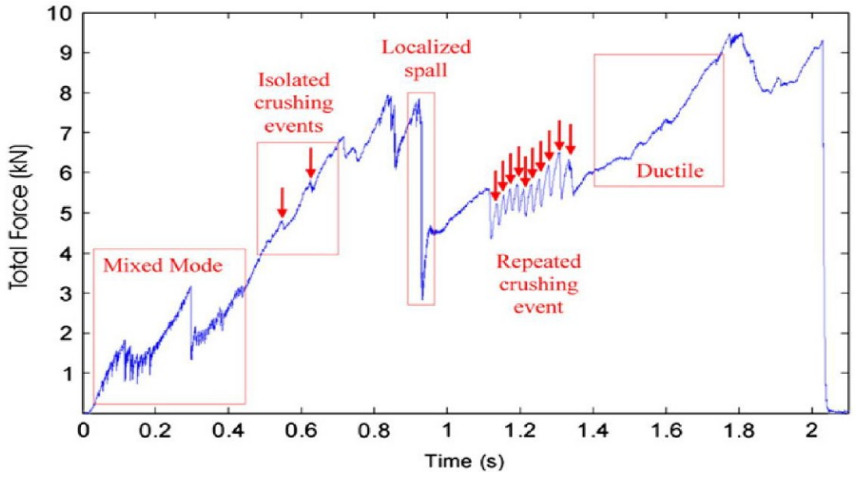

Figure 2.13: Five different failure modes under compressive ice failure (Wells et al., 2010).

Small scale indentation tests were carried out by Browne (2012) and Browne et al. (2013) on confined cylindrical ice samples of different sizes (150 mm and 300 mm in diameter) at temperatures ranging from -5°C to -15°C. Indenters of various sizes (20 mm and 40 mm in diameter) and different indentation systems (two rigid and four compliant) were used to model a single high-pressure zone and study the effects of various parameters on the compressive ice failure. The tests were carried out using a Materials Testing System in a cold room at indentation rates ranging from 2 mm/s to 10 mm/s. Polycrystalline freshwater ice seeds ranging from 2 mm to 5 mm were used for ice sample preparation and the tests were conducted in a cold room at temperatures ranging from -5°C to -15°C. The tests were carried out on six different testing systems; four of which were compliant systems and the other two were rigid systems. Each of the compliant systems had different stiffness, length and natural frequencies whereas the rigid systems were used to eliminate the structural feedback.

The effects of temperature on the ice failure were studied by analyzing the thin sections and the loading patterns (Browne, 2012). Thin sections for warm ice (-5°C) showed that the indented area was heavily recrystallized whereas the cold ice (-15°C) majorly comprised of microfractures. Ice at -10°C showed a mixture of recrystallization as well as microfractures. Analysis of the loading patterns showed that ice failed in a ductile manner with rare spalling events which resulted in a damage layer dominated by recrystallized layer at warm temperatures, while the ice failure at cold temperatures was a combination of crushing and localized spalling that often led to cyclic loading.

Each load drop was associated with a cyclic loading crushing failure mechanism. The average load drops for compliant systems were higher than for rigid systems. A linear relationship was observed between the speed of indentation and the frequency of the cyclic loading pattern. The cyclic loading pattern was significantly higher in the case of compliant systems. This was due to the presence of the structural feedback that led to the storage of energy due to the structural deflection and the eventual sudden release during failure. The relationship was consistent with rigid and compliant systems, though the frequencies were greater for the rigid systems.

Indentation tests on unconfined conical ice specimens were performed by Habib (2014), Habib et al. (2015) to study the compressive ice failure mechanism and the factors that affect the formation of spalling, crushing and high-pressure zones. 28 tests were carried out by varying different factors like grain size (0-4 mm, 4-10 mm), indenter shape (flat plate, spherical), indentation rate (0.1 mm/s, 1 mm/s and 10 mm/s), taper angle of the ice cones (13°, 21° and 30°) and temperature (-5°C, -10°C). The conical ice samples were prepared using different grain sizes and chilled, distilled, deaerated water in a confining mold. The ice sample of 268.8 mm diameter was then shaped at certain angles to form a conical shape in such a way that the top of the ice had a diameter of 25.4 mm. A Materials Testing System was used to test these conical ice samples in a cold room.

On analyzing the effects of indentation rates on the ice failure mechanism, it was observed that ice shows ductile failure at slow rates (0.1 mm/s), as continuous crushing failure with increasing loads were observed. In the case of medium rate (1 mm/s), brittle failure was observed in addition to cyclic loading for the first few seconds followed by

ductile failure. At higher rates (10 mm/s), ductile behavior and cyclic loading were observed throughout the test. Changes in the shape of the ice specimen also had an effect on the failure mechanism and crushing phenomenon. Habib et al. (2015) observed that the ice samples with smaller taper angles (13°) underwent higher forces due to the increase in contact area that led to continuous random spalling and cyclic loading. These ice samples were also dominated by recrystallization due to the high local stresses. As the samples became steeper, the forces reduced considerably and the samples failed due to continuous crushing of the indented area. In the case of the grain size, the samples with smaller grain size were stronger than the larger grain size samples. Warm tests (-5°C) showed ductile failure and the damaged indented area was dominated by recrystallization while the cold tests showed a continuous cyclic loading pattern with huge load drops with microfractures dominating the indented area.

Building on the work of Browne (2012), additional small-scale indentation tests on confined ice samples at -10°C were carried out for compliant and stiff structural configurations using single indenter (O'Rourke et al., 2016 a), and double indenter configurations (O'Rourke et al., 2016 b). Seed ice that ranged between 2 to 3.35 mm and chilled, distilled, deaerated water was used to prepare ice samples in a confined steel cylinder of diameter 154 mm and 150 mm height at -10°C. Two compliant beams of different stiffness, length and natural frequencies were used to perform tests on a Materials Testing System in a cold room set at -10°C. A 20 mm spherical indenter was used at indentation speeds that ranged from 4 to 19 mm/s.

The test data and analysis showed that sawtooth failure was observed in many tests with evidence of locked-in phenomenon in some tests. Regular sawtooth loading was more predominant in the tests that were performed on more flexible beams, whereas the tests with the stiffer beam exhibited different types of failure modes, like continuous crushing with abrupt spalls and irregular sawtooth failure. It was also observed that this sawtooth activity increased with an increase in indentation speed. Locked-in conditions were observed on a stiffer beam at higher indentation speeds when the frequency of the sawtooth failure matched the natural frequency of the structure. These conditions were observed only during the initial phase of the testing when the contact areas were small. The thin sections of the indented ice suggest that the sawtooth failure showed an increase in layer thickness, whereas the locked-in loading involved vibrations within the damaged layer.

Chapter 3: Experimental Setup

3.1 Overview

The medium-scale laboratory tests conducted as part of this research program investigate the effects of structural feedback, indenter size and ice temperature on fracture and spalling when ice undergoes compressive failure.

Some of the questions this research has tried to answer are:

- What are the ice failure processes responsible for the formation and evolution of high-pressure zones during the medium-scale indentation tests?
- How does the change in ice temperature affect the compressive ice failure phenomenon?
- What are the implications of scale effects i.e. the change in indenter size on ice failure?
- What are the implications of structural compliance of the system on the indented ice sample?
- How do the different parameters affect the formation of high-pressure zones and the cyclic loading patterns?
- What are the implications of the results from medium-scale tests for full-scale structures?

The research is divided into two separate phases. The first phase, Phase 1A, is comprised of indentation tests using a compliant beam, whereas the second phase, Phase 1B, is comprised of indentation tests using a rigid beam. Four shakedown tests were carried out before the actual tests. Phase 1A consisted of nine tests and Phase 1B had six tests. Factors like structural feedback, indenter size and sample temperature were varied during the test program.

The sample preparation was carried out in the cold rooms at MUN and C-CORE, while the tests were conducted in the Strength Laboratory at MUN. To study the effects of different parameters on the compressive ice failure phenomenon, relevant data was collected from various sources. These include the use of Resistance Temperature Detectors (RTDs) and a non-contact infrared thermometer for recording the sample temperatures, Linear Variable Differential Transformer (LVDTs) for recording structural deflection and indentation displacement and a load cell to record and calculate the force and pressure distribution at the ice-indenter interface. GoPro® and high-speed cameras were used to capture the ice failure videos, thus providing a visual record of the different ways in which ice fails due to changes in the testing parameters.

3.2 Experimental Design

To study the effect of structural feedback on the ice crushing process, tests were conducted using both compliant and rigid indentation systems. In Phase 1A, a compliant indentation system was used. This indentation system comprised of an indenter mounted on a compliant beam. As the compliant beam deflected elastically when loaded, structural

feedback of the indentation system was analyzed using this beam. Phase 1B, on the other hand, consisted of a rigid indentation system with an indenter mounted directly on a rigid beam. A hydraulic ram was used to push this rigid indentation system. Due to its high stiffness and inability to deflect under load, the indentation tests carried out on the rigid system did not have any structural feedback.

Barrette et al. (2002), Mackey et al. (2007), Wells et al. (2010), Browne et al. (2013) and O'Rourke et al. (2016 a, b) have carried out small-scale indentation tests using various setups. Different studies and observations on the formation and evolution of single and multiple high-pressure zones, the effects of various factors on crushing and compressive ice failure and the in-depth analysis of the failed ice at the microstructural level were carried out in these research programs. The indenters used ranged from 10 mm to 40 mm with the indentation speeds varying between 0.1 mm/s to 19 mm/s. All the tests mentioned above were scaled down version of medium-scale field tests carried out by Frederking et al. (1990) at Pond Inlet, Canada.

Temperature effects, scale effects and the role of structural feedback on the compressive ice failure were the primary focus of the small-scale indentation tests performed by Browne (2012) and O'Rourke et al. (2016 a, b). The experiments performed in the present research program were medium-scale indentation tests using confined ice samples. These tests were also based on the work carried out by Frederking et al. (1990), and the indenters used during testing were scaled down by a factor of 20 (50 mm indenter), 10 (100 mm indenter) and 6.67 (150 mm indenter). Polycrystalline, freshwater ice was used due to its uniform microstructure. The use of polycrystalline ice was also beneficial in

terms of comparative studies as most of the earlier small-scale indentation programs were carried out using polycrystalline ice samples. Cylindrical ice holders (1000 mm diameter x 500 mm height) were used for preparing the confined ice samples as shown in Figure 3.1.

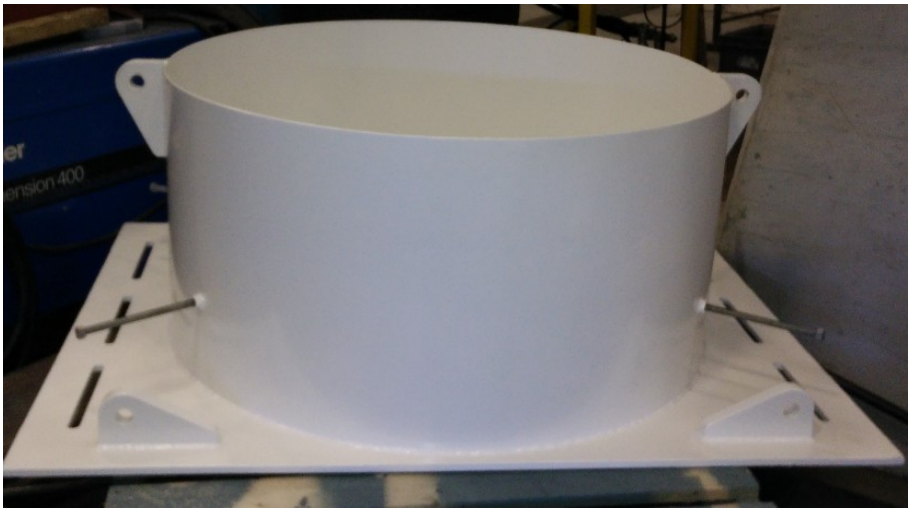

Figure 3.1: Ice holder, 1000 mm in diameter, used for preparing ice specimens.

3.2.1 Test Plan Design

During the testing, some factors of the experiments were varied while keeping the others constant. The medium-scale tests performed in this research program were mainly focused on studying the effect of temperature, indenter size and structural feedback on the formation and the evolution of high-pressure zones that eventually result in compressive ice failure and cyclic loading patterns.

Ice Temperature: To study the temperature effects, all the tests were carried out at two different temperatures. Eight samples were tested at approximately -5°C (warm

temperature) and seven samples were tested at approximately -20°C (cold temperature). However, it should be noted that while attempts were made to maintain the target temperatures, not all the samples were tested at the exact temperatures. Since the Strength laboratory was at room temperature despite insulating the specimens, over time there was a gradual increase in the sample temperatures. The ice sample temperatures for the warm tests ranged from -1°C to 7°C while the testing temperatures for the cold tests ranged from -14°C to -19°C. RTDs and a non-contact infrared thermometer were used throughout the tests to measure the actual temperatures during the testing phase. These temperatures were chosen in order to observe and compare the ice failure modes for warm and cold ice.

Indenter Size: Three different indenter sizes were used to study the scale effects on the formation of high-pressure zones and cyclic loading phenomenon. 50, 100 and 150 mm diameter indenters were designed with a radius of curvature of 64, 127 and 192 mm respectively. Six tests with the small indenter (50 mm diameter), five tests with the medium indenter (100 mm diameter) and four tests with the large indenter (150 mm diameter) were carried out during the program. The specifications and the photographs of the indenters used are provided in Table 3.1 and Figure 3.2 respectively.

Table 3.1: Indenter specifications.

Diameter (mm)	Radius of Curvature (mm)	Indenter Height (mm)	Nominal Surface Area (m^2)
50	64	90	1.96×10^{-3}
100	127	90	7.85×10^{-3}
150	192	60	17.6×10^{-3}

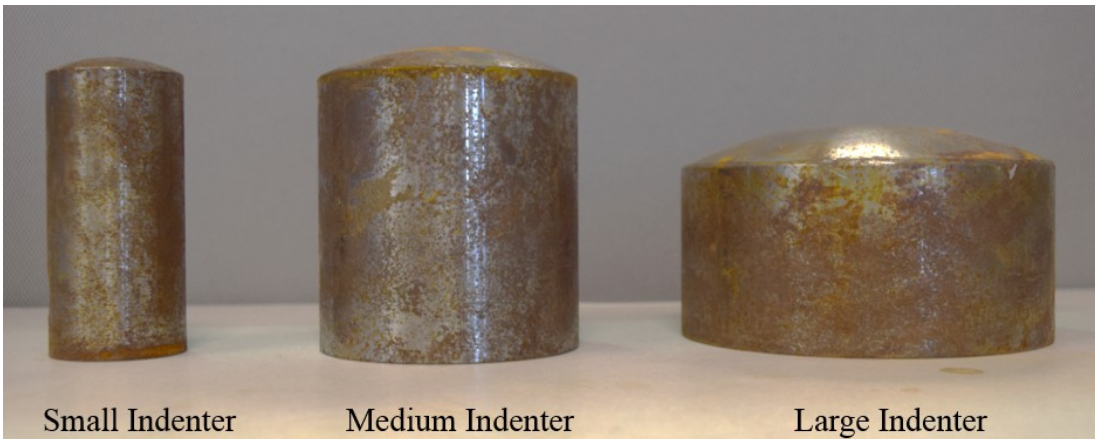

Figure 3.2: Different indenter sizes used for the medium-scale tests.

Structural Compliance: In practice, there are no perfectly rigid structures, since all real structures deform to some extent. Ice-structure interactions on full-scale structures, therefore, will always increase the presence of some structural response (i.e. energy is stored in the structure in the form of elastic deflection during the loading phase and this energy is released through ice failure during the unloading phase). To study the interaction between ice failure and structural response, a 2.28 m long W8x21 mild steel I-beam was used selected as an appropriate compliant beam based on the anticipated structural loading range during the Phase 1A of ice crushing dynamics tests. To analyze the crushing and failure phenomenon in the absence of significant structural feedback, a

3.91 m W12x170 mild steel I-beam was selected as a rigid base beam for Phase 1B of the ice crushing dynamics tests.

Other factors, such as the indentation rate, grain size, sample size and sample shape were constant throughout the tests. All the tests were carried out at a constant indentation speed of 2.5 mm/s, which was the maximum speed possible for the current test apparatus.

To capture variability in temperatures, the sample's surface temperature and the indenter temperature were measured throughout the test, as is discussed below.

3.2.2 Overview of Test Set-up

The test apparatus for this research program was located in the Strength Laboratory at Memorial University of Newfoundland. The apparatus consisted of the following:

- Concrete structure
- Self-reacting frame
- Instrumentation
- Data acquisition system
- Ice holder
- Indentation system

The concrete slab testing apparatus was used as the starting base structure for this testing program. This structure consisted of four concrete pillars on which the self-reacting frame was mounted. The upper and lower support rings rested on these four pillars. These support rings were assembled and aligned with the ram mount assembly, providing

additional support to the entire testing frame. Pillar reinforcement plates were mounted on two of these concrete pillars to provide additional strength and redistribute intense local ice loads across the face of the concrete structure. These plates were also used as a mounting assembly for the ice sample holder. The hydraulic ram was mounted on the ram mount assembly between the other pair of concrete pillars.

The self-reacting frame consists of an upper support ring and a lower support ring. Each support ring consists of four girders bolted together surrounding the concrete structure. Four 305x305 mm columns and ring stiffeners were bolted to these eight main girders, two on the top and two on the bottom. The upper and lower girders were connected by two 152x152 mm box beams on each side. Two 100 mm schedule 80 rails were horizontally mounted on the box beams on both the sides of the structure. Four guide bushings with Teflon sleeves were mounted on all four rails to ensure smooth movement across the rails. These bushings were bolted together to a rigid beam that was attached to either a compliant beam (Phase 1A) or directly to an indenter (Phase 1B). Figures 3.3 and 3.4 illustrate the CAD drawing and the actual test setup for this research program.

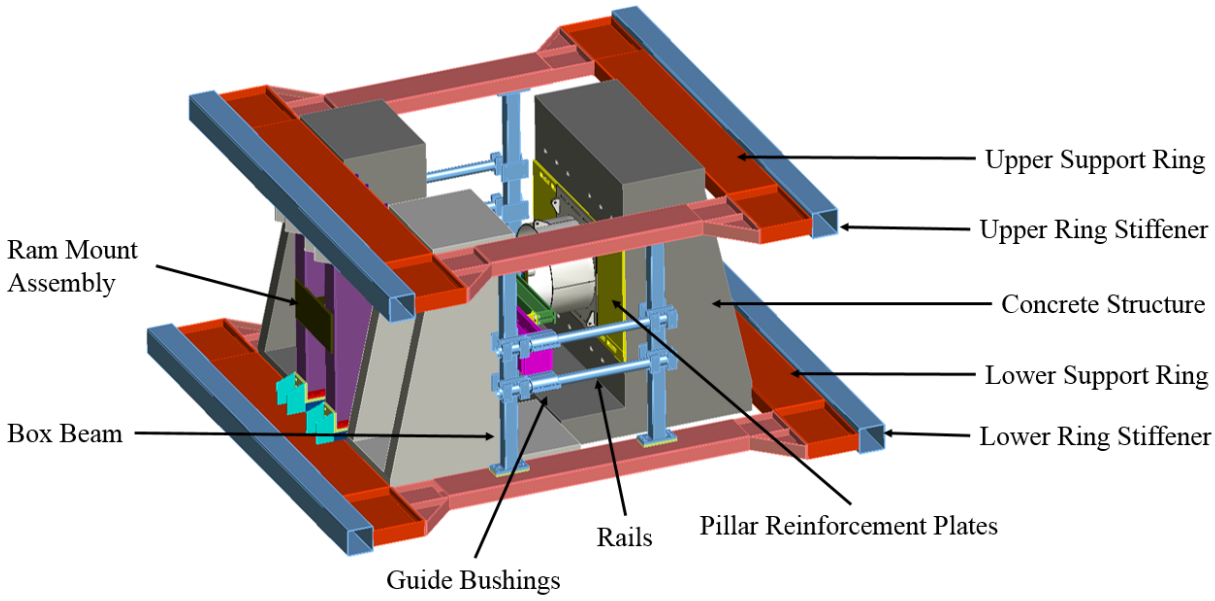

Figure 3.3: CAD drawing of the test apparatus.

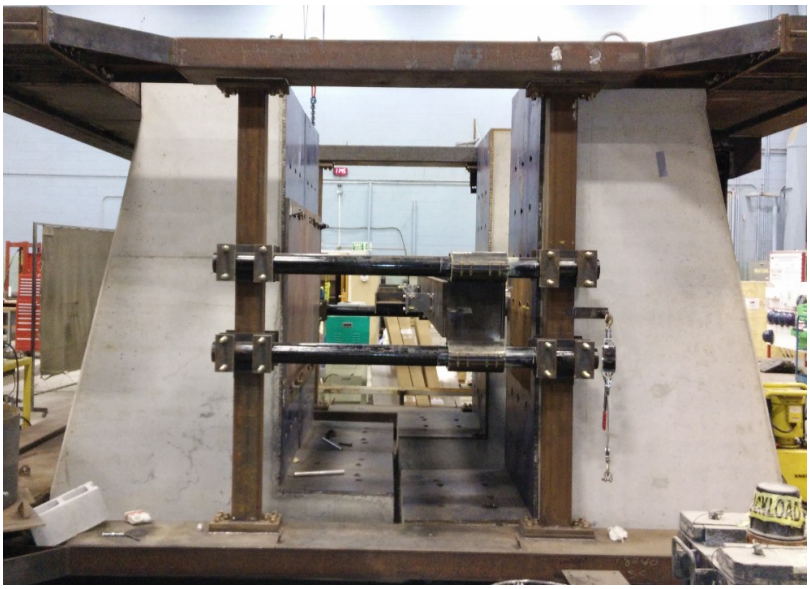

Figure 3.4: Side view of the test apparatus.

3.2.3 Test Structure for Phase 1A

3.2.3.1 Indentation system for Phase 1A

During this first phase of the tests, a compliant beam was used in the indentation system. The aim of using a compliant beam was to study the compressive ice failure and ice crushing dynamics in the presence of structural feedback.

Two beams were used for the Phase 1A indentation system setup, a compliant beam (test beam) and a rigid beam (support beam). A 2.28 m long W8x21 mild steel I-beam was used as a compliant beam that had a design load of 444.82 kN and maximum allowable elastic deflection of 45.72 mm. The compliant beam was mounted to a 3.91 m W12x170 mild steel rigid I-beam using two flex links made of SAE 4140 alloy steel. The indenter was mounted on an indenter base plate that connected to a load cell mounted on a load cell base plate. The whole assembly was attached to the complaint beam using two flex links. Each flex link (flange dimensions 127x127x12.7 mm) had a maximum allowable deflection of 0.04318 mm and a maximum allowable load of 444.82 kN. The rigid bas beam had a maximum allowable deflection of 3.556 mm and a design limit load of 1334.5 kN. The rigid beam was mounted on guide rails that provided lateral forces needed to maintain alignment during indentation. To ensure smooth movement across the rails, the beam was bolted by four guide bushings with Teflon sleeves.

Table 3.2 shows the dimensions, stiffness values and natural frequencies for the W8x21 compliant beam and W12x170 rigid beam. These design values were calculated using

simply-supported beam equations and verified by performing frequency tests on the beams.

Table 3.2: Properties of rigid and compliant beams.

Beam Type / Properties	Compliant	Rigid
Length (m)	2.28	3.91
Mass (kg)	71.3	963.88
Theoretical Stiffness (N/m)	8.84E+06	8.842E+08
Actual Stiffness (N/m)	9.729E+06	3.842E+08
Theoretical Natural Frequency (Hz)	120	89.5
Actual Natural Frequency (Hz)	107	65

An electric pump (Enerpac GPEx5 series) was used to power the high capacity hydraulic ram (Enerpac CLRG 50012) located between the two concrete columns behind the rigid beam. The hydraulic pump had a reservoir capacity of 40 liters, a flow rate of 2 l/min and a maximum operating pressure of 70 MPa. The ram had a loading capacity of 4.5 MN, a maximum speed of 2.536 mm/s and a maximum stroke of 70 cm. The hydraulic ram was used for the horizontal displacement of the compliant beam and the indenter. A remote control is used to operate the hydraulics, which allowed the team to remain at a safe distance from the structure and the ice sample during tests. Figures 3.5 and 3.6 illustrate the CAD drawing and the actual setup for the Phase 1A indentation system.

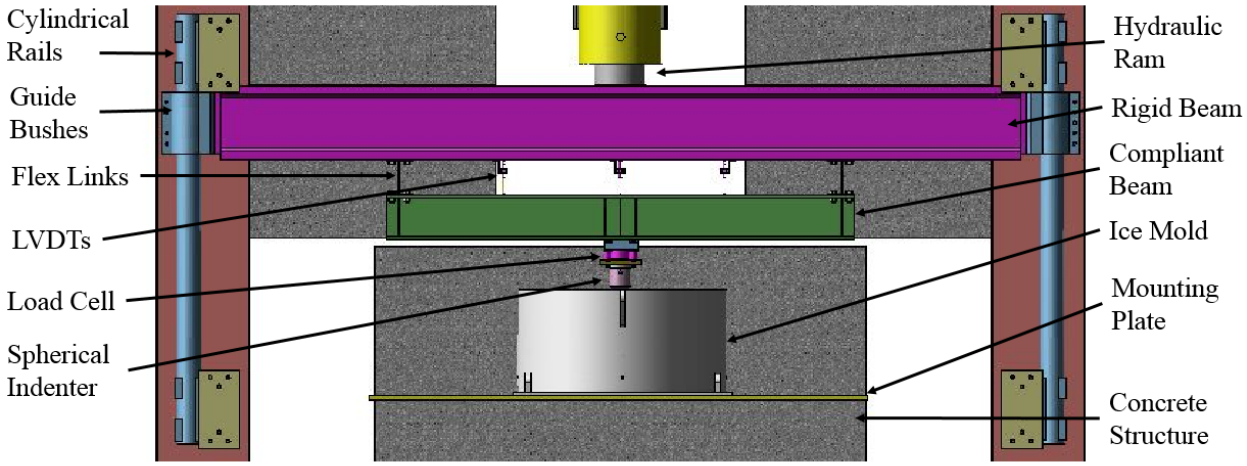

Figure 3.5: CAD drawing of the Phase 1A indentation setup.

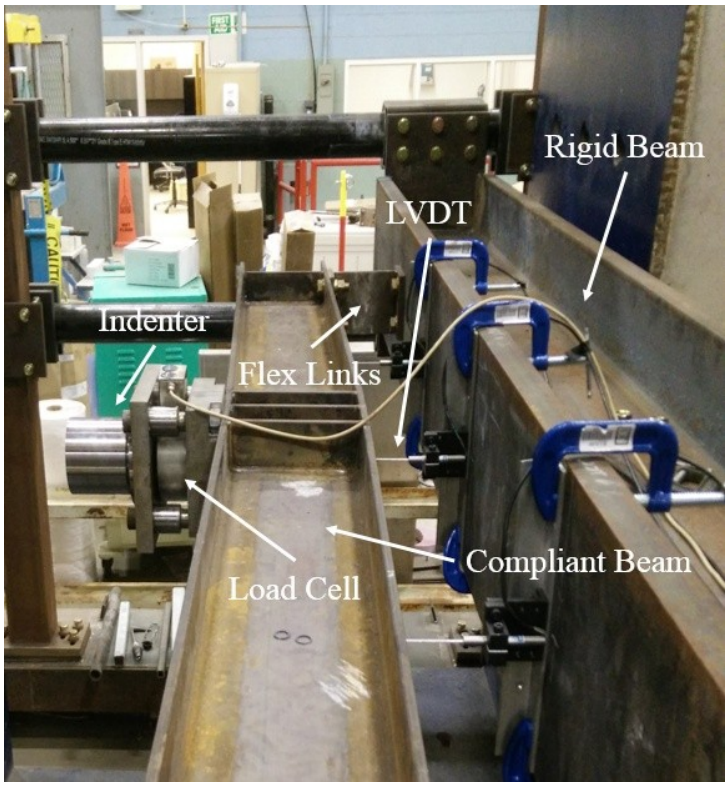

Figure 3.6: Phase 1A indentation setup.

In addition to studying the effects of structural feedback on compressive ice failure, effects of other factors such as ice-sample temperature and indenter size were also

analyzed. Though all nine tests were carried out using the same compliant beam, each test had a unique combination of ice temperature and indenter size. Besides the six tests that were initially planned, an extra three tests were repeated due to some errors in the tests that are discussed below. Three indenters fabricated from SAE 4140 alloy steel were used for the indentation tests.

3.2.3.2 Instrumentation for Phase 1A

Various instrumentation and data recording devices were used during the Phase 1A indentation tests. Structural response, force, indentation rate, surface and subsurface temperatures of ice were measured using a data acquisition system.

Structural response of the compliant system and the indentation displacement were measured using an array of linear variable differential transformers (LVDTs). The LVDTs used for the Phase IA tests were Series 330, Model 0337-0000, A.C. LVDTs and MHR series, Model MHR 500, A.C. LVDTs. Series 330 LVDTs had a working range of ±25.4 mm, maximum non-linearity of < ±0.20% and an operating temperature range between -20°C and 80°C. These LVDTs were used to measure the indentation displacement i.e. the distance traveled by the indenter into the ice sample. The MHR series, Model MHR 500 LVDTs had a stroke range of ±12.7 mm, maximum non-linearity of < ±0.25% and an operating temperature range of -55°C to 150°C. These LVDTs were used to measure the structural deflection of the compliant beam.

Ice strength has a strong dependence on the loading rate and the structural response. Thus data collected from these LVDTs were of significant interest. Three MHR series LVDTs

were installed between the compliant beam and the rigid beam assembly as shown in Figure 3.7. These LVDTs were used to measure the deflection of the compliant beam. The deflection of the compliant beam was useful in determining the effects of indenter size and the relative indentation rate on the loading phenomenon in ice. The LVDTs were positioned in a row along the length of the compliant beam, with the central LVDT located directly at the center of the compliant beam and the other two LVDTs spaced at a distance of 560 mm from the center. The LVDTs were bolted on an aluminum slab and clamped to the compliant beam using two C-clamps. The Series 330 LVDT was used to measure the distance traveled by the indenter inside the ice sample. This LVDT was bolted to an aluminum slab and clamped to the compliant beam using three C-clamps behind the rigid beam, besides the hydraulic ram.

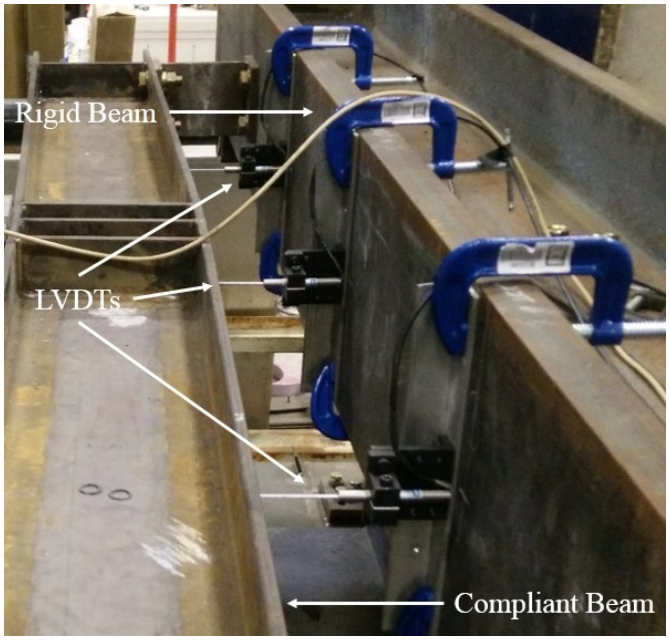

Figure 3.7: Three MHR series LVDTsinstalled between the compliant beam and the rigid beam.

A load cell was used to measure loads at the ice-indenter surface. This LGP 312 - Pancake Load Cell was mounted on a load cell base plate located between the indenter and the underside of the compliant beam. The pancake load cell is a compression-only load cell with a load capacity of 445 kN. Figure 3.8 shows the indenter, the indenter base plate and the load cell mounted on a load cell plate. The calibration records for the pancake load cell and the four LVDTs are included in Appendix B.

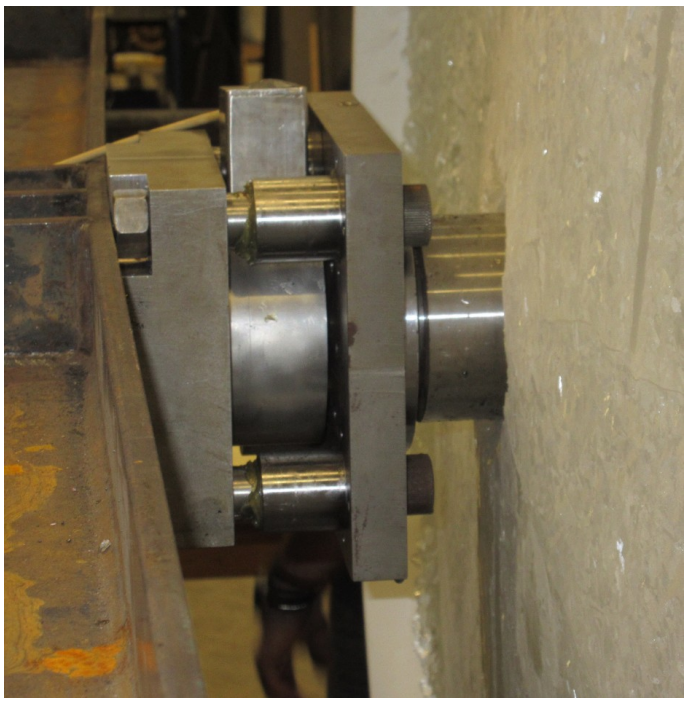

Figure 3.8: Load cell mounted on the indenter assembly

The temperature variations in the ice sample during the indentation tests were measured using resistance temperature detectors (RTDs). The probes of the two RTDs were placed at 30 and 50 mm under the ice surface at a distance of approximately 150 mm from the center of the ice sample. The RTDs used for Phase 1A were Model 12590-6, manufactured by the RTD Company. The operating temperatures of the RTDs ranged

from -30°C to 100°C. The RTDs also had an accuracy of ±1 °C. To ensure the accuracy of the temperature measurement, each RTD was calibrated at different temperature ranging from -5°C to 80°C. Figure 3.9 shows the location of the RTDs in of the samples before the indentation tests.

Figure 3.9: RTD probes placed in an ice specimen.

A Mastercraft Non-Contact InfraRed Thermometer was used to measure the surface temperature of the ice sample before and after every test. The range of the thermometer ranged from -50°C to 538°C while the operating temperature ranged between 0°C and 50°C. The thermometer had an accuracy of ±2°C.

A Panasonic Toughbook CF-53 installed with the Catman Easy AP DAQ software was used for the data acquisition of the four LVDTs, two RTDs, the high-speed camera trigger and one load cell. A QuantumX MX840A data acquisition system was used to capture the data at a sampling rate of 4800 Hz.

A high-speed camera (Olympus i-SPEED TR) and two GoPro® 3+ cameras were used to capture test videos at 200FPS and 30FPS respectively. The high-speed videos had a detailed view of the indenter and the ice surface that allowed the study of the failure behavior of ice during indentation. The GoPro® videos captured the entire indentation system including the structural feedback of the compliant beam and the ice failure behavior. Though the high-speed camera was used only for the shakedown tests, the regular video provided sufficient details about the ice failure processes and the spalling phenomenon. A point-and-shoot camera (Canon® PowerShot ELPH 340 HS) was used to capture images during the different stages of ice formation, ice sample setup, indentation test and post-test sample analysis.

3.2.4 Test Structure for Phase 1B

3.2.4.1 Indentation system for Phase 1B

During the second phase of the indentation tests, a rigid beam was used in the indentation system. The aim of using a rigid beam was to study the ice failure behavior and the formation of high-pressure zones and cyclic loading in the absence of significant structural response. For these tests, the indenter was mounted directly on the rigid beam to minimize the structural feedback during indentation. This absence of significant structural feedback during indentation tests is the basic distinction between Phase 1A and Phase 1B.

The indenter and indenter base plate were directly mounted on the same rigid base beam used in Phase 1A. A 350 mm long schedule-100 6061 aluminum cylinder attached to two

305x305x10 mm 6061 aluminum flanges was used as a spacer to provide additional clearance between the hydraulic ram and the rigid beam. The rigid base beam was connected to an aluminum spacer to provide the additional clearance. The hydraulic ram pushed the aluminum spacer, which in turn helped the rigid beam to move forward during the indentation. The rigid beam carried and endured lateral forces. To ensure smooth movement across the rails, the beam was bolted by four guide bushings with Teflon sleeves. Figures 3.10 and 3.11 illustrate the CAD drawing and the actual setup for the Phase 1B indentation system.

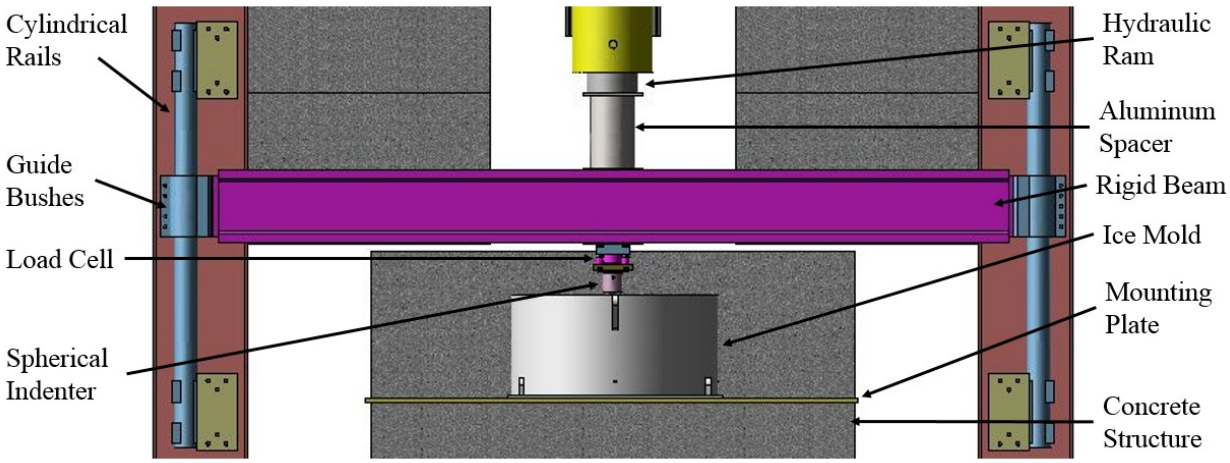

Figure 3.10: CAD drawing of the Phase 1B indentation setup.

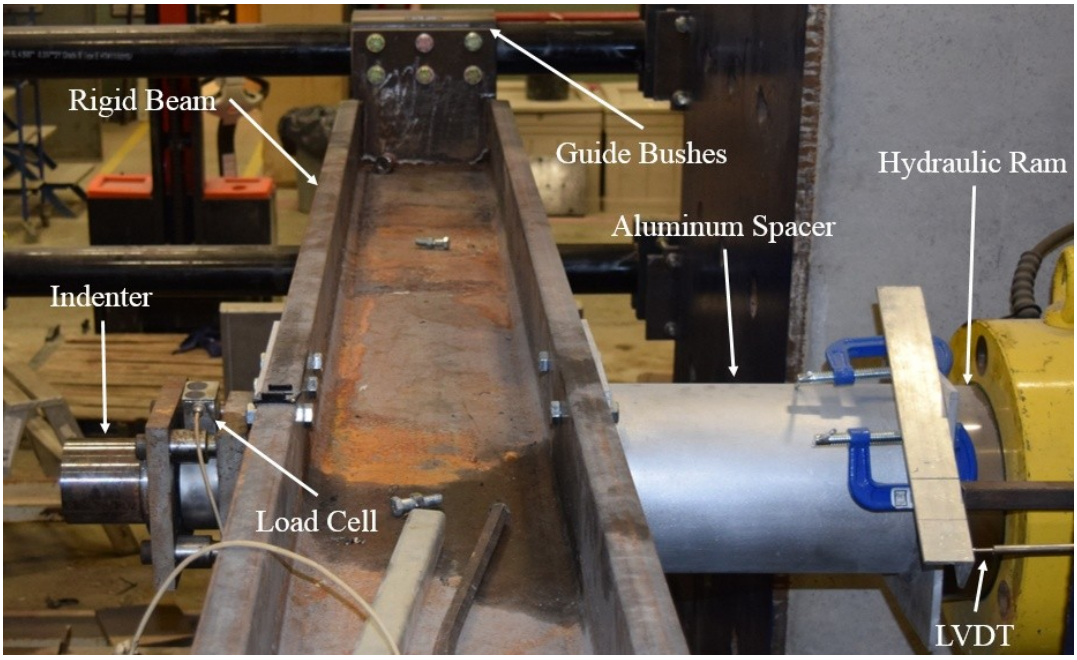

Figure 3.11: Phase 1B indentation setup.

For Phase 1B, the same three sizes of indenters were used i.e. small indenter (50 mm), medium indenter (100 mm) and large indenter (150 mm). Other components of the apparatus, such as the hydraulic pump and hydraulic ram were the same for both the test phases.

3.2.4.2 Instrumentation for Phase 1B

Various instrumentation and data recording devices were used during the Phase 1B indentation tests. Factors such as structural response, force, indentation rate, surface and subsurface temperatures of ice and ice failure mechanisms were recorded using the data acquisition system. The instrumentation for the rigid beam tests was reduced due to the absence of structural response.

Due to absence of structural compliance, the three MHR series LVDTs were not used. Only one LVDT was used for the rigid tests. Similar to the Phase 1A tests, this LVDT was a Series 330, Model 0337-0000, A.C. LVDT used to measure the distance traveled by the indenter inside the ice sample. This LVDT was bolted to an aluminum slab and clamped around the hydraulic ram holder using C-clamps behind the aluminum spacer as shown in Figure 3.12.The LGP 312 - Pancake Load Cell was mounted on a load cell base plate located between the indenter and the rigid beam. The compression-only pancake load cell was the same load cell used for the compliant beam tests. The RTDs and the non-contact thermometer used during the Phase 1A tests were again used for the Phase 1B tests to record the surface and the sub-surface temperatures of the ice sample.

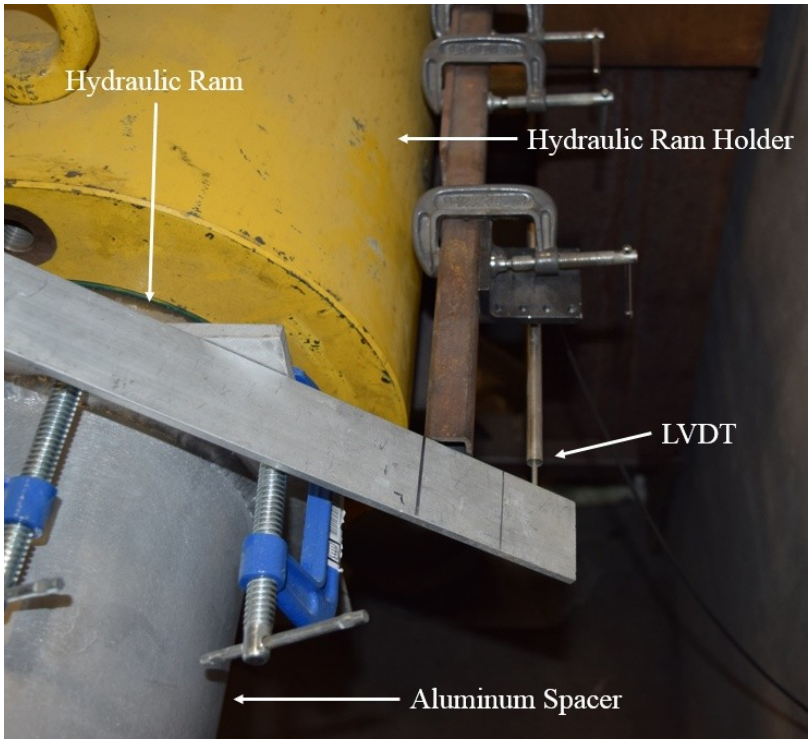

Figure 3.12: Series 330 LVDT bolted clamped around the hydraulic ram.

A Panasonic Toughbook CF-53 installed with the Catman Easy AP DAQ software was used for the data acquisition of one LVDT, two RTDs and one load cell. A QuantumX MX840A data acquisition system was used to acquire data at a sampling rate of 4800 Hz in Phase 1A. Two GoPro® 3+ cameras were used to capture test videos at 30FPS. These GoPro® cameras captured the indentation tests and the ice failure behavior. A point-and-shoot camera (Canon® PowerShot ELPH 340 HS) was used to capture images during the different stages of the ice formation, ice sample setup, indentation test and post-test sample analysis.

3.3 Ice Sample Preparation

The cold room facilities at C-CORE and MUN were used throughout the project to prepare and store the ice samples. All the tests in this research program used confined ice samples. Freshwater, polycrystalline ice specimens were used for all the tests. Figure 3.12 (a) shows the commercially purchased, bubble-free, sculptor's ice cubes used for the ice sample preparation. Tap water used for the ice sample preparation was chilled at 0°C.

(a) (b) (c)

Figure 3.12: Types of ice used during the ice sample preparation (a) ice cubes, (b) crushed ice, (c) sieved ice

The ice sample preparation took place in two stages. During the first stage, 250 mm of the ice holder was filled with ice cubes and chilled water. Ice cubes and water were stirred thoroughly to remove the air bubbles from the mixture. The ice holder was covered with insulation to prevent bulging and cracking of ice. Insulation also helped in the unidirectional ice growth, thus allowing air to be pushed upwards during freezing. The sample was allowed to freeze for three days. Figure 3.13 (a) shows the first stage of the ice sample preparation before freezing while Figure 3.13 (b) represents the frozen ice sample at the end of the first stage.

(a) (b)

Figure 3.13: First stage of ice preparation (a) before freezing, (b) after freezing.

The second stage required sieved ice and chilled water. Crushed ice was obtained by crushing the ice cubes using a commercial ice crushing machine (Clawson Hail Queen Model HQ-C Ice Crusher) in the cold room at MUN. Figures 3.12 (b) shows the crushed ice. The crushed ice was sieved using a 4-10 mm sieve to obtain ice seeds ranging from 4 mm to 10 mm as shown in Figure 3.12 (c). These ice seeds were used to prepare the next

stage of the ice sample. After filling the ice holder with sieved ice and chilled water for 200 mm, the mixture was allowed to freeze for three days. Precautions were taken to remove the air bubbles from the mixture. Before this layer was frozen, two RTD's were placed inside the mixture, one at 30 mm deep and the other at 50 mm deep, both located at about 150 mm from the center of the ice sample. One day before the test, a hot plate was used to smooth the surface of ice specimen and remove the irregularities. Figure 3.14 (a) shows the second stage of the ice sample preparation before freezing while Figure 3.14 (b) represents the frozen ice sample at the end of the second stage.

(a) (b)

Figure 3.14: Second stage of ice preparation (a) before freezing, (b) after freezing.

3.4 Testing Procedure

Fifteen tests were conducted using the test apparatus installed in the Strength Laboratory at MUN. Tests were conducted at room temperature that ranged between 14°C and 20°C. Before the ice sample was brought in for testing, the testing equipment and the

instrumentation was already prepared to reduce the testing time and prevent the ice sample from melting.

LVDTs, RTDs and load cells were connected to the data acquisition system using VGA cables. The GoPro® cameras and a flood light were installed before the ice sample was mounted. The ice sample was moved from the cold room to the Strength Laboratory using a forklift. The sample was lifted using an industrial crane and aligned to the mounting plate attached to the concrete structure. The ice sample was bolted to the mounting plate and positioned to allow the indenter to make contact with the ice sample at the center. The ice holder was attached to the crane throughout the testing process for safety purposes. The ice sample was insulated during the entire installation process.

The indenter used for the test was stored in the cold room along with the ice sample. To prevent the test results from getting affected due to the temperature difference between the indenter and the ice sample. The indenter was brought to the Strength Laboratory in an ice cooler and stored at sub-zero temperatures. The indenter was installed on the indenter holder assembly just before the ice sample was aligned and bolted to the concrete structure. Ice packs were placed around the indenter to maintain its low temperature.

The final steps included the removal of the thermal insulation from the ice holder and bringing the indenter closer to the ice sample. The LVDTs and load cells were adjusted and reset to zero, and the subsurface temperatures of the surface as indicated by the RTDs were noted. A non-contact thermometer was used to check the temperatures of the

indenter and the ice sample surface before and after each test. Figure 3.15 shows the final image of the test setup, right before the indentation of the ice sample commenced.

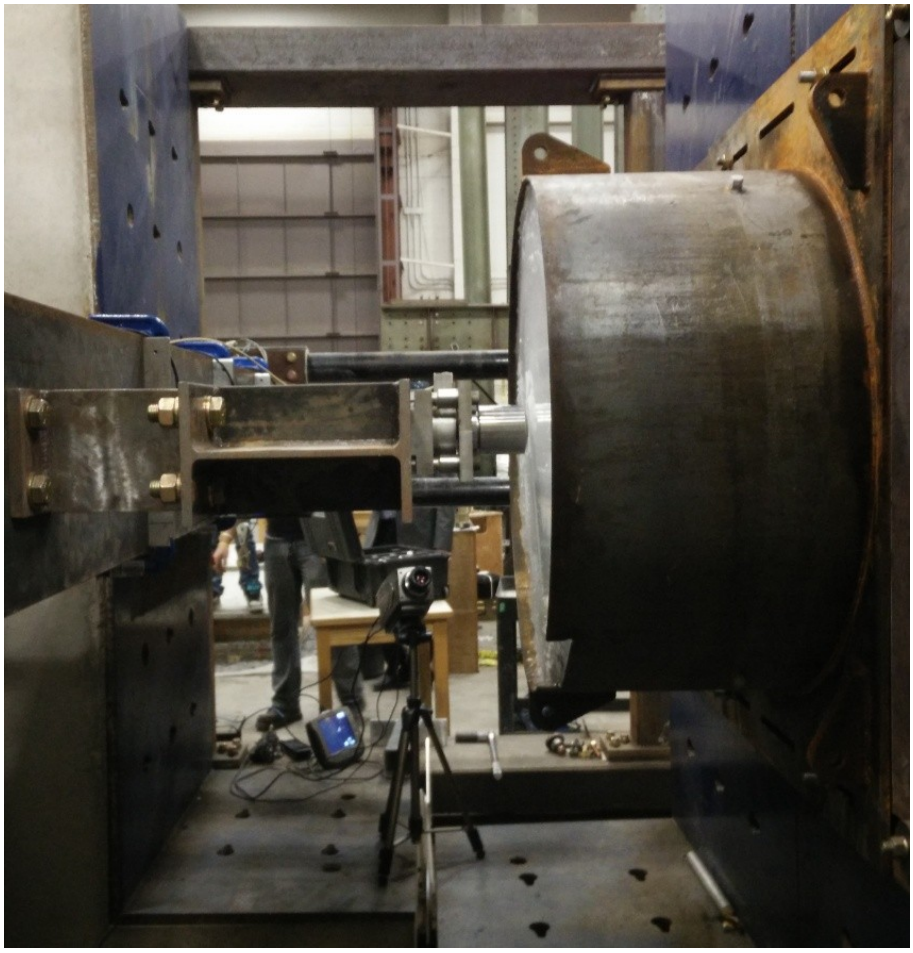

Figure 3.15: Ice sample mounted and ready to be tested.

At the beginning of each test, the Catman DAQ software was used to record load, displacement and temperature recordings simultaneously. At the same time, the video recordings were captured using the GoPro® app. The start time and the end time for each test were noted for further analysis. The hydraulic pump used to push the hydraulic ram was operated using a remote control. Each test was conducted at a uniform indentation

speed of 2.5 mm/s. Data was collected at a sampling rate of 4800 Hz. The indenter temperature and ice surface temperature were noted at the end of each test.

Following each indentation test, the hydraulic ram was backed away from the ice holder and the specimen was removed from the mounting plate. A point-and-shoot camera was used to take detailed pictures of the indented area and the different failure processes that occurred during indentation.

3.5 Shakedown Tests

Shakedown tests are conducted to identify opportunities for improvement and remove any discrepancies in the testing procedure before the main tests are performed. These preliminary tests are also carried out to determine if the apparatus is working properly. Four shakedown tests were conducted by varying different attributes such as sample preparation procedure, sample temperatures and the ice size used for the ice samples. Besides improving ice preparation procedures, improvements in testing, data analysis and post-processing procedures were also identified. Table 3.3 shows a comprehensive list of all the shakedown tests, the mistakes identified in each test and the corrective action applied to them. All these tests were performed at a speed of 2.5 mm/s using a 100 mm spherical indenter on a compliant beam indentation system.

Table 3.3: Shakedown tests

Test No.	Test Specifications	Issues Identified	Suggested Improvements
1	Shakedown test at -1°C	Sample prepared in a single stage.	Samples to be prepared in multiple stages.
		Sample was not insulated that led to the bulging and cracking.	Samples to be insulated to avoid cracking of ice and promote bottom-up freezing.
		Sample was prepared at -1°C, very close to the melting point.	Ice samples to be prepared at -5°C, -10°C and -20°C.
		No indentation test was carried out due to the warm ice and cracks on the surface of the ice sample.	
2	Shakedown test at -10°C	Sample was prepared in three stages that led to non-uniform ice formation.	Sample to be prepared in two stages: ice-cubes for first 250 mm and crushed ice for next 200 mm.
		Indentation was carried out in steps, rather than at a constant increment to check the loading capacity.	Constant uniform indentation to be carried out for actual tests.
		Friction near the guide bushings during indentation.	Guide bushings to be checked for friction and realigned.

3	Shakedown test at -20°C	Sample was prepared in two stages with insulation.	Two stage ice preparation method was finalized.
		Default sampling frequency was 50 Hz. This sampling rate was very low for these tests.	Tests to be performed in order to determine the perfect sampling rate.
		Neither surface temperature nor the variation in temperature during testing were recorded.	RTDs and non-contact thermal gun to be used for recording the temperature profile of ice samples.
4	Frequency Tests	Sampling rate of 50 Hz did not provide any information about the local spalling and smaller load drops.	Performing frequency tests by hitting a hammer on the indenter and recording the response at different sampling rates was suggested.
		Based on previous tests, higher sampling rates of 4800 Hz and 9600 Hz were selected.	Comparative tests were performed by recording the hammer hits at 50 Hz, 4800 Hz and 9600 Hz respectively.
		50 Hz sampling rate did not provide vital data whereas the 9600 Hz sampling rate provided good data but with added noise that could distort the results. 4800 Hz sampling rate proved to be the best option.	4800 Hz sampling rate was selected for the test as they provided intricate details without compromising the data due to the minimal added noise.

		It was difficult to find the actual natural frequency for the compliant and rigid beams due to the low sampling rate.	Sampling rate of 4800 Hz was used to find the actual natural frequencies of both beams.
5	Shakedown test at -5°C	No faults were identified. The test was successful. Constant and continuous indentation of ice was recorded throughout the test.	The testing method was finalized.
		Previous tests suggest that tests at -20°C and -10°C give similar results.	Tests at -5°C and -20°C were finalized.
		The indenter used for the test was at room temperature. The temperature difference between the ice specimen and the indenter could have affected the ice failure behavior.	Indenters were to be chilled at sub-zero temperatures to avoid any changes in the loading due to the heat transfer between the indenter and the ice sample.

As shown in Table 3.3, the shakedown tests proved to be helpful in recognizing and resolving initial issues faced during the pre-testing and testing phase. Each test revealed some opportunities for improvement during the ice preparation method, the actual testing phase and the post-processing operations.

Figure 3.16 shows the plots acquired from the frequency tests performed to select the sampling rate for the indentation tests. Figure 3.16 event (a) and Figure 3.17 illustrate that

the 50 Hz sampling rate was inefficient as it did not capture crucial data when a hammer was hit against the surface of the indenter. Not only was the hit barely recorded, but the data required to determine the natural frequency was also not acquired. Figure 3.16 event (b) and Figure 3.18 show the plot comparing the data obtained from 4800 Hz and 9600 Hz sampling frequencies. The plot focuses on the data that was recorded when the indenter was at an idle state i.e. no external force was applied. As seen, the data acquired from the 9600 Hz sampling frequency had a greater tendency to record high frequency noise when compared to the 4800 Hz sampling rate. There were no additional benefits of using a higher sampling rate than 4800 Hz since the hammer hit was recorded appropriately and the natural frequencies could be readily calculated without the addition of excess noise.

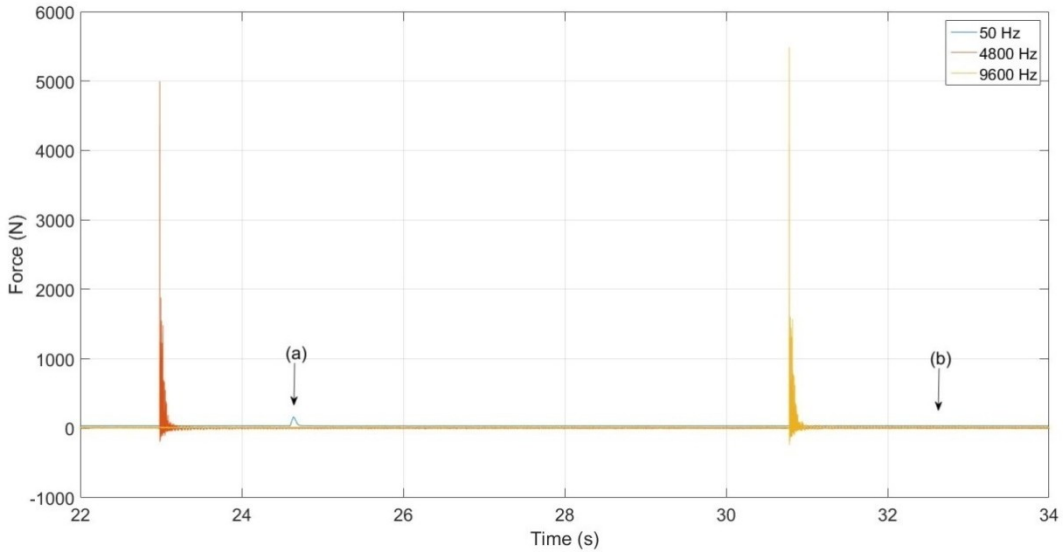

Figure 3.16: Frequency tests performed at different sampling rates.

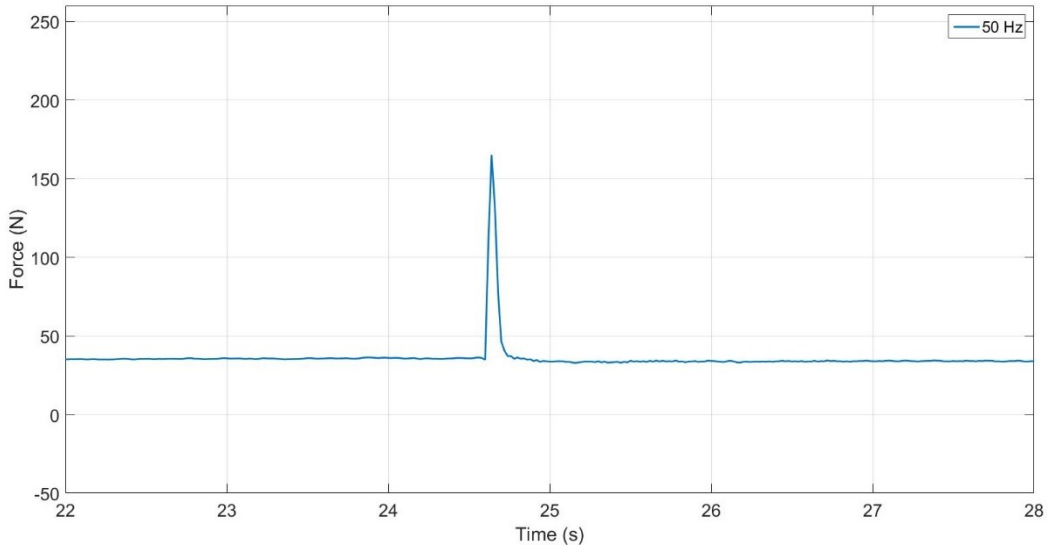

Figure 3.17: Frequency tests performed at 50 Hz sampling rate.

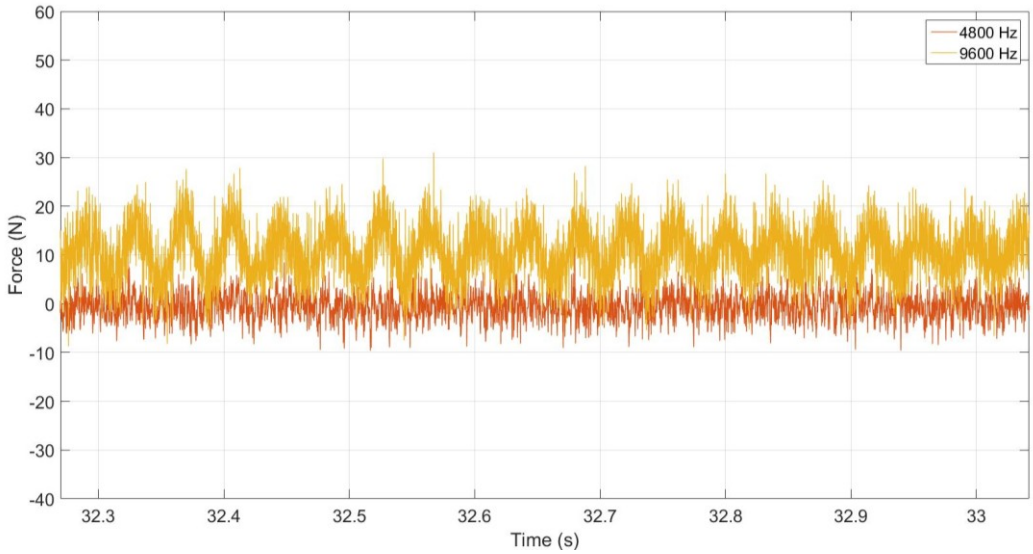

Figure 3.18: Frequency tests performed at 4800 Hz and 9600 Hz sampling rates.

3.6 Summary

This test program was divided into two phases, Phase 1A and Phase 1B. The primary objective of this research program was to study the effects of different test parameters on

the formation of cyclic loading pattern and improve our understanding of compressive ice failure behavior and ice crushing dynamics during ice-structure interaction.

Confined ice samples were used in both phases to prevent the splitting of the ice samples. Beam compliance was studied to observe its effects on the ice failure processes in the presence or absence of structural feedback. Ice temperatures were varied to study the effect of warm ice and cold ice on ice failure. Similarly, the indenter sizes were varied to study the scale effects. Data measuring equipment and data acquisition system were used to record the data during the tests. High speed, GoPro® and point-and-shoot cameras were used to capture videos and images throughout the test program. These visuals helped in the analysis of ice failure behavior and the microstructural changes in the ice.

Chapter 4: Results

4.1 Overview

In this chapter, selected representative results for the tests described in Chapter 3 are presented. Due to the extensive volume of data collected from these tests, only a representative sample of the entire test program are presented in this chapter. An exhaustive collection of the test results is presented in Appendix A.

One of the primary objectives of these tests was to capture the load, pressure and cyclic loading data observed during the ice crushing dynamics tests. Results for two Phase 1A tests and two Phase 1B tests are presented in this chapter. Each test described below had different test parameters and they were used to describe the loading pattern and the failure behavior encountered during testing. Pressure-time and force-time plots are presented for each of these results. In addition to the load and pressure plots, time traces for the structural deflection are also provided for Phase 1A. However, structural deflection was not a factor for Phase 1B. Video recordings captured from the high-speed and GoPro® cameras provided valuable insights into the effects of brittle failure of ice and sudden load drops on the formation of a cyclic loading pattern. A point-and-shoot camera was used to capture and study the damaged region and the edges surrounding the indentation zone.

Force and nominal area of the indenter were used to calculate the pressure applied by the indenter on the ice surface. Nominal area refers to the surface area of the indenter during the indentation of the ice at a particular time. The indenters used for the tests were

spherical in nature. Consequently, the nominal area of the indenter increases with the depth of penetration of the indenter. A method to calculate the nominal area is presented in Appendix C. This method has been previously applied by Wells et al. (2010). According to this method, it takes approximately 2.03 seconds for the 50 mm indenter, 4.1 seconds for the 100 mm indenter and 6.1 seconds for the 150 mm indenter to reach full envelopment at an indentation speed of 2.5 mm/s and maintain a constant area of contact with the ice sample.

The naming convention assigned for both phases provides details of the testing parameters used for each test. Figure 4.1 shows an example of the naming convention used for the indentation tests.

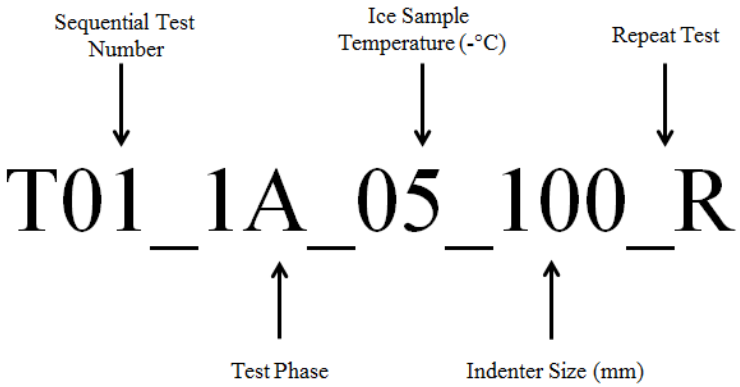

Figure 4.1: Test Naming Convention.

4.2 Results for Phase 1A

Phase 1A consisted of nine tests. Test parameters included ice temperature, indenter size and structural compliance of the indentation system. Data such as force, surface and

subsurface temperatures, structural deflection and indented distance were collected for each test. Video recordings and photos were captured before, during and after every test. A summary of results obtained from Phase 1A are presented below.

4.2.1 Tests Matrix for Phase 1A

Phase 1A originally had six tests, three tests at warm temperature (-5°C) and three tests at cold temperatures (-20°C) using 50 mm, 100 mm and 150 mm indenters. All the tests were performed using the compliant beam configuration. The loading rate of 2.5 mm/s was constant for all the tests.

After analyzing these tests, three additional tests were performed. These repeat tests were carried out due to some issues identified with the apparatus and the testing procedure. For instance, test T01_1A_01_100 was a warm test that was originally planned to be tested at -5°C. Since all the tests were performed at room temperature, the temperature of the ice samples increased over time. Thus, by the time this test was performed, the sample temperature had increased to -1°C, which was close to its melting temperature. To rectify this problem, warm ice samples were prepared at cooler temperatures and a repeat test T09_1A_07_100_R was carried out. Tests T03_1A_04_50 and T04_1A_16.5_50 had to be repeated to correct an error that resulted in the indenter fabrication. The indenter design specification was to have a radius of 50 mm and a radius of curvature of 64 mm. The actual indenter used for tests T07_1A_4.5_50_R and T08_1A_19_50_R had a radius of 50 mm and a radius of curvature of 127 mm. The repeated experiments T09_1A_07_100_R and T09_1A_07_100_R were tested by using the correct indenter

dimensions. Table 4.1 shows the test matrix for the indentation tests carried under Phase 1A.

Table 4.1: Test Matrix for Phase 1A.

Test	Indentation System	Indentation Rate (mm/s)	Temperature (°C)	Indenter Size (mm)
T01_1A_01_100	Compliant	2.5	-1°C	100
T02_1A_18.5_100	Compliant	2.5	-18.5°C	100
T03_1A_04_50	Compliant	2.5	-5°C	50
T04_1A_16.5_50	Compliant	2.5	-16.5°C	50
T05_1A_06_150	Compliant	2.5	-6°C	150
T06_1A_19_150	Compliant	2.5	-19°C	150
T07_1A_4.5_50_R	Compliant	2.5	-5°C	50
T08_1A_19_50_R	Compliant	2.5	-19°C	50
T09_1A_07_100_R	Compliant	2.5	-7°C	100

4.2.2 Sample Test 1: T08_1A_19_50_R

Time series plots for pressure, force and structural deflection for the indentation test T08_1A_19_50_R are presented in Figure 4.2. The test was conducted on the compliant beam indentation system at an indentation rate of 2.5 mm/s using a 50 mm spherical

indenter. The temperature of ice sample was –19°C. The maximum peak load attained was approximately 113.7 kN whereas the average peak load was approximately 79.2 kN. Similarly, the maximum peak pressure attained was approximately 58 MPa whereas the mean peak pressure was approximately 40.39 MPa. The load cycling frequency was close to 0.35 Hz and the indentation depth was approximately 50 mm.

Videos captured using the GoPro® cameras provide valuable visual information about the various failure processes that occur during the indentation tests. These videos when synchronized with the pressure-time and force-time plots, provide insights about the failure behavior. Figure 4.3 shows some stages of the indentation tests corresponding to the pressure and force time series plots presented in Figure 4.2. As shown in Figure 4.2, the pressure and force time series plots clearly indicate that a regular sawtooth loading pattern was developed after the first load drop occurs at approximately 3 seconds. This sawtooth loading and unloading continued throughout the test. This was associated with spalling and extensive microfractures at the indented area.

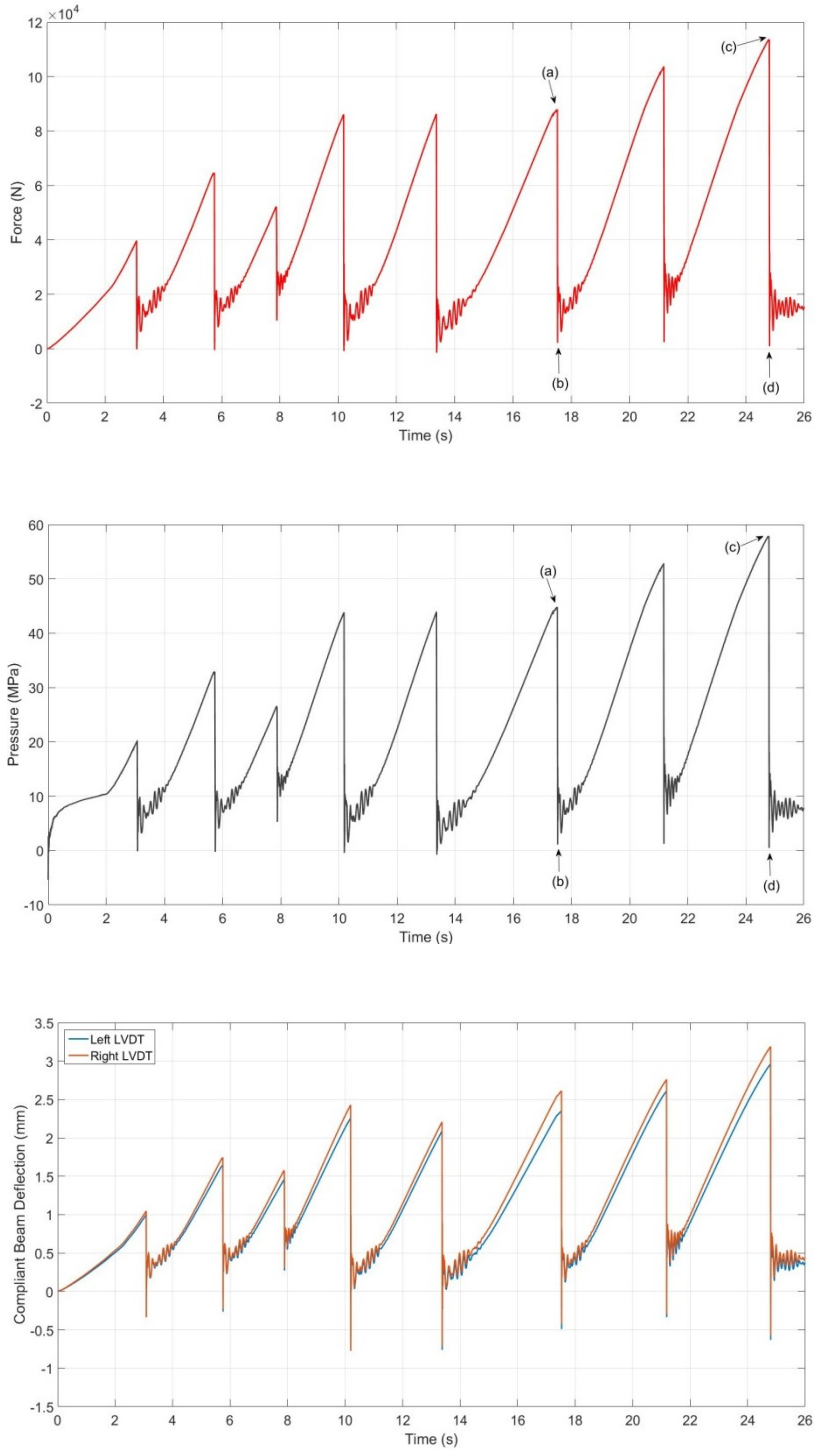

Figure 4.2: Time series plots for the test T08_1A_19_50_R showing total force on the indenter (Top), total pressure on the indenter (Middle) and structural deflection (Bottom).

Figure 4.3 (left) and the event (a) in Figure 4.2 illustrate the condition of the ice sample after five large load drops approximately 17 seconds into the test. Though the indented area and its surrounding edges were damaged, the rest of the ice sample was intact. After the sixth load drop, a big radial crack was observed across the surface of the ice sample as shown in Figure 4.3 (center). This was also accompanied by a very large pressure drop (45 MPa) as represented by the event (b) in Figure 4.2. Event (c) in Figure 4.2 represents the last peak pressure of the test. At almost 58 MPa, this was the highest peak pressure in the entire indentation test. Event (d) in Figure 4.2 represents the final load drop of the test after the indenter reached its maximum indentation depth. As shown in Figure 4.3 (right), the ice surrounding the indented area had developed extensive microfractures; observed by the bulged and extruded white surfaces around the indented edges. The white and opaque zone seen in Figure 4.4 represents the microfractures and microcracks that dominate the damaged area, with small zones of recrystallized ice at the center.

Figure 4.3: GoPro® images captured during the indentation test T08_1A_19_50_R corresponding to the different events identified in the time series plots in Figure 4.2.

Figure 4.4: Post-test image of the indented area.

4.2.3 Sample Test 2: T05_1A_06_150

Time series plots for pressure, force and structural deflection for the indentation test T05_1A_06_150 are presented in Figure 4.5. The test was conducted on the compliant indentation system at an indentation rate of 2.5 mm/s using a 150 mm spherical indenter. The temperature of ice sample was –6°C. The maximum peak load was around 160 kN whereas the average peak load was approximately 155 kN. Similarly, the maximum peak pressure attained was around 9MPa whereas the mean peak pressure was about 8.7 MPa. The frequency of the sawtooth loading was close to 0.1 Hz and the indentation depth was approximately 50 mm.

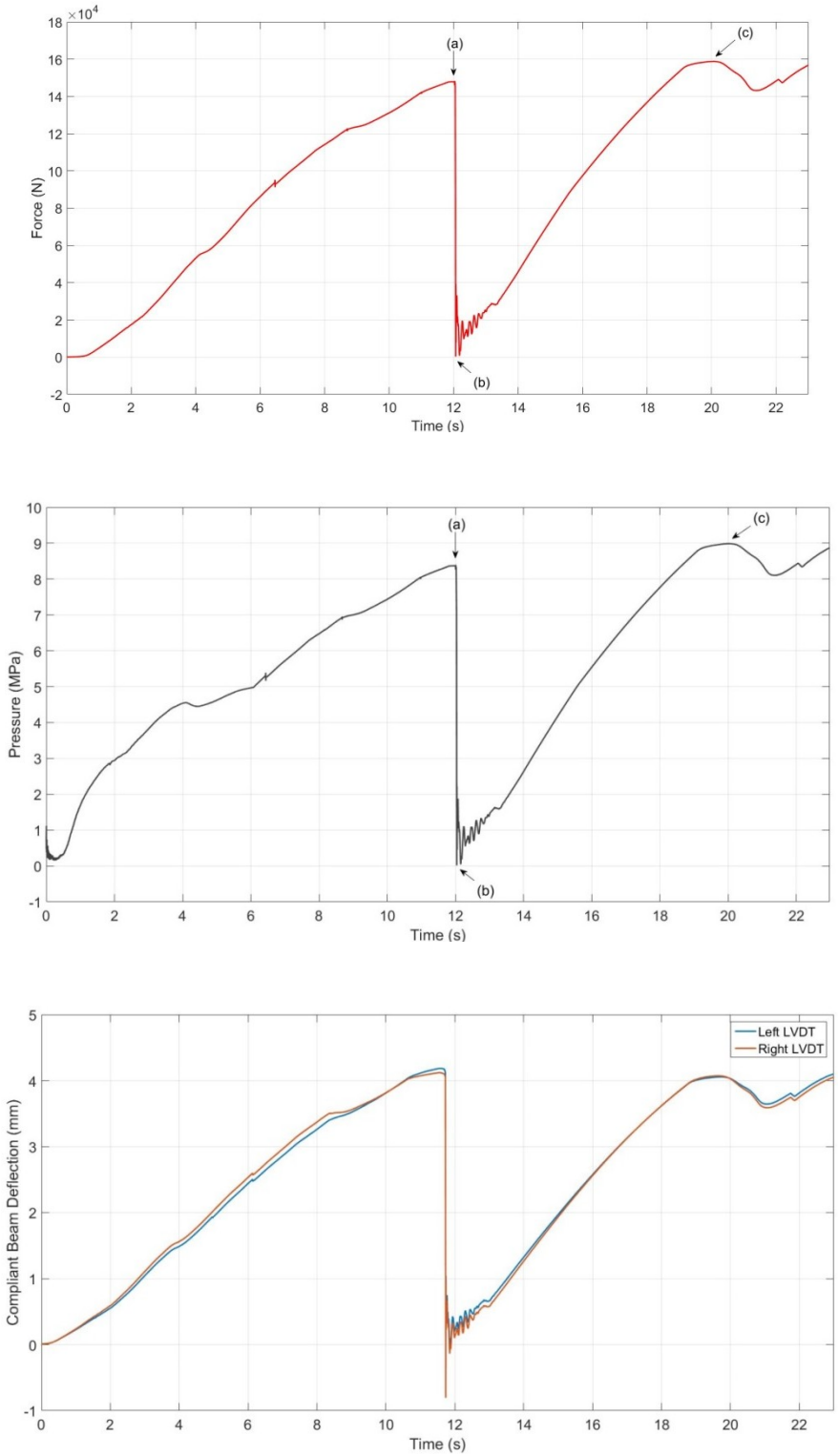

Figure 4.5: Time series plots for the test T05_1A_06_150 showing total force on the indenter (Top), total pressure on the indenter (Middle) and structural deflection (Bottom).

Figure 4.6 represents the different stages of an indentation test captured using a GoPro® camera and Figure 4.5 illustrates the corresponding time series plots that provide detailed insights into the failure behavior. As shown in Figure 4.5, the pressure time series plot indicates a gradual increase in the pressure as the spherical surface of the indenter came into contact with the ice sample completely, at approximately 6.1 seconds. The pressure continued this gradual ascension, till 10 seconds, when it reached a peak pressure of 8.4 MPa. Figure 4.6 (left), the corresponding image to the event (a) in Figure 4.5, shows that the ice underwent continuous extrusion and fine crushing with evidence of fine-grained ice observed near the indented area. Event (b) in Figure 4.5 and the corresponding pressure and force time plots in Figure 4.6 (center) indicate that heavy spalling and crushing of ice resulted in the huge pressure drop to almost zero MPa and the loss of contact with the indented area. Once the indenter regained contact, another instance of gradual pressure ascension was observed from 13 to 20 seconds. Small, intermittent spalls around the surrounding edges and heavy extrusion at the indented area were observed throughout the remainder of the test. The small drop in the pressure around 21 seconds was observed due to the lateral movement of the compliant beam and the deflection of the indenter from the indented area. Figure 4.6 (right) and the event (c) in Figure 4.5 represents the indentation process at around 20 seconds when the ice reached the highest peak pressure of 9 MPa. The test was stopped once the indenter reached its maximum indentation depth. Figure 4.7illustrates the indented area of the ice surface after the test.

Figure 4.6: GoPro® images captured during the indentation test T05_1A_06_150 corresponding to the different events identified in the time series plots in Figure 4.5.

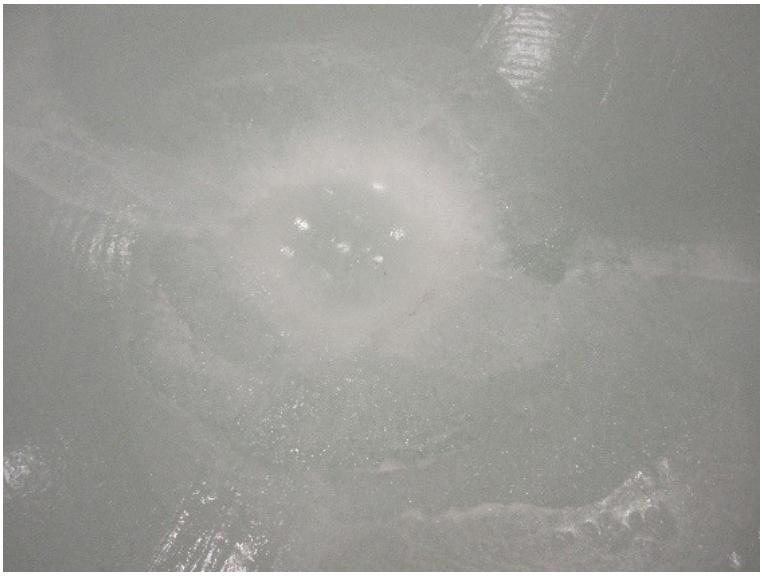

Figure 4.7: Post-test image of the indented area.

4.3 Results for Phase 1B

Building on the results of Phase 1A, the Phase 1B series of tests were conducted to study ice failure in the absence of the significant structural feedback. The lack of structural compliance helped simplify the indentation tests. The same indentation rate, sample

temperatures, ice-sample preparation method, indenter size and ice sample dimensions were used as in Phase 1A.

4.3.1 Test Matrix for Phase 1B

Phase 1B consisted of six tests, three at warm temperature (-5°C) and three at cold temperatures (-20°C) using 50 mm, 100 mm and 150 mm indenters for two tests each. The structural compliance was constant for all the Phase 1A tests. The loading rate of 2.5 mm/s was constant for all the tests. The tests had a maximum indentation depth of 55 mm and maximum loading capacity of 267 kN.

Indentation tests performed under Phase 1B are presented in Table 4.2. The same naming convention is used for rigid beam tests as they were for the compliant beam tests illustrated in Figure 4.1. The actual ice temperatures for the warm ice ranged between -5°C and -6°C whereas the actual ice temperatures for the cold ice ranged between -14°C and -15°C.

Two tests in Phase 1B had to be stopped due to some problems encountered with the apparatus while testing using the large (150 mm) indenter. Test T11_1B_14.5_150 was stopped as the data acquisition software used to operate the data acquisition system was not calibrated and reset to zero. This resulted in the collection of erroneous data and inaccurate results. The indenter loading on the warm ice sample in Test T15_1B_05_150 was on the verge of exceeding the maximum load capacity of the test apparatus. To prevent the apparatus from damage, the test was stopped. Due to time constraints, these

tests were not repeated. Two representative sample tests from Phase 1B are presented below. Time series plots for all the tests are presented in Appendix A.

Table 4.2: Test Matrix for Phase 1B.

Test	Indentation System	Indentation Rate (mm/s)	Temperature (°C)	Indenter Size (mm)
T10_1B_15_50	Rigid	2.5	-15°C	50
T11_1B_14.5_150	Rigid	2.5	-15°C	150
T12_1B_14_100	Rigid	2.5	-14°C	100
T13_1B_07_50	Rigid	2.5	-06°C	50
T14_1B_06_100	Rigid	2.5	-06°C	100
T15_1B_05_150	Rigid	2.5	-05°C	150

4.3.2 Sample Test 3: T13_1B_07_50

Time series plots for pressure and force for the indentation test T13_1B_07_50 are presented in Figure 4.8. The test was conducted on the rigid indentation system at an indentation rate of 2.5 mm/s using a 50 mm spherical indenter. The temperature of ice sample was –6°C. The maximum peak load attained was around 71.5 kN whereas the average peak load was approximately 59 kN. Similarly, the maximum peak pressure attained was around 36.5 MPa whereas the mean peak pressure was about 30.8 MPa. The indentation depth was about 52 mm.

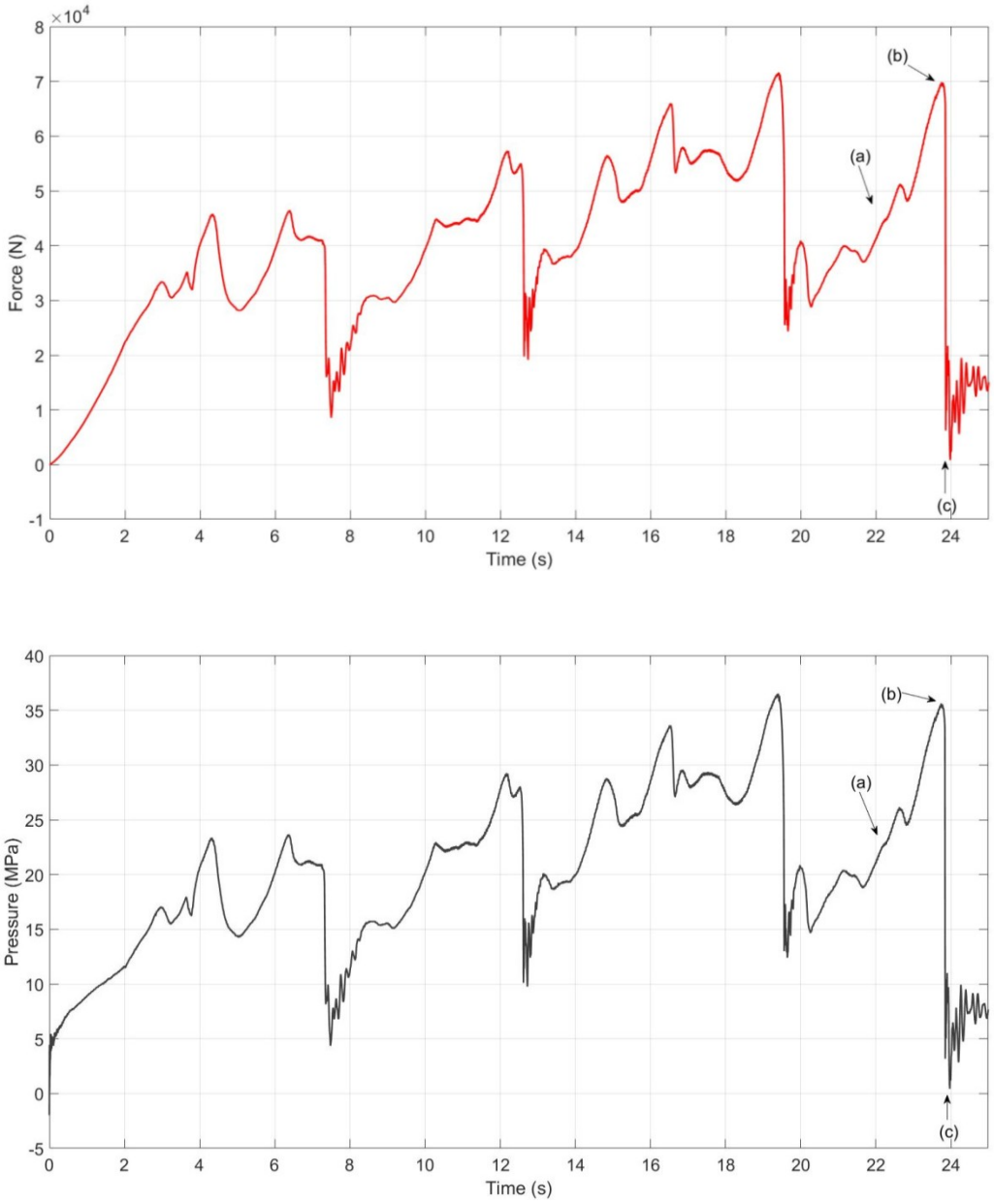

Figure 4.8: Time series plots for the test T13_1B_07_50 showing total force on the indenter (Top) and total pressure on the indenter (Bottom).

Figure 4.9 represents the different stages of an indentation test captured using a GoPro® camera and Figure 4.8 illustrates the corresponding time series plots that provide detailed insights about the failure behavior. As shown in Figure 4.8, the pressure-time plot

indicates a mixture of ductile behavior and brittle failure patterns. A gradual increase in the pressure was observed as the spherical surface of the indenter indented the ice specimen. The pressure continued to increase until 3 seconds when the first signs of ductile failure were observed. Extensive extrusion and crushing was observed throughout the tests with intermittent spalls and load drops occurring, giving rise to intermittent loading patterns. As illustrated in Figure 4.8, the events discussed for this test took place during the last 2 seconds of the test. After undergoing a pressure drop from 36.5 MPa to 12.4 MPa at around 19.5 seconds, the indenter regained contact with the indented surface and pressure increased again. Continuous extrusion with intermittent, small spalls were observed at event (a) as shown in Figure 4.8 and Figure 4.9 (left). The pressure and load increased until event (b), when a radial crack was observed across the surface of the ice sample as seen in Figure 4.9 (right). Almost instantly, a sudden pressure drop from 35.6 MPa to almost zero was observed with very large spalls and loss of contact at the indented surface as presented in Figure 4.8 event (c) and Figure 4.9 (right) .The test was soon stopped as it reached it maximum indentation depth.

Figure 4.9: GoPro® images captured during the indentation test T13_1B_07_50 corresponding to the different events identified in the time series plots in Figure 4.8.

A warm ice sample (–6°C) was used for the indentation test. Thus, the ice failed in a ductile manner for the majority of the test, with pressure drops due to spalls occurring randomly. The intermittent, small spalls and the regular load drops limited the maximum achievable load. Figure 4.10 shows that the warm ice was heavily dominated by recrystallization. Though microfractures were observed, the depth of the damaged layer was shallow. The opaque indented zone represents a smooth and slippery area of highly pulverized and fine-grained damaged surface.

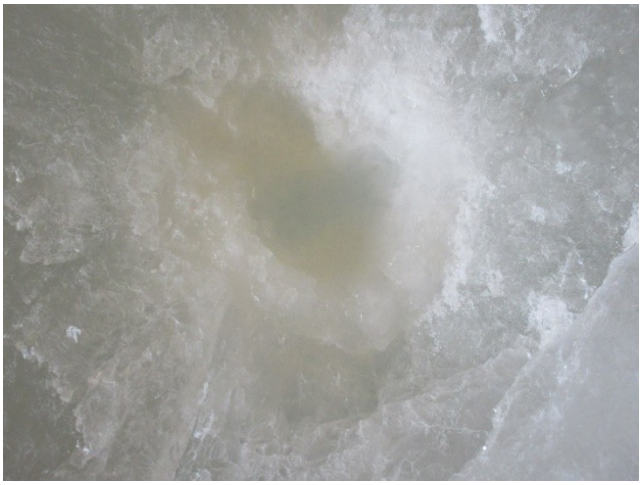

Figure 4.10: Post-test image of the indented area.

4.3.3 Sample Test 4: T12_1B_14_100

Pressure-time and force-time plots for the indentation test T12_1B_14_100 are presented in Figure 4.11. The test was conducted on the rigid indentation system at an indentation rate of 2.5 mm/s using a 100 mm spherical indenter. The temperature of the ice sample was -14°C. The maximum peak load attained was around 213.5 kN whereas the average peak load was approximately 145.3 kN. Similarly, the maximum peak pressure attained was around 27.22 MPa and the mean peak pressure was about 19.12 MPa. The load

cycling frequency was close to 0.35 Hz and the indentation depth was approximately 48 mm.

Figure 4.12 represents the different stages of an indentation test captured using a GoPro® camera and Figure 4.11 illustrates the corresponding time series plots that provide detailed insights about the failure behavior. As shown in Figure 4.11, the ice sample undergoes a constant loading and unloading phase, giving rise to a sawtooth loading pattern. Though it takes approximately 4.1 seconds for the spherical surface of the indenter to be fully enveloped in the ice sample, the first pressure drop was observed at around 3 seconds.

A radial crack was also observed across the surface of the ice sample after the first pressure drop as shown in Figure 4.12 (left). The small spikes represented by event (a) in Figure 4.11 indicate the intermittent spalling and small pressure drops that occurred throughout the entire loading. The pressure drop for the second load cycle was very large as it dropped from 24 MPa to almost zero. Event (b) in Figure 4.11 shows another load cycle. Unlike the previous pressure drops, the pressure drop here was not immediate and sudden. Figure 4.12 (center) illustrates that there was evidence of ductile failure and significant extrusion of failed ice before the pressure drop. A small drop in the pressure was associated with a localized spall at 20.5 seconds during the final loading cycle. Extensive spalling and crushing of ice resulted in a large pressure drop of almost 27 MPa and the loss of contact with the indented area. Event (c) of Figure 4.11 and Figure 4.12 (right) show the spalled and fractured ice sample after the huge pressure drop. The test was stopped after it reached the maximum indentation depth.

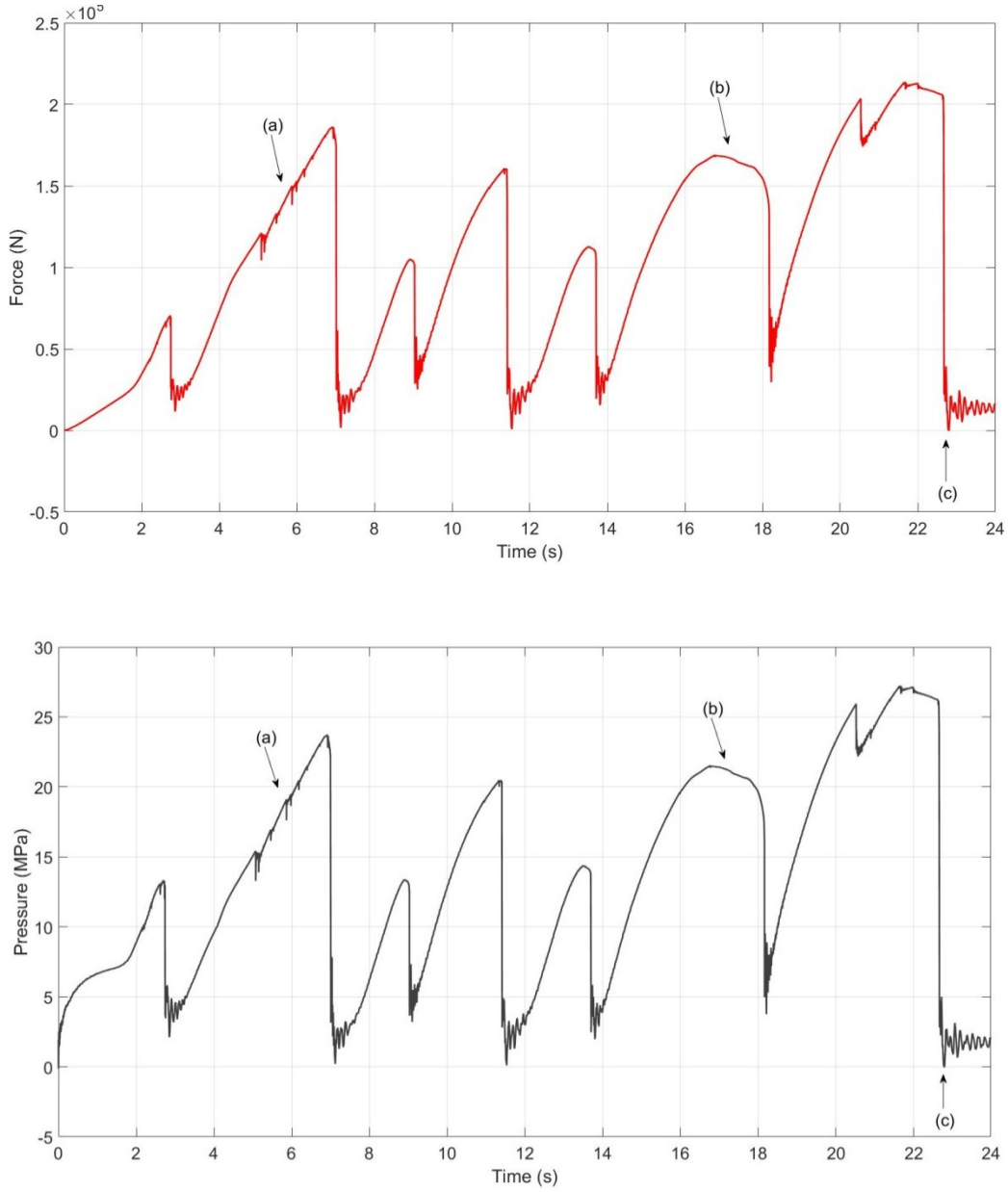

Figure 4.11: Time series plots for the test T12_1B_14_100 showing total force on the indenter (Top) and total pressure on the indenter (Bottom).

Figure 4.12: GoPro® images captured during the indentation test T12_1B_14_100 corresponding to the different events identified in the time series plots in Figure 4.11.

Temperature was observed to have an effect on the behavior of the damaged layer. The white and opaque zone seen in Figure 4.13 represents the microfractures and cracks that dominate the damage area, with small zones of highly damaged ice at the center.

Figure 4.13: Post-test image of the indented area.

4.4 Summary

An overview of each testing phase and four representative sample results were presented and discussed in this chapter. The tests are representative of the tests performed throughout this indentation program. All the tests were carried at a constant indentation rate of 2.5 mm/s with variations in indenter size, ice sample temperature and the structural compliance. The small (50 mm) indenter, due to its smaller nominal area, induced the highest peak pressure on an ice sample. The cold ice produced the highest peak loads and peak pressures. It was also observed that the compressive failure of polycrystalline ice samples led to the formation sawtooth loading patterns under certain circumstances. Cyclic loading was more prominent when small spherical indenters were used on cold ice specimens and were more pronounced during the indentation of the ice sample using the compliant configuration. The warm ice showed little evidence of cyclic loading. Similarly, the use of large indenters reduced the severity of cyclic loading patterns.

Video recordings captured using GoPro® cameras provide detailed insights about the failure behavior when synchronized with time series plot acquired from the load cell data. Post-test images provide further assessment of the failure types and microstructural behavior observed after the indentation test. Most of the indented surfaces had some amount of microfractures and damaged layers. The damaged layer for the warm ice showed more evidence of damaged enhanced creep whereas the damaged layer for the cold ice was much thinner and was accompanied by extensive microfractures and spalls surrounding the indented area.

Chapter 5: Analysis

5.1 Overview

This chapter deals with the comparison and the analysis of all the tests performed in both phases of this research program. The influence of parameters such as ice temperature, indenter size and the structural compliance on the ice failure behavior, the formation of *hpz*s and the eventual cyclic loading patterns are discussed. Load limiting factors and the test conditions that influence these mechanisms are also considered.

Time series plots and GoPro® video recordings were synchronized to observe and analyze the failure mechanisms like spalling and crushing in greater detail. Further assessment of the effects of various parameters on the failure mechanisms and the damaged layer of the ice are also presented in this chapter.

5.2 Ice Failure Processes

The tests performed in this research programs were studied and analyzed individually to determine the ice failure process, and the nature of *hpz*s at the indented surface. Particular attention was paid to the load limiting failure mechanisms during periods of cyclic loading. The synchronization of time series plots and video recordings help associate the load drops and cyclic loading patterns with the ice failure processes; such as spalling and crushing. A detailed description of observed failure processes associated with crushing and spalling for representative sample events is provided below.

5.2.1 Crushing

Crushing failure is a critical load limiting failure mechanism which can be observed during indentation and is associated with the failure of *hpz*s and load variations. Crushing refers to the pulverization and extrusion of fine-grained, soft ice from the edges of *hpz*s. For small-scale tests, the cyclic loading behavior associated with crushing is due to the continuous pressure softening and the hardening of the damaged layer.

Crushing failure leads to a decrease in the intensity of the *hpz* without any significant change in the position or the loss of contact area. Video recordings from the present program captured the indentation tests, and indicate that the crushing failure corresponds with observations of continuous extrusion of the fine-grained pulverized ice from around the indenter after the failure of a high pressure zone. A sample test is presented below to discuss the crushing failure behavior. The pressure-time plot for the T10_1B_15_50 test, and synchronized video recordings are illustrated in Figures 5.1 and 5.2.

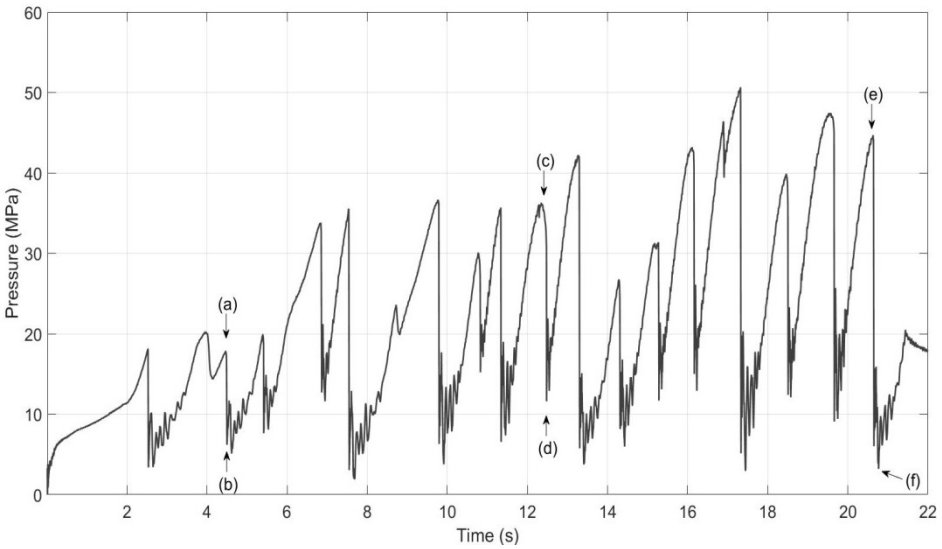

Figure 5.1: Pressure-time plot identifying crushing failure for the test T10_1B_15_50.

From these videos, the load drop can be attributed to the failure mode of observed *hpz*s. The corresponding images captured for the synchronized video recordings are presented in Figure 5.2. Events (a) and (c) represent the peak pressures of their respective cycles, whereas events (b) and (d) represent the corresponding load drops due to extrusion events.

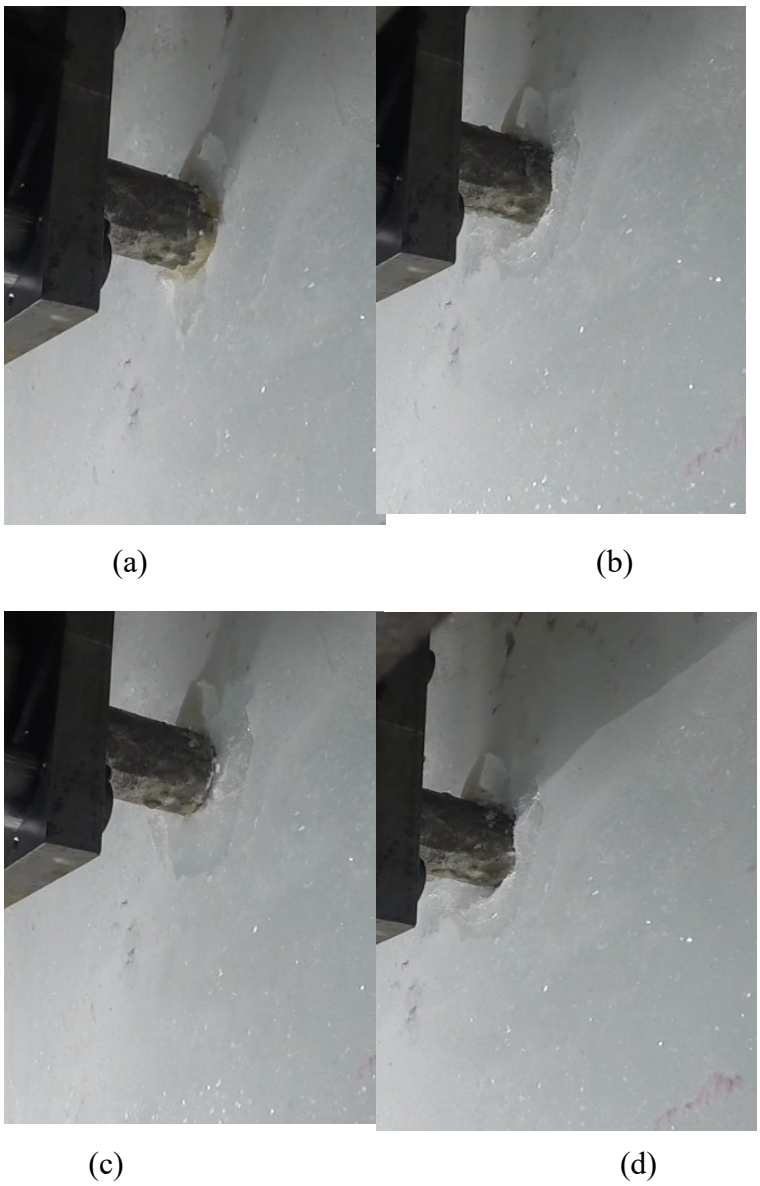

(a) (b)

(c) (d)

Figure 5.2: Images of crushing failure from the video recording of the test T10_1B_15_50

Spalling

Spalling fracture is another load limiting failure mechanism that has been associated with compressive ice failure. A spall is a series of localized fractures that initiate from the cracks near the *hpz*s. Spalls are intermittent and irregular in nature that are influenced by the flaws in ice. Spalling fracture also depends on the rate of indentation, with higher instances of spalling occurring at indentation rates greater than 1 mm/s.

(a) (b) (c)

Figure 5.3: Images of spalling failure from the video recording of the test T10_1B_15_50

Examination and analysis of each indentation test revealed that spalls dominate the failure of ice for the scales of interest in this program. Spalling fractures are often associated with a significant loss of contact area at the indented surface. Loss of contact area is accompanied by a significant load drop within a fraction of a second. Images captured for the synchronized video recordings are presented in Figure 5.3. Figure 5.3 (a) illustrates

the ice sample right before the spall. Event (b) in Figure 5.3 represents a spalling fracture and the separation of a large fragment of ice from the ice sample, accompanied with a huge pressure drop. Figure 5.3 (c) represents the spalled area and the loss of contact area at the indented surface as a result of the spalling event.

5.3 Analysis of Phase 1A Tests

5.3.1 Temperature Effects

To examine the effect of temperature on ice failure and associated interaction dynamics, a comparison of three experiments carried out at 2.5 mm/s using a 100 mm indenter is given in Figure 5.4. These results include experiments carried out at temperatures of -1°C (T01_1A_01_100), -7°C (T09_1A_07_100_R) and -18.5°C (T02_1A_18.5_100). As observed from this figure, differences in ice failure behaviour can be observed for the range of temperatures considered. The coldest specimen (-18.5°C) produced the highest initial peak pressure and failed in a brittle manner due to large spall events, while the ice tested at -7°C also failed in a brittle manner but produced a lower initial peak that was followed by several cycles of sawtooth type failures. For the tests at -7°C and -18.5°C, failure of the ice consistently resulted in a very large load drop (nearly to zero for all failure events). By comparison, during the test at -1°C, the pressure increased steadily until it reached a limit of about 15 MPa, after which the pressure remained almost constant for the remainder of the test. Under these conditions, the ice failed in a more ductile manner due to the flow of highly damaged ice and continuous extrusion from beneath the indenter, without any significant load drops or cyclic loading character.

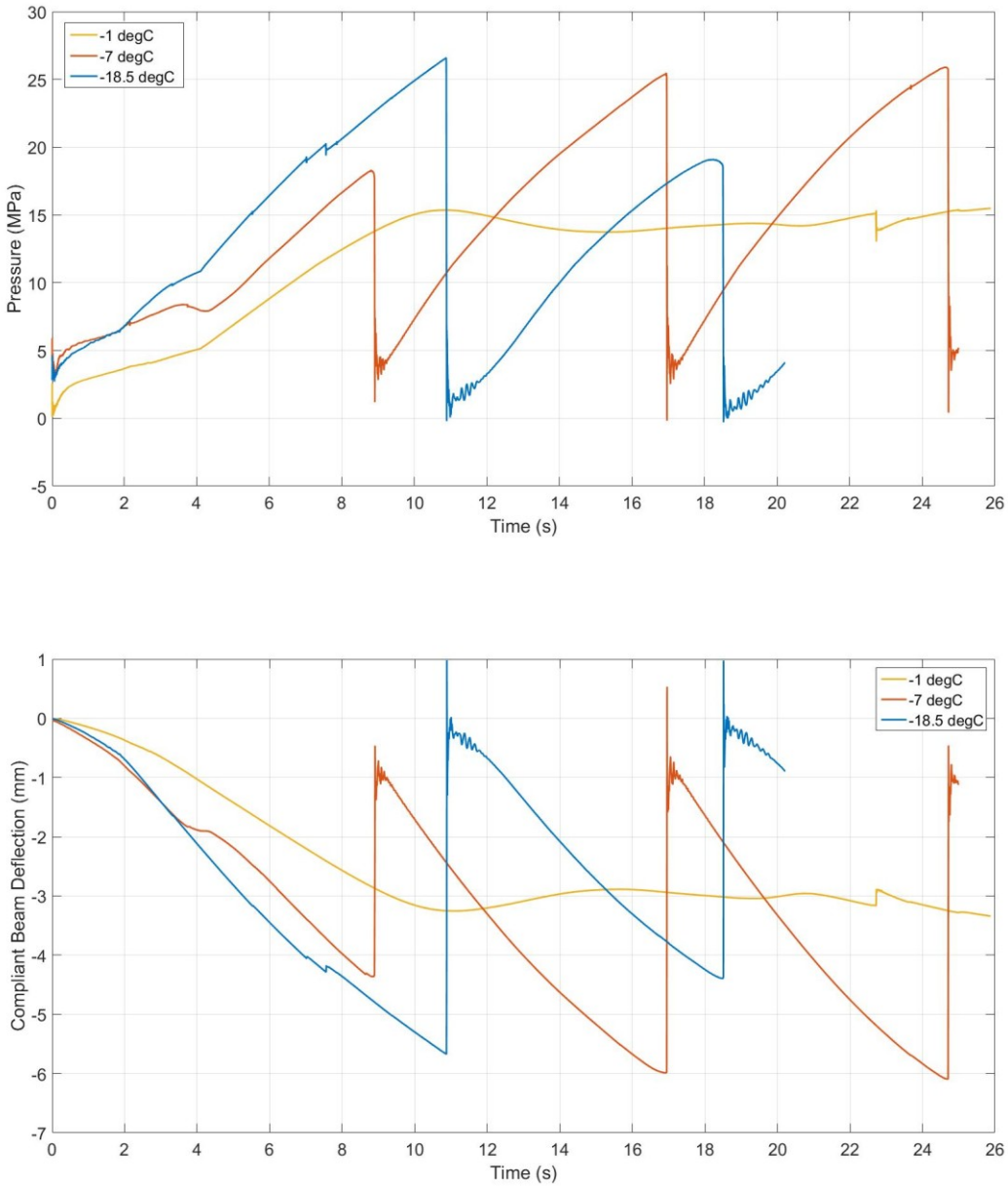

Figure 5.4: Pressure-time plot (top) and beam deflection-time plot (bottom) for tests conducted at different temperatures using a 100 mm indenter.

Photographs of the indented ice surface taken at the end of each test illustrated in Figure 5.5 (for 100 mm indenter, 2.5 mm/s) establish clear links between the failure modes corresponding to the loading patterns observed in Figure 5.4. As observed from the

picture in Figure 5.5 (left), during the indentation test at -1°C, highly damaged ice was continuously extruded from beneath the indented surface. There was no evidence of sudden load drops due to the failure, structural rebounding and clearance of damaged ice from beneath the indenter. This damaged-enhanced creep process is markedly different than observed brittle failure since it resulted in the accumulation of a mass of extruded, damaged ice directly surrounding the indenter. In comparison, observed brittle failure consisted of a combination of spalling and crushing, due to the rapid rebound of the structure following the formation of a spall, which resulted in further crushing and clearing of the ice from beneath the indenter; see images in Figure 5.5 (center and right).

Figure 5.5: Images taken after indentation tests (100mm indenter; 2.5 mm/s) at temperatures: (Left) -1°C; (Centre) -7°C; (Right) -18.5°C.

These results suggest that ice warmer than some critical limit would be expected to fail in a ductile manner, making interactions involving such ice less likely to excite ice-induced

vibrations in the structure. Further study to better understand and characterize such critical temperature limits are needed for a range of scales and indentation rates.

5.3.2 Scale Effects

To study the effect of indenter size on ice failure processes and the associated loading dynamics in the case of the compliant indentation system, data from three tests (T08_1A_07_50_R, T02_1A_18.5_100_R, T06_1A_19_150) having different nominal areas ($1.96x10^{-3}m^2$ for the 50 mm indenter, $7.85x10^{-3}$ m^2 for the 100 mm indenter and $17.6x10^{-3}$ m^2 for the 150 mm indenter) have been plotted; see Figure 5.6 below. Other conditions (temperature ≈ -19°C; indentation rate = 2.5 mm/s) were held constant for each of these tests. Due to the spherical shape of the indenters, the nominal area increases as the indentation proceeds. This area continues increasing until the indenter becomes fully enveloped, after which the area remains constant. As shown in the Figure 5.6 (bottom), the time required for full envelopment of the indenter is approximately 2.03, 4.1 and 6.1 seconds for the 50, 100 and 150 mm indenters, respectively.

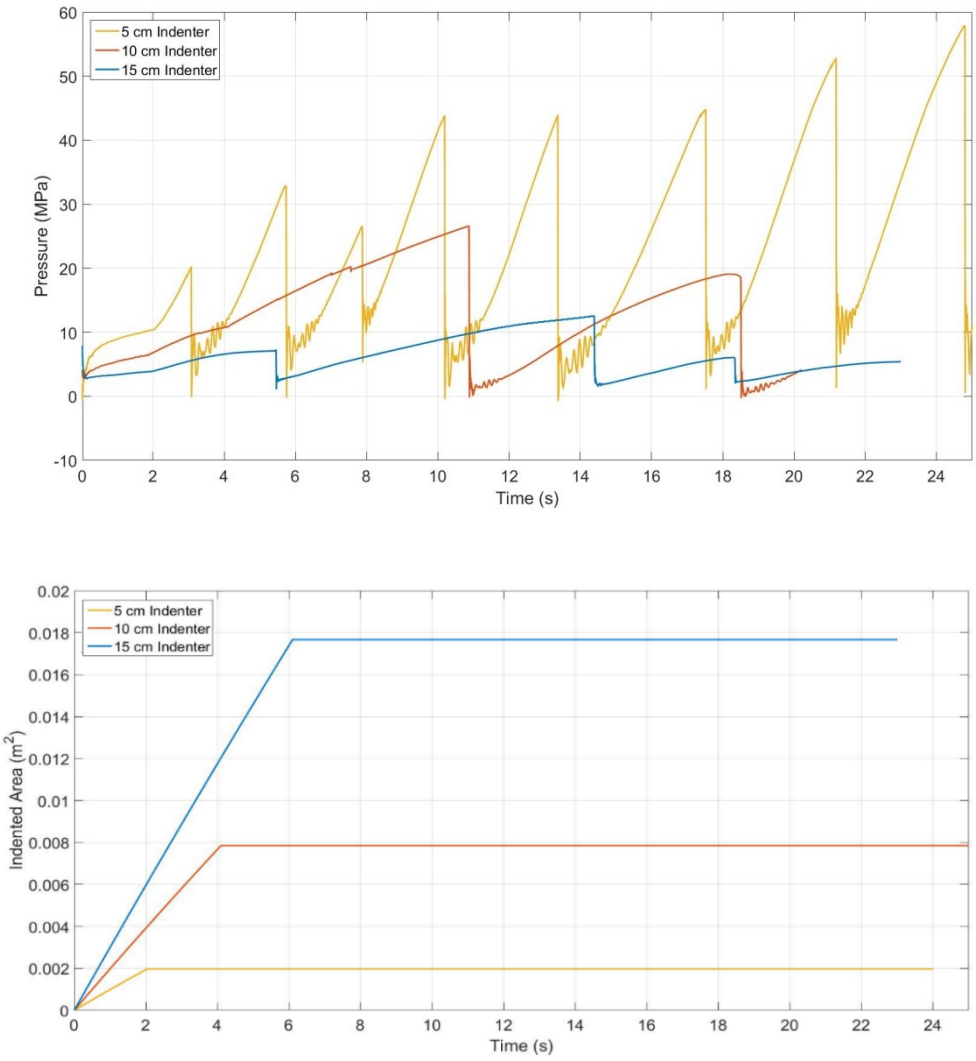

Figure 5.6: Plots of: (Top) Pressure vs. time; (Bottom) Nominal area vs. time; Three different indenter sizes (50 mm, 100 mm, 150mm) are used for each test, while speed and temperature remain constant (2.5mm/s, -19°C).

From the pressure-time results shown in the Figure 5.6 (top), it is observed that all three tests exhibit brittle-type failure with sawtooth cyclic loading patterns characterized by significant load drops occurring during each ice failure event. The overall peak pressure observed (58 MPa) from these tests corresponds to the smallest (50 mm) indenter and is nearly double the peak pressure from the 100 mm indenter test and about five times the

peak pressure from the test with the 150 mm indenter. It is also interesting to note that the frequency of the sawtooth loading varies as a function of scale, with a higher frequency of about 0.3 Hz observed for the 50 mm indenter, whereas the frequency of the load drops for the 100 mm and 150 mm indenters are lower at about 0.1 and 0.15 Hz, respectively. This indicates that the size of the individual *hpz*s will influence the frequency of associated ice-induced vibrations, even if the structure, temperature and interaction speed remain constant. This result highlights the need for improved understanding of *hpz* behavior over multiple scales and in the context of dynamic ice-structure interactions.

A possible explanation for these observations is that for small indenters, contact forces are concentrated over smaller areas and therefore less indentation depth is required to impart sufficient energy to trigger a failure event in the cracked and damaged layer of ice immediately beneath the indenter. Since smaller, higher pressure indenters would need to indent less depth into the ice to reach a given critical failure energy limit, one would expect them to have more indentation cycles per unit time (hence higher frequency) than larger, lower pressure indenters (assuming a constant indentation rate).

Another important observation from these tests is that the dominant ice failure mode noted during the test conducted using the 50 mm indenter consisted of small, intermittent spalls with some ice crushing. Observations from the medium (100 mm) and large (150 mm) indenter tests indicate that failure events for those tests were associated more with massive spalls and very large associated load drops, with crushing only occurring as a consequence of the clearing of ice around the indenter during rebounding of the structure, not as the triggering mechanism. This result indicates that fracture processes may play a

more dominant role in failure and associated loading dynamics during larger scale interactions with compliant structures.

Figure 5.7 shows the time series plots illustrating first peak pressures, mean peak pressures and maximum peak pressures for each test performed using a compliant indentation system. These plots summarize the pressure results for all the tests carried out in Phase 1A. The peak pressures plot (Figure 5.7 top) indicates the peak pressure of the first cyclic loading event; the mean peak pressure plot (Figure 5.7 middle) indicates the average of all the peak pressures during the test while the maximum peak pressure plot (Figure 5.7 bottom) indicates the maximum pressure observed during the indentation phase.

The pressures for cold tests using increasing indenter sizes produced decreasing pressures, with the peak pressures for the 50 mm indenter tests being the highest and gradually decreasing as indenter size is increased. All three plots indicate that the peak pressures for the 50 mm indenter tests are almost twice the pressures for the 100 mm indenter tests and three to five times the pressures for the 150 mm indenter tests.

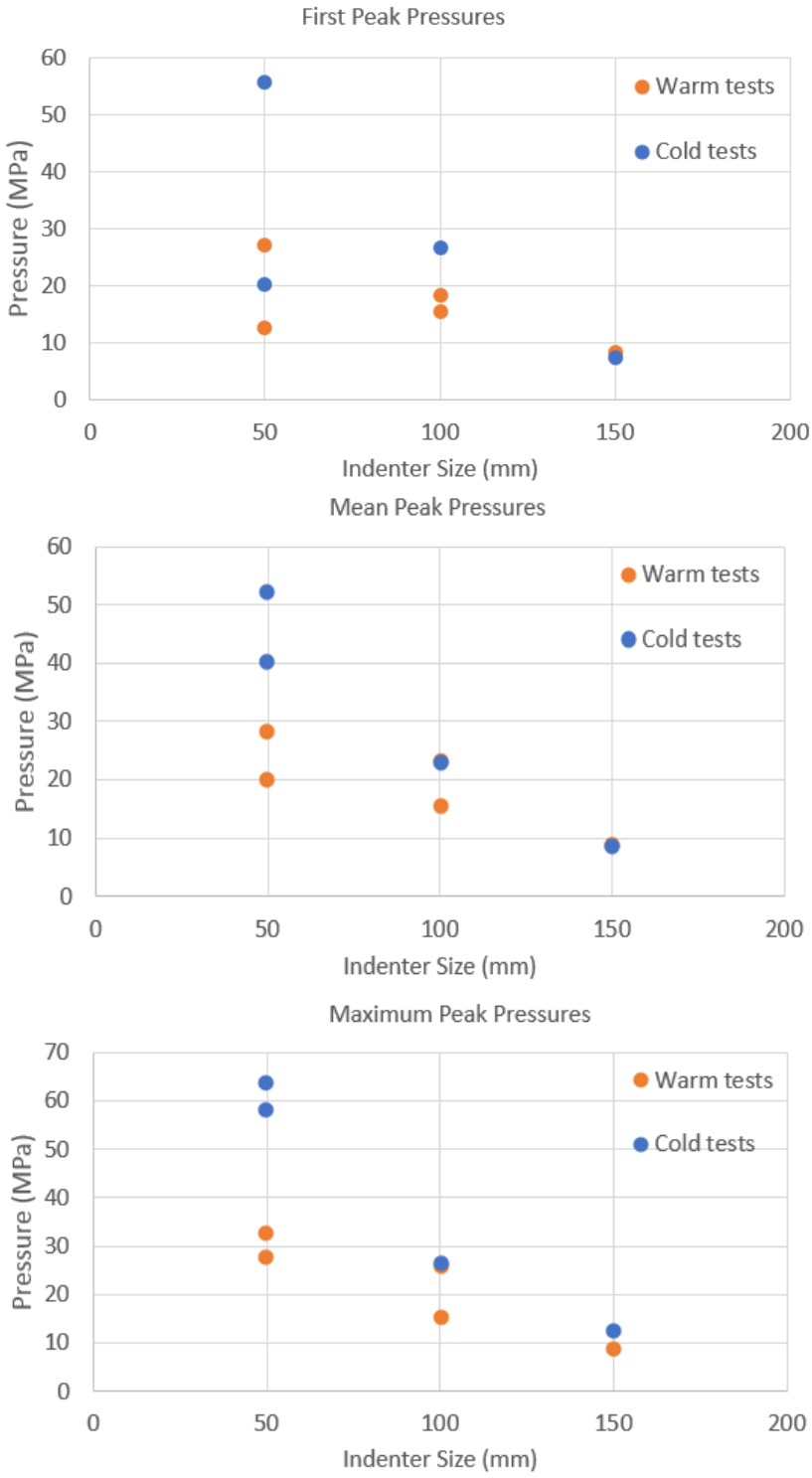

Figure 5.7: First peak pressure-time plot (top); mean peak pressure-time plot (middle) and maximum peak pressure-time plot (bottom) for Phase 1A tests.

The differences between the peak pressures for the warm tests also showed a similar pattern, albeit drastic pressure differences were not observed. In all cases, the pressures observed during a 50 mm indenter test were the highest, with peak pressures decreasing with increasing indenter size. The pressures on the 50 mm indenter tests were approximately 30% higher than the 100 mm indenter tests and about 60% higher than the 150 mm indenter tests.

Figure 5.7 also shows that the cold tests, on average, had much higher peak pressures when compared to the warm indenter tests, regardless of the indenter size used.

5.4 Analysis of Phase 1B Tests

5.4.1 Temperature Effects

To examine the effect of temperature on the compressive failure of ice and the associated interaction dynamics in case of a rigid indentation system, a comparison of two experiments carried out at 2.5 mm/s using a 100 mm indenter is made in Figure 5.8. These results include experiments carried out at temperatures of -6°C (T14_1B_06_100) and -14°C (T12_1B_14_100). As may be observed from this figure, differences in ice failure behaviour can be observed for the range of temperatures considered. The cold ice specimen (-14°C) produced a regular cyclic loading pattern, with the peak pressures ranging from 13 to 27 MPa. These cold ice samples failed in a brittle manner due to the large spalling events that contributed to the constant loading and unloading of pressure on the ice. For the most part, the warm ice specimen (-6°C) fails in a highly ductile manner. The pressure reaches a peak limit of almost 13 MPa within the first 4 seconds of the test

when the spherical surface of the indenter is achieving complete contact with the surface of the ice. After the pressure drop, the ice experienced a damaged enhanced creep response. Under these conditions, the ice failed in a more ductile manner due to the continuous extrusion and the flow of highly damaged ice from beneath the indenter, without any significant load drops or cyclic character. In the case of the cold ice specimen, the intermittent sawtooth loading limited the maximum achievable load, while the warm ice specimen was characterized by a steadily increasing load.

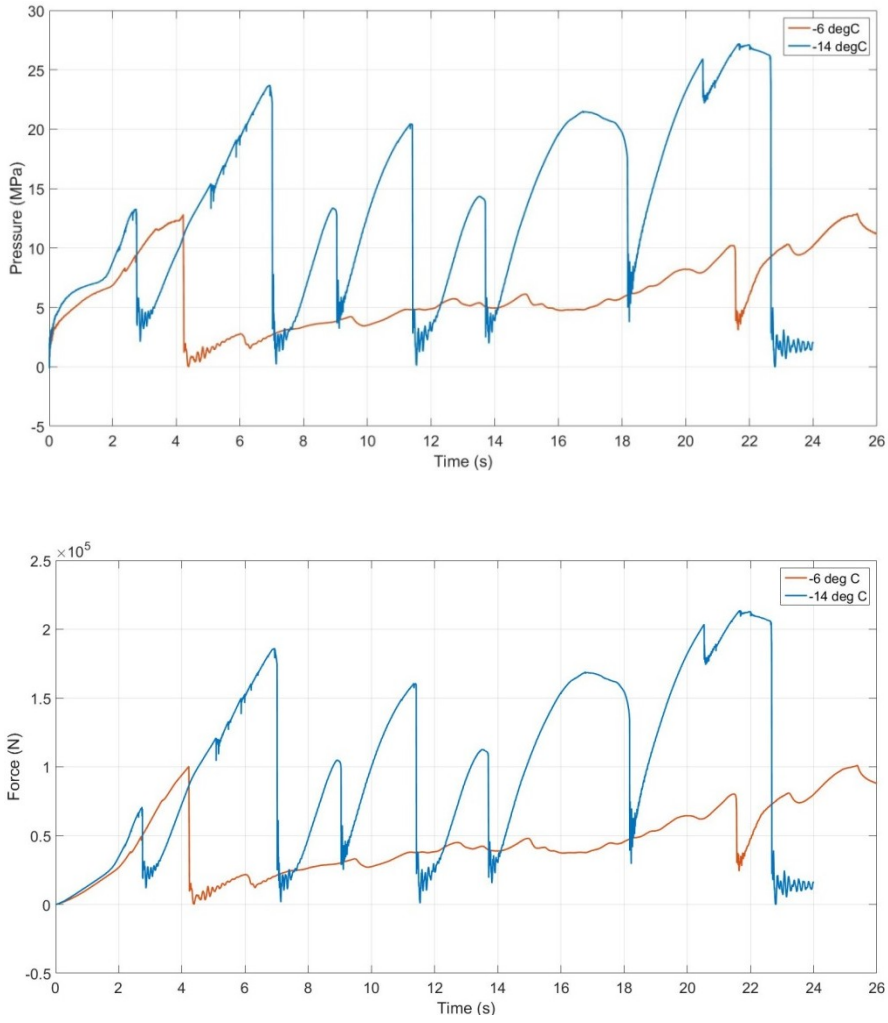

Figure 5.8: Pressure-time plot (top) and force-time plot (bottom) for tests conducted at different temperatures using a 100 mm indenter.

Photographs of the indented ice surface taken at the end of each test shown in Figure 5.9 (for 100 mm indenter, 2.5 mm/s) establish clear links between the failure modes corresponding to the loading patterns observed in Figure 5.8. As observed from the left picture in Figure 5.9, the indented surface of the warm ice specimen was heavily dominated by a permanent indentation, indicative of damage enhanced creep with very small areas of microfractures present at the edges. By comparison, the indented surface of the cold ice specimen was dominated by zones of extensive spalls, microfractures and only a small damaged ice layer at the center as observed in Figure 5.9 (right). Barrette et al. (2002), Li et al. (2004) and Browne (2012) also observed similar findings in their research.

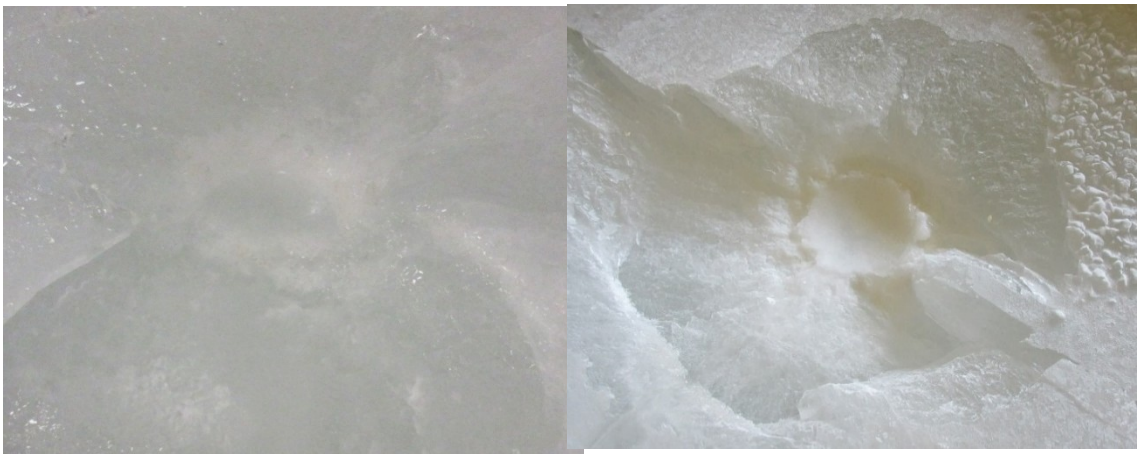

Figure 5.9: Images taken after indentation tests (100mm indenter; 2.5 mm/s) at temperatures: (Left) -6°C; (Right) -14°C.

5.4.2 Scale Effects

To study the effect of indenter size on ice failure processes and associated loading dynamics for the rigid indentation system, data from two tests (T10_1B_15_50; T12_1B_14_100) having different nominal areas (1.96×10^{-3} m^2 for the 50 mm indenter

and 7.85×10^{-3} m^2 for the 100 mm indenter) have been plotted; see Figure 5.10 below. Other conditions (indentation rate = 2.5 mm/s; temperature ≈ -15°C) were held constant throughout each of these tests. As explained in Section 5.3.2, the time required for full envelopment of the indenter is approximately 2.03 and 4.1 seconds for the 50 and 100 mm indenters, respectively.

The cold test T11_1B_14.5_150 using a large (150 mm) indenter was not considered for the scale effects comparison. The T11_1B_14.5_150 test was stopped abruptly due an operating problem encountered during the data acquisition process that resulted in the collection of erroneous data and inaccurate results. From the pressure-time results shown in Figure 5.10 (top), it is observed that both tests exhibit brittle-type failure with sawtooth cyclic loading patterns characterized by significant load drops occurring during each ice failure event. The maximum peak pressure of the small (50 mm) indenter test was 50.5 MPa, nearly twice the peak pressure (27MPa) for the 100 mm indenter test. Despite having higher pressure drops, almost every peak pressure in the 100 mm indenter test dropped to around zero. On the contrary, the pressure drops for the small indenter test did not drop to zero for this experiment. This pattern led to an increase in the peak pressures that developed during the later loading cycles. It is also observed that the frequency of the sawtooth loading varies as a function of scale, with a higher frequency of about 0.9 Hz observed for the 50 mm indenter, whereas the frequency of the load drops for the 100 mm was lower at about 0.36 Hz.

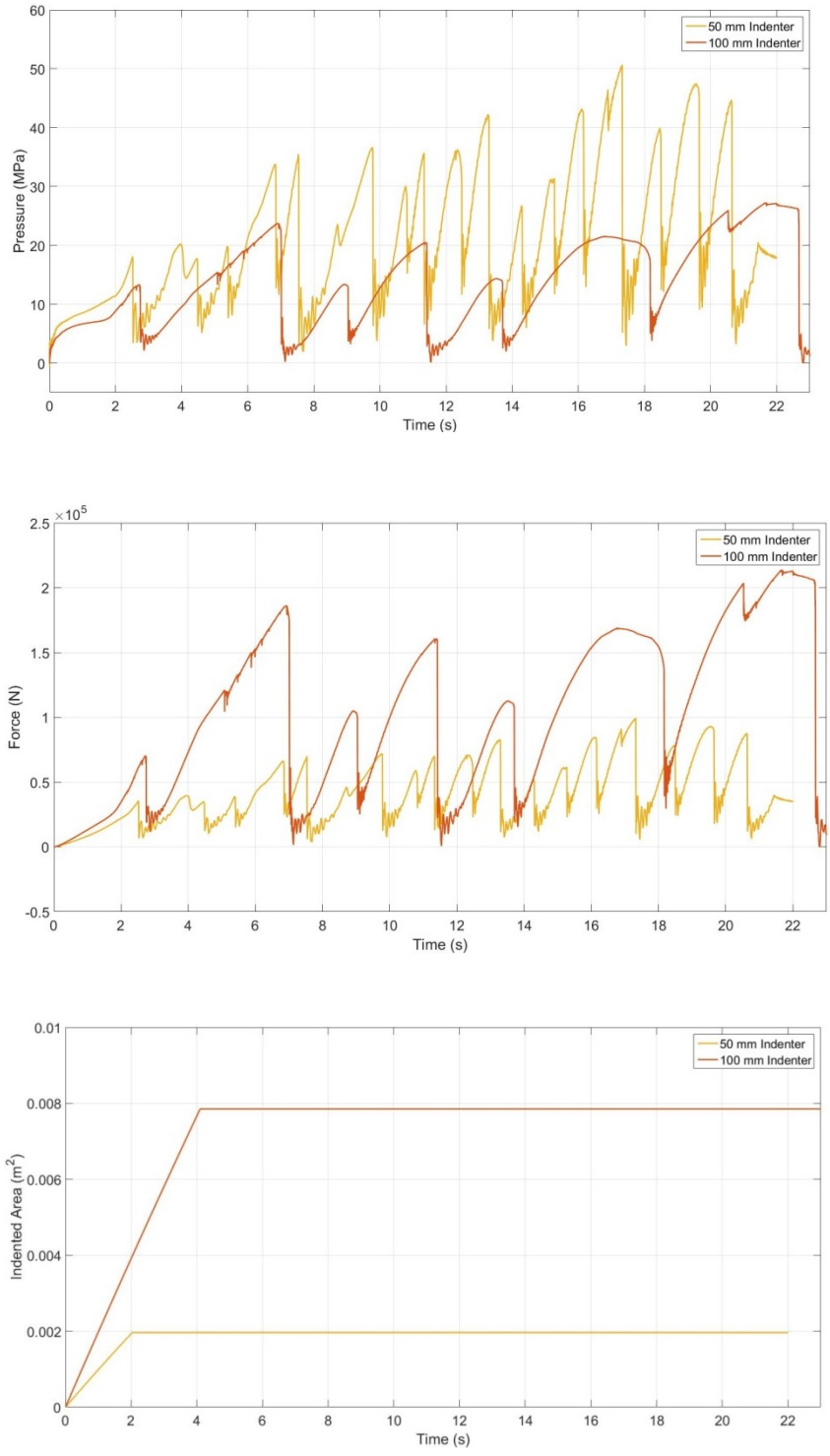

Figure 5.10: Plots of: (Top) Pressure vs. time; (Center) Force vs. time; (Bottom) Nominal area vs. time; Two different indenter sizes (50 mm, 100 mm) are used for each test, while speed and temperature remain constant (2.5mm/s, -15°C).

Thus, it can be concluded that the frequency and amplitude of the cyclic loading patterns is higher for the tests performed using a smaller indenter. These observations indicated that the size of the individual *hpz*s will influence the frequency of associated ice-induced vibrations, even if the structure, temperature and interaction speed remain constant. Another important observation from these tests is that the dominant ice failure mode noted during the test conducted using the 50 mm indenter consisted of small, intermittent spalls with some ice crushing. Observations from the medium (100 mm) indenter test indicate that failure events for those tests were associated more with massive spalls and very large associated load drops, with crushing only occurring as a consequence of the clearing of ice around the indenter.

Figure 5.11 shows the time series plots illustrating first peak pressures, mean peak pressures and maximum peak pressures for each test performed using a rigid indentation system. These plots summarize the pressure results for all the tests carried out in Phase 1B. The peak pressures plot (Figure 5.11 top) indicates the peak pressure of the first cyclic loading event; the mean peak pressure plot (Figure 5.11 middle) indicates the average of all the peak pressures during the test while the maximum peak pressure plot (Figure 5.11 bottom) indicates the maximum pressure observed during the indentation phase.

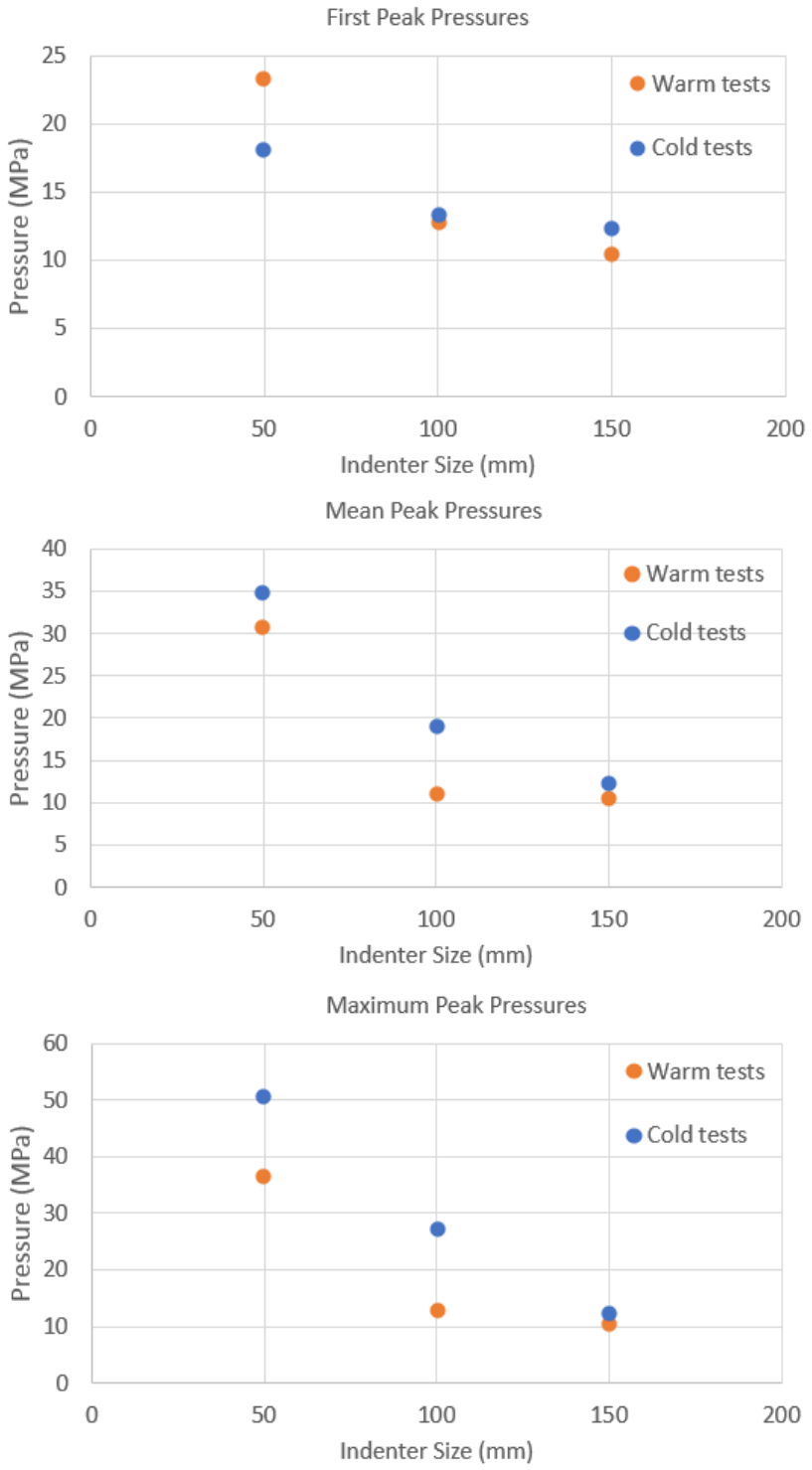

Figure 5.11: First peak pressure-time plot (top); mean peak pressure-time plot (middle) and maximum peak pressure-time plot (bottom) for Phase 1B tests.

All three plots indicate that the pressures for the 50 mm indenter tests are almost two times the pressures for the 100 mm indenter tests, and nearly two to five times the pressures for the 150 mm indenter tests. The differences between the peak pressures for the warm tests also showed a similar pattern, albeit drastic pressure differences were not observed. As indicated, the pressures observed during a 50 mm indenter test were the highest, with peak pressures decreasing with increasing indenter size. The pressures on the 50 mm indenter tests were approximately two to three times higher than the 100 mm indenter tests and about three to four times higher than the 150 mm indenter tests. For these data, the peak pressures for the medium and the large indenter tests were almost the same, which may be due to effects of natural variability in the ice failure process due to random fractures. Figure 5.11 also shows that the cold tests, on an average, had much higher peak pressures when compared to the warm indenter tests, regardless of the indenter size used.

5.5 Effect of Structural Compliance

Two different indentation systems were used throughout the course of this research program. A compliant indentation system was used in Phase 1A while a rigid indentation system was used in Phase 1B. The following observations have been linked to the presence of structural feedback, or lack thereof:

- For the conditions considered, the actual indentation rate, also known as the relative indentation rate experienced by the ice during the loading phase, under the

compliant system is lower than the indentation rate under the rigid system, due to the elastic deformation of the compliant beam during testing.

- The frequency of the cyclic loading has a strong dependence on the structural compliance of the system and it has also been noted that the amplitudes of the cyclic loads for the tests with structural compliance are higher than the tests without any structural compliance.

5.5.1 Relative Indentation Rate

The compliant indentation system in Phase 1A deflected due to its compliance. During the loading phase, the indented ice exhibits the formation of several microcracks in the ice that do not propagate unsteadily. The resistance of the ice is thus maintained and the ice force continues to increase. The structure deflects elastically, resulting in a decreased loading rate. The deflection continues until the microcracks reach a critical level, leading to the total failure of the indented ice. The ice cannot take more load and the structure starts to spring back, resulting in an increased loading rate. Peyton (1968) suggested that the strength of the ice has a strong dependence on the loading rate. The decreased loading rate during the loading phase causes an increase in the ice strength that eventually results in the total loading force to go up. On the contrary, failure in ice during the unloading phase leads to an increase in loading rate and a decrease in the strength of ice. The relative indentation rates constantly cycled between decreased rates during the loading phase and increased rates during the unloading phase throughout the periods of cyclic loading.

Figure 5.12 shows a displacement plot for test T05_1A_06_150. The plot consists of the nominal loading rate imposed by the hydraulic ram, structural deflection recorded by the LVDTs and the resulting relative indentation rate (nominal rate minus structural deflection). As observed, the loading rate during the loading phase of the test has been reduced. Around 11 seconds into the test, the nominal rate of 2.5 mm/s was reduced to approximately 2.1 mm/s. Around 11.7 seconds, a large pressure drop was observed and within milliseconds the deflected compliant beam sprung back to its original position. The indentation rate during this unloading phase had increased to 941 mm/s, almost 375 times the nominal loading rate and 450 times the relative loading rate during the loading phase. As shown in Figure 5.13, the relative rate continued changing once the indenter surface came in contact with the indented surface and the ice strength started building. It was during this unloading phase that much of the crushed ice was extruded.

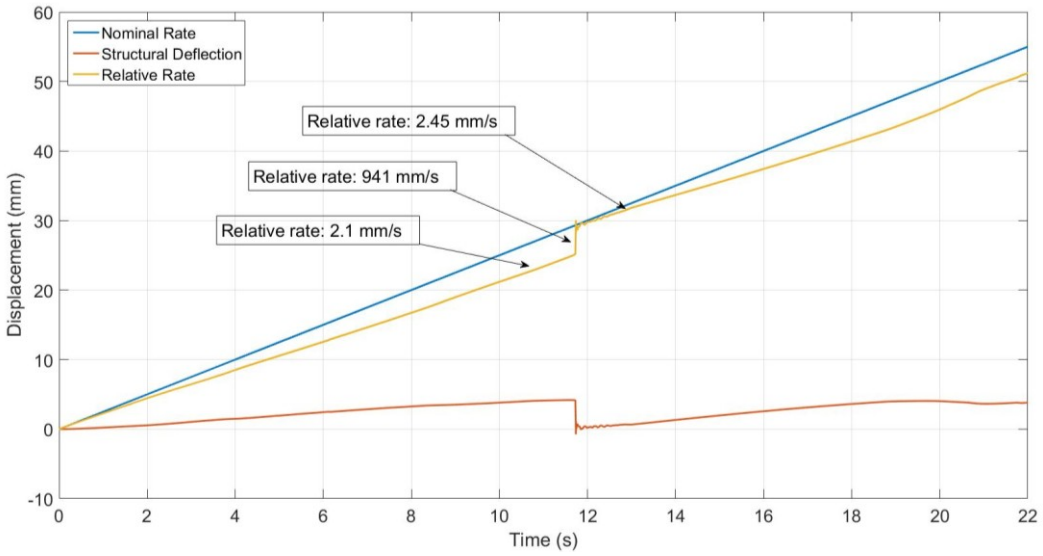

Figure 5.12: Displacement vs. time plot for the test T05_1A_06_150 comparing nominal rate, structural deflection and relative indentation rate.

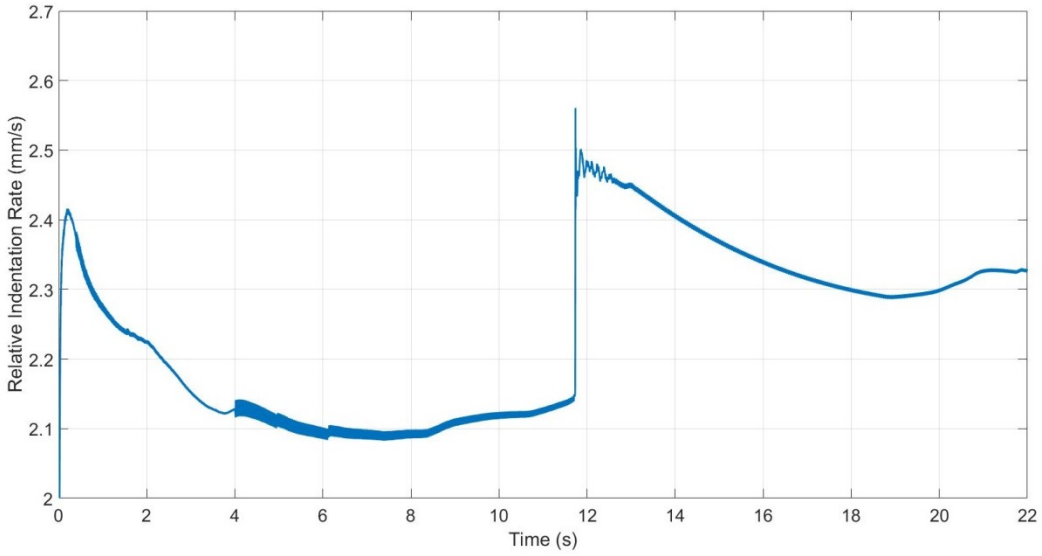

Figure 5.13: Plot of the relative indentation rate for test T05_1A_06_150.

The relative indentation rates are also affected by the ice sample temperatures. The relative indentation rates decrease with decreasing temperature. Thus, the warmer ice samples will have a lower relative indentation rate when compared to the colder ice samples.

5.5.2 Amplitude and Frequency of Cyclic Loading

It has been observed that the amplitude and the frequency of cyclic loading patterns are affected by the presence of structural compliance or lack thereof. Figures 5.14 and 5.15 illustrate the pressure-time plots, comparing the compliant (Phase 1A) and rigid indentation systems (Phase 1B). Figure 5.14 compares tests T08_1A_19_50_R (Phase 1A) and T10_1B_15_50 (Phase 1B). Both the tests were performed using a cold ice sample and a 50 mm indenter at an indentation rate of 2.5 mm/s. Similarly, Figure 5.15 compares tests T09_1A_07_100_R (Phase 1A) and T14_1B_06_100 (Phase 1B). Both

the tests were performed using a warm ice sample and a 100 mm indenter at an indentation rate of 2.5 mm/s.

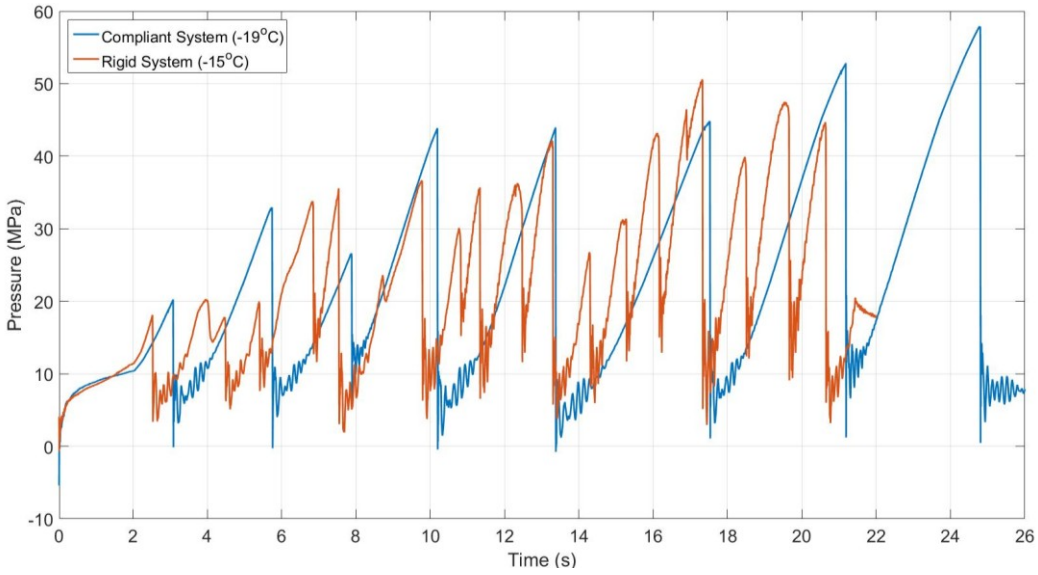

Figure 5.14: Pressure-time plot for tests conducted on different indentation systems using a 50 mm indenter and cold ice specimens.

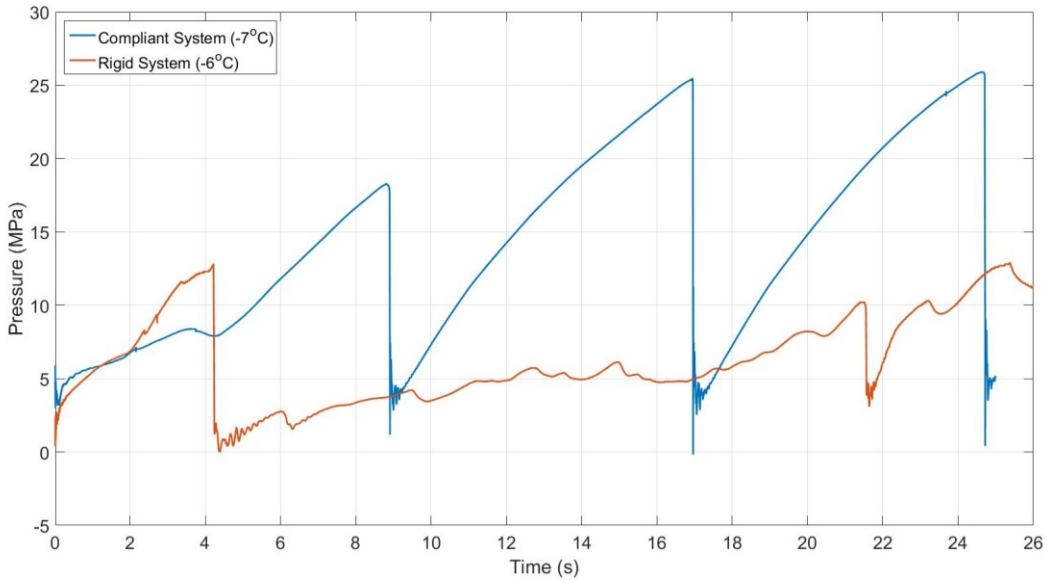

Figure 5.15: Pressure-time plot for tests conducted on different indentation systems using a 100 mm indenter and warm ice specimens.

At cold temperatures, the test samples in both the phases underwent regular sawtooth loading patterns. The frequency of the sawtooth loading for the compliant test was 0.35 Hz while the rigid test had a cyclic loading frequency of almost 1 Hz. The pressure amplitudes for both the tests were almost similar with mean overall mean peak pressures of 34 MPa and 40 MPa for the rigid and compliant tests respectively. Pressure drops were greater for the compliant test with almost every pressure drop reaching to zero. This phenomenon can be attributed to the increased relative indentation rates that develop during the unloading phase when the ice fails and the structure springs back, causing a decrease in the ice strength and the corresponding pressure drop. On the contrary, the pressure drops for the rigid test did not drop to zero due to significantly low structural feedback and corresponding increase in the relative loading rate.

At warm temperatures, the compliant test showed sawtooth loading patterns which was triggered by large spalls, while the rigid test underwent ductile failure. The frequency of the cyclic loading for the compliant test was 0.14 Hz. The average peak pressures for the rigid test was 12 MPa while the mean peak pressures for the compliant test was 23 MPa, almost double the pressure of the rigid test. The difference in the pressure amplitudes was likely due to the relative indentation rate caused by the structural deflection in the compliant system.

5.6 Summary

A series of medium-scale laboratory indentation tests were conducted to advance understanding of the compressive ice failure, and the links between ice failure processes

corresponding with the formation of *hpz*s, and the development of cyclic loading patterns. It was observed that the spalling of ice was responsible for the formation of the high-pressure zones and the associated regular sawtooth phenomenon. Spalling, the other load limiting failure mechanism, occurred only as a consequence of the clearing of ice around the indenter during rebounding of the structure.

High-pressure zones, dominated by spalling and brittle failure of ice were observed for the cold ice samples. These failure processes contributed to the development of regular sawtooth loading patterns. In comparison, warm ice failed in a more ductile manner due to the continuous extrusion of highly damaged ice, without any significant load drops or cyclic character. The microstructural behavior of ice was also affected by changes in temperature. The damaged layer of the warm ice samples showed very little evidence of microcracks while the damaged layer of the cold ice samples were dominated by zones of extensive spalling and microfractures with much less damaged ice beneath the indenter.

The peak pressures on the 50 mm indenter were significantly higher than the pressures on the 100 mm and 150 mm indenters. The frequency of the cyclic loading was also higher for the 50 mm indenters. The dominant ice failure mode for the tests conducted using the 50 mm indenter consisted of small, intermittent spalls with some ice crushing, while failure events for the medium (100 mm) and large (150 mm) indenter tests were associated more with very large spalls and associated load drops.

Structural deflection in the compliant system caused a decrease in the relative indentation rate during the loading phase, as compared with the rigid system. However, the relative

rate increased during the unloading phase due to the spring back action of the deflected beam, causing extrusion of pulverized ice. This resulted in higher peak pressures, when compared to the rigid indentation tests. It was also observed that the frequency and the amplitude of the cyclic loading patterns were higher for the compliant tests than the rigid tests.

Chapter 6: Conclusions

Medium-scale indentation tests on confined ice samples were carried out to improve understanding of compressive ice failure, and the formation of ice crushing dynamics during an ice-structure interaction. The formation, evolution and failure of high-pressure zones, and their role in the development of cyclic loading patterns were also a significant part of this research program. The effects of temperature, indenter size and structural compliance on the load-limiting ice failure mechanisms were also discussed. Based on the analysis of the observed data, the conclusions discussed below were drawn.

6.1 Crushing, Spalling and Cyclic Loading

During the indentation tests, failure processes like crushing and spalling were often observed. Spalling failure is a load limiting failure mechanism responsible for the cyclic loading phenomenon. The failure of high-pressure zones was linked to the regular load drops observed after significant localized spalls occurred, thus leading to the separation of spalled ice from the ice surface, and a sudden decrease in contact area. Crushing failure, unlike spalling, occurred only as a consequence of the clearing of ice around the indenter during rebounding of the structure. Crushing of ice resulted in the extrusion of fine-grained soft ice from *hpz* edges. Crushing was not the triggering mechanism responsible for initiating structural rebounding in these tests.

6.2 Temperature Effects

The indentation tests were planned to be carried out at two different temperatures: warm ice specimens at -5°C, and cold ice specimens at -20°C. The actual testing temperatures, however, ranged from -4.5°C to -7°C (the test at -1°C was an outlier) for the warm temperature tests and -14°C to -19°C for the cold temperature tests. Changes in the temperature had a significant effect on the ice failure processes that occurred during the indentation tests. At warmer temperatures, the ice failed in a more ductile manner due to the flow of highly damaged ice and continuous extrusion, without any significant load drops or cyclic character. By comparison, the cold ice samples produced high initial peak pressures, followed by brittle failure, large spalling events and sudden large load drops. All of the failure mechanisms mentioned above often led to the development of regular cyclic loading patterns.

The microstructural behavior of ice was also affected by the changes in the temperature. Due to ductile failure, the spalls in warmer ice were smaller in magnitude and size. The damaged layer in the indented area was heavily dominated by fine-grained crushed ice with microfractured ice at the edges. For colder ice samples, a considerable amount of spalling and microfractures was observed on the outer edges surrounding the indented area, with a distinct layer of damaged ice directly beneath the contact zone. Fractures became more dominant for lower temperatures.

6.3 Scale Effects

Three spherical indenters (50 mm small indenter, 100 mm medium indenter and 150 mm large indenter), scaled to different dimensions, were used for this research program. The load cell data showed that the use of large (150 mm) indenter results in the loading of very high forces on the ice specimen during indentation. The loads for the large indenter were almost three to five times the loads recorded for the small (50 mm) indenter. However, due to the smaller nominal area, the overall peak pressure corresponding to the small (50 mm) indenter was nearly double the peak pressure for the medium (100 mm) indenter and about five times the peak pressure for the large (150 mm) indenter.

Though cyclic loading patterns were observed in the majority of the tests, particularly for cold ice, their characteristics vary with changes in scale. For smaller indenters, the pressure drops were higher and the amplitudes of the cyclic loads were greater, when compared to the larger indenters. Similarly, the frequencies of cyclic loading patterns for the small indenter tests were almost two to three times the frequencies for the larger indenter tests.

6.4 Effect of Structural Compliance

For compliant tests, the relative indentation rate decreases during the loading phase of the ice, subsequently increasing the ice strength and peak pressures. On failure of the ice, the deflected beam springs back, increasing the relative indentation rate and reducing the ice strength. These fluctuations in the relative indentation rate assists in the development of

regular cyclic loading patterns. In addition, the release of stored elastic energy also helped clear the damaged ice from beneath the indenter, resulting in load drops to near zero.

The frequency and the amplitude of cyclic loading have a strong dependence on structural compliance of the system. It was observed that the frequency of the cyclic loading was higher for the rigid indentation system. The load cycling amplitude for compliant indentation tests were higher than those for the rigid tests i.e. the load drops were bigger due to the presence of structural deflection and the feedback energy from the structure onto the ice.

6.5 Recommendations for Future Work

Compressive ice failure is a complex process that needs to be studied and analyzed in greater detail. Several recommendations for future work have emerged throughout the course of this testing program. Medium-scale laboratory testing is an efficient and cost-effective way to study the compressive ice failure and the ice crushing dynamics during ice-structure interactions. However, data obtained from full-scale testing would be extremely helpful to better understand the actual failure processes observed during ice-structure interactions.

A number of recommendations can be made within the scope of this testing program. All the tests in this program were performed at an indentation speed of 2.5 mm/s. However, the crushing rates of the ice sheet against offshore structures range from 0.001 mm/s to 1800 mm/s. Therefore, performing medium-scale tests using a broad range of indentation rates is highly recommended. Ice encountered in the Arctic and sub-Arctic environments

have temperatures ranging from -40°C to 0°C. Increasing the temperature range of the ice samples is suggested for further testing. Scale effects were quite prominent during the tests. It helped in understanding the implications of cyclic loading patterns and the formation of high-pressure zones on a larger structure. Increasing the scale of the tests can further assist in reducing the gap between the full-scale offshore tests and the medium-scale laboratory tests. Thin sections of the damaged layer were not analyzed in this test program. To gain insights into the microstructural modifications and behavior of ice, further examination of the horizontal and vertical thin-sections of the damaged ice adjacent to the indented area are recommended.

The complete testing process was carried out at room temperature and precautions were taken to reduce the action of room temperature on the ice samples. However, it was observed that the temperature of most ice specimens varied from the ideal temperatures. Using a dedicated cold space that can accommodate the testing apparatus to perform further medium-scale tests is recommended.

Two rigid tests using a large indenter had to be stopped abruptly due to some technical errors encountered while testing, one of them being inadequate load testing capacity of some testing equipment. Increasing the load capacity of the test apparatus will help in preventing these issues. During calibrations tests, the compliant beam was overloaded which caused a small amount of permanent deflection in the beam. Due to eccentricities in the loads, the compliant beam experienced significant torsional loading and bending moments. Using an indenter of shorter size and a beam with higher torsional rigidity are recommended for future tests.

In conclusion, the results from this test program look promising and are currently being used to plan and design the upcoming tests using multiple ice specimens and indenters to analyze the formation of multiple high-pressure zones, and the transmission of loads onto the structure. Simulating multiple high-pressure zones on the same structure can help in investigating synchronized crushing failure, cyclic loading patterns and other multiple high-pressure zones failure processes. The results of this thesis are a step forward in improving our understanding of compressive ice failure and ice crushing dynamics during ice-structure interactions.

Bibliography

Akagawa, S., Nakazawa, N., and Sakai, M. 2000. Ice failure mode predominantly producing peak-ice-load observed in continuous ice load records. Proceedings of the l0th International Offshore and Polar Engineering Conference, pp. 613.

Barrette, P., Pond, J., and Jordaan, I. 2002. Ice damage and layer formation in small-scale indentation experiments. Ice in the Environment, Proceedings of the 16th International Symposium on Ice, IAHR, Dunedin, New Zealand, 2002, Vol. 3, pp. 246-253.

Björk, B. 1981. Ice induced vibrations of fixed offshore structures, Part 2: Experiences with Baltic Lighthouses. In Marine Structures and ships in Ice, Rep. 81-06/2, pp. 100.

Blenkarn, K.A. 1970. Measurement and analysis of ice forces on Cook Inlet Structures. Proc. 2ndOffshore Technology Conference, Houston, TX, OTC 1261, Vol. 2, pp. 365-378.

Browne, T. (2012).Analysis of compressive ice failure during ice-structure interaction. M. Eng. Thesis, Memorial University of Newfoundland, St. John's, Canada.

Browne, T., Taylor, R., Jordaan, I., and Gürtner, A. 2013. Small-scale ice indentation tests with variable structural compliance. Cold Regions Science and Technology, 88, 2-9.

Croasdale, K.R. 1975. Ice forces on marine structures. Proceedings 3rd IAHR Symposium on Ice. Hanover, New Hampshire, pp. 317-337.

Croasdale, K.R, Morgenstern, N.R., and Nuttal, J.B. 1977. Indentation tests to investigate ice pressures on vertical piers. Journal of Glaciology, 19(81), pp. 301-312.

Duval, P., Ashby, M. F., and Anderman, I. 1983.Rate-controlling processes in the creep of polycrystalline ice. The Journal of Physical Chemistry, 87(21), pp. 4066-4074.

Engelbrektson, A. 1977. Dynamic Ice Loads on a Lighthouse Structure. In Proceedings of International Conf. on Port and Ocean Eng. under Arctic Cond. (POAC), St. John's, Canada, 3: 654-663.

Engelbrektson, A., and Janson, J. E. 1985.Field observations of ice action on concrete structures in the Baltic Sea. Concrete International, 7(8), pp. 48-52.

Engelbrektson, A. 1989.An ice-structure interaction model based on observations in the Gulf of Bothnia. Proc. International conf. on Port and Ocean Eng. under Arctic Cond. (POAC), Luleå, Sweden, (3), pp. 504-517.

Fransson, L., and Danielsson, G. 1985. Ice conditions and ice properties close to the light pier Björnklacken shortly after failure due to forces from a moving ice sheet. Department of Structural Engineering. Luleå University of Technology, Sweden, Skrift, 85: 13.

Frederking, R.M.W., Jordaan, I.I., and McCallum, J.S. 1990. Field-tests of ice indentation at medium scale: Hobson's Choice ice island 1989. Proceedings of 10th International Symposium on Ice, IAHR, Espoo, Finland, Vol. 2, pp. 931-944.

Frost, H. 1995. Mechanisms of crack nucleation in ice. Ice Mechanics, ASME, 207, pp. 1-8.

Frost, H. 2001. Mechanisms of crack nucleation. Engineering Fracture Mechanics, 68 (200 1), pp. 1823-1837.

Gagnon, R.E., and Sinha, N .K.1991. Energy dissipation through melting in large-scale indentation experiments on multi-year sea ice. Proceedings of OMAE, Vol. IV, pp. 157-161.

Gagnon, R.E. 1998. Analysis of visual data from medium scale indentation experiments at Hobson's Choice Ice Island. Cold Regions Science and Technology, 28:45-58.

Glen, J.W. 1975. The mechanics of ice: cold regions science and engineering monograph IIC2b. Cold Regions Research and Engineering Laboratory, Hanover, New Hampshire, pp. 29-33.

Gold, L.M. 1972.The failure process in columnar-grained ice. Technical Paper No. 369, Division of Building Research, NRC.

Gudmestad, O. T., Løset, S., Alhimenko, A. I., Shkhinek, K. N., Tørum, A., and Jensen, A. 2007. Engineering aspects related to Arctic offshore developments. St. Petersburg, Lan, pp. 255.

Habib, K. B. 2014. Experimental investigation of compressive failure of truncated conical ice specimen. M. Eng. Thesis, Memorial University of Newfoundland, St. John's, Newfoundland, Canada.

Habib, K. B., Taylor, R. S., Bruneau, S., and Jordaan, I. J. 2015. Experimental study of dynamics during crushing of freshwater truncated conical ice specimens. In ASME 2015 34th International Conference on Ocean, Offshore and Arctic Engineering, St John's, Newfoundland, Canada.

Hobbs, P.V. 1974. Ice physics. Clarendon Pres, Oxford.

ISO 19906.Petroleum and natural gas industries - Arctic offshore structures.ISO Draft International Standard.ICS 75.180.10.

Jefferies, M. G., and Wright, W. H. 1988.Dynamic response of Molikpaq to ice-structure interaction. In Proceedings of the Conference on Offshore Mechanics and Arctic Engineering, pp. 201-220.

Jonas, J.J., and Muller, F. 1969. Deformation of ice under high internal shear stresses, Canadian Journal of Earth Sciences, Vol. 6, pp. 963-968.

Jordaan, I., and McKenna, R., 1988. Constitutive relations for creep of ice. Proceedings of 9th IAHR International Symposium on Ice, Sapporo, Japan, Vol. 3, pp. 47-58.

Jordaan, I. J., and Xiao, J. 1992. Interplay between damage and fracture in ice-structure interaction. Proceedings of the 11th International Symposium on Ice, IAHR, Banff, Alberta, Vol. 3, pp. 1448- 1467.

Jordaan, I.J., and Singh, S.K. 1994. Compressive ice failure: critical zones of high pressure. Proc. 12th International IAHR Ice Symposium, Vol. I, Trondheim, Norway, pp. 505-514.

Jordaan, I. J., Matskevitch, D. G., and Meglis, I. L. 1999. Disintegration of ice under fast compressive loading. International Journal of Fracture, 97(1-4), pp. 279-300.

Jordaan, I.J. 2001.Mechanics of ice-structure interaction. Engineering Fracture Mechanics, 68:1923-1960.

Jordaan, I., and Pond, J. 2001. Scale effects and randomness in the estimation of compressive ice loads. In IUTAM Symposium on Scaling Laws in Ice Mechanics and Ice Dynamics, pp. 43-54.

Jordaan, I.J. 2005.Decisions under uncertainty: probabilistic analysis for engineering decisions. Cambridge University Press.

Jordaan, I., Li, C., Sudom, D., Stuckey, P., and Ralph, F. 2005a. Principles for local and global ice design using pressure area relationships. In Proceedings of the International Conference on Port and Ocean Engineering Under Arctic Conditions, Potsdam, N.Y., Vol. 1, pp. 375-385.

Jordaan, I., Frederking, R., and Li, C. 2006. Mechanics of ice compressive failure, probabilistic averaging and design load estimation. Proceedings of 18th International Symposium on Ice, IAHR, Sapporo, Japan, Vol. 2, pp.223-230.

Jordaan, I.J., Wells, J., Xiao, J., and Derradji-Aouat, A. 2008.Ice crushing and cyclic loading in compression. Proceedings 19th IAHR Symposium on Ice, Vancouver, British Columbia, Canada.

Kamio, Z., Takawaki, T., Matsushita, H., Takeuchi, T., Sakai, M., Terashima, T., Akagawa, S., Nakazawa, N., and Saeki, H. 2000.January. Medium scale field indentation tests: physical characteristics of first-year sea ice at Notoro Lagoon, Hokkaido. In The Tenth International Offshore and Polar Engineering Conference. International Society of Offshore and Polar Engineers, pp. 562.

Kheisin, D.E., and Cherepanov, N.V. 1976. Change of ice structure in the zone of impact of a solid body against the ice cover surface. Problems of the Arctic and Antarctic, 33: 239-245.

Kurdyumov, V. A., and Kheisin, D. E. 1976.Hydrodynamic model of the impact of a solid on ice. International Applied Mechanics, 12(10), pp. 1063-1068.

Li, C. (2007). Probability and fracture mechanics applied to ice load estimation and associated mechanics. Ph.D. Thesis, Memorial University of Newfoundland, St. John's, NL, Canada.

Lockett, F. J. 1972. Nonlinear Viscoelastic Solids. Academic Press, New York.

Masterson, D.M., Frederking, R.M.W., Jordaan I.J., and Spencer, P.A. 1993. Description of multi-year ice indentation tests at Hobson's Choice ice island- 1990. Proceedings of 12th International Conference on Offshore and Arctic Engineering, Glasgow, UK, Vol. 4, pp. 145-55.

Määttänen, M. 1975. Ice forces and vibrational behavior of bottom-founded steel lighthouses. In Proc. 3rd IAHR Ice Symposium, Hanover, New Hampshire, USA, pp. 345-355.

Määttänen, M. 1977. Ice-force measurements at the Gulf of Bothnia by the instrumented Kemi I Lighthouse, In Proc. International conf. on Port and Ocean Eng. under Arctic Cond., St. Johns, Canada, (2): 730-740.

Määttänen, M. 1983. Dynamic ice-structure interaction during continuous crushing. (CRREL Rep. 83-5) Cold Regions Research and Engineering Lab, Hanover, New Hampshire, USA.

Määttänen, M. 1988. Ice-induced vibrations in structures – self-excitation. IAHR Ice Symposium, Sapporo, Japan.2: 658-665.

Määttänen, M., and Hoikkanen, J. 1990.The effect of ice pile-up on the ice force of a conical structure. In Proc. IAHR Symposium on Ice, Vol. 2, pp. 1010-1021.

Määttänen, M. 2008. Ice velocity limit to frequency lock-in vibrations. In International Symposium on Ice. IAHR, Vancouver, Canada, pp. 1265-1276.

Mackey, T. 2005. Laboratory indentation of polycrystalline ice: an investigation of fracture. M.Eng. Thesis, Memorial University, St. John's, NL, Canada.

Mackey, T., Wells, J., Jordaan, I.J., and Derradji-Aouat, A. 2007.Experiments on the fracture of polycrystalline ice. Proceedings of POAC 2007. Dalian, China.

Masterson, D.M., Nevel, D.E., Johnson, R.C., Kenny, J.J., and Spencer, P.A. 1992. The medium scale iceberg impact test program. Proceedings of IAHR Ice Symposium, Banff, Alberta.

Masterson, D. M., and R.M.W. Frederking. 1993. Local contact pressures in ship/ice and structure/ice interactions. Cold Regions Science and Technology, 21: 169-185.

Masterson, D. M., Spencer, P. A., Nevel, D. E., and Nordgren, R. P. 1999. Velocity effects from multiyear ice tests. Proceedings 18th OMAE Conference, S. John's, Canada.

Matsushita, H., Takawaki, T., Hirayama, K.I., 1997.Medium scale field indentation tests-physical properties and strength of the ice sheet. Proceedings of the 7th International Offshore and Polar Engineering Conference, Vol. 2, pp. 368.

Meglis, I., Melanson, P., and Jordaan, I. 1999. Microstructural change in ice: II. Creep behavior under triaxial stress conditions. Journal of Glaciology, 45(151), pp. 438-448.

Muggeridge, K. and Jordaan, I., 1999. Microstructural change in ice: III. Observations from an iceberg impact zone. Journal of Glaciology 45(151), pp. 449-455.

Nadreau, J.P., and Michel, B. 1984.Ice properties in relation to ice forces. Proceedings of 2nd State-of-the-Art IAHR Working Group on Ice Forces, Hamburg, Germany, 4: 105-113.

Niell, C.R., 1975. Force fluctuations during ice-floe impact on piers. Proceedings of IAHR Symposium, Lenningrad, pp. 44-50.

Nordell, B., 1990. Measurement of a P-T coexistence curve for ice-water mixture. Cold Regions Science and Technology, 19: 83-88.

O'Rourke, B.J., Jordaan, I.J., Taylor, R.S., and Gürtner.A. 2016 a. Experimental investigation of oscillation of loads in ice high-pressure zones, Part 1: Single indenter system. J. Cold Reg. Sci. Technol, 124: 25–39.

O'Rourke, B. J., Jordaan, I. J., Taylor, R. S., and Gürtner, A. 2016 b. Experimental investigation of oscillation of loads in ice high-pressure zones, Part 2: Double indenter system—coupling and synchronization of high-pressure zones. Cold Regions Science and Technology, 124: 11-24.

Peyton, H. R. 1968. Sea ice forces. National Research Council of Canada, Technical Memo 92, pp. 117-123.

Sanderson, T.J.O. 1988. Ice mechanics: Risks to offshore structures. Graham and Trotman, London.

Sinha, N.K. 1977. Technique for studying the structure of sea ice. Journal of Glaciology, Vol. 18, No. 79, pp. 315-323.

Sinha, N.K. 1979. Grain boundary sliding in polycrystalline materials. Phil. Mag. A, Vol. 40, pp. 825-842.

Sinha, N. 1989.Elasticity of natural types of polycrystalline ice. Cold Regions Science and Technology, Vol. 17, No.2, pp. 127–135.

Sinha, N. K., and Cai, B. 1992. Analysis of ice from medium-scale indentation tests. National Research Council of Canada Report IME-CRE-LM-002, Ottawa, Ontario, Canada.

Schapery, R.A. 1997. Nonlinear viscoelastic and viscoplastic constitutive equations based on thermodynamics. Mechanics of Time-Dependent Materials, Vol. 1, pp. 209-240.

Schulson, E.M., and Cannon, N.P. 1984. The effect of grain size on the compressive strength of ice. IAHR Ice Symposium, Hamburg, Germany, pp. 24-38.

Sodhi, D.S., Takeuchi. T., Nakazawa, N., Akagawa, S., and Saeki, H. 1998. Medium-scale indentation tests on sea ice at various speeds. Cold Regions Science and Technology, (28): 161-182.

Takeuchi, T., Masaki, T., Akagawa, S., et al., 1997. Medium-scale indentation tests (MSFIT) - ice failure characteristics in ice/structure interactions. Proceedings of 7th International Offshore and Polar Engineering Conference, Vol. 2, pp. 376.

Taylor, R.S., Frederking, R., and Jordaan, I. J. 2008. The nature of high pressure zones in compressive ice failure. Proceedings 19th IAHR Symposium on Ice, Vancouver, British Columbia, Canada.

Taylor, R.S., Jordaan, I.J., Derradji-Aouat, A., and Bugden, A. 2010.Laboratory investigation of compressive failure of freshwater ice sheets. Technical Report. National Research Council of Canada.

Taylor, R. S., Murrin, D. C., Kennedy, A., and Randell, C. 2012. Arctic Development Roadmap: Prioritization of R&D. In Offshore Technology Conference, Houston, Texas, USA.

Timco, G., and Frederking, R. 1986. The effects of anisotropy and microcracks on the fracture toughness of freshwater ice. In the Proceedings of the 5th International OMAE Conference, Tokyo, Japan, Vol. 4, pp. 341-348.

Timco, G. W., and Weeks, W. F. 2010. A review of the engineering properties of sea ice. Cold Regions Science and Technology, 60(2), pp. 107-129.

Timoshenko, S., and Goodier, J.N. 1951. Theory of elasticity. McGraw-Hill.

Urai, J.L., Means, W.D.M. and Lister, G.S. 1986. Dynamic recrystallization of minerals. American Geophysical Union, Geophysical Monograph, 36, pp. 161-199.

Vernon. R.H. 1981. Optical microstructure of partly recrystallized calcite in some naturally deformed marbles. Tectonophysics, Vol. 78, pp. 601-612.

Wei, Y., and Dempsey, J.P. 1991. Fractographic examinations of fracture in polycrystalline S2 ice. Journal of Materials Science, 26: 5733-5740.

Wells. J., Jordaan, I., Derradji-Aouat, A., and Taylor. R. 2010. Small-scale laboratory experiments on the indentation failure of polycrystalline ice in compression: Main results and pressure distribution. Cold Regions Science and Technology, Vol. 65, No.3, pp.314-325.

Xiao, J., 1997. Damage and fracture of brittle viscoelastic solids with application to ice load models. Ph.D. Thesis, Memorial University, St. John's, NL, Canada.

Xu, J., Shi, Q., and Meng, Z. 1983. Features of frequency and amplitude in ice-induced vibration of a jacket platform. IAHR Ice Symposium, Espoo, Finland, pp. 952-959.

Yue, Q., Zhang, X., Bi, X., and Shi, Z. 2001. Measurements and analysis of ice induced steady state vibration. In Proceedings of the 16th International Conference on Port and Ocean Engineering Under Arctic Conditions, 1: 413-420.

Yue, Q., Guo, F., and Kärnä, T. 2009. Dynamic ice forces of slender vertical structures due to ice crushing. Cold Regions Science and Technology, 56 (2): 77-83.

APPENDIX A – Test Results and Images

Phase 1A

Test T01_1A_01_100

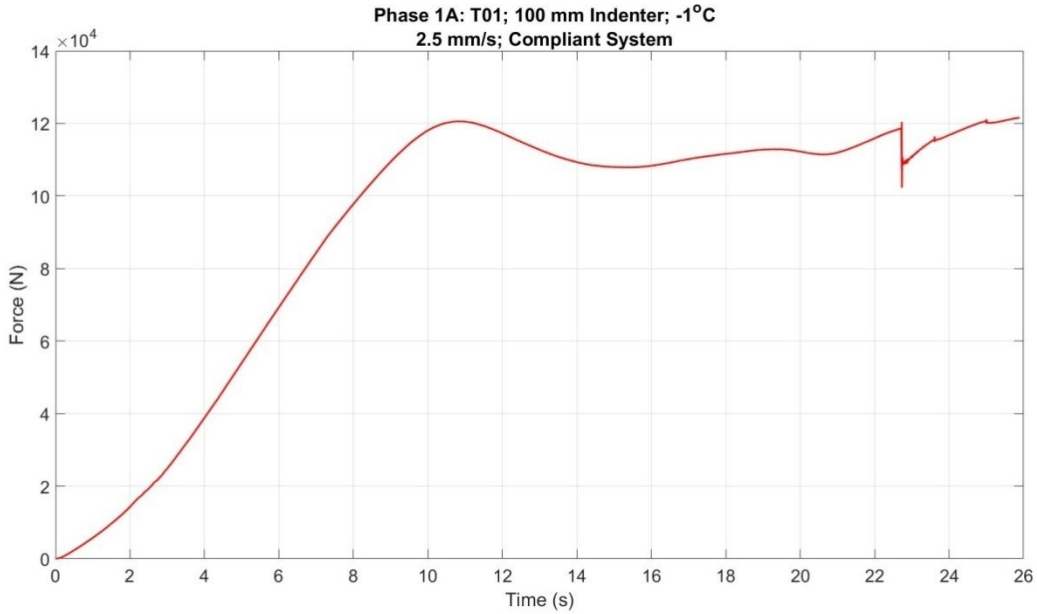

Figure A1.1: Force vs. time plot.

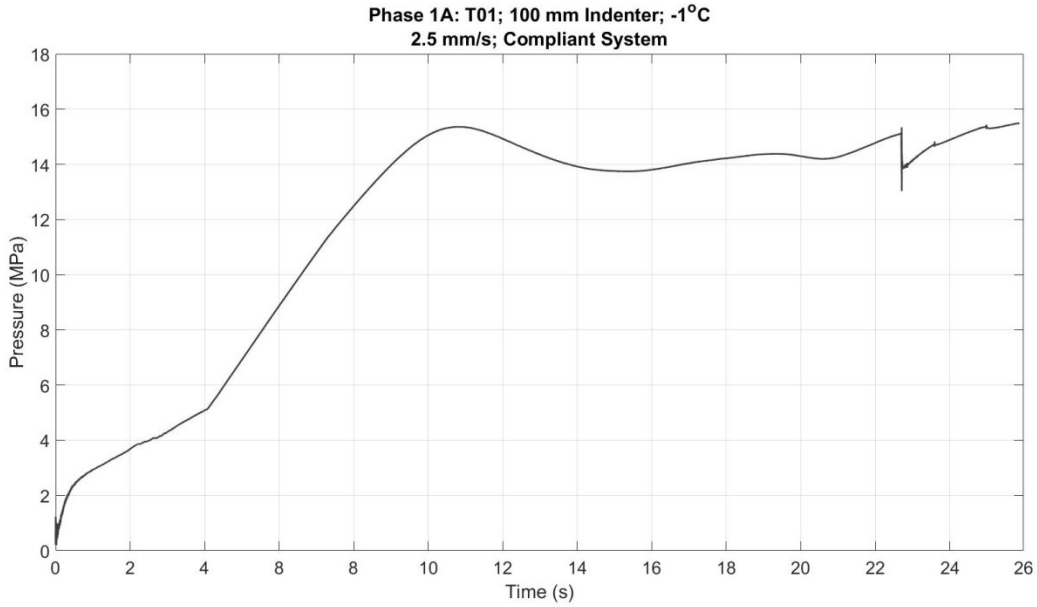

Figure A1.2: Pressure vs. time plot.

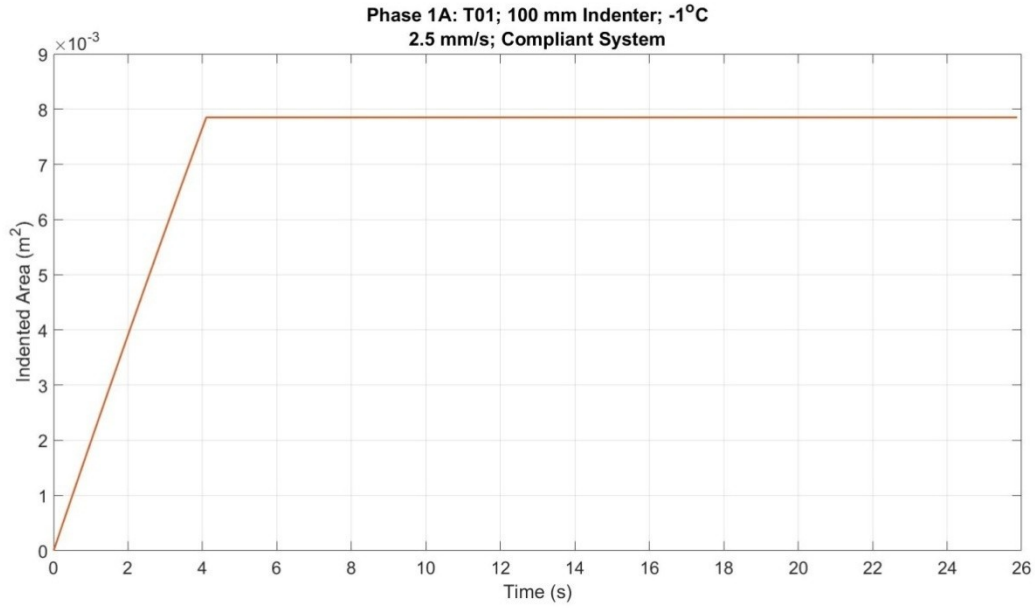

Figure A1.3: Indented area vs. time plot.

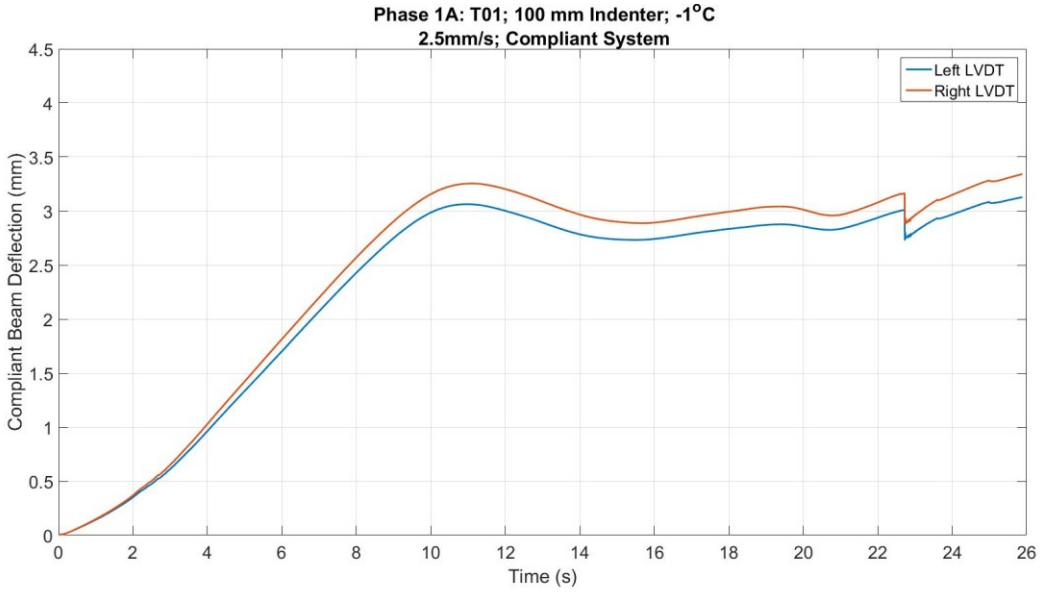

Figure A1.4 a: Compliant beam deflection vs. time plot.

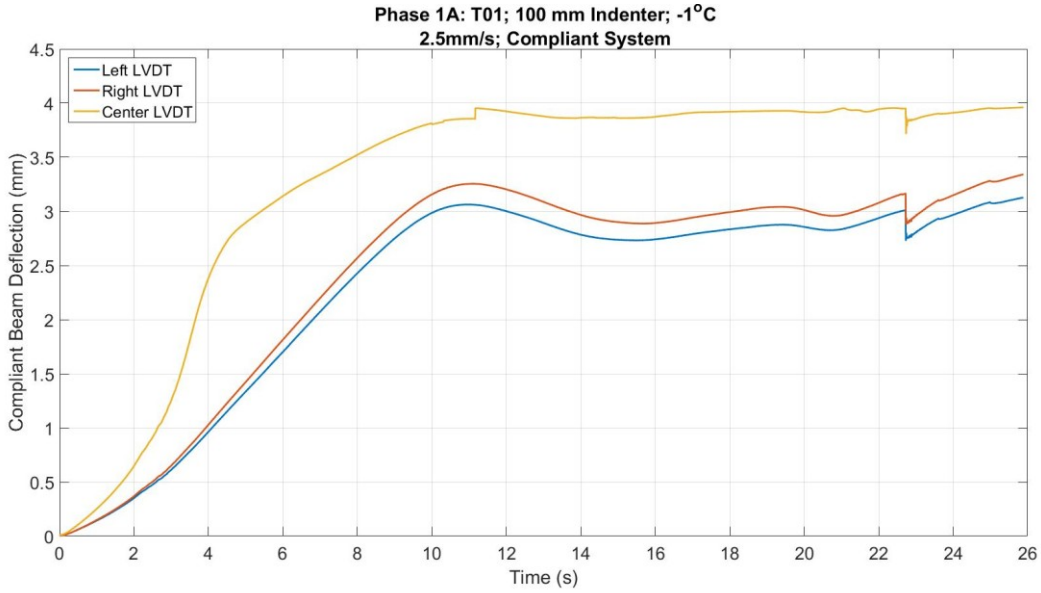

Figure A1.4 b: Compliant beam deflection vs. time plot.

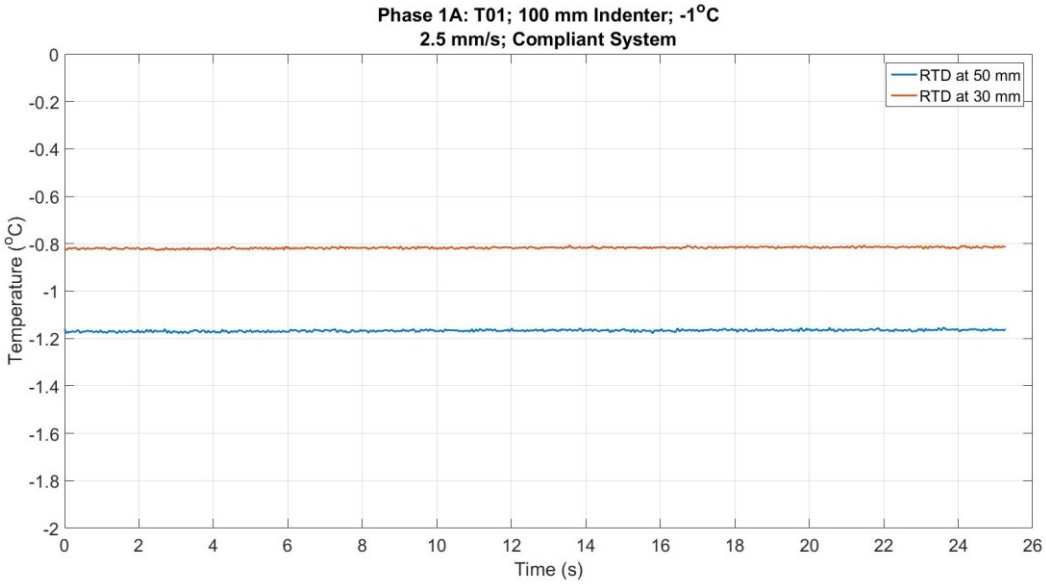

Figure A1.5: Temperature vs. time plot.

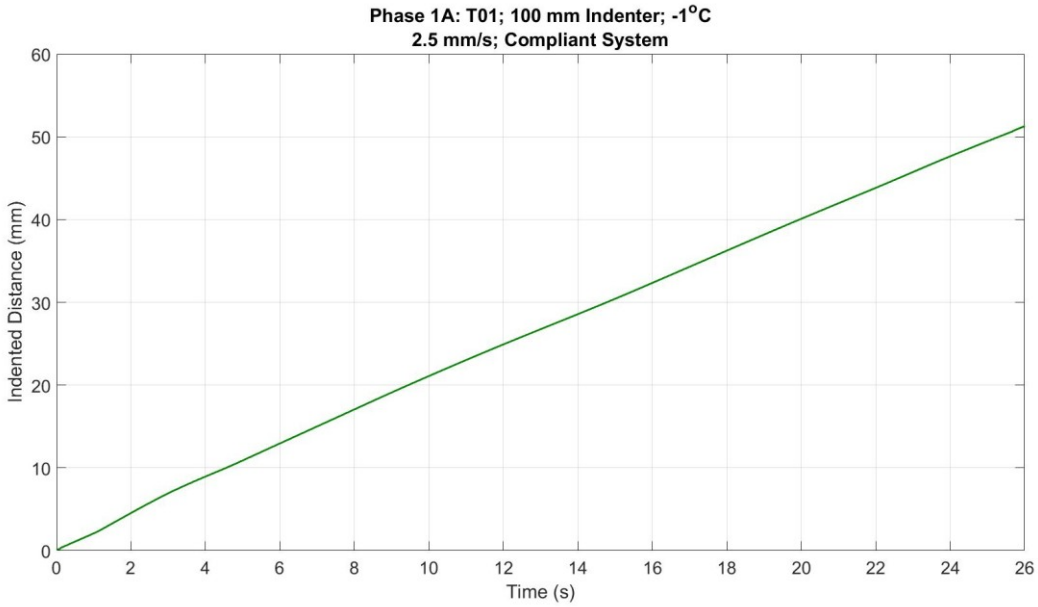

Figure A1.6: Indented distance vs. time plot.

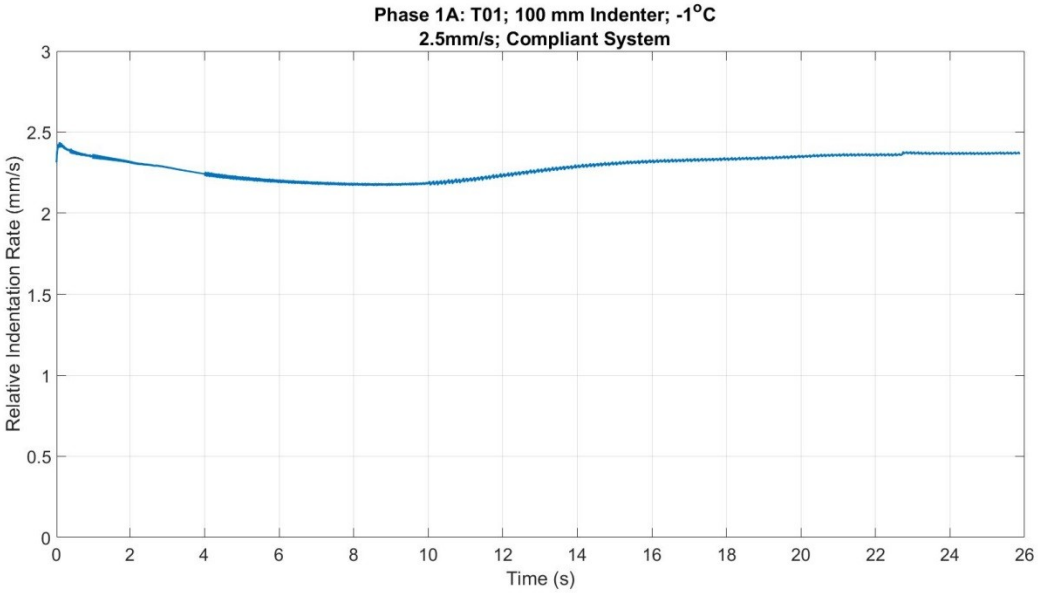

Figure A1.7: Relative loading rate vs time plot.

Figure A1.8 (a): Post-test images for test T01_1A_01_100.

Figure A1.8 (b): Post-test images for test T01_1A_01_100.

Figure A1.8 (c): Post-test images for test T01_1A_01_100.

Test T02_1A_18.5_100

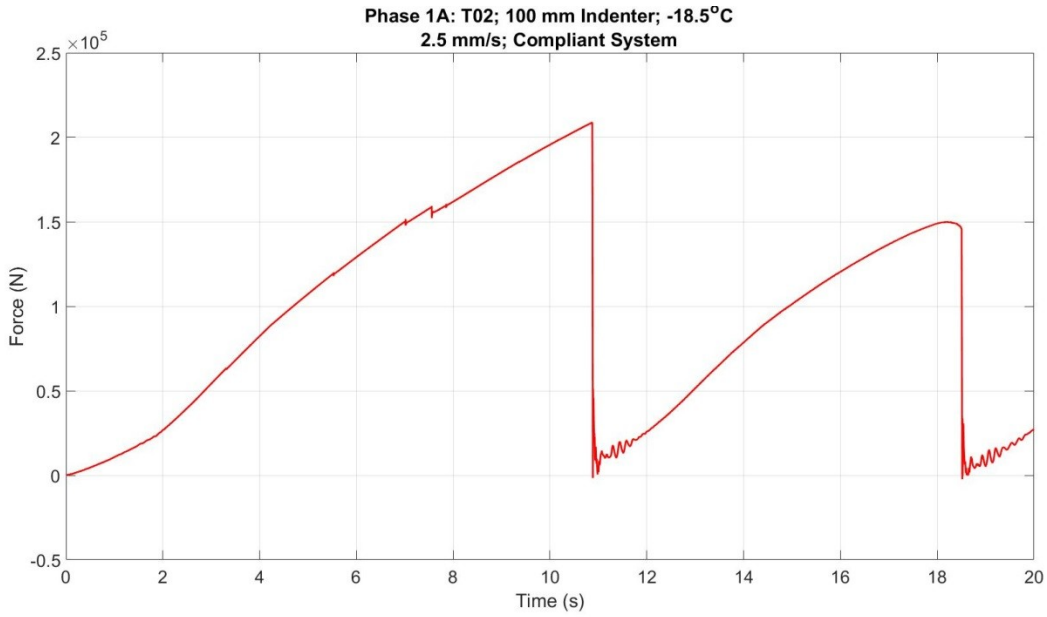

Figure A2.1: Force vs. time plot.

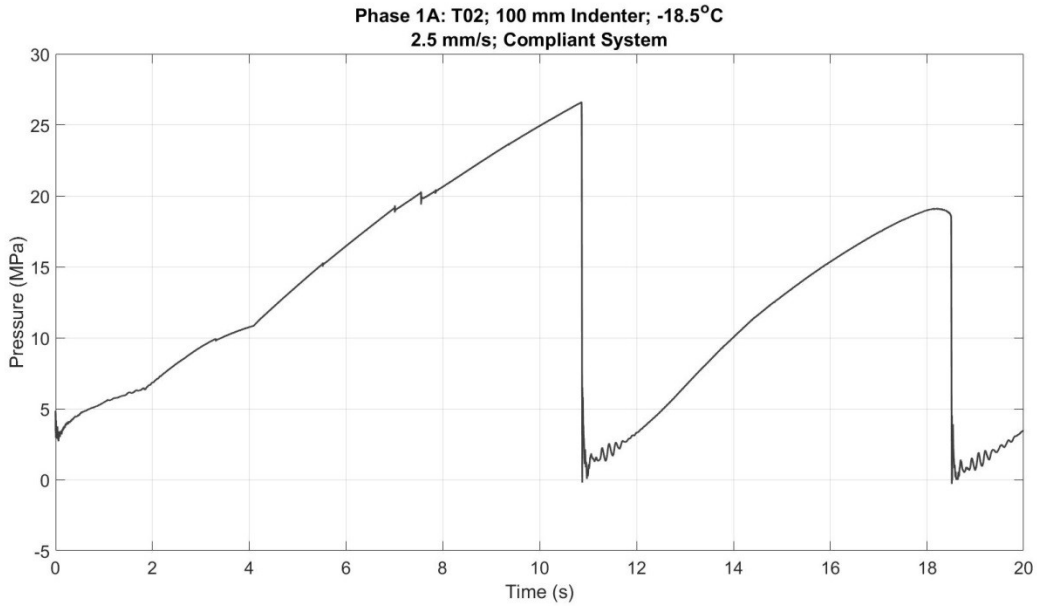

Figure A2.2: Pressure vs. time plot.

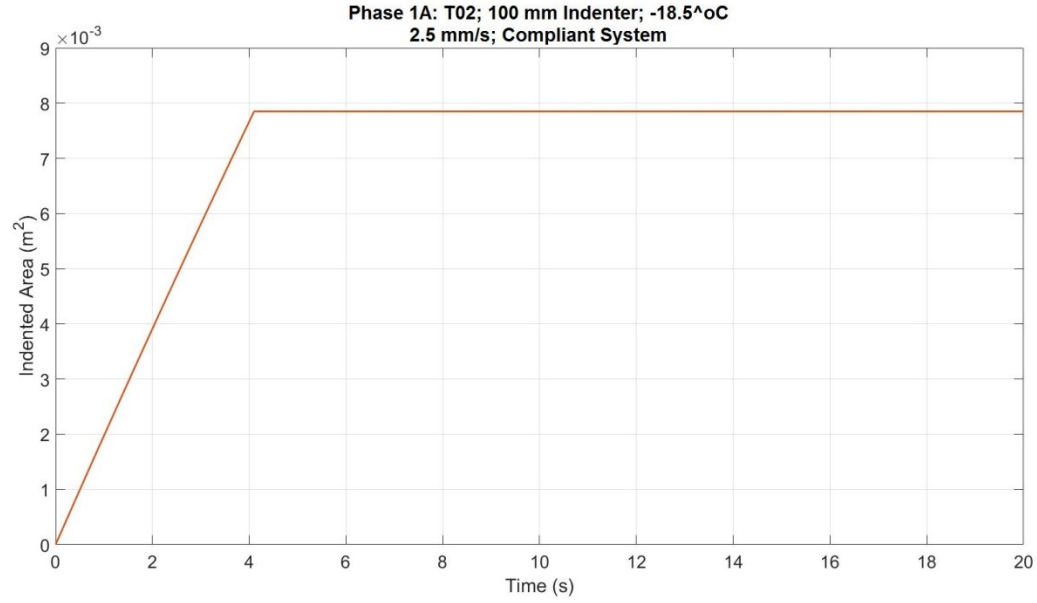

Figure A2.3: Indented area vs. time plot.

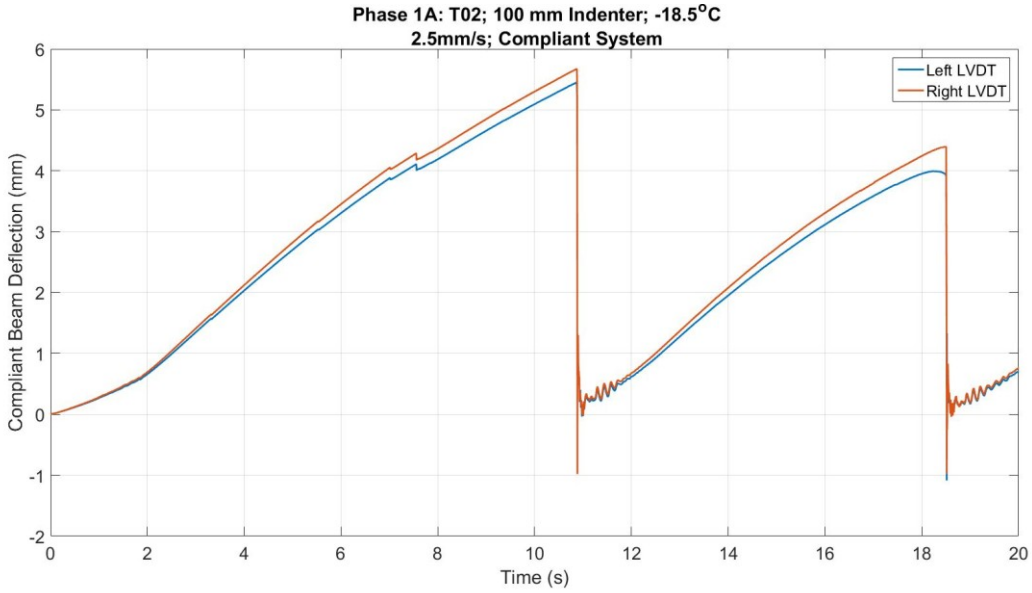

Figure A2.4 a: Compliant beam deflection vs. time plot.

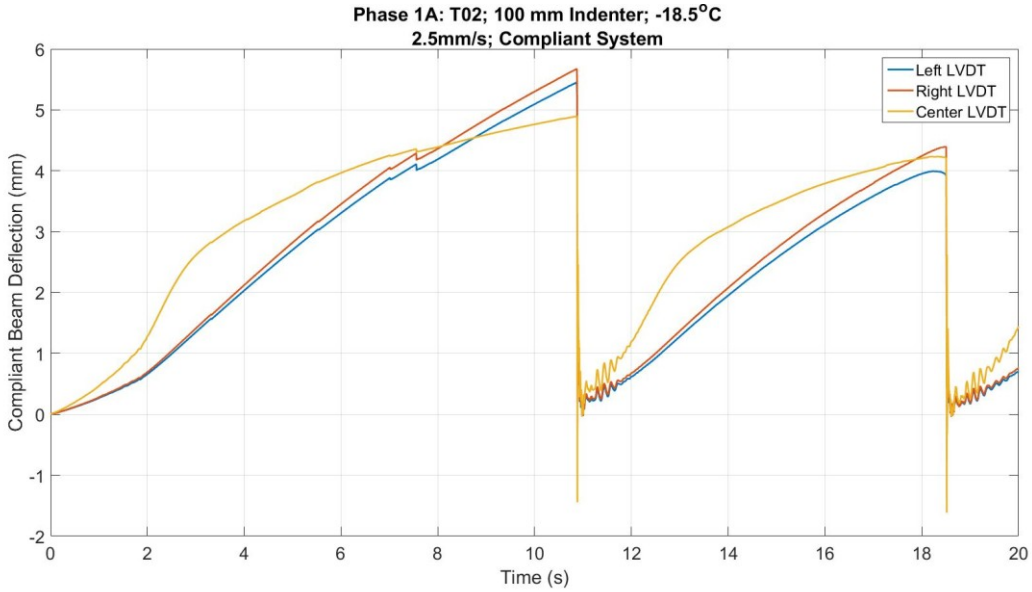

Figure A2.4 b: Compliant beam deflection vs. time plot.

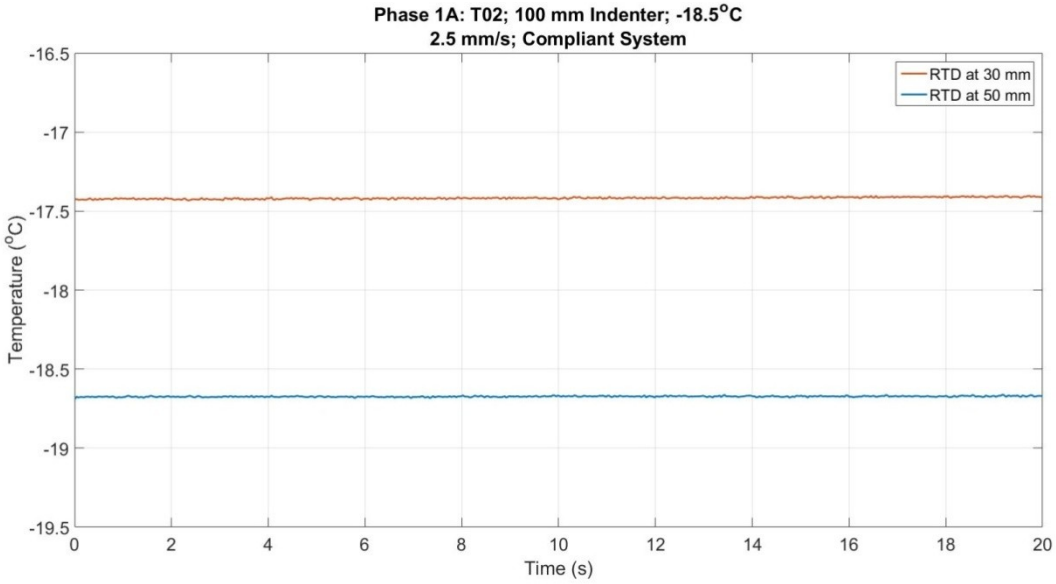

Figure A2.5: Temperature vs. time plot.

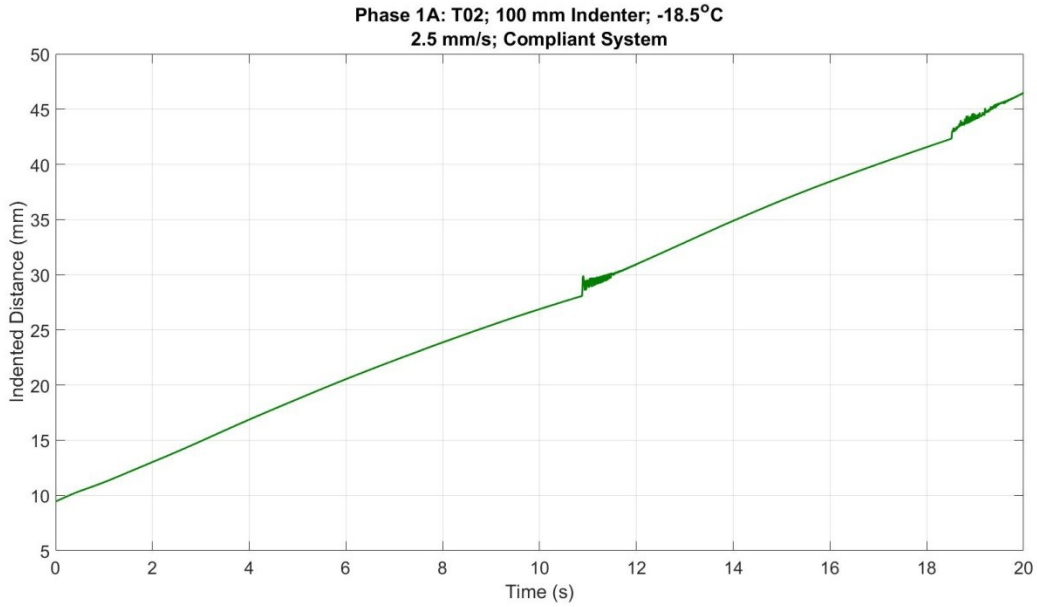

Figure A2.6: Indented distance vs. time plot.

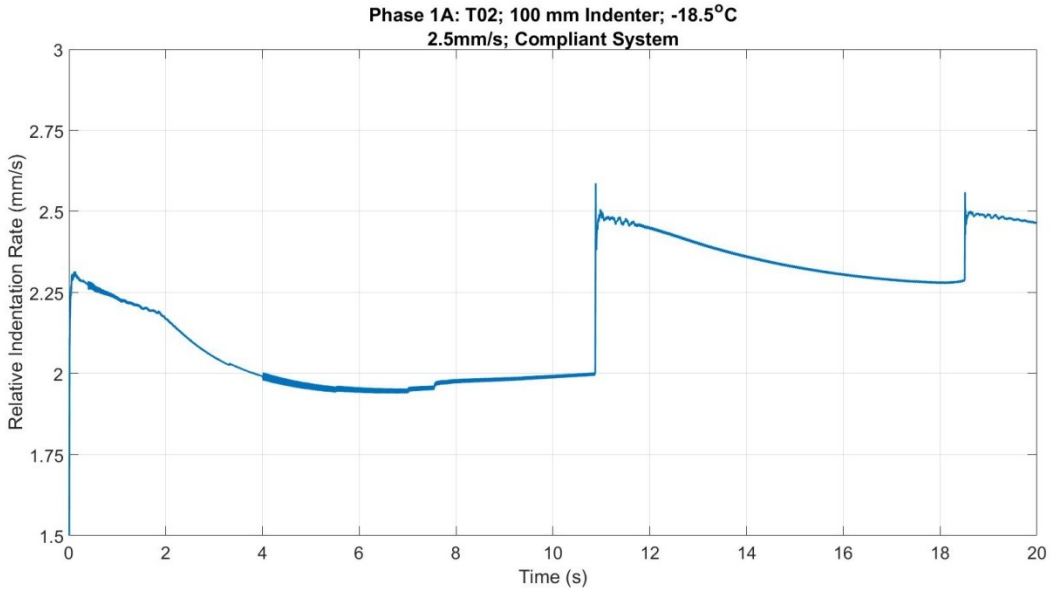

Figure A2.7: Relative loading rate vs time plot.

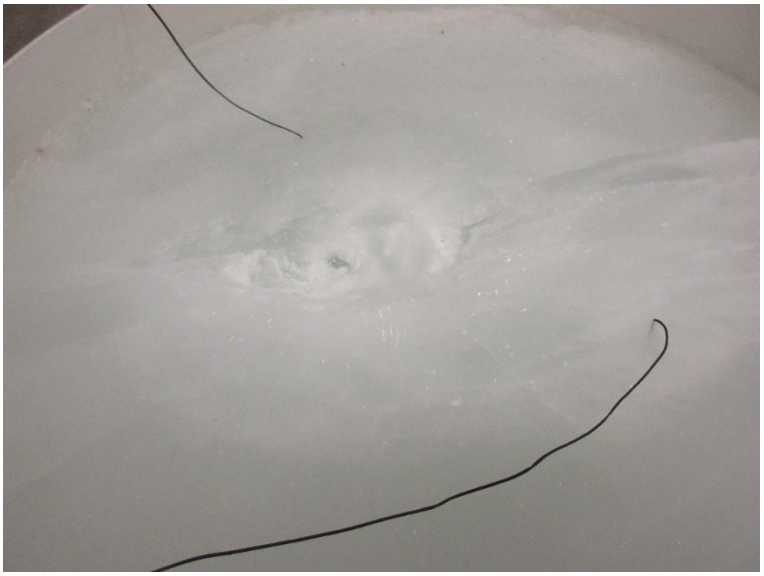

Figure A2.8 (a): Post-test images for test T02_1A_18.5_100.

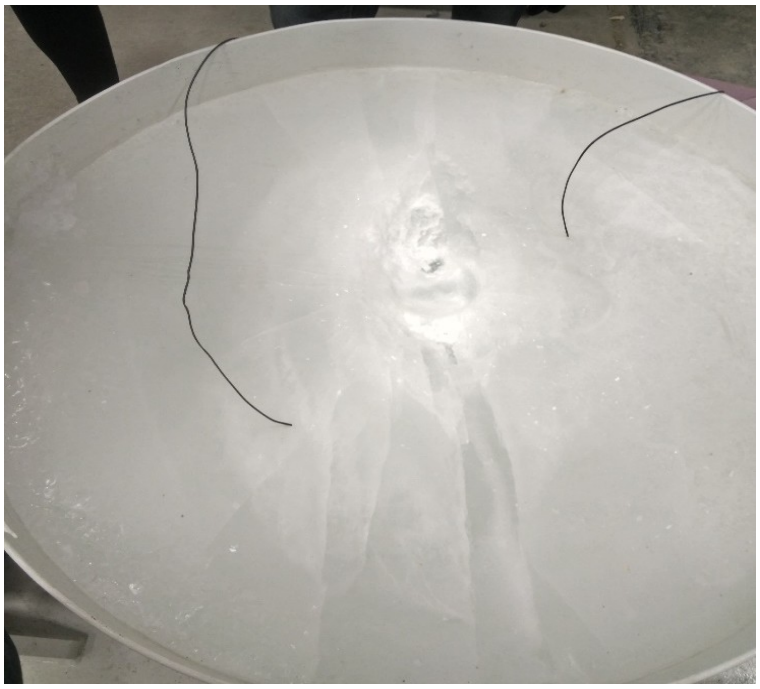

Figure A2.8 (b): Post-test images for test T02_1A_18.5_100.

Test T03_1A_04_50

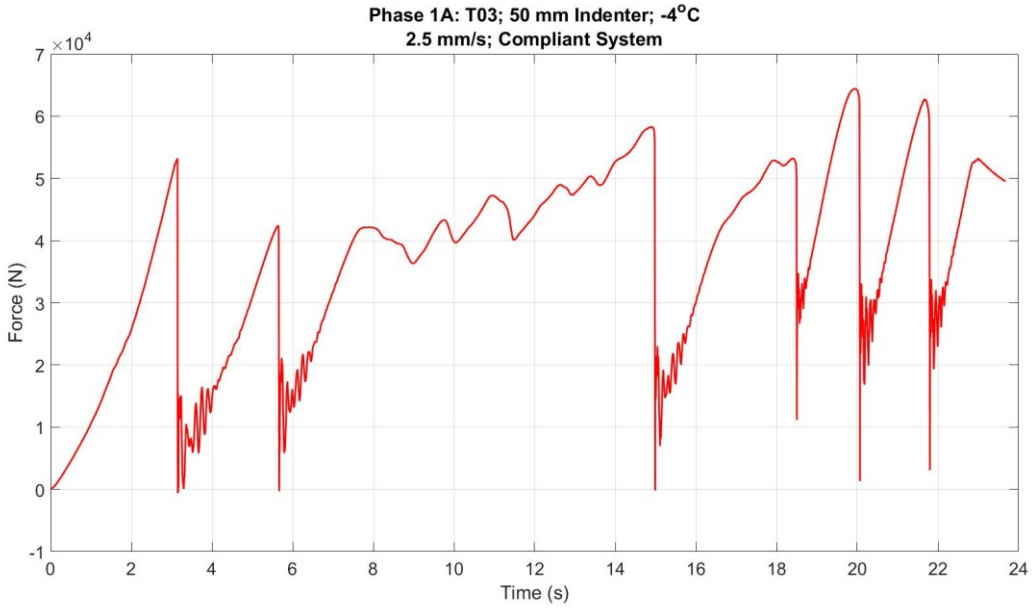

Figure A3.1: Force vs. time plot.

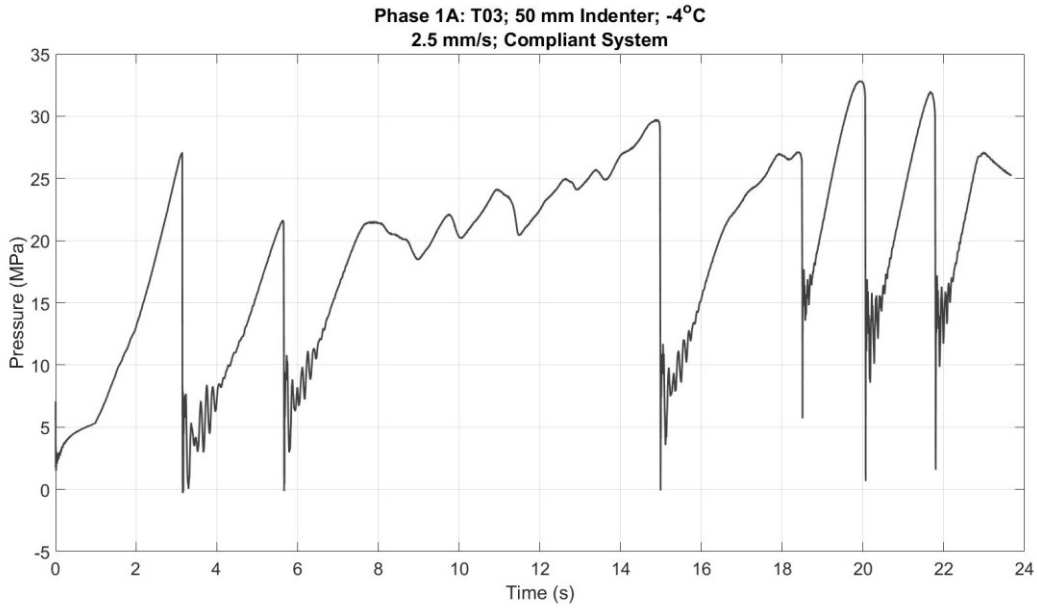

Figure A3.2: Pressure vs. time plot.

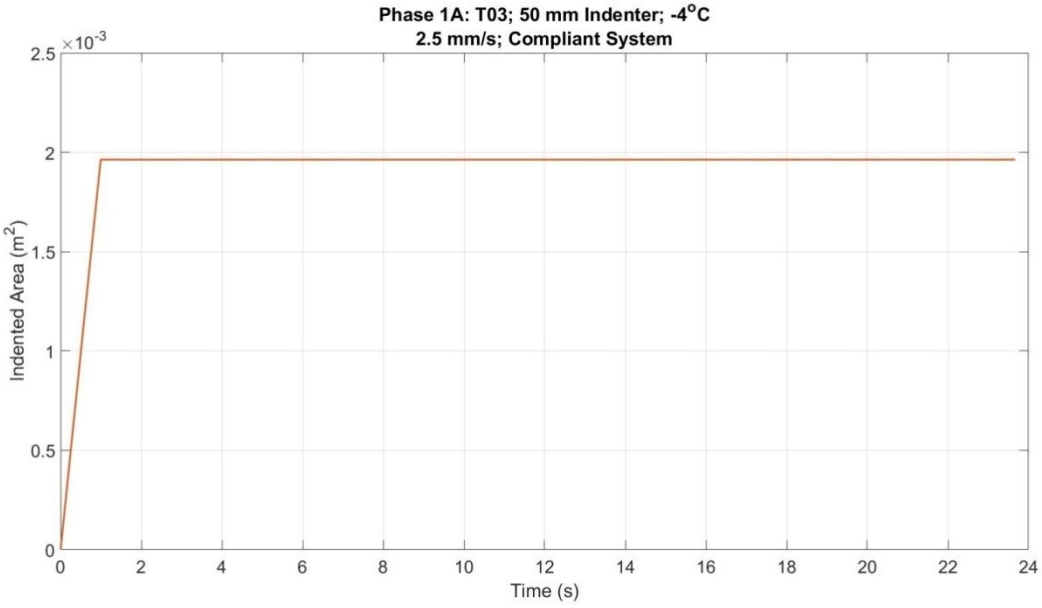

Figure A3.3: Indented area vs. time plot.

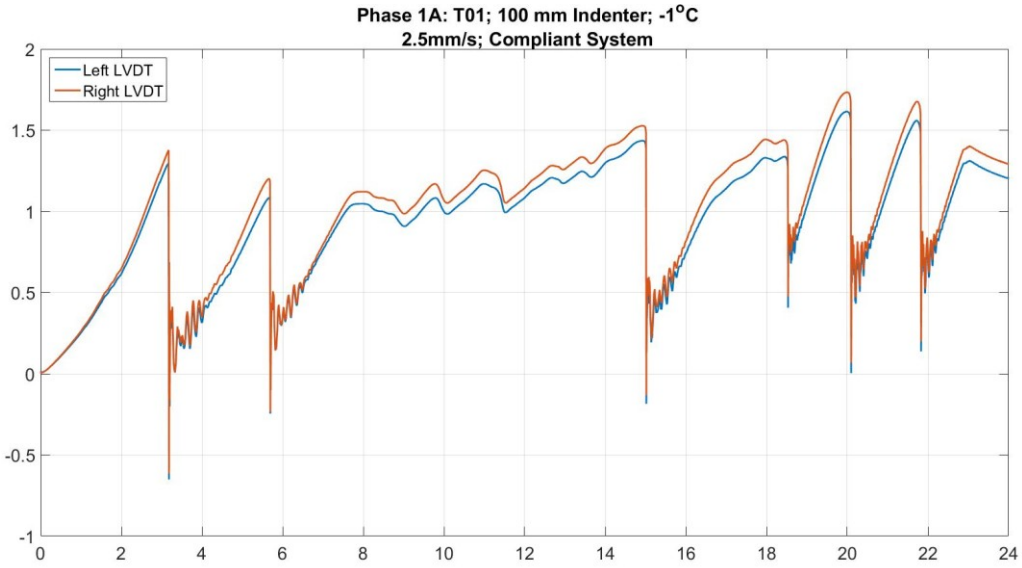

Figure A3.4 a: Compliant beam deflection vs. time plot.

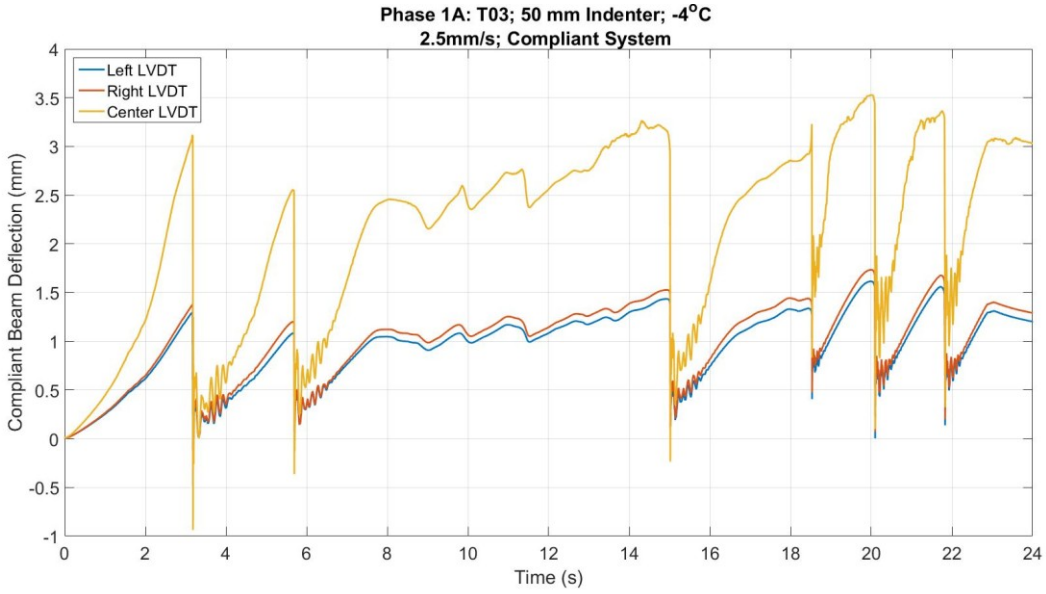

Figure A3.4 b: Compliant beam deflection vs. time plot.

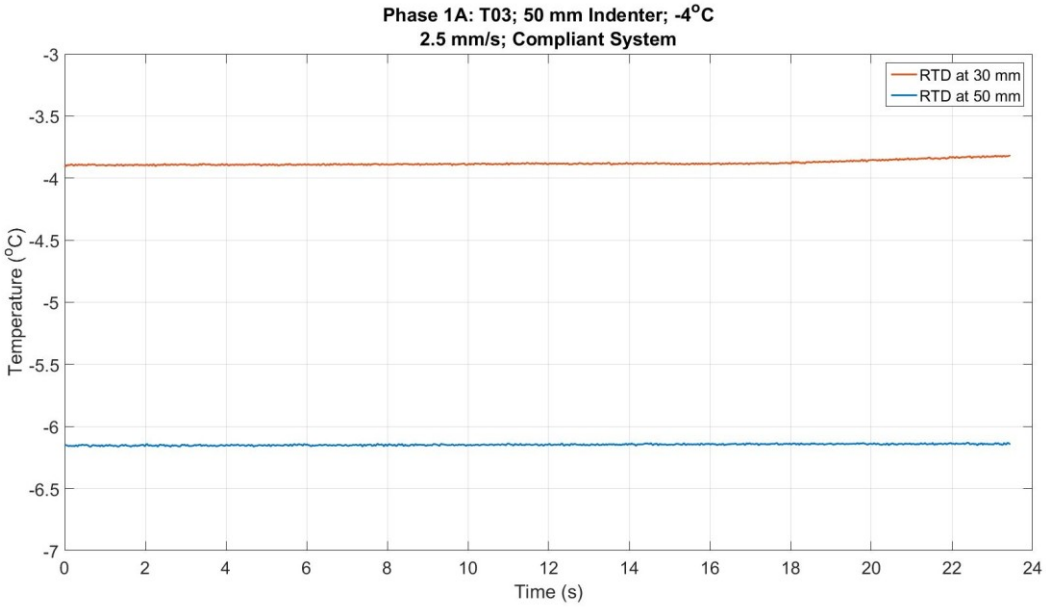

Figure A3.5: Temperature vs. time plot.

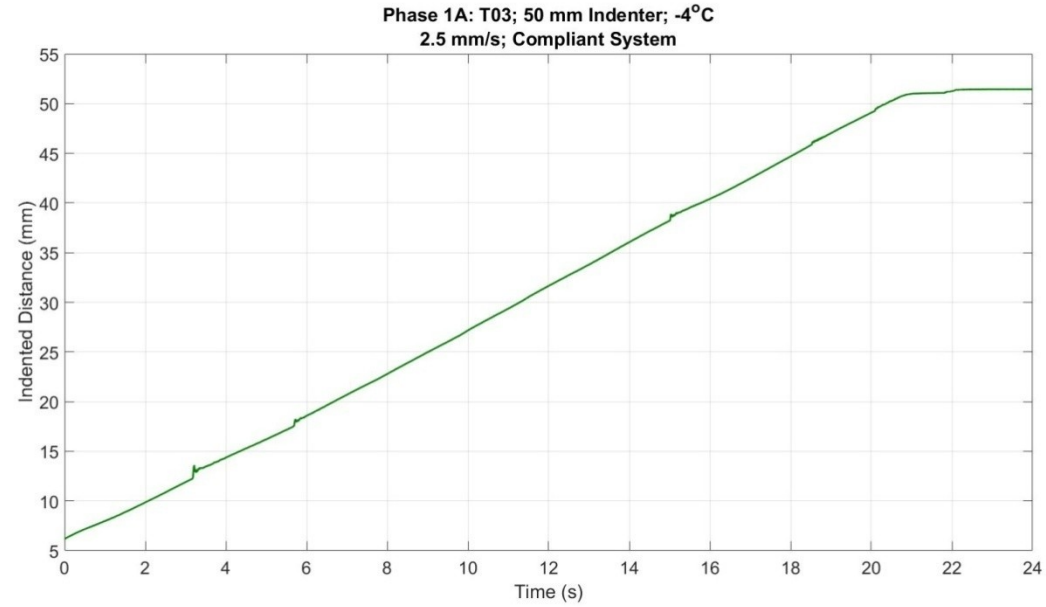

Figure A3.6: Indented distance vs. time plot.

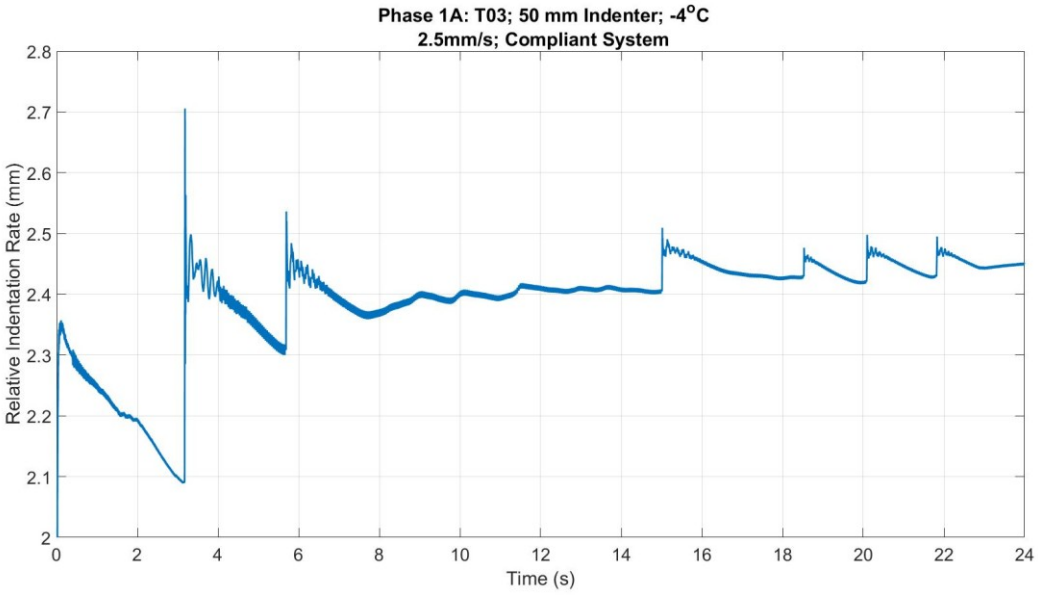

Figure A3.7: Relative loading rate vs time plot.

Figure A3.8 (a): Post-test images for test T03_1A_04_50.

Figure A3.8 (b): Post-test images for test T03_1A_04_50.

Test T04_1A_16.5_50

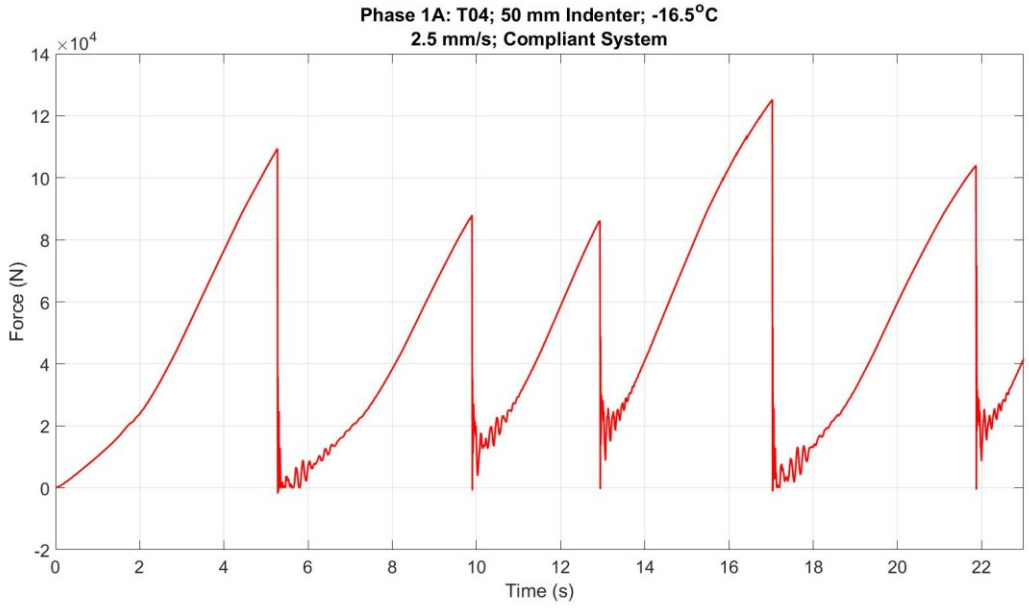

Figure A4.1: Force vs. time plot.

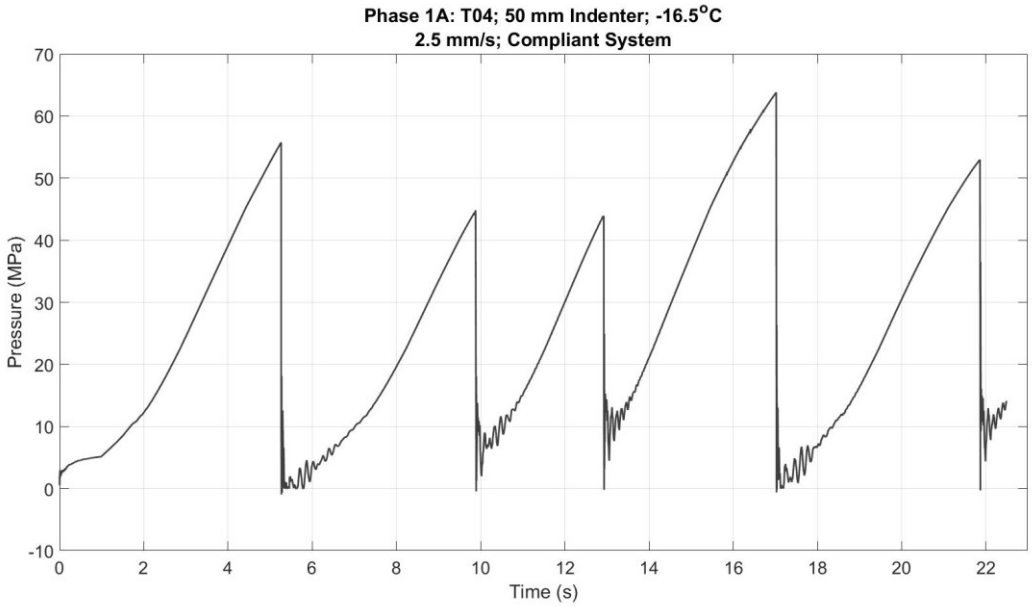

Figure A4.2: Pressure vs. time plot.

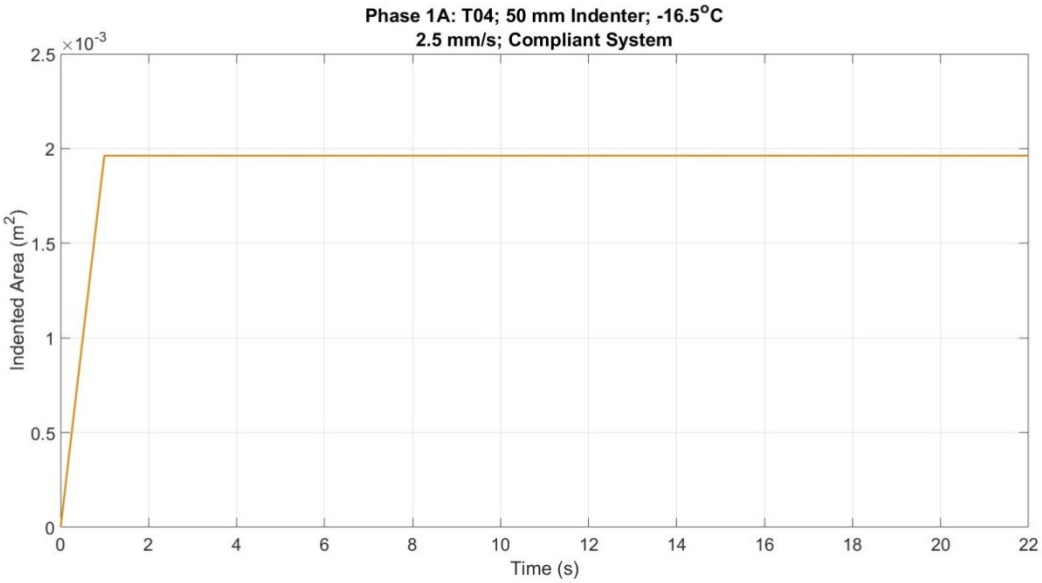

Figure A4.3: Indented area vs. time plot.

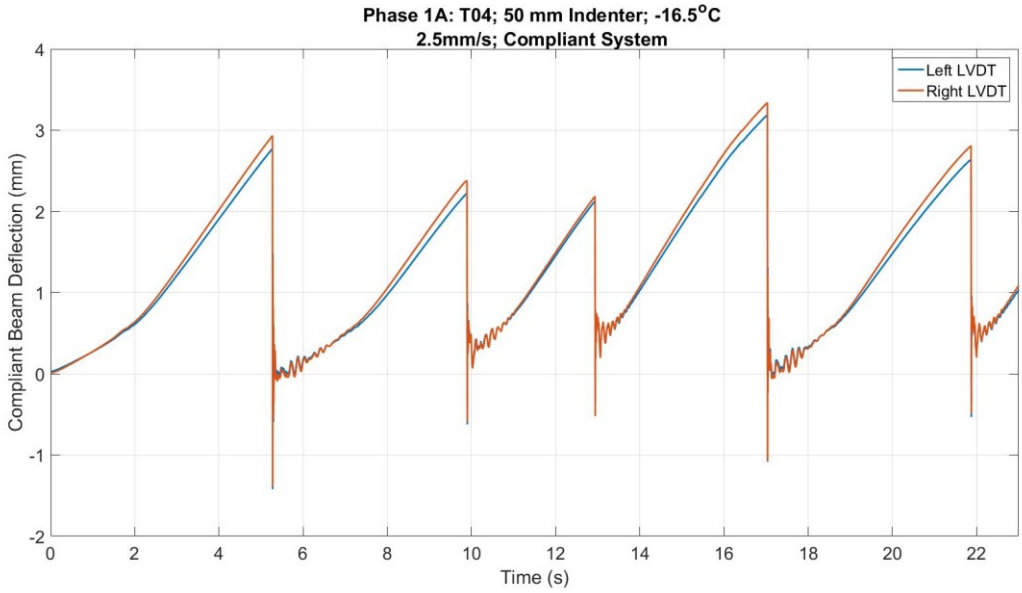

Figure A4.4 a: Compliant beam deflection vs. time plot.

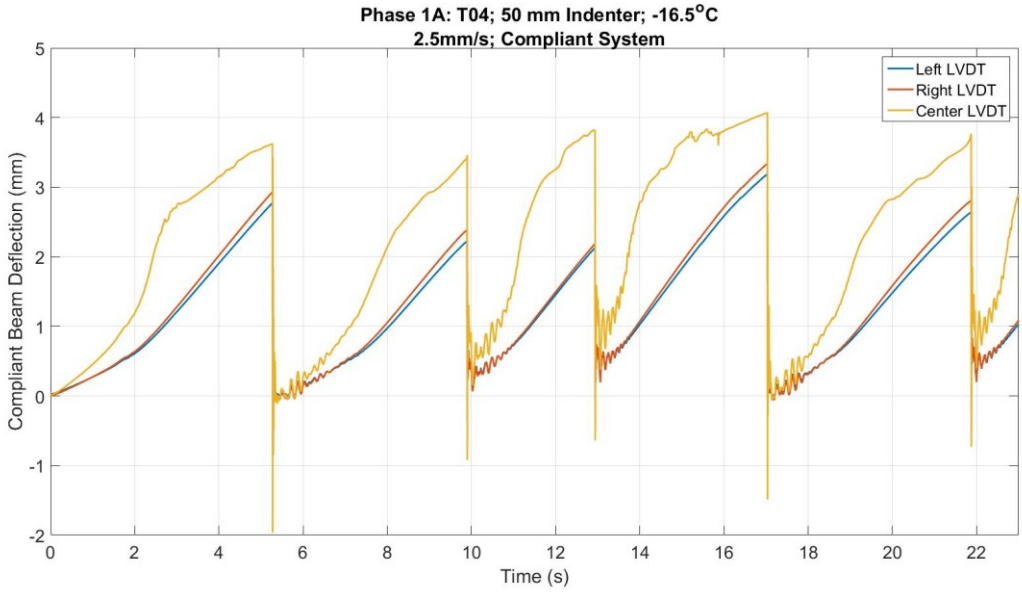

Figure A4.4 b: Compliant beam deflection vs. time plot.

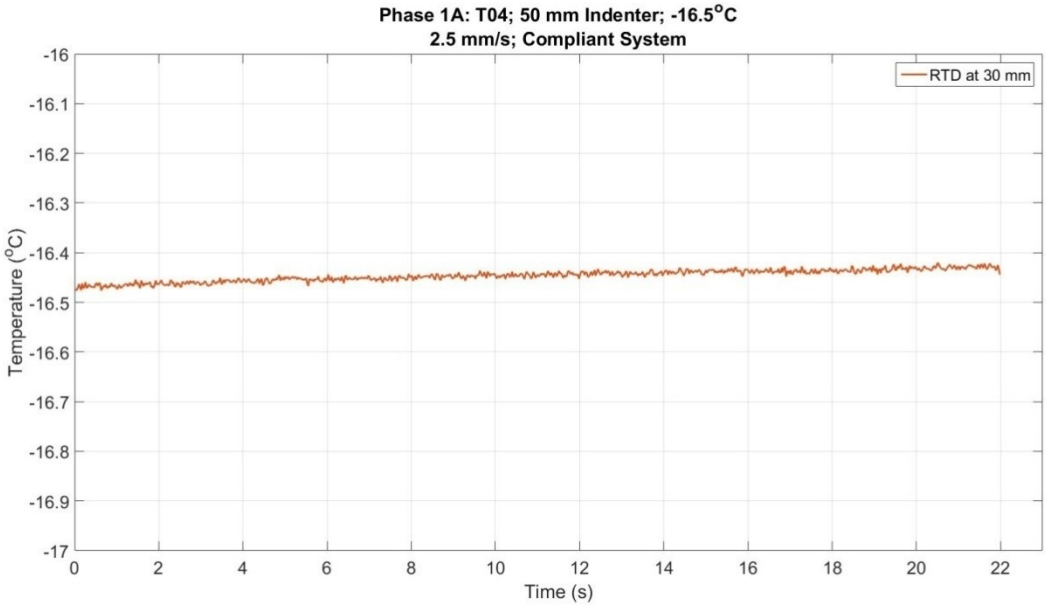

Figure A4.5: Temperature vs. time plot.

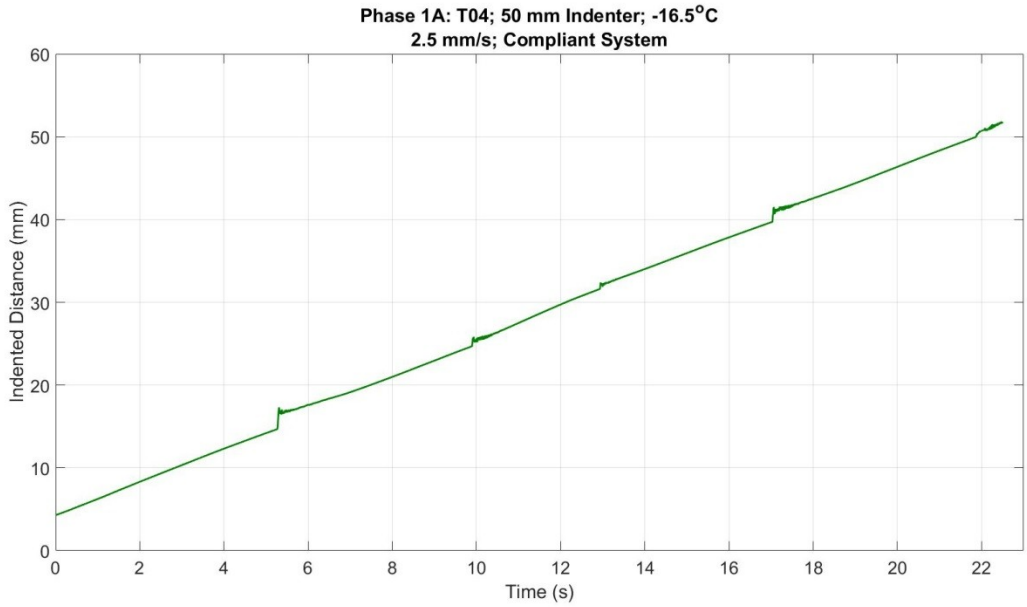

Figure A4.6: Indented distance vs. time plot.

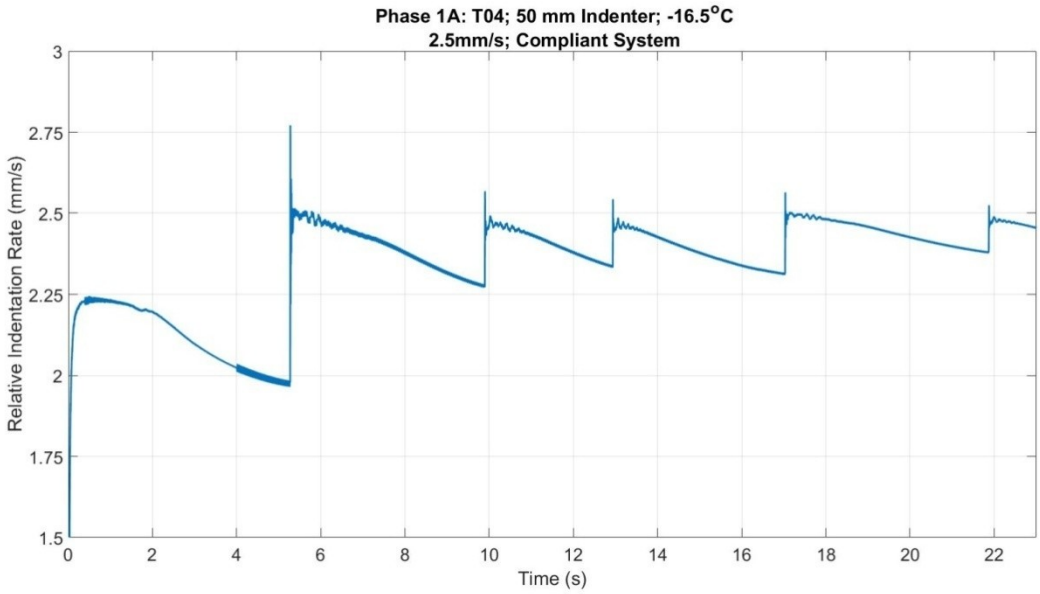

Figure A4.7: Relative loading rate vs time plot.

Figure A4.8 (a): Post-test images for test T04_1A_16.5_50.

Figure A4.8 (b): Post-test images for test T04_1A_16.5_50.

Figure A4.8 (c): Post-test images for test T04_1A_16.5_50.

Test T05_1A_06_150

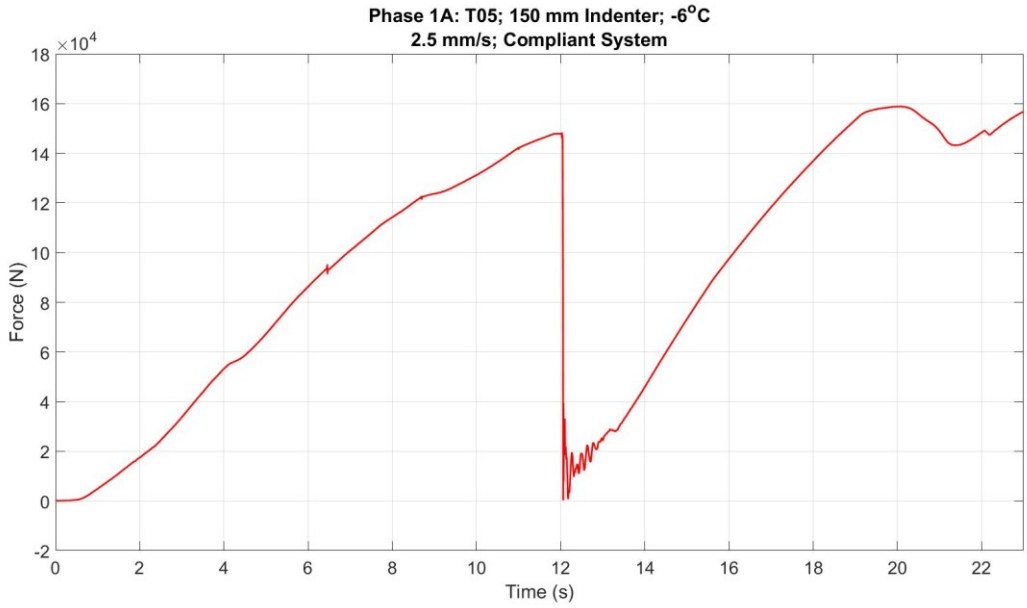

Figure A5.1: Force vs. time plot.

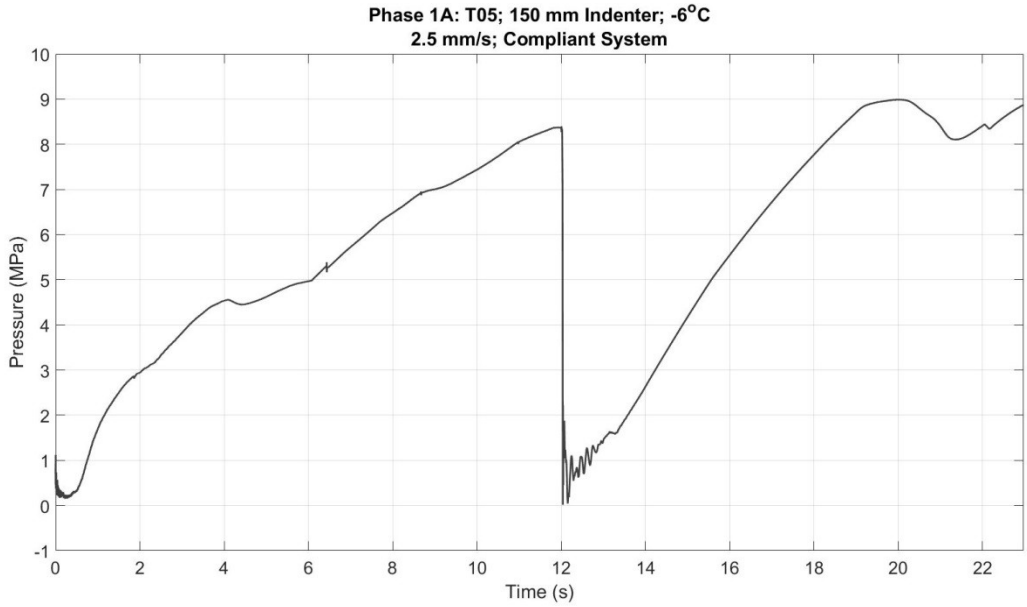

Figure A5.2: Pressure vs. time plot.

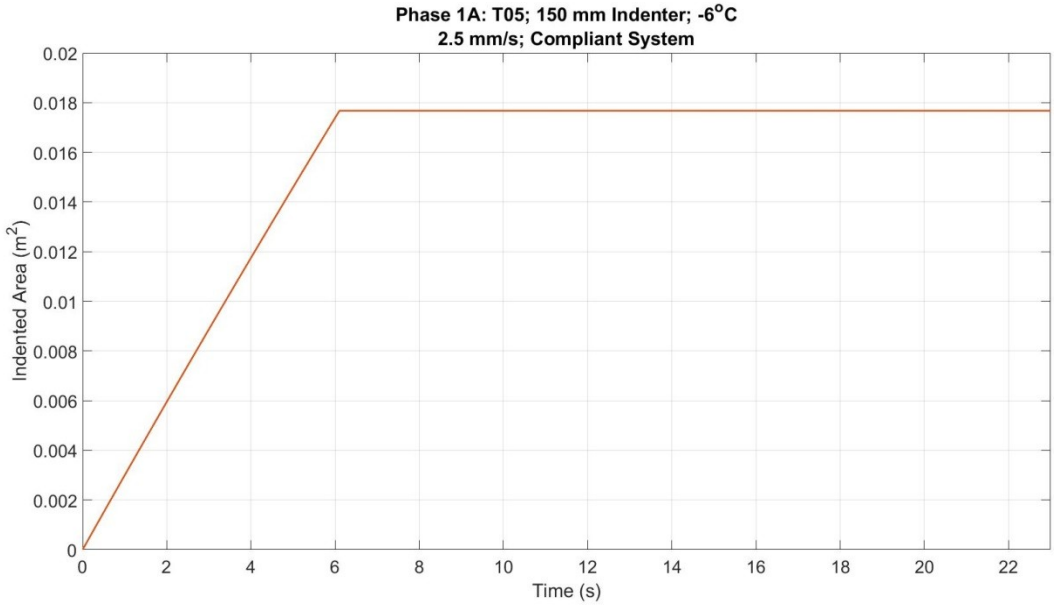

Figure A5.3: Indented area vs. time plot.

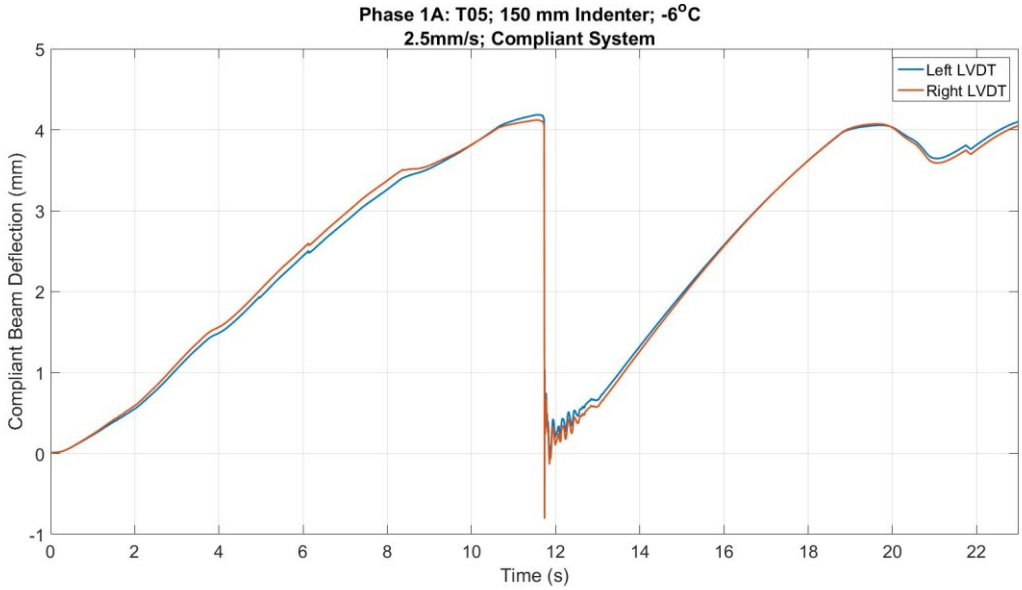

Figure A5.4 a: Compliant beam deflection vs. time plot.

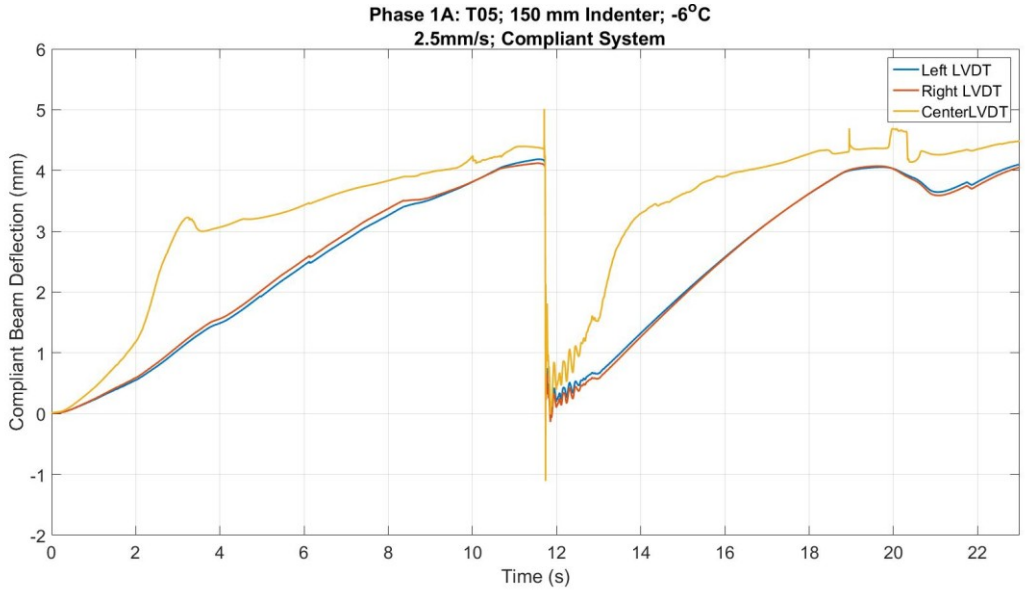

Figure A5.4 b: Compliant beam deflection vs. time plot.

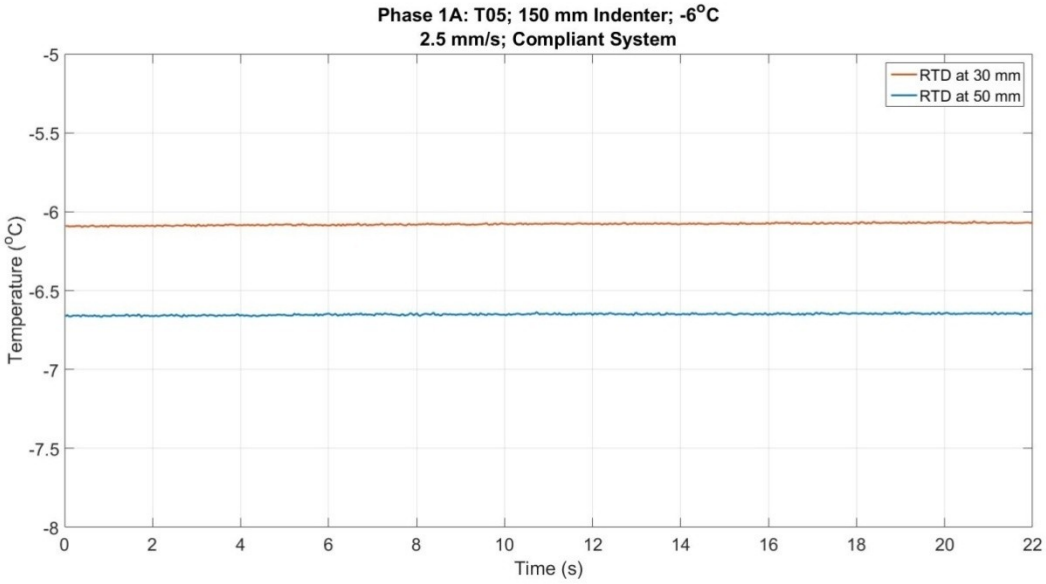

Figure A5.5: Temperature vs. time plot.

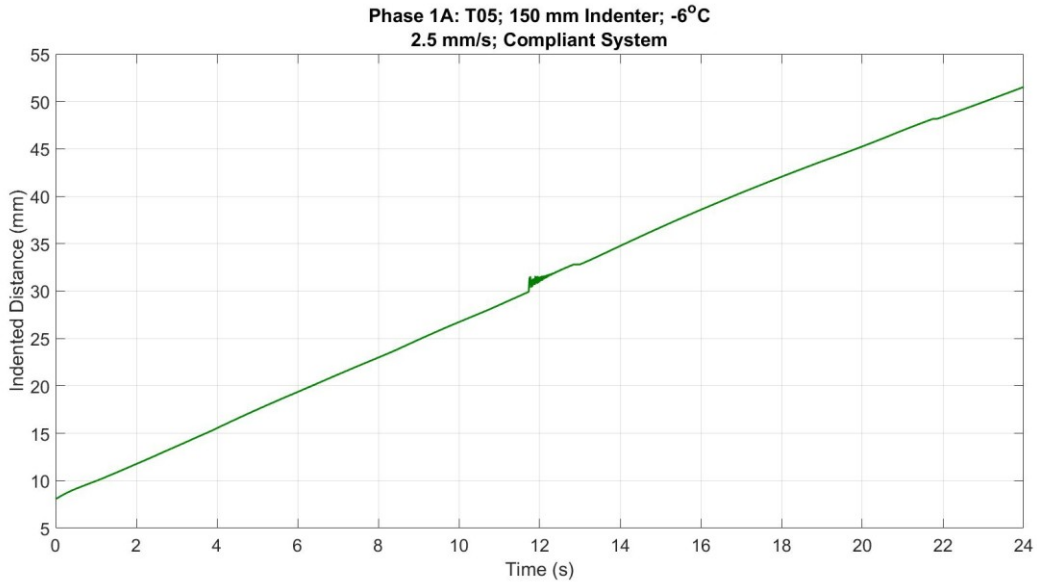

Figure A5.6: Indented distance vs. time plot.

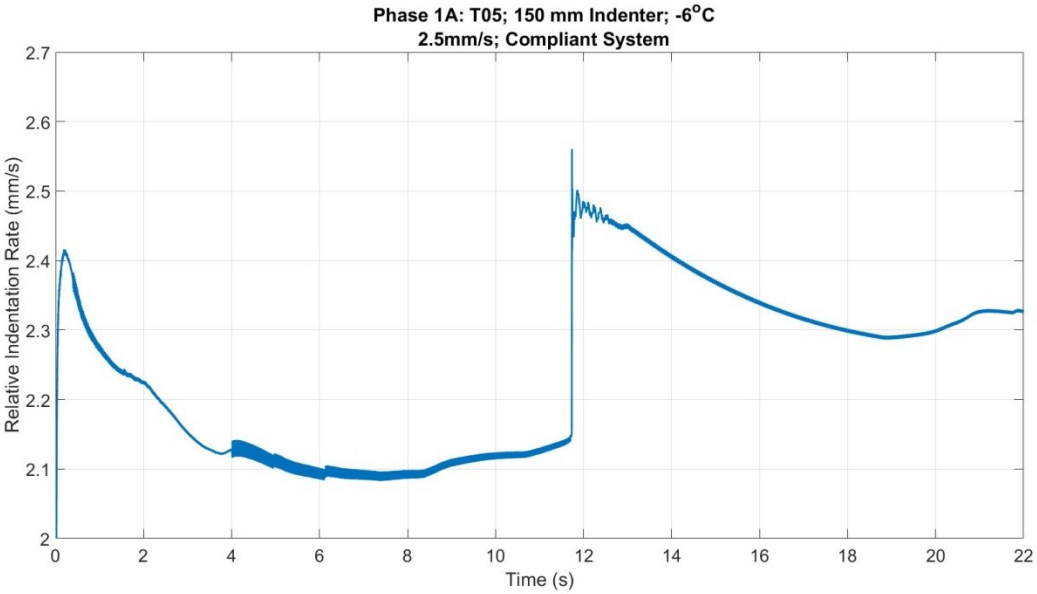

Figure A5.7: Relative loading rate vs time plot.

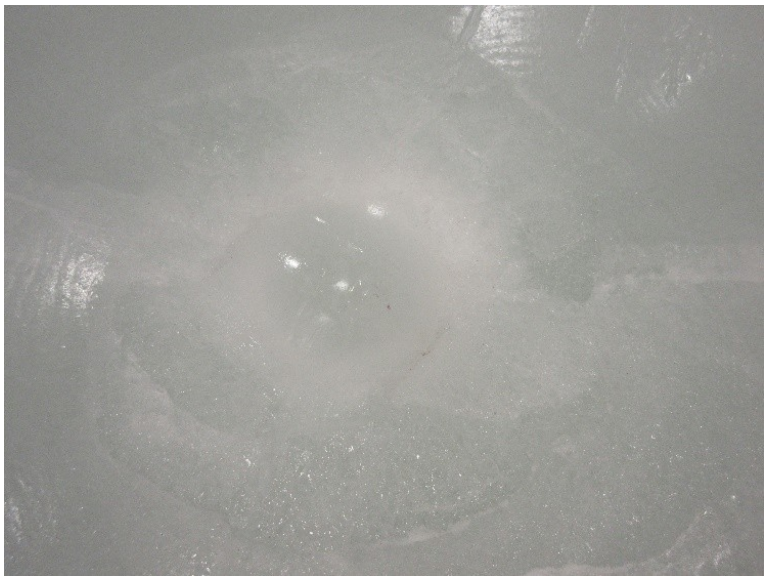

Figure A5.8 (a): Post-test images for test T05_1A_06_150.

Figure A5.8 (b): Post-test images for test T05_1A_06_150.

Test T06_1A_19_150

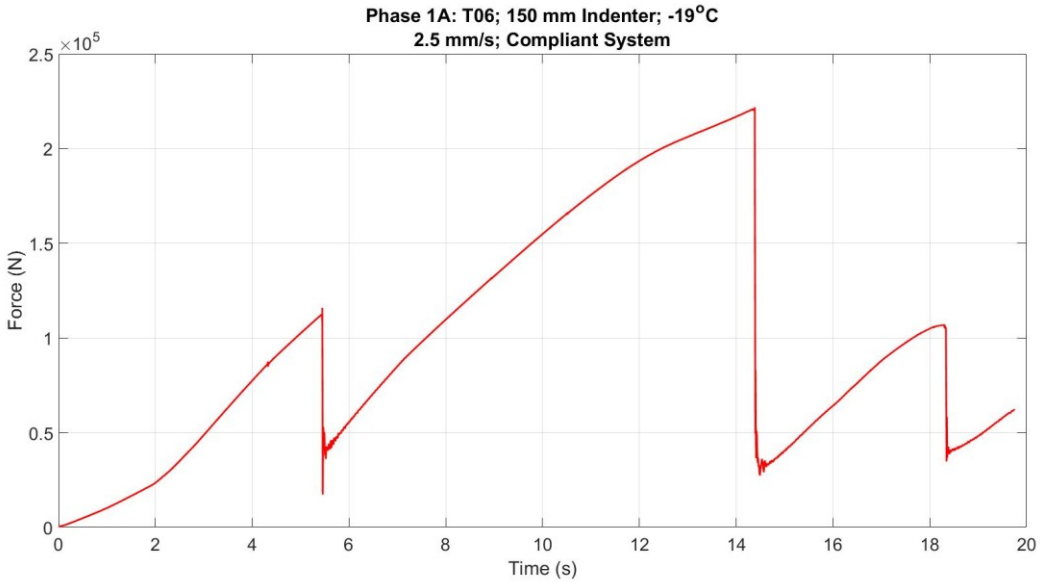

Figure A6.1: Force vs. time plot.

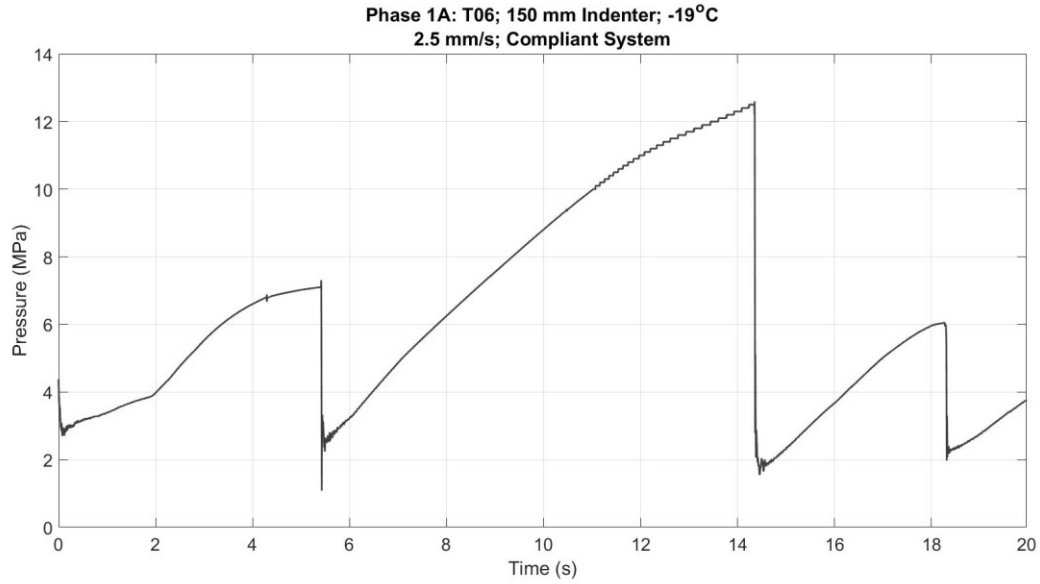

Figure A6.2: Pressure vs. time plot.

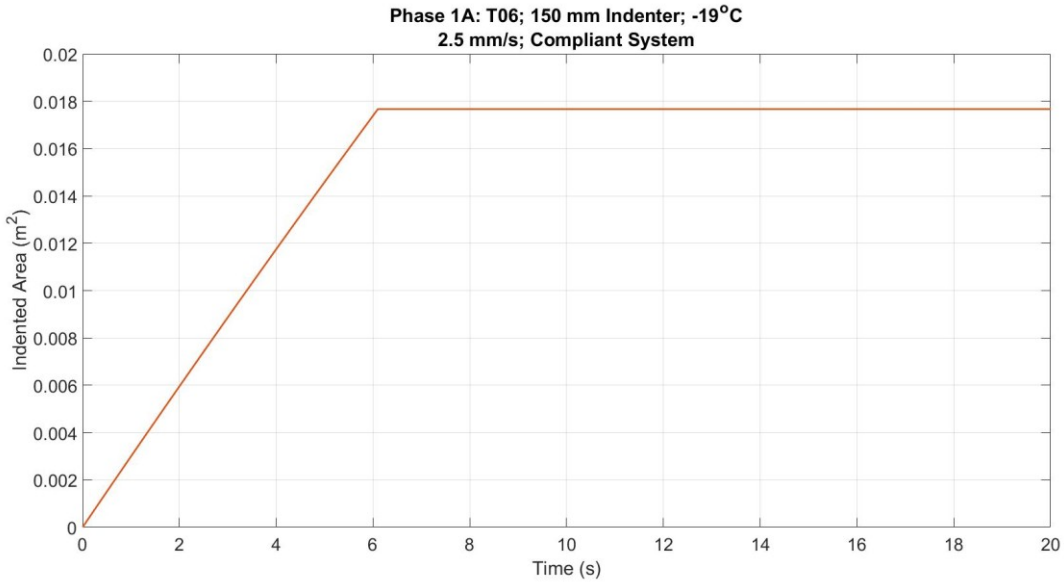

Figure A6.3: Indented area vs. time plot.

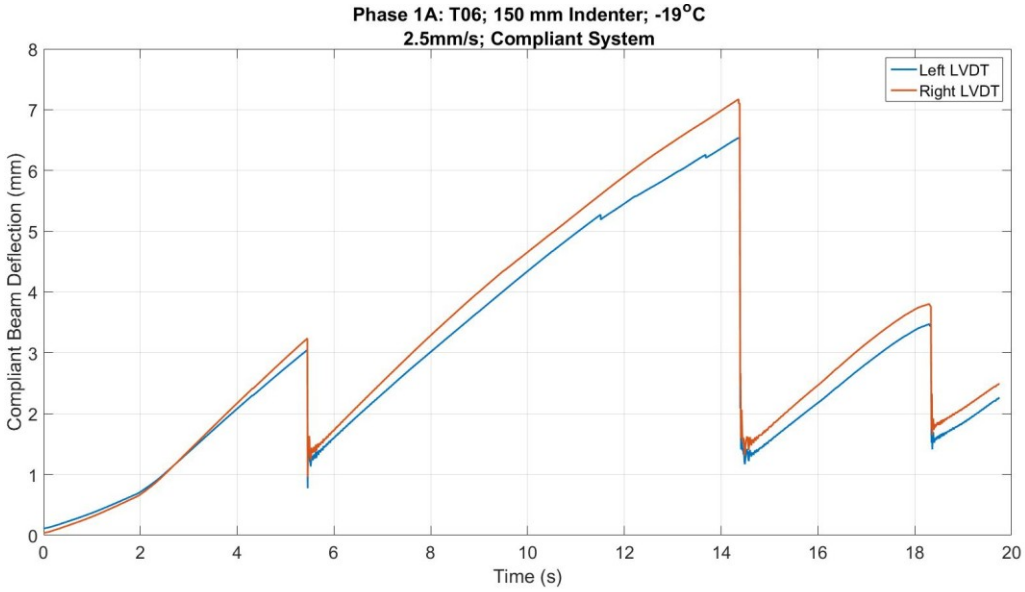

Figure A6.4 a: Compliant beam deflection vs. time plot.

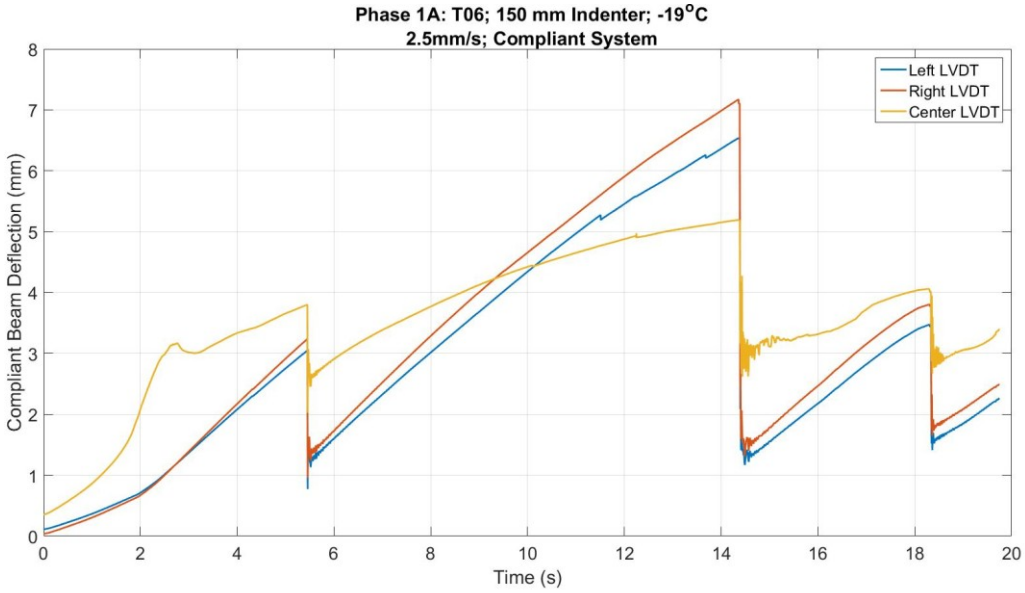

Figure A6.4 b: Compliant beam deflection vs. time plot.

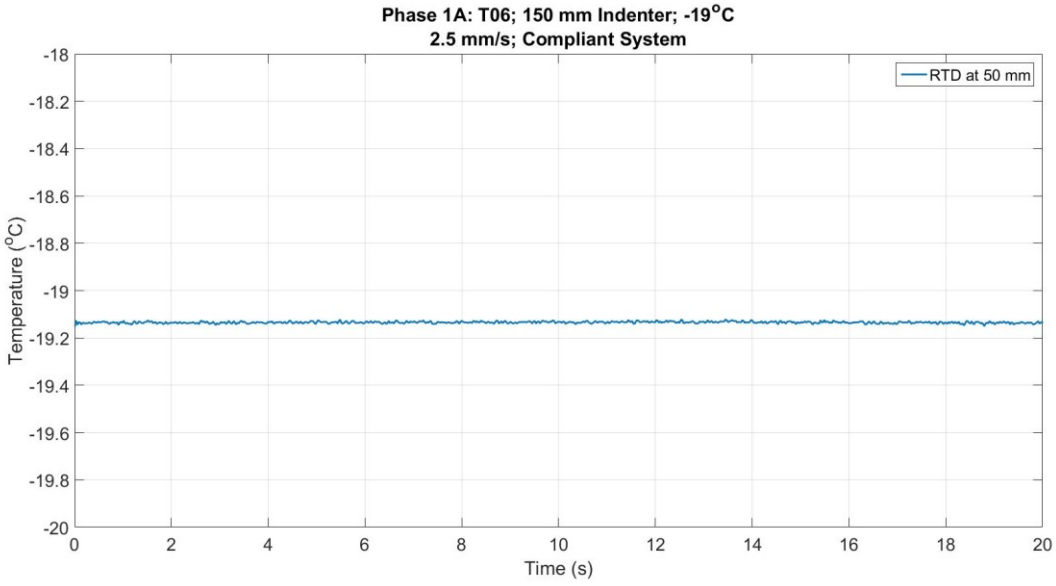

Figure A6.5: Temperature vs. time plot.

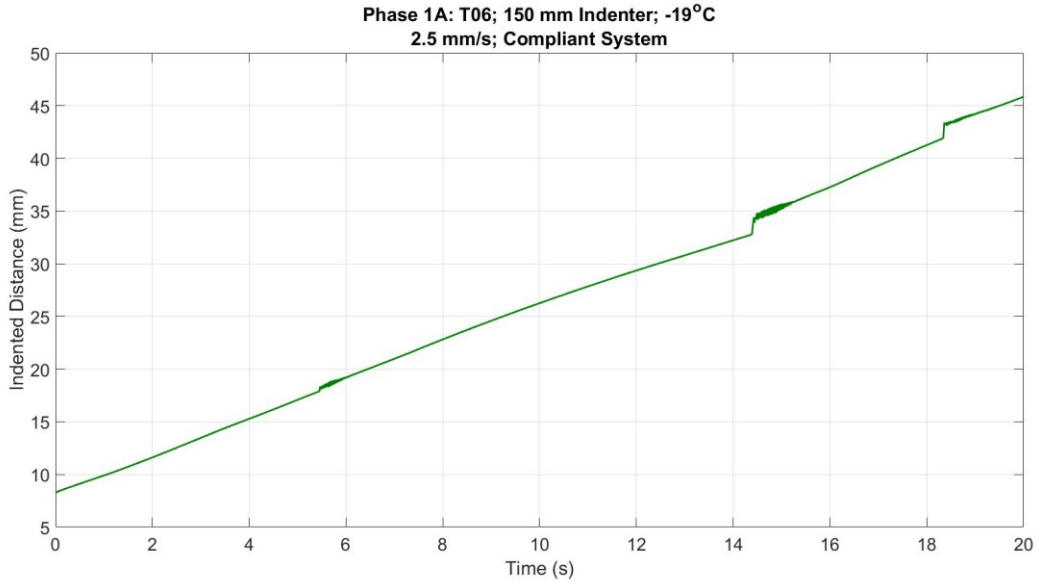

Figure A6.6: Indented distance vs. time plot.

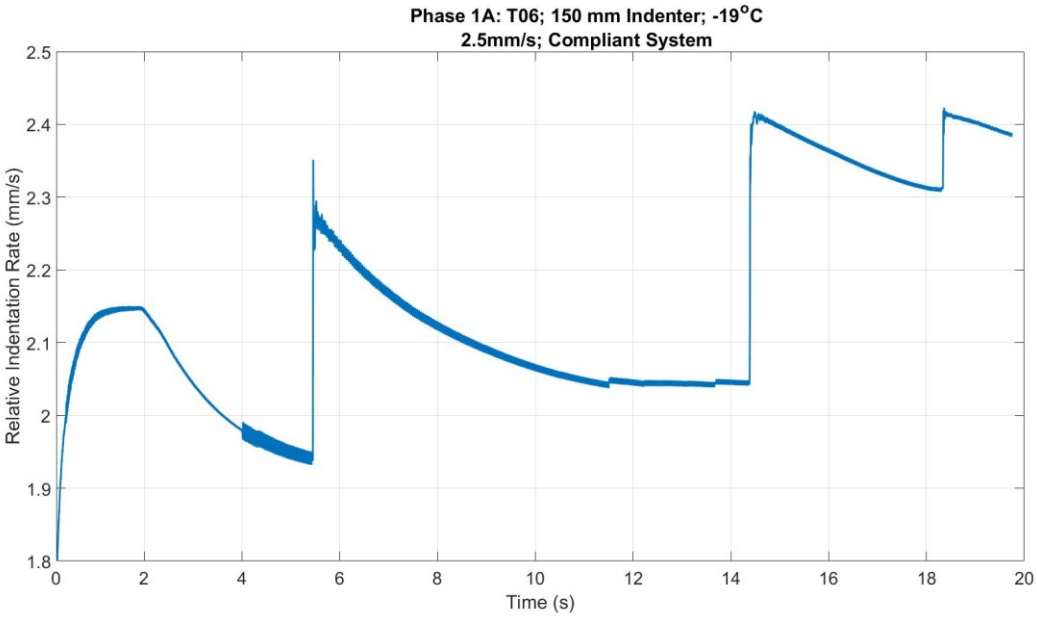

Figure A6.7: Relative loading rate vs time plot.

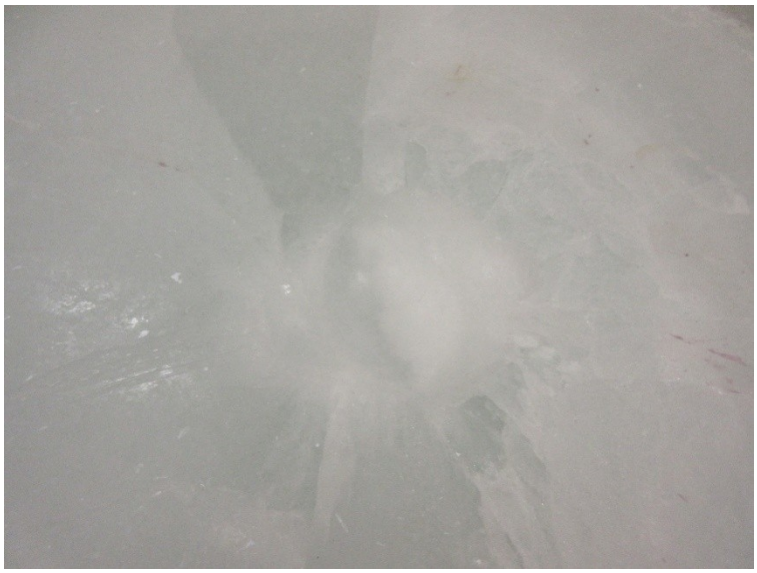

Figure A6.8 (a): Post-test images for test T06_1A_19_150.

Figure A6.8 (b): Post-test images for test T06_1A_19_150.

Test T07_1A_4.5_50_R

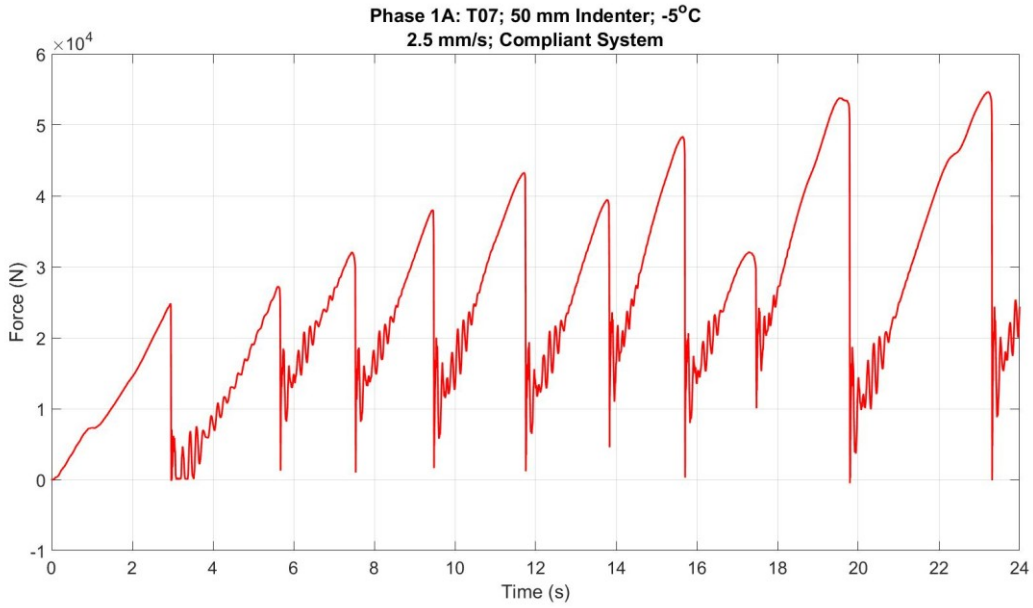

Figure A7.1: Force vs. time plot.

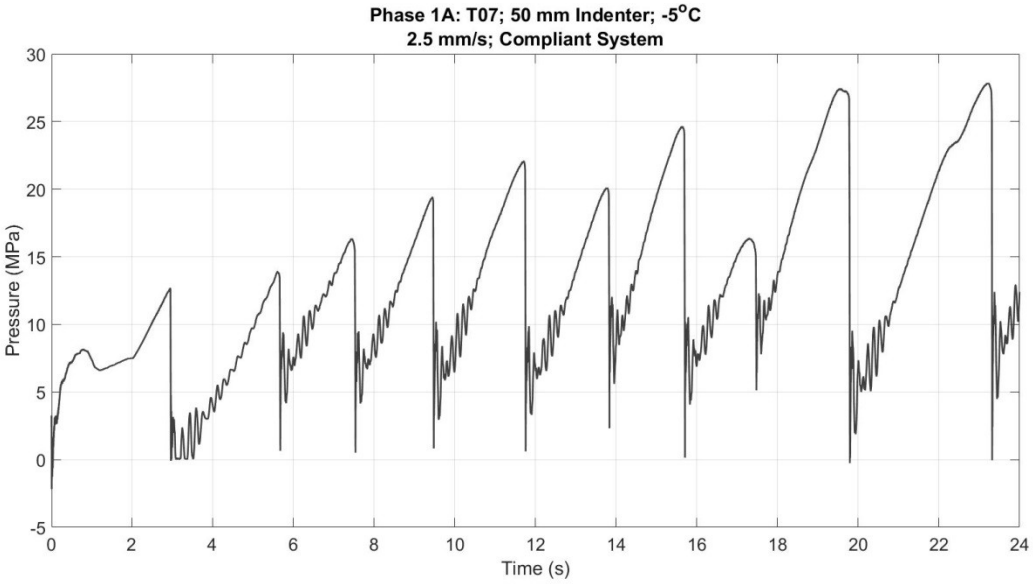

Figure A7.2: Pressure vs. time plot.

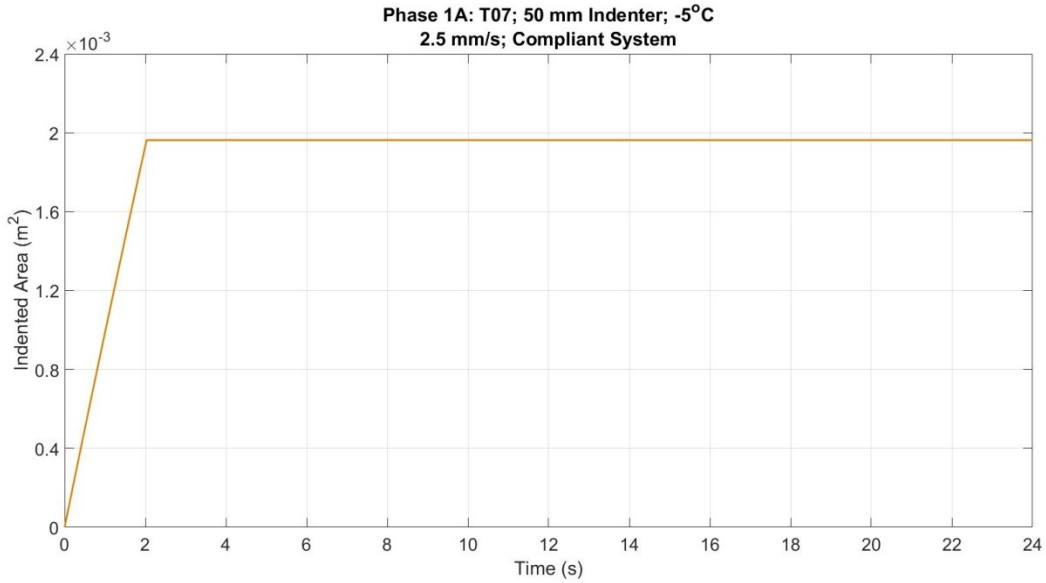

Figure A7.3: Indented area vs. time plot.

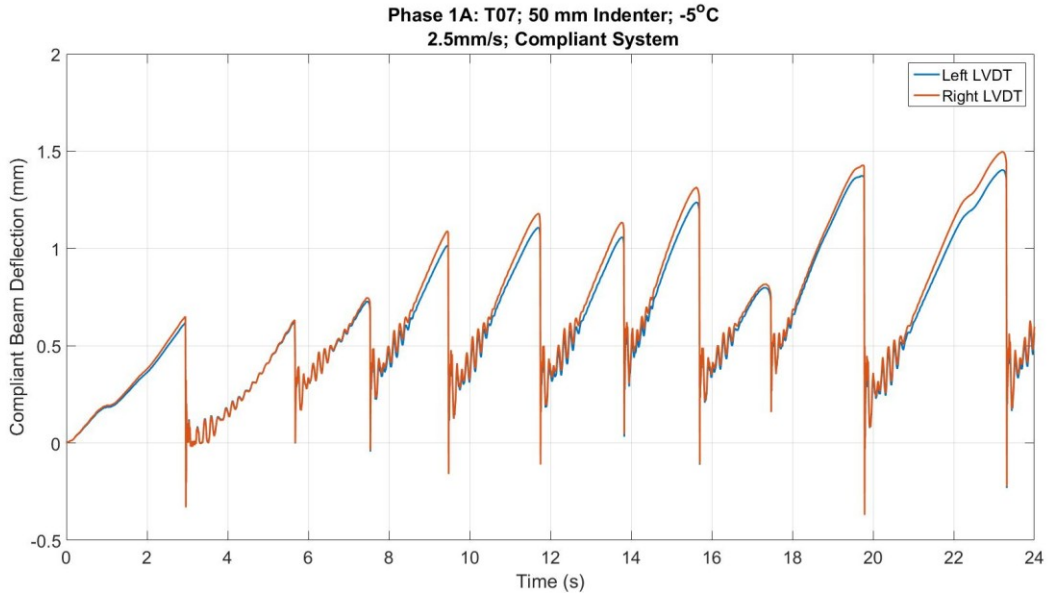

Figure A7.4 a: Compliant beam deflection vs. time plot.

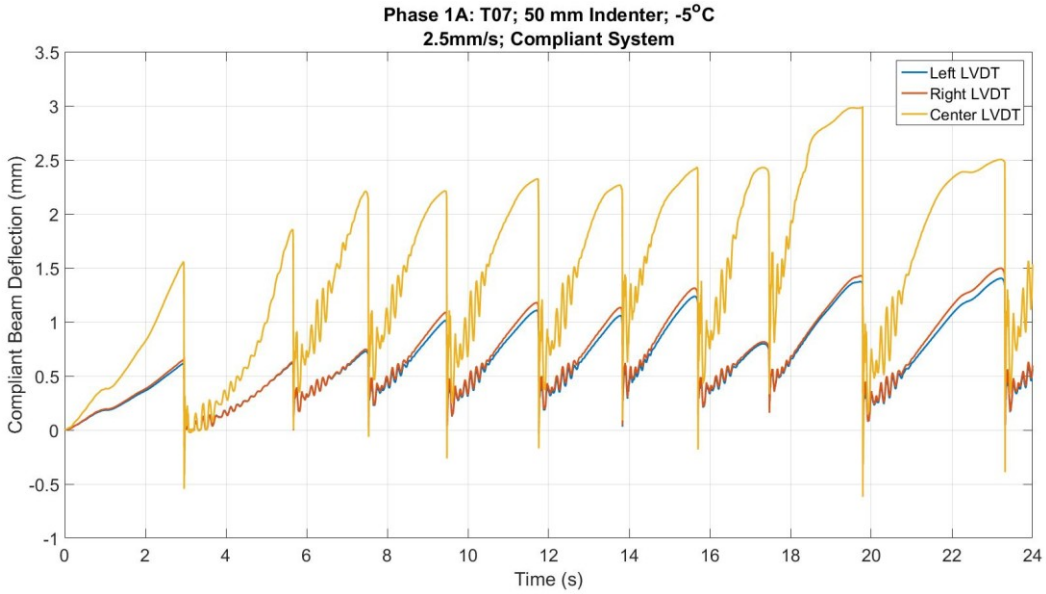

Figure A7.4 b: Compliant beam deflection vs. time plot.

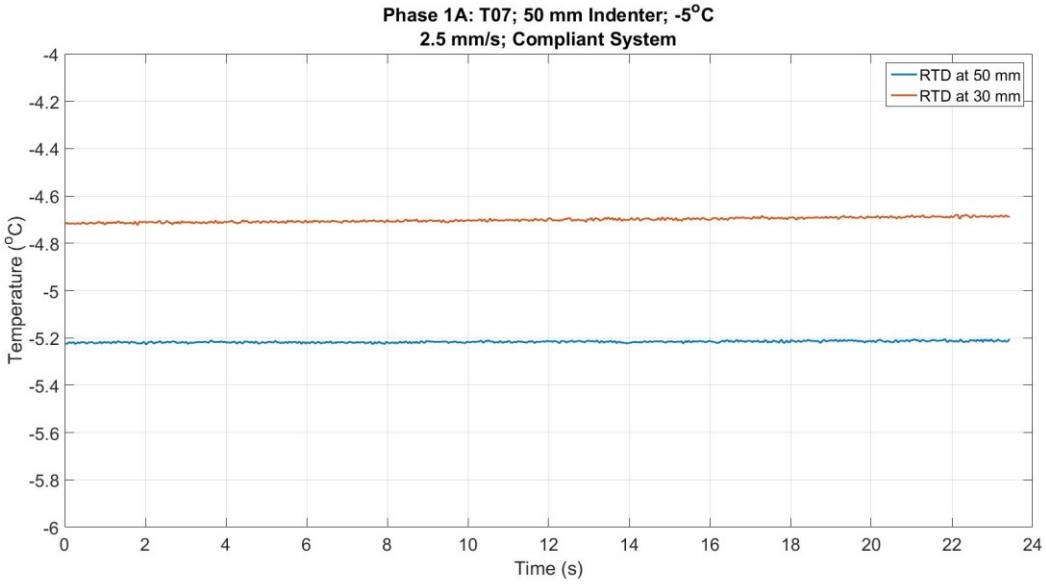

Figure A7.5: Temperature vs. time plot.

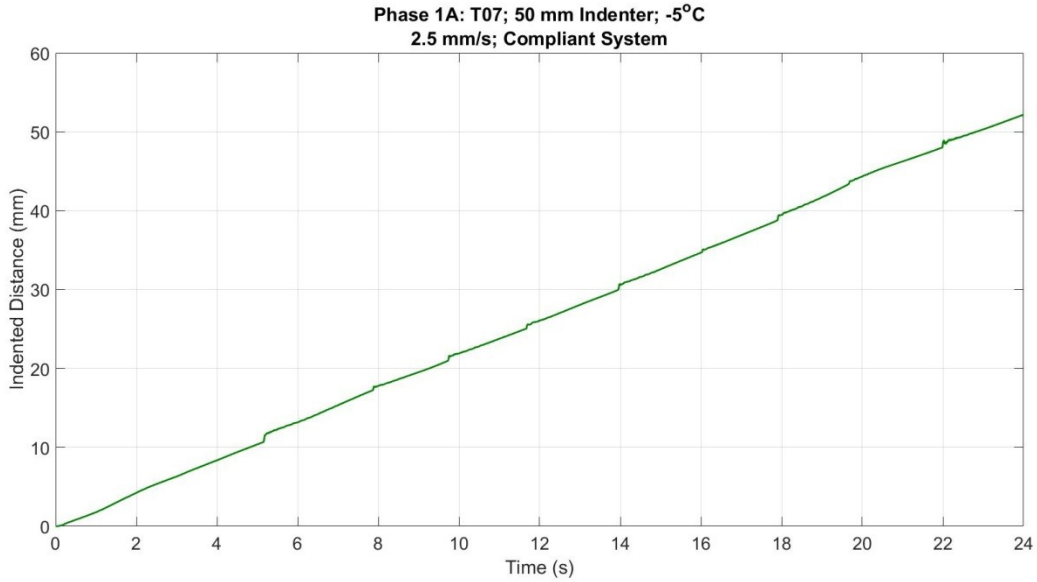

Figure A7.6: Indented distance vs. time plot.

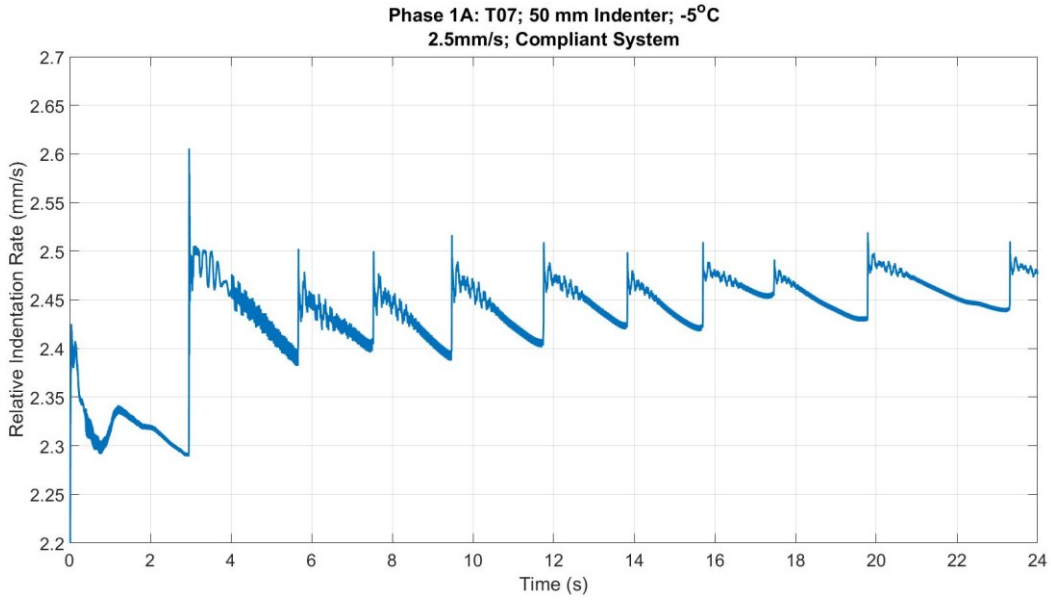

Figure A7.7: Relative loading rate vs time plot.

Figure A7.8 (a): Post-test images for test T07_1A_4.5_50_R.

Figure A7.8 (b): Post-test images for test T07_1A_4.5_50_R.

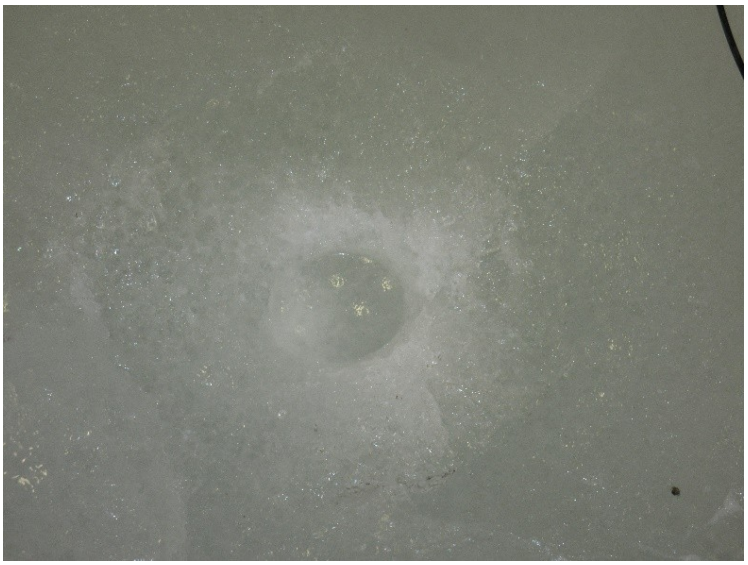

Figure A7.8 (c): Post-test images for test T07_1A_4.5_50_R.

Test T08_1A_19_50_R

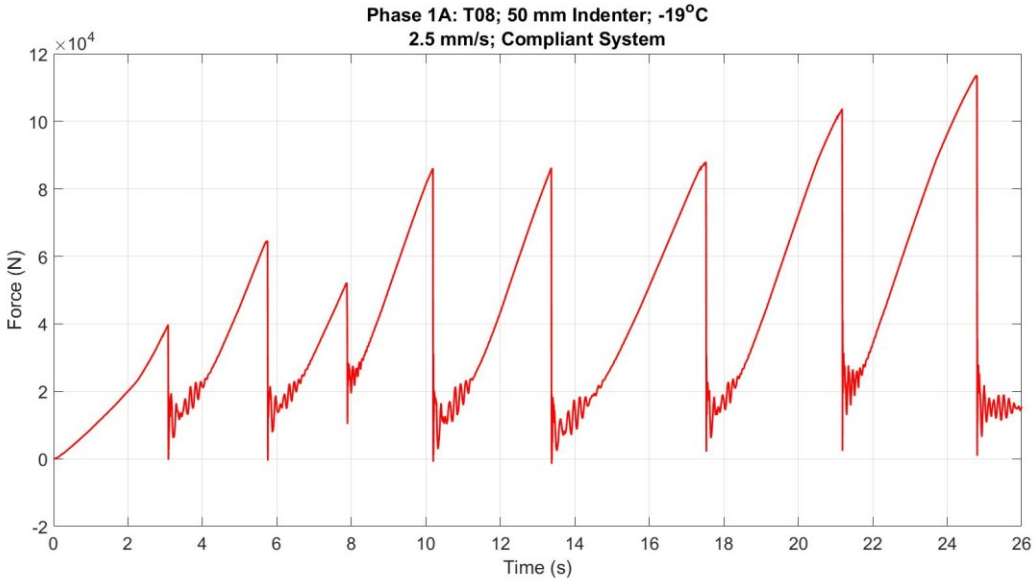

Figure A8.1: Force vs. time plot

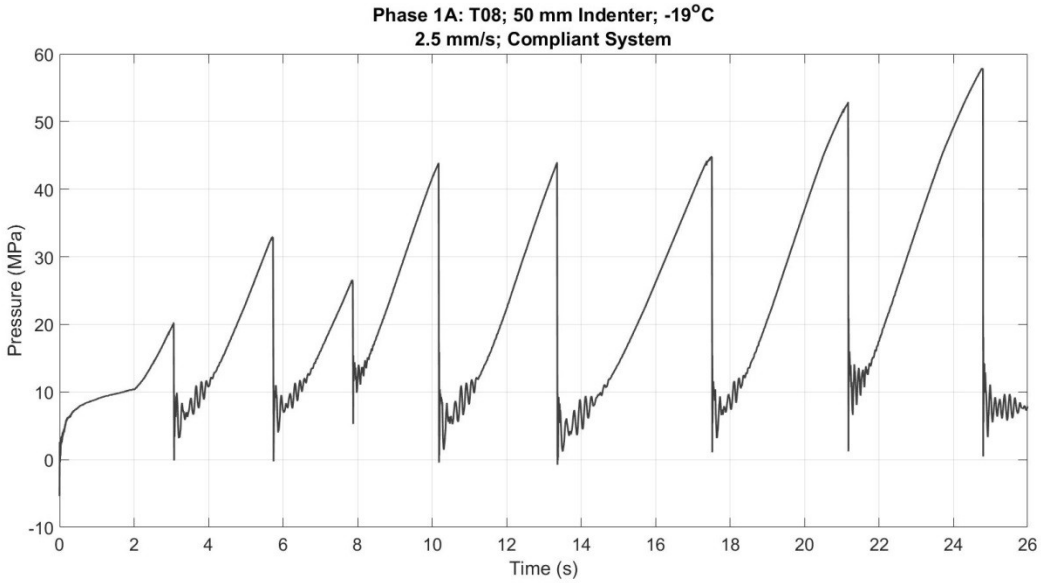

Figure A8.2: Pressure vs. time plot

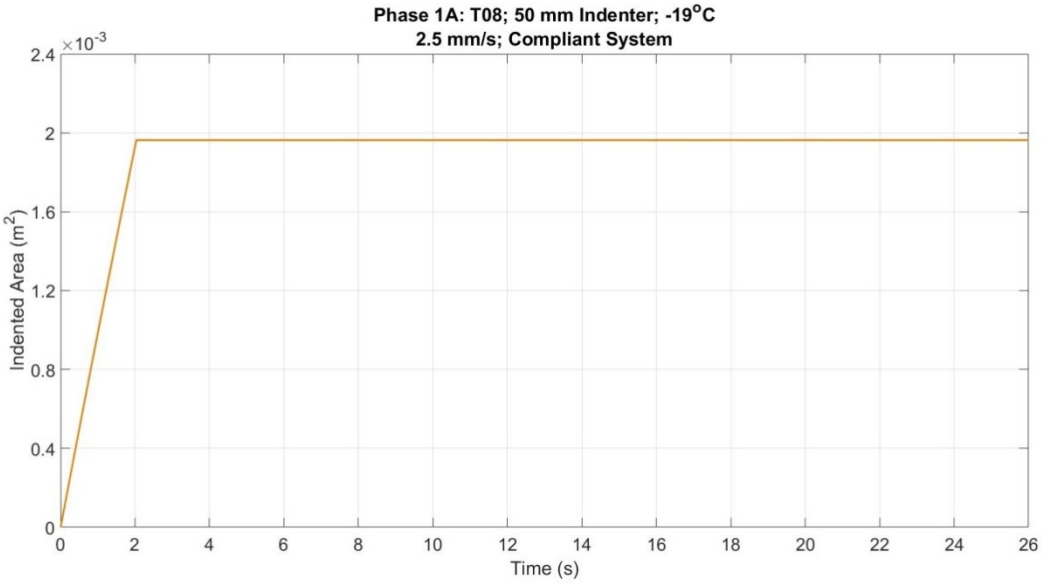

Figure A8.3: Indented area vs. time plot

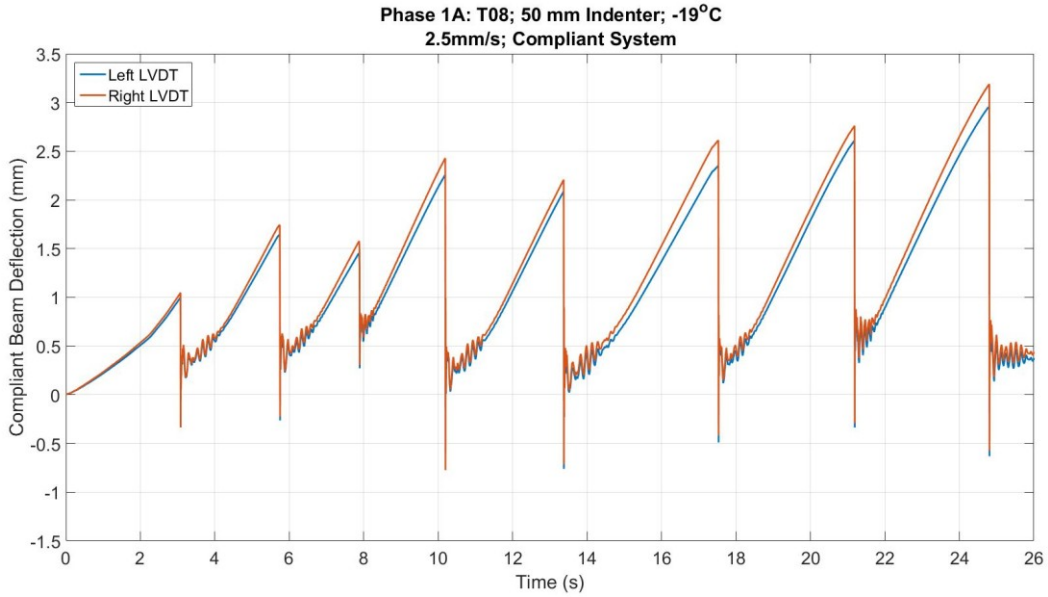

Figure A8.4 a: Compliant beam deflection vs. time plot

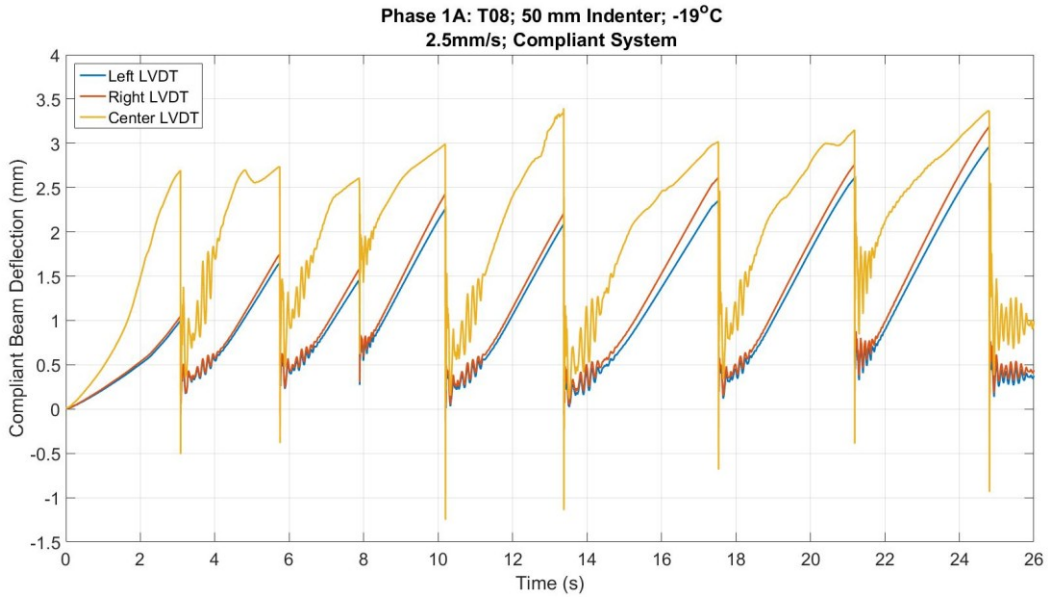

Figure A8.4 b: Compliant beam deflection vs. time plot

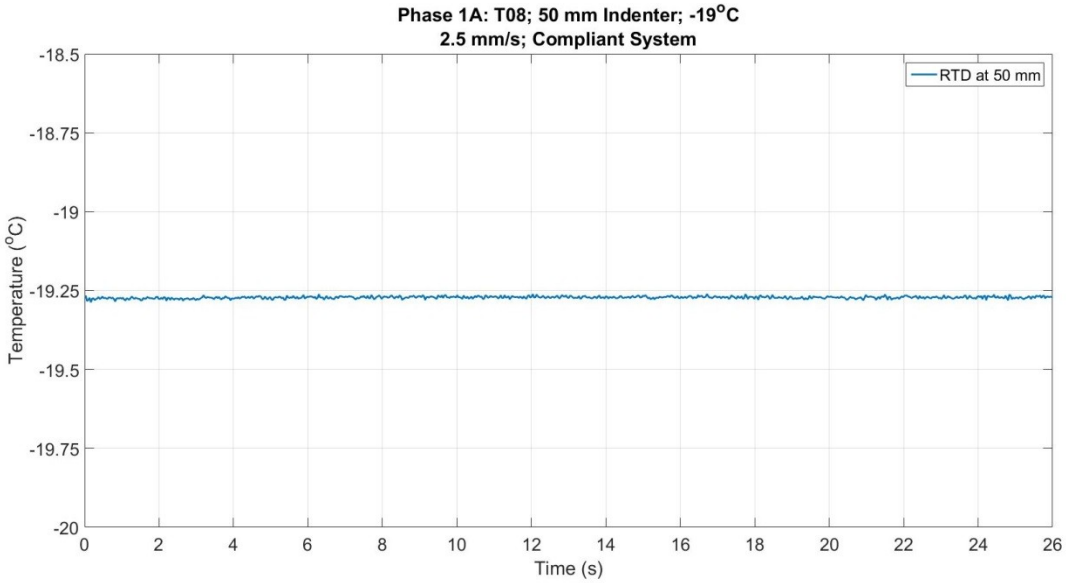

Figure A8.5: Temperature vs. time plot

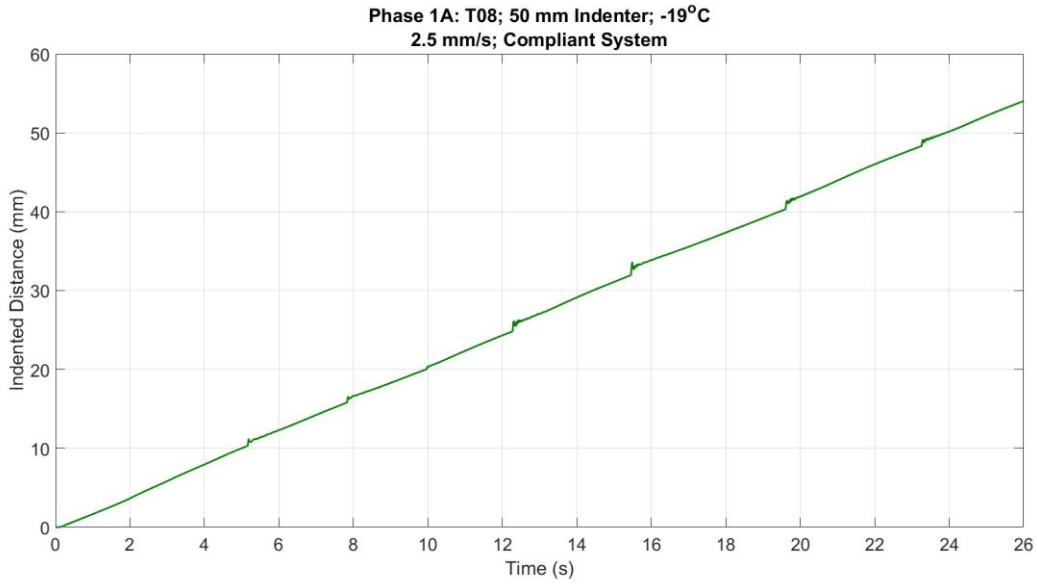

Figure A8.6: Indented distance vs. time plot

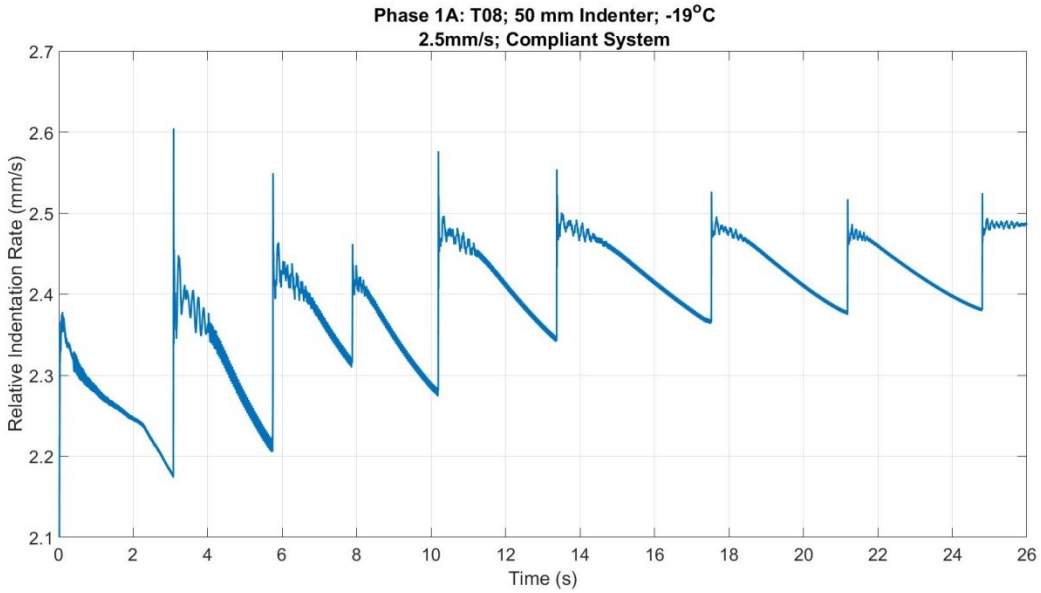

Figure A8.7: Relative loading rate vs time plot

Figure A8.8 (a): Post-test images for test T08_1A_19_50_R.

Figure A8.8 (b): Post-test images for test T08_1A_19_50_R.

Figure A8.8 (c): Post-test images for test T08_1A_19_50_R.

Test T09_1A_07_100_R

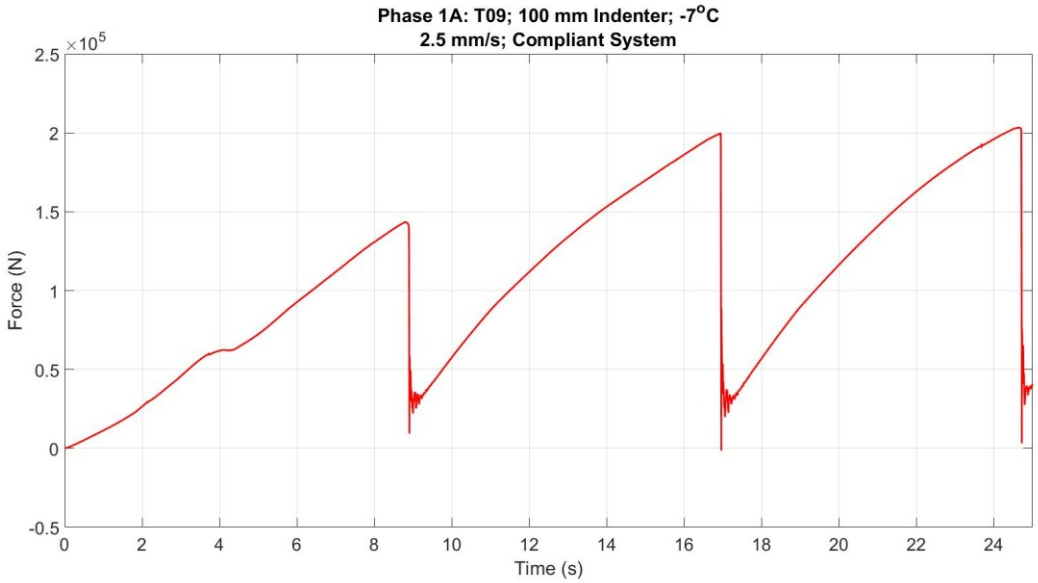

Figure A9.1: Force vs. time plot

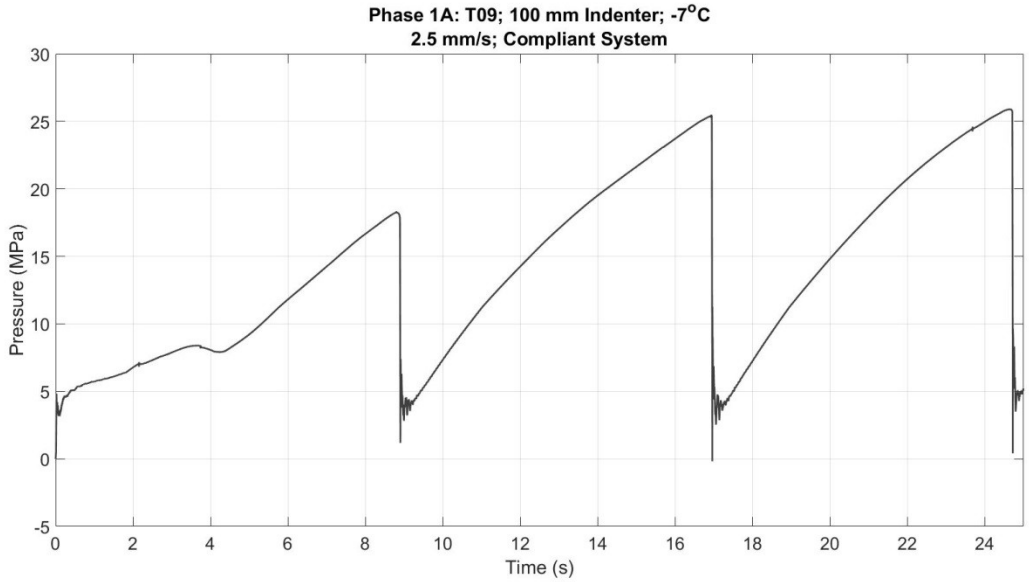

Figure A9.2: Pressure vs. time plot

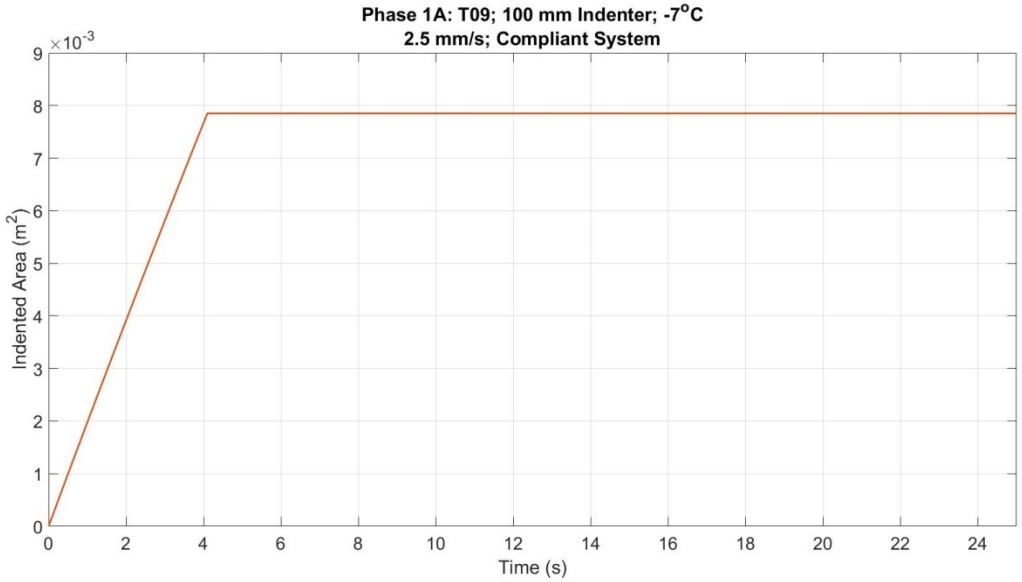

Figure A9.3: Indented area vs. time plot

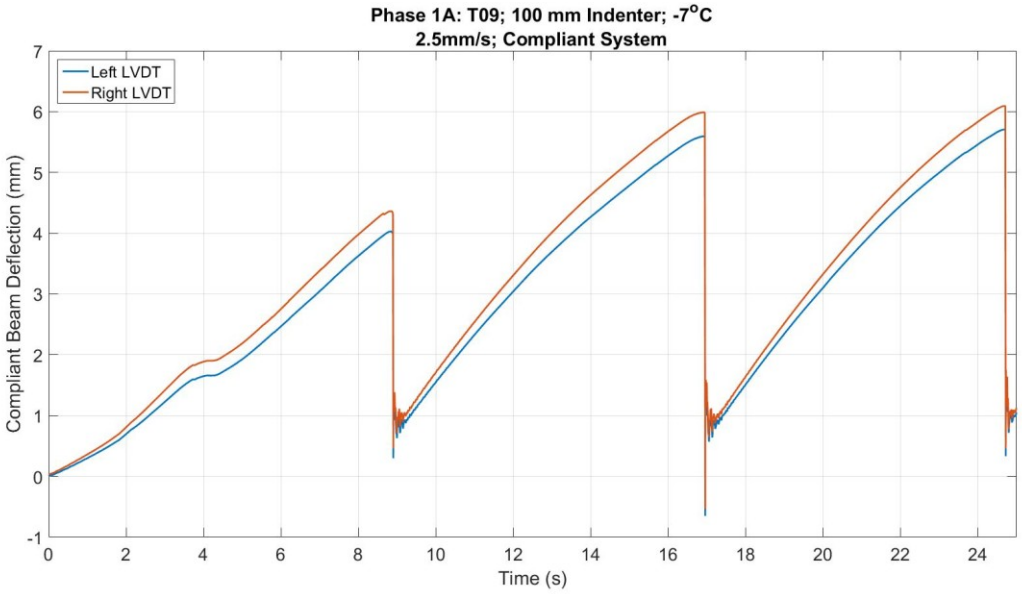

Figure A9.4 a: Compliant beam deflection vs. time plot

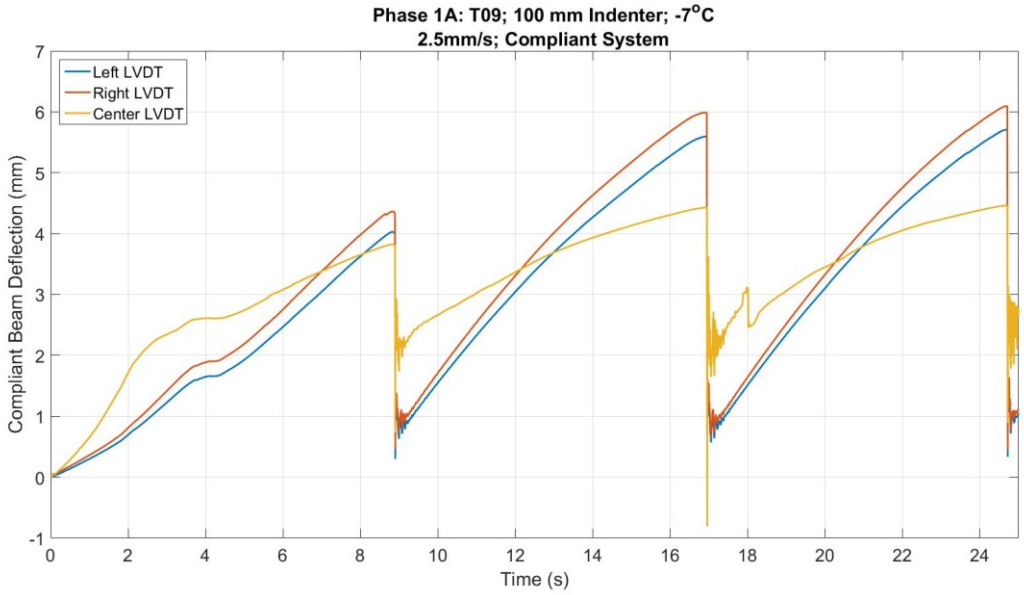

Figure A9.4 b: Compliant beam deflection vs. time plot

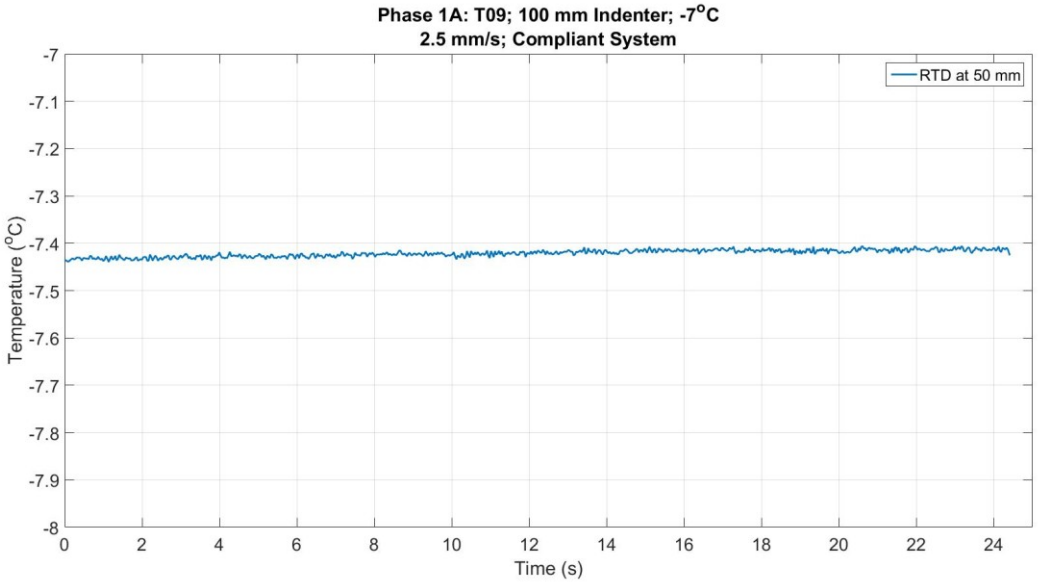

Figure A9.5: Temperature vs. time plot

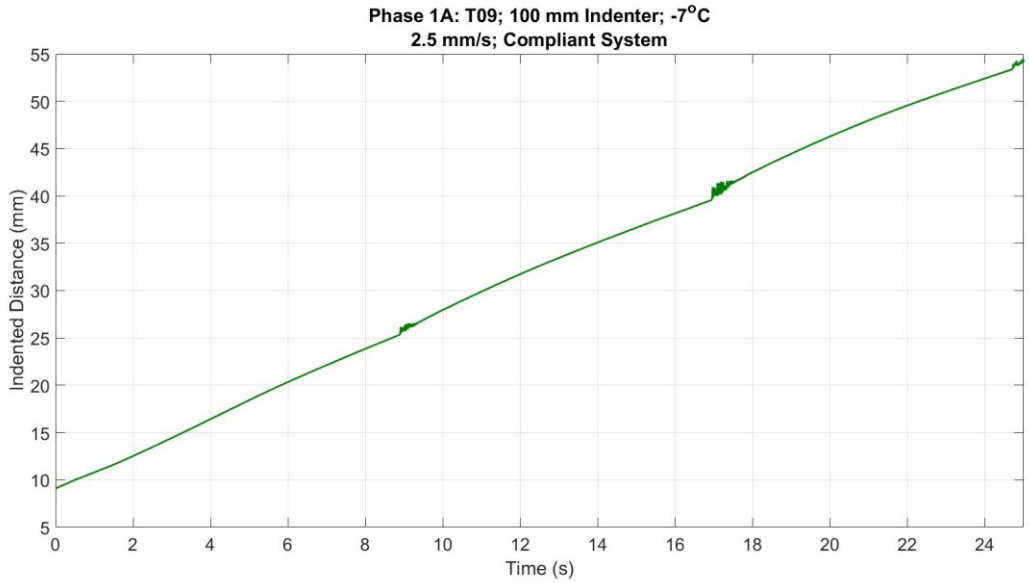

Figure A9.6: Indented distance vs. time plot

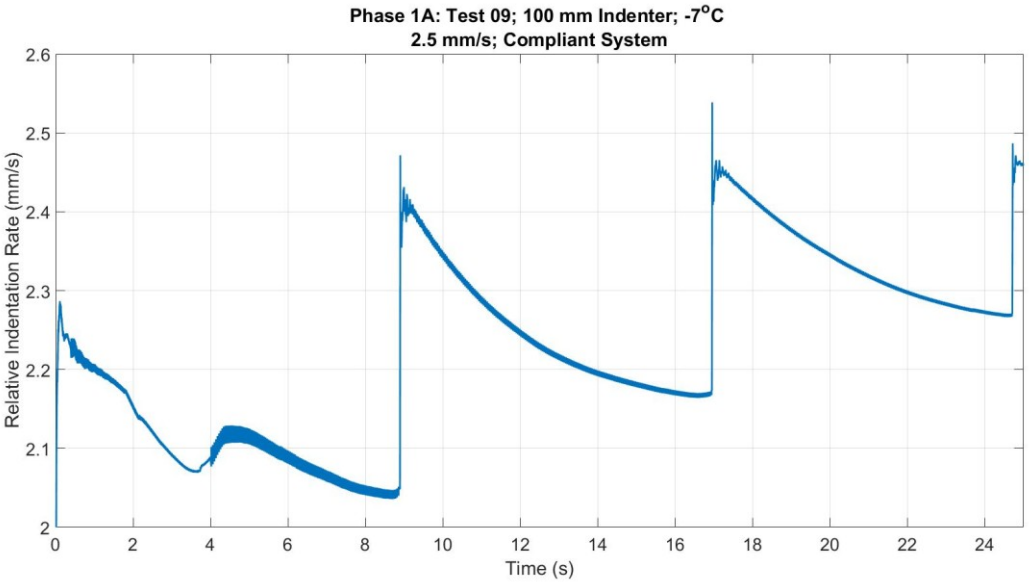

Figure A9.7: Relative loading rate vs time plot

Figure A9.8 (a): Post-test images for test T09_1A_07_100_R.

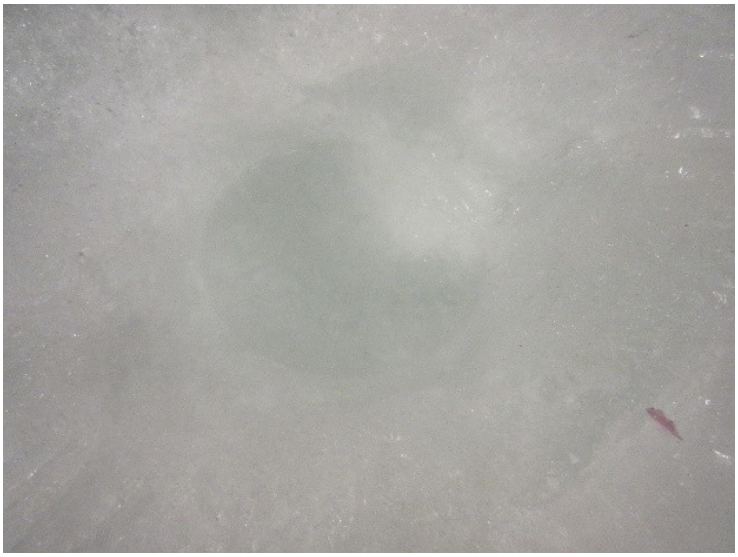

Figure A9.8 (b): Post-test images for test T09_1A_07_100_R.

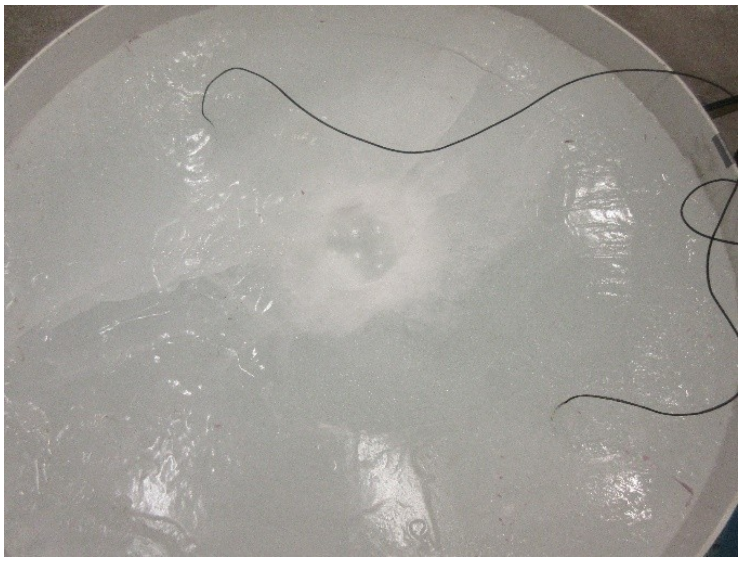

Figure A9.8 (c): Post-test images for test T09_1A_07_100_R.

Phase 1B

Test T10_1B_15_50

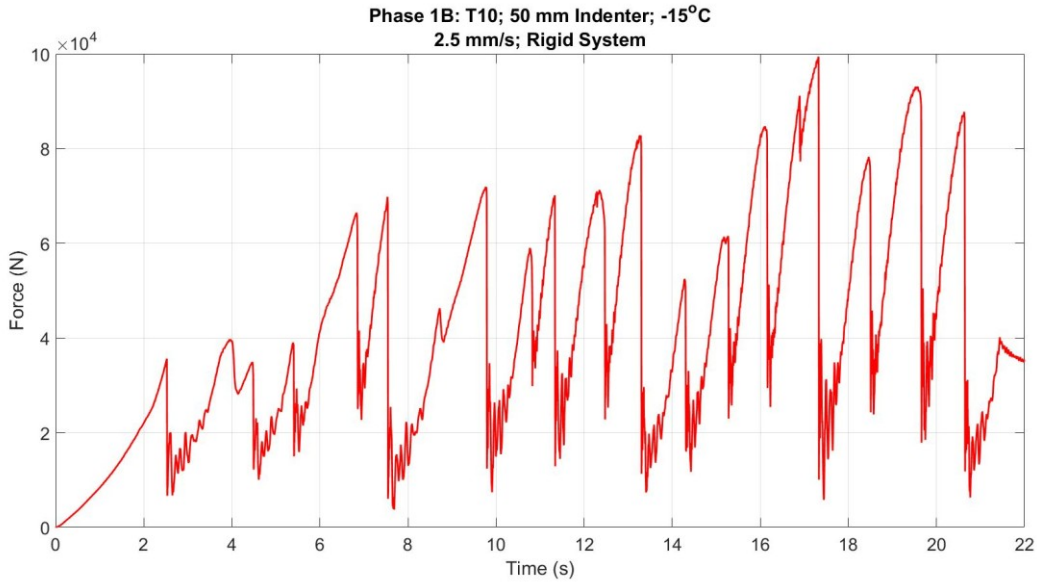

Figure A10.1: Force vs. time plot.

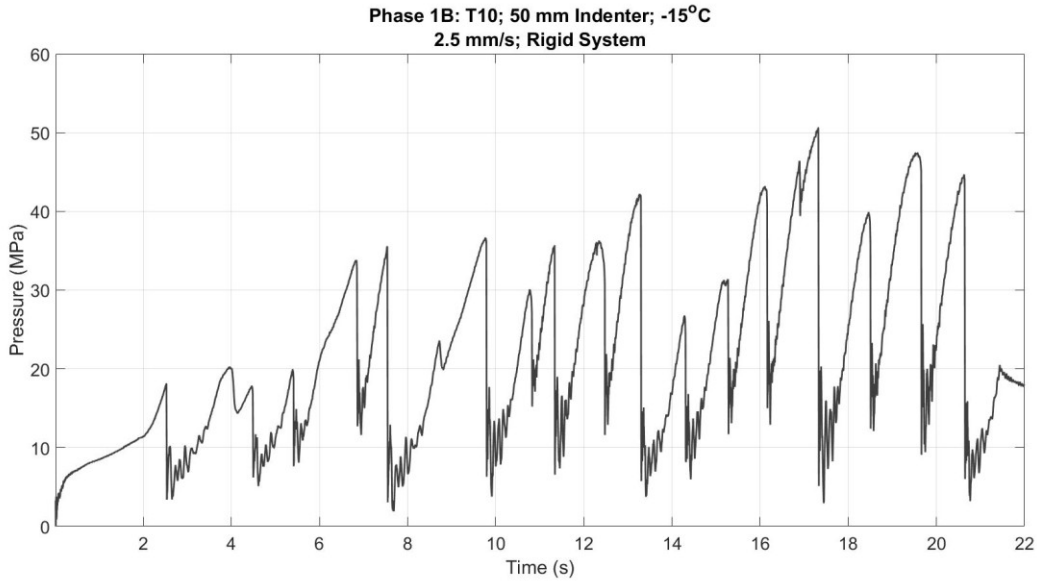

Figure A10.2: Pressure vs. time plot.

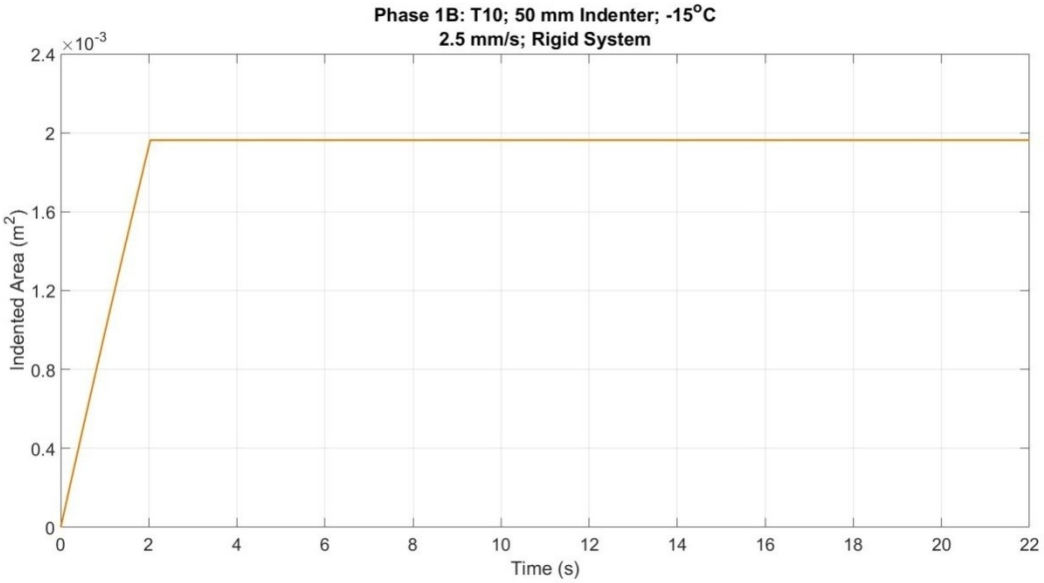

Figure A10.3: Indented area vs. time plot.

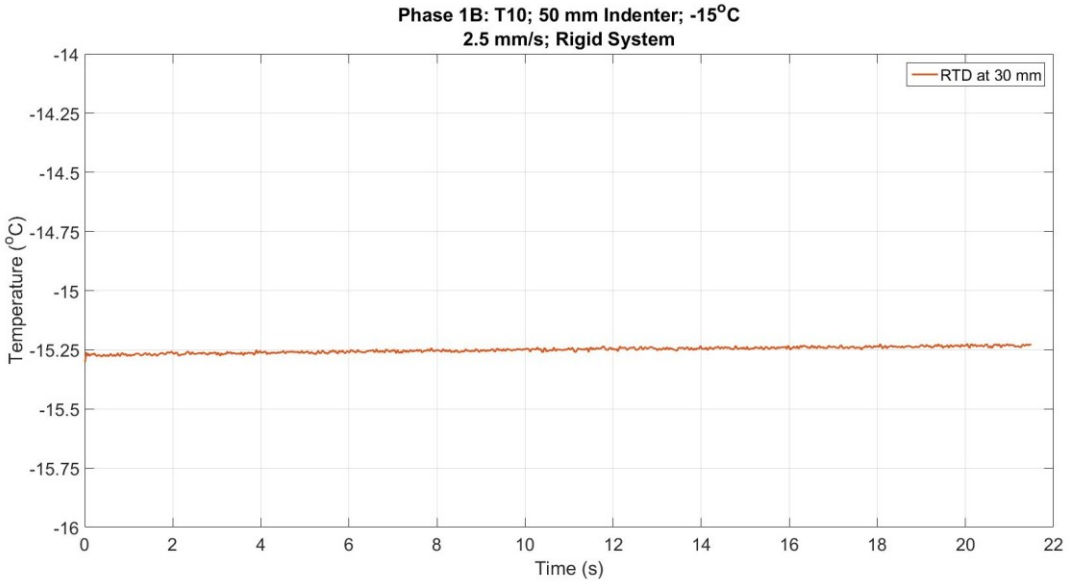

Figure A10.5: Temperature vs. time plot.

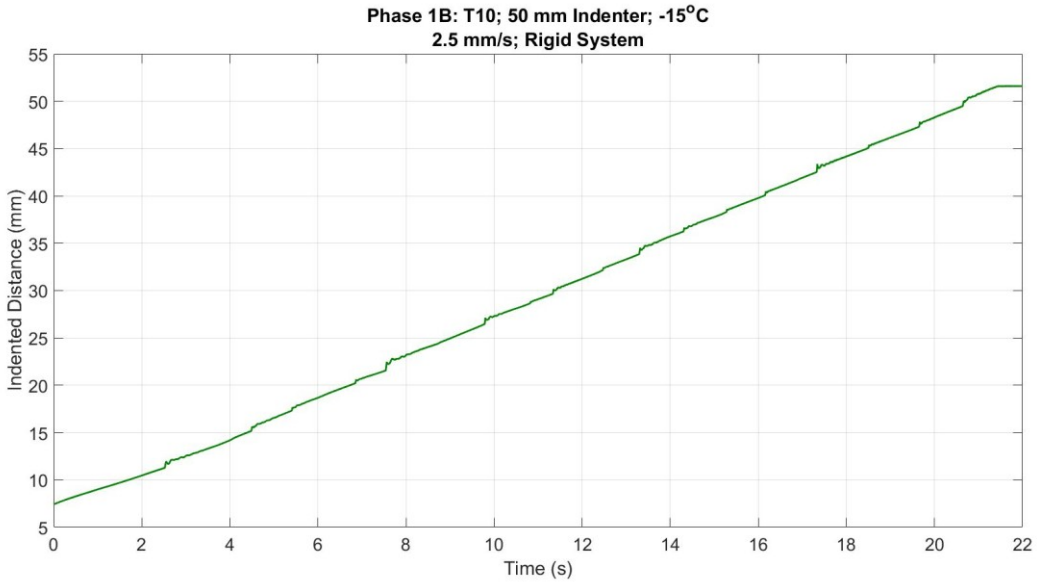

Figure A10.6: Indented distance vs. time plot.

Figure A10.7 (a): Post-test images for test T10_1B_15_50.

Figure A10.7 (b): Post-test images for test T10_1B_15_50.

Figure A10.7 (c): Post-test images for test T10_1B_15_50.

Test T11_1B_14.5_150

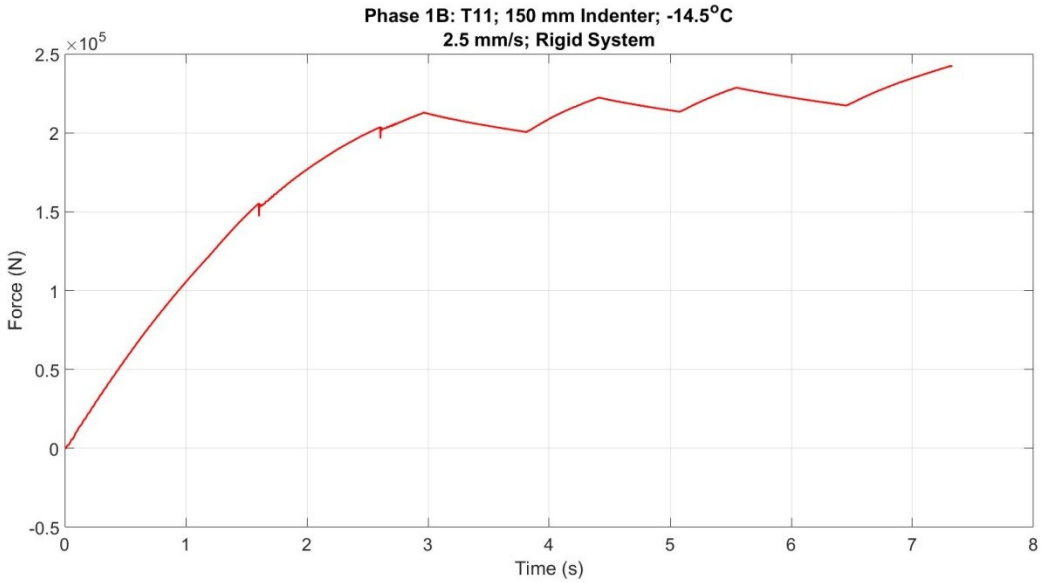

Figure A11.1: Force vs. time plot.

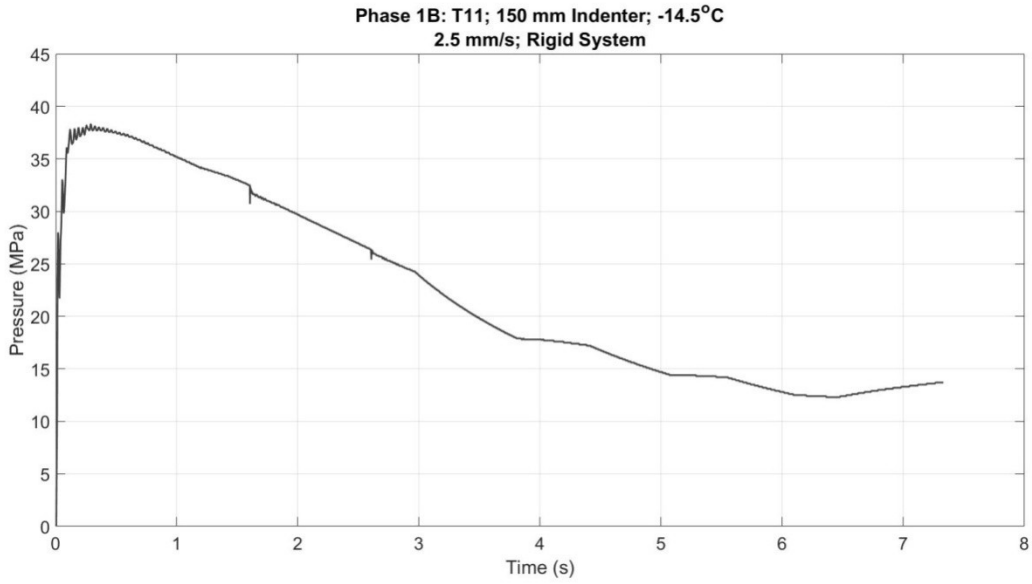

Figure A11.2: Pressure vs. time plot.

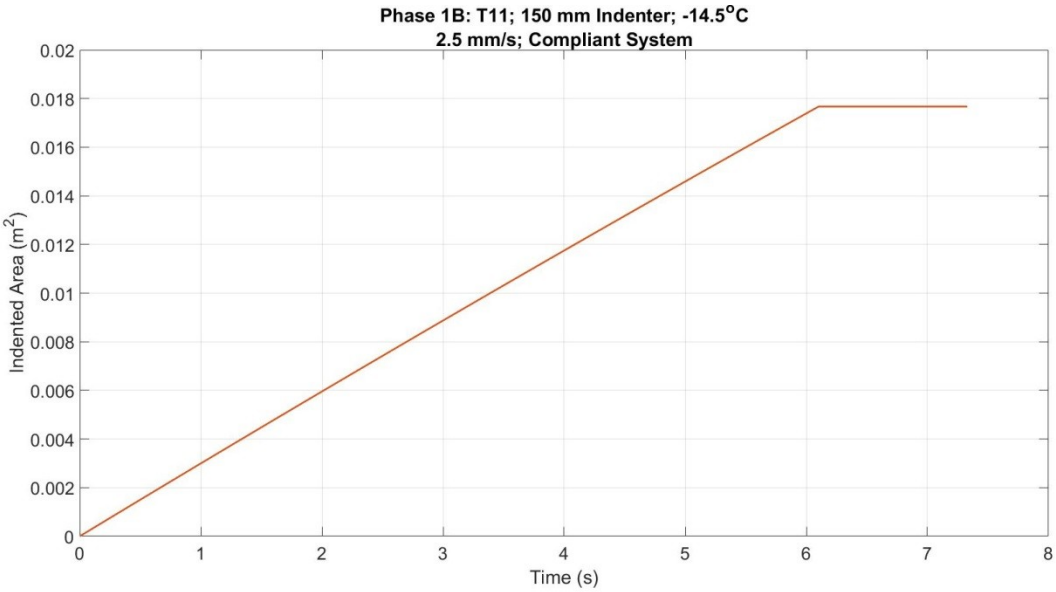

Figure A11.3: Indented area vs. time plot.

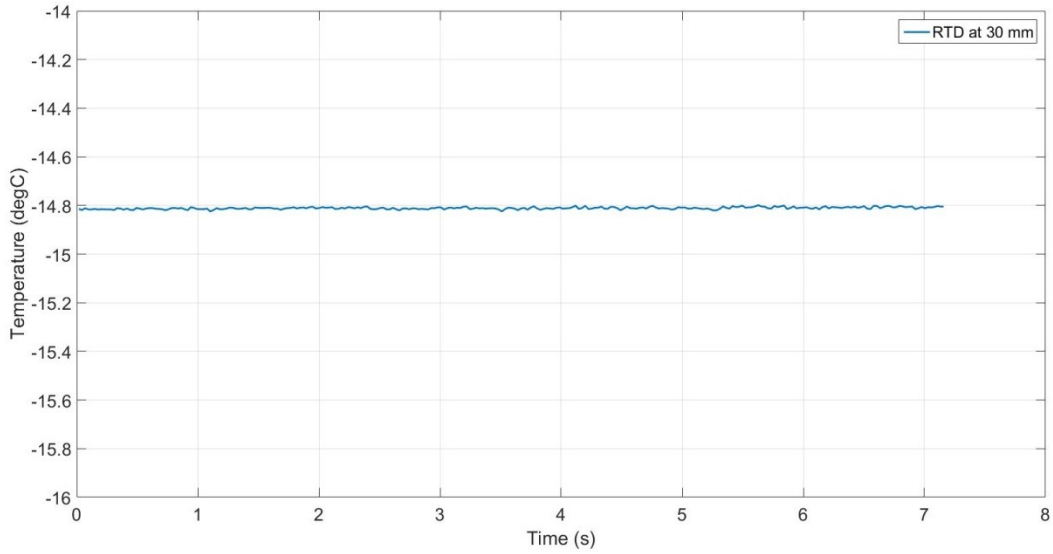

Figure A11.5: Temperature vs. time plot.

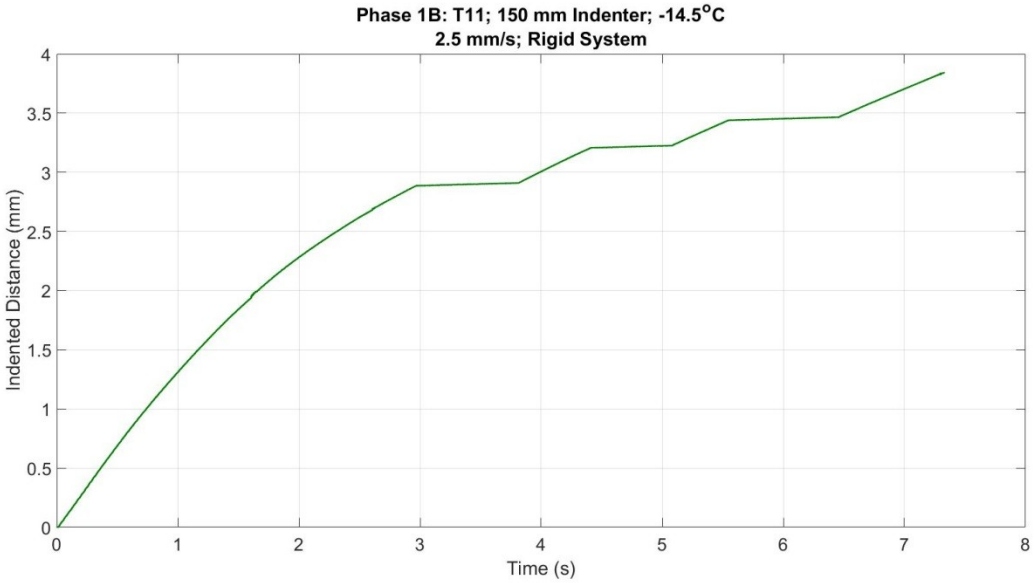

Figure A11.6: Indented distance vs. time plot.

Figure A11.7 (a): Post-test images for test T11_1B_14.5_150.

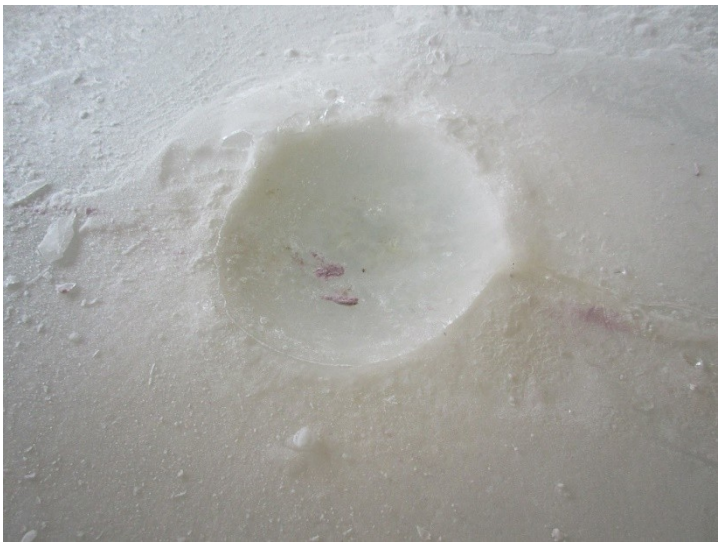

Figure A11.7 (b): Post-test images for test T11_1B_14.5_150.

Test T12_1B_14_100

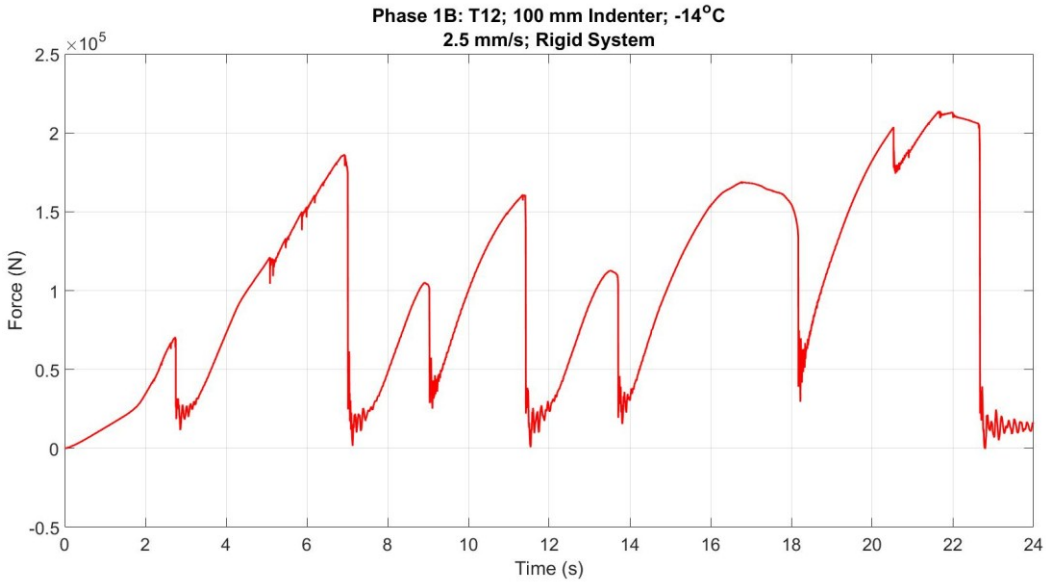

Figure A12.1: Force vs. time plot.

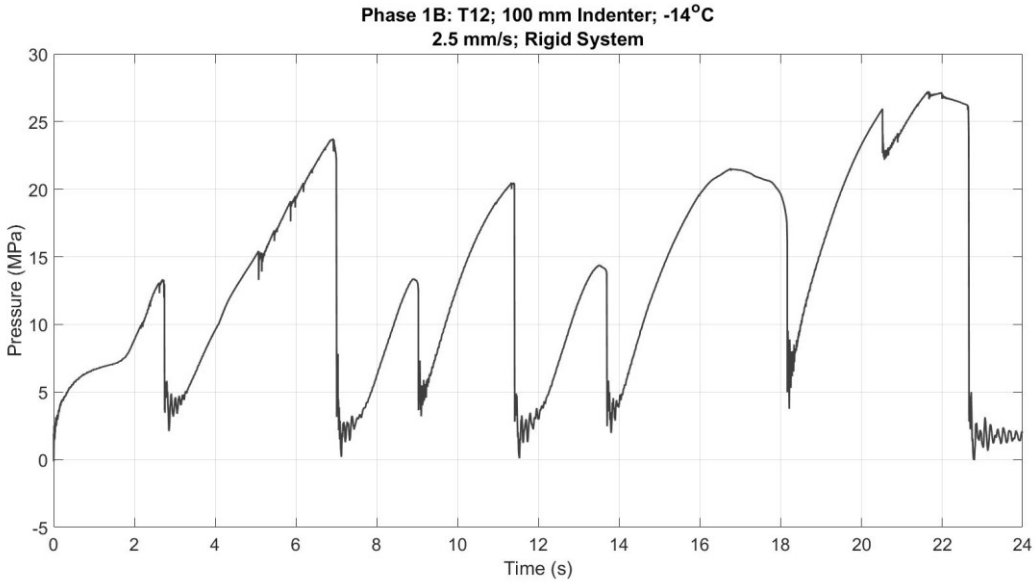

Figure A12.2: Pressure vs. time plot.

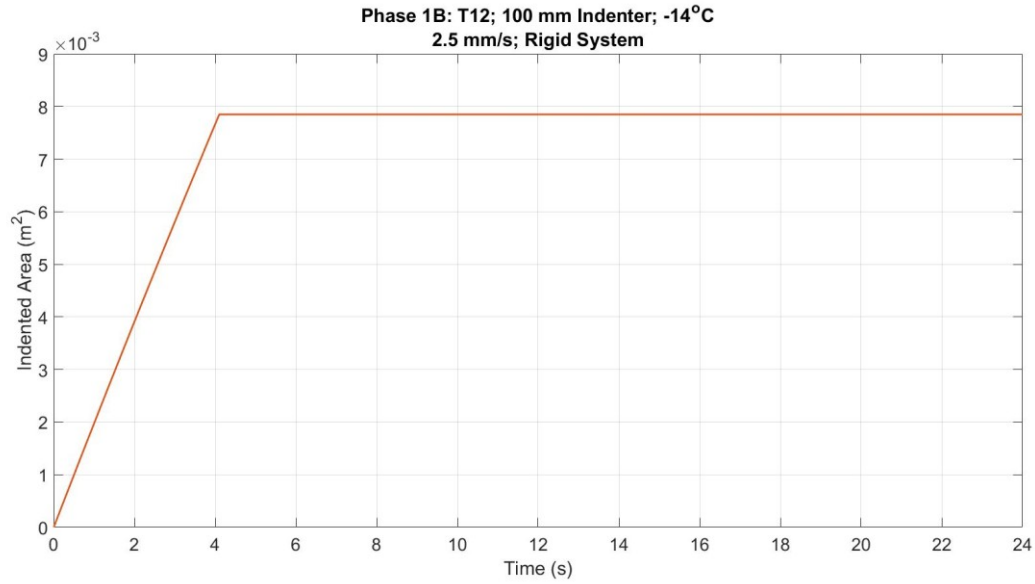

Figure A12.3: Indented area vs. time plot.

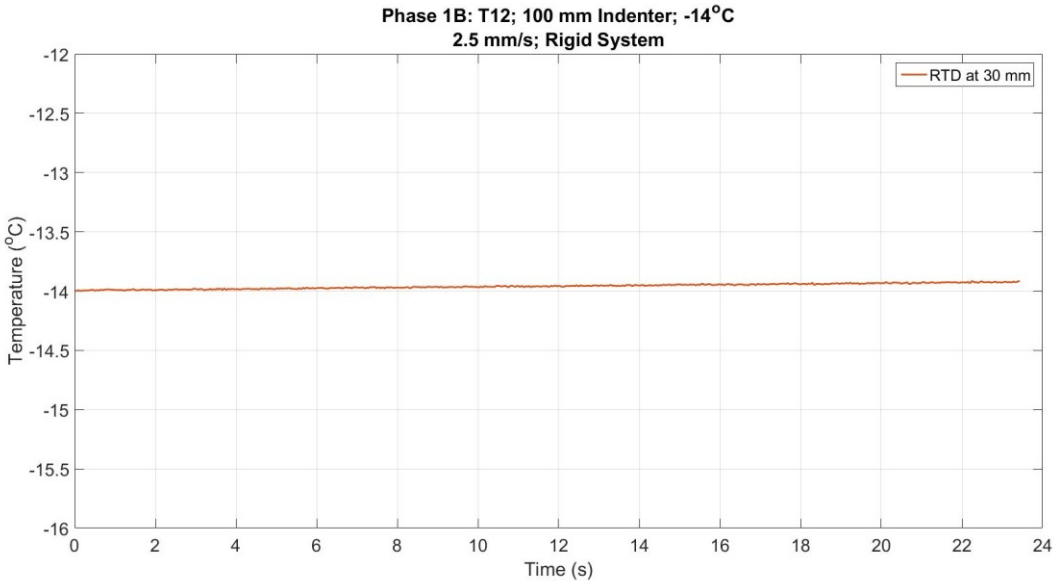

Figure A12.5: Temperature vs. time plot.

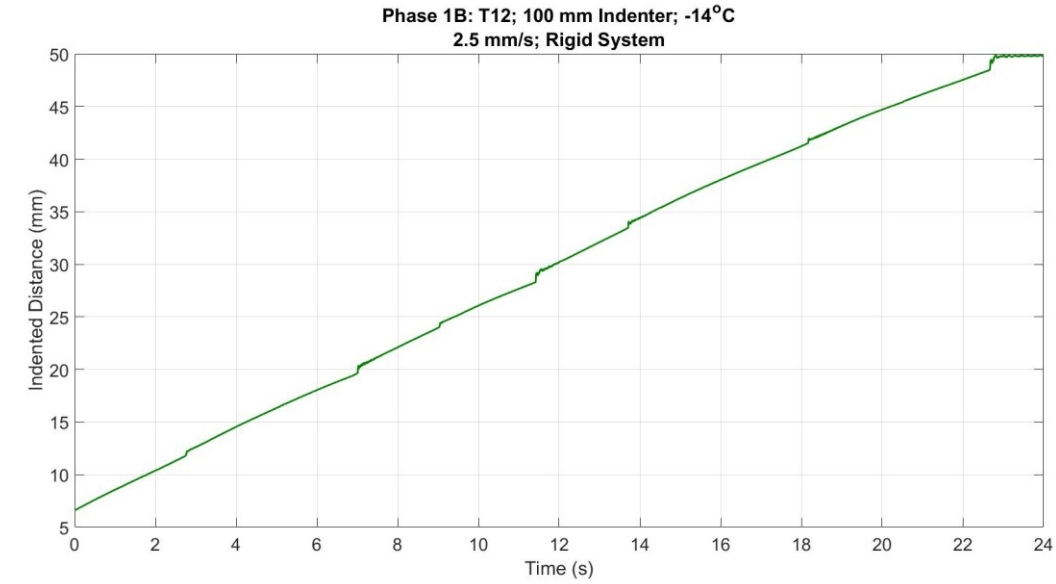

Figure A12.6: Indented distance vs. time plot.

Figure A12.7 (a): Post-test images for test T12_1B_14_100.

Figure A12.7 (b): Post-test images for test T12_1B_14_100.

Test T13_1B_07_50

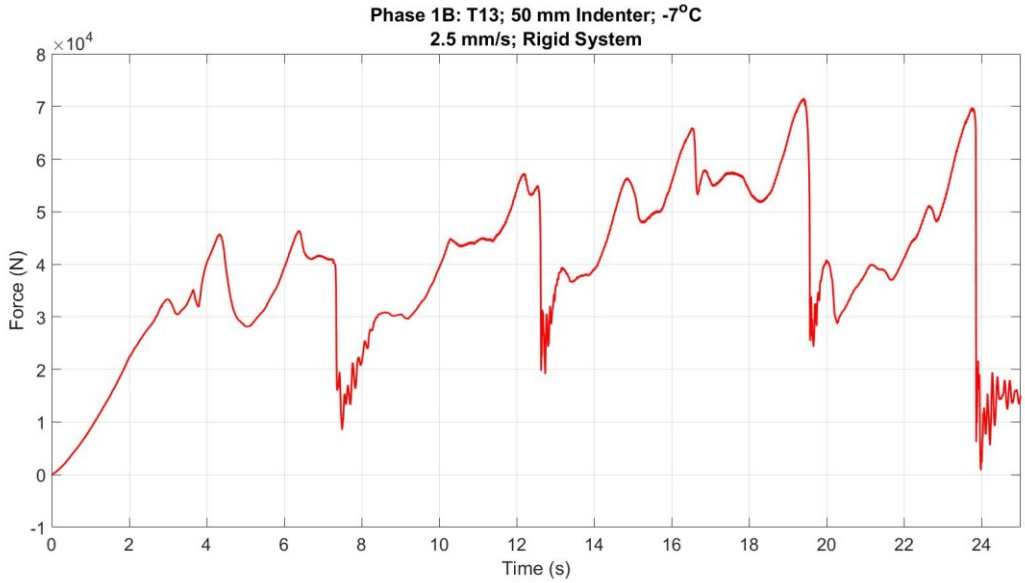

Figure A13.1: Force vs. time plot.

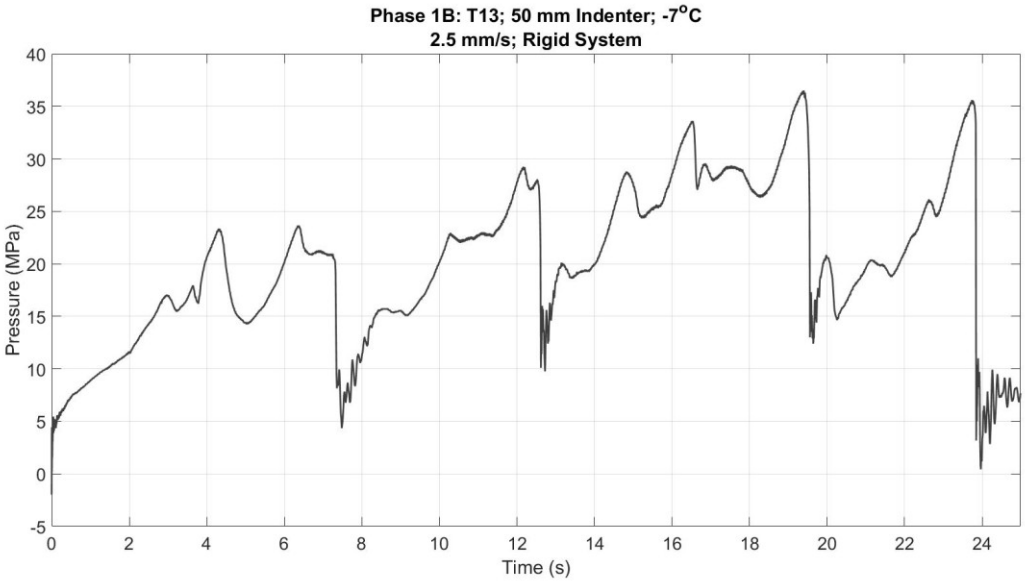

Figure A13.2: Pressure vs. time plot.

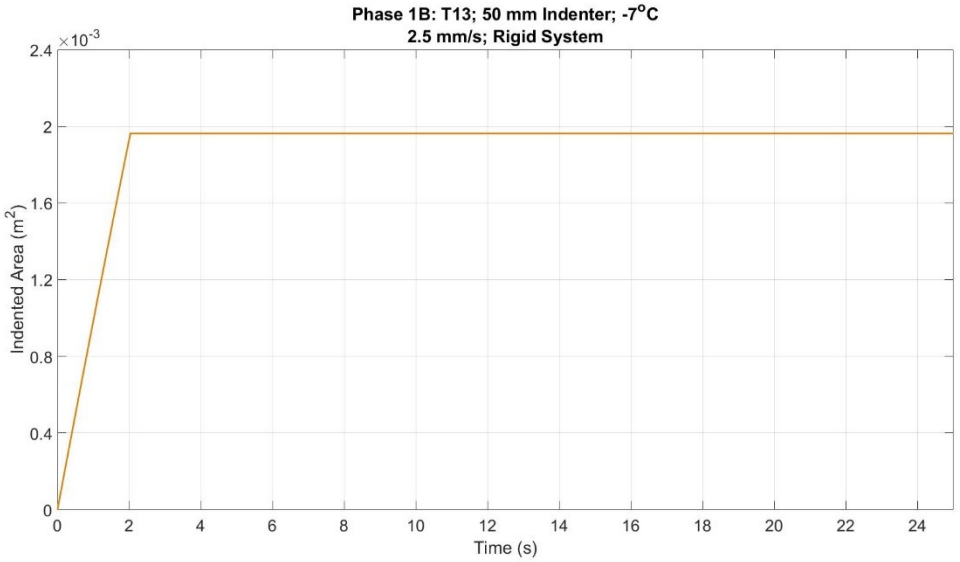

Figure A13.3: Indented area vs. time plot.

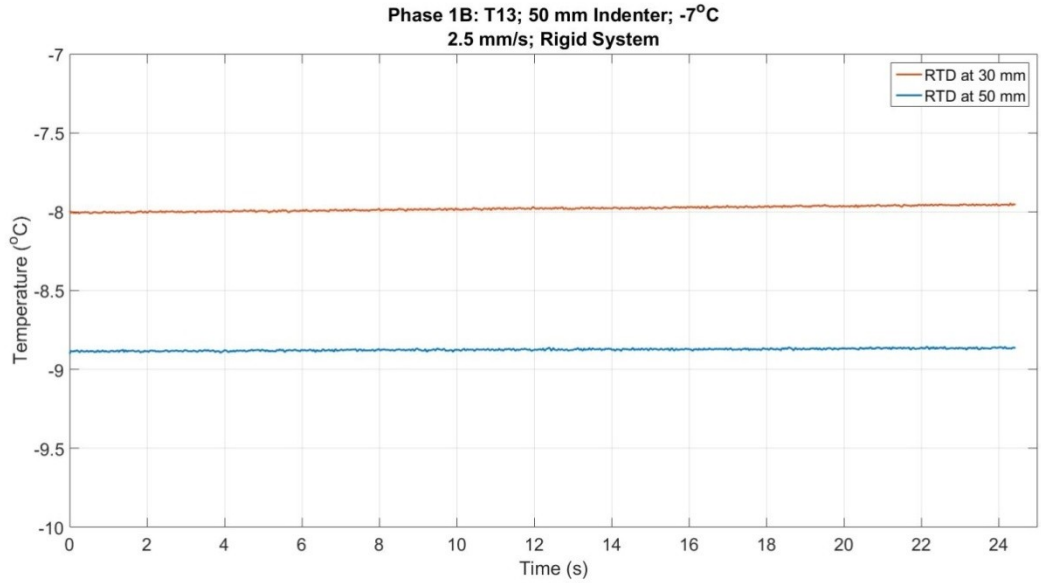

Figure A13.5: Temperature vs. time plot.

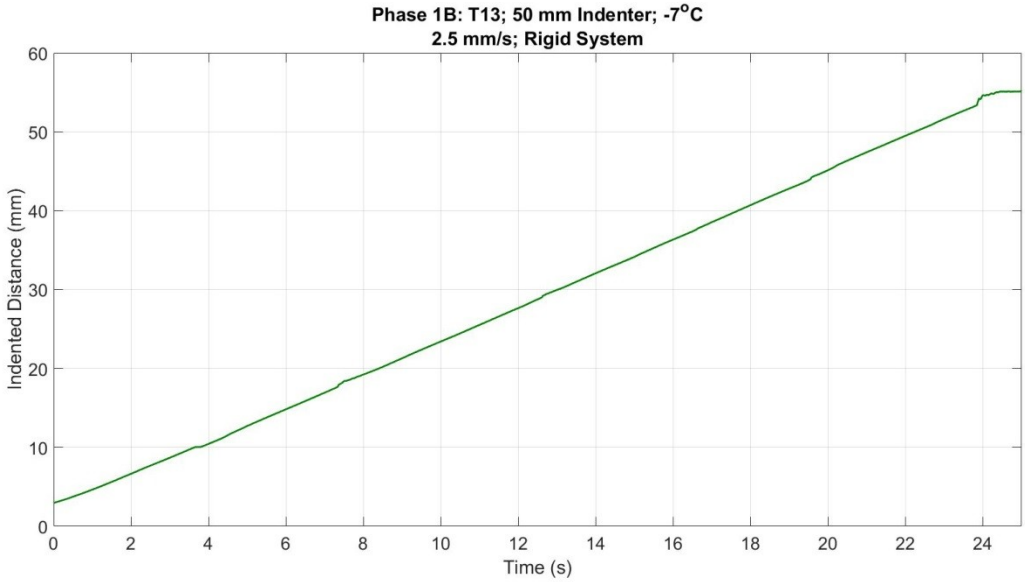

Figure A13.6: Indented distance vs. time plot.

Figure A13.7 (a): Post-test images for test T13_1B_07_50.

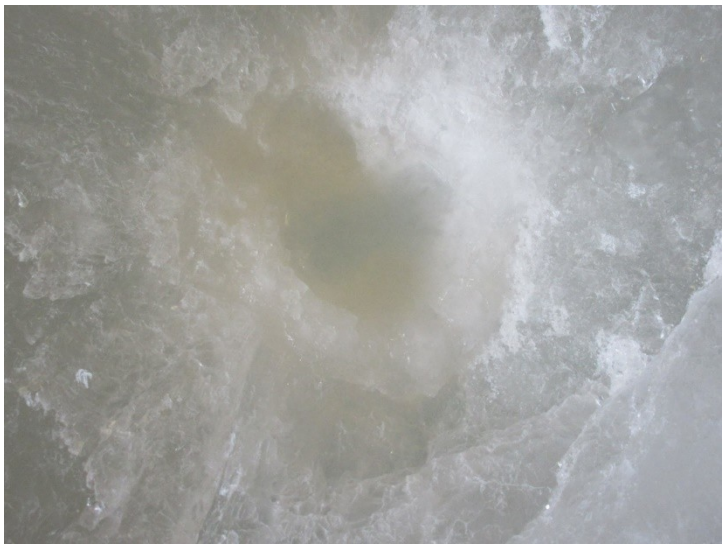

Figure A13.7 (b): Post-test images for test T13_1B_07_50.

Test T14_1B_06_100

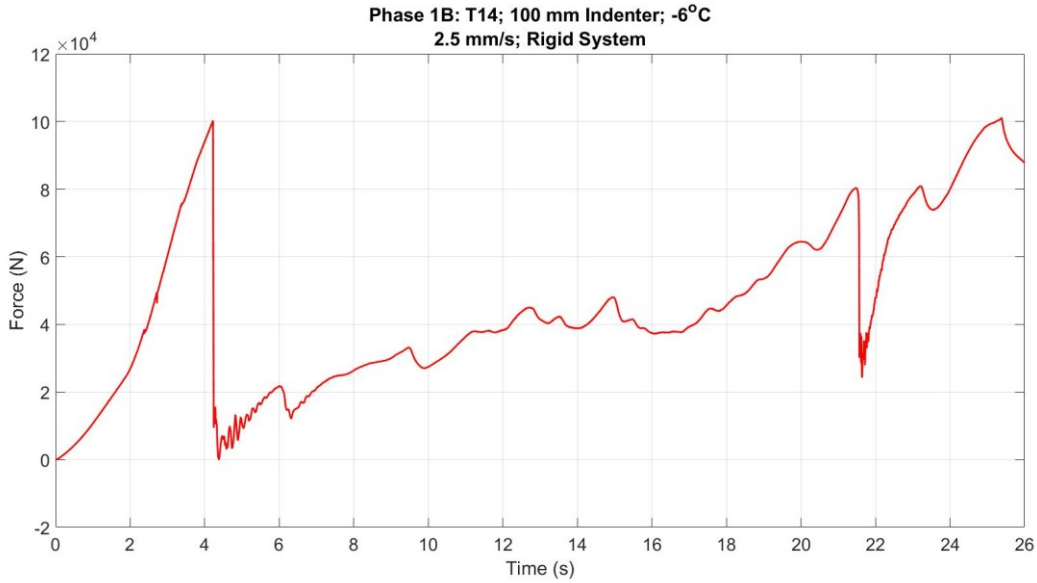

Figure A14.1: Force vs. time plot.

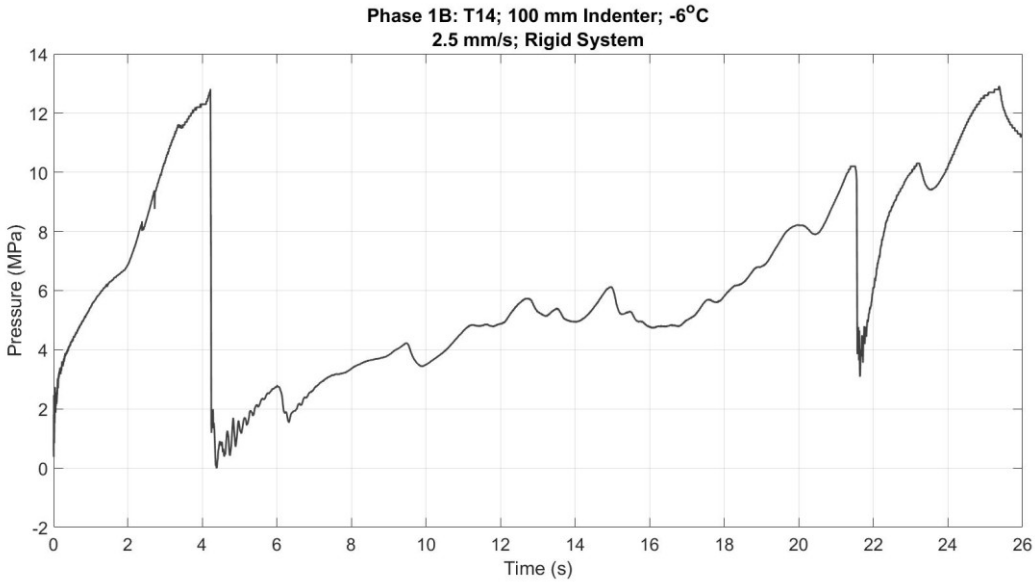

Figure A14.2: Pressure vs. time plot.

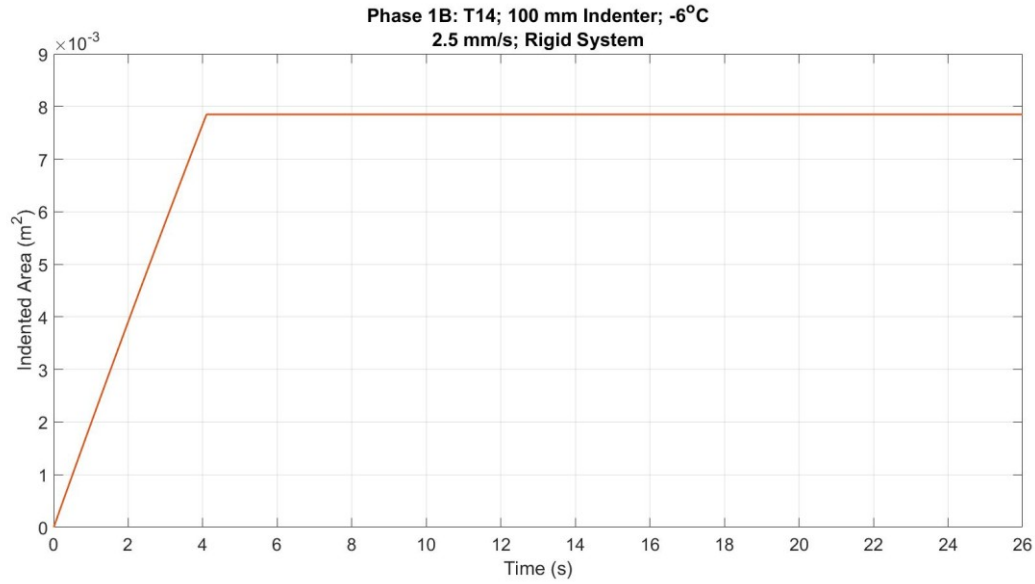

Figure A14.3: Indented area vs. time plot.

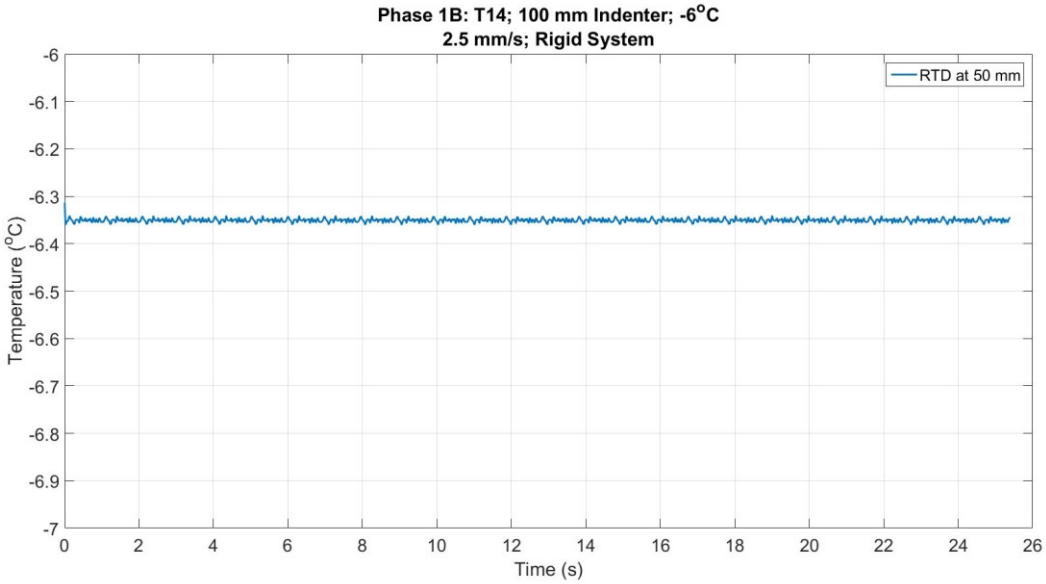

Figure A14.5: Temperature vs. time plot.

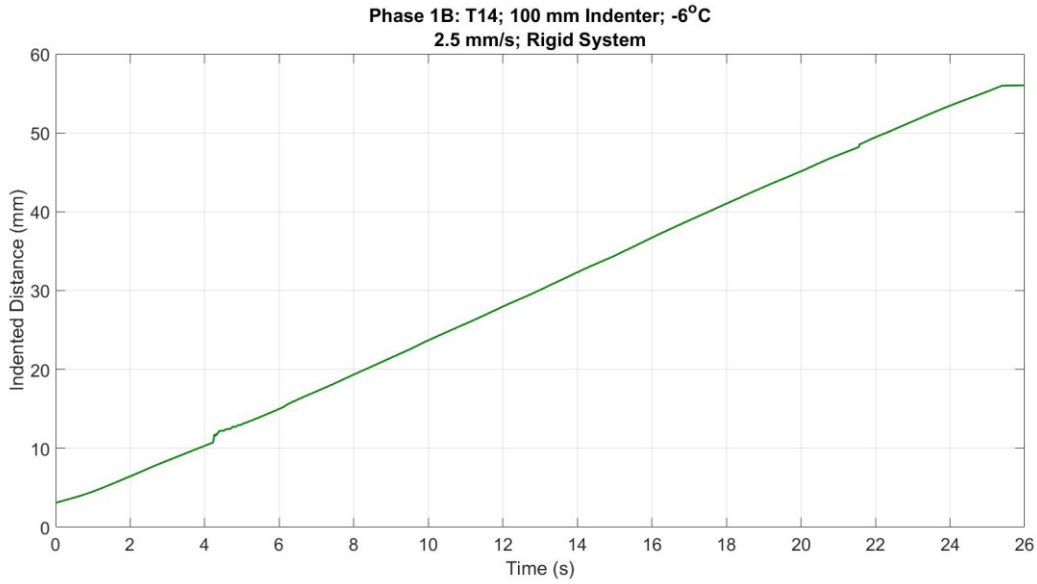

Figure A14.6: Indented distance vs. time plot.

Figure A14.7 (a): Post-test images for test T14_1B_06_100.

Figure A14.7 (b): Post-test images for test T14_1B_06_100.

Figure A14.7 (c): Post-test images for test T14_1B_06_100.

Test T15_1B_05_150

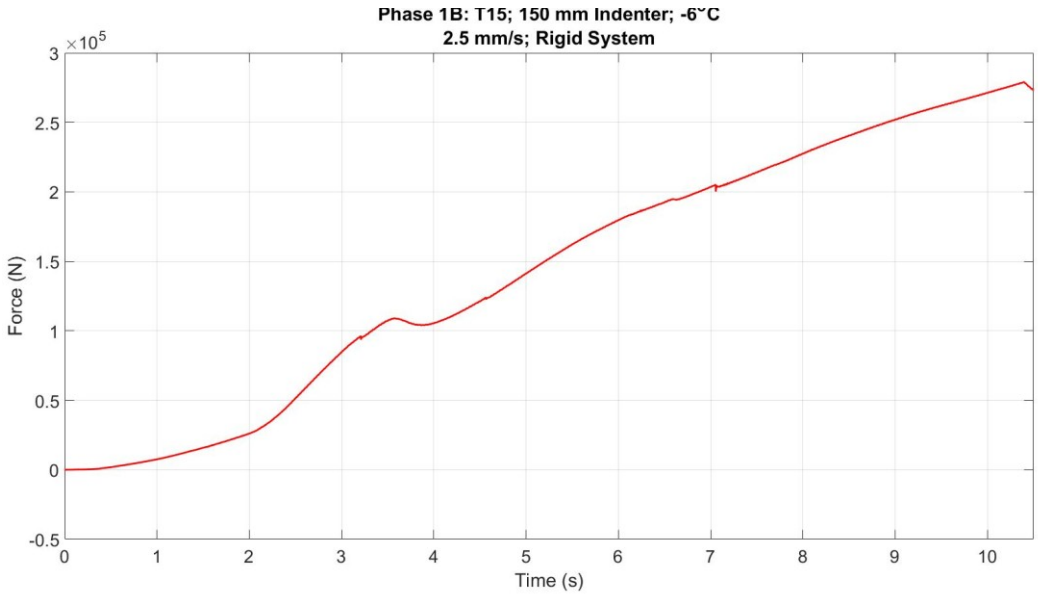

Figure A15.1: Force vs. time plot

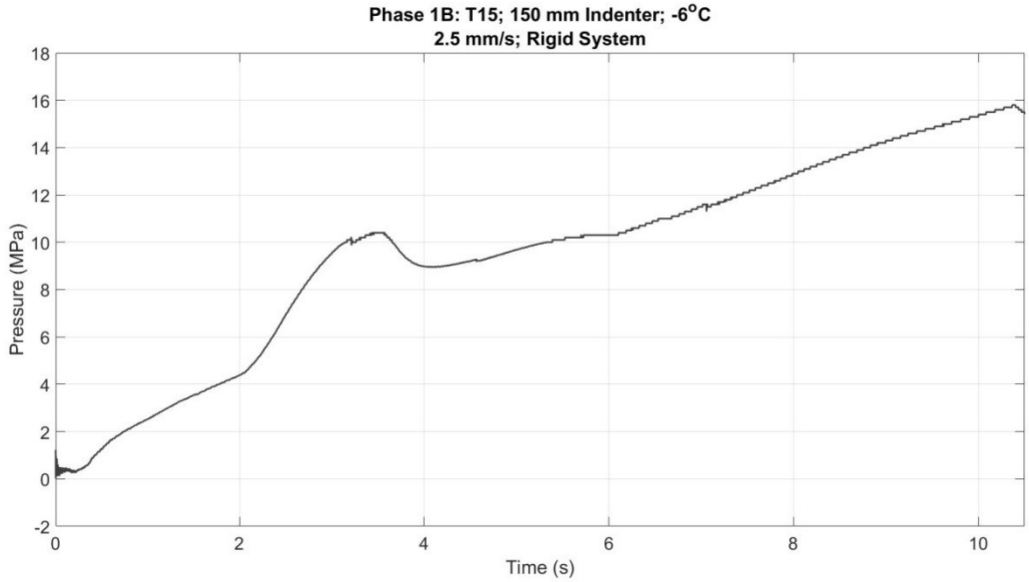

Figure A15.2: Pressure vs. time plot.

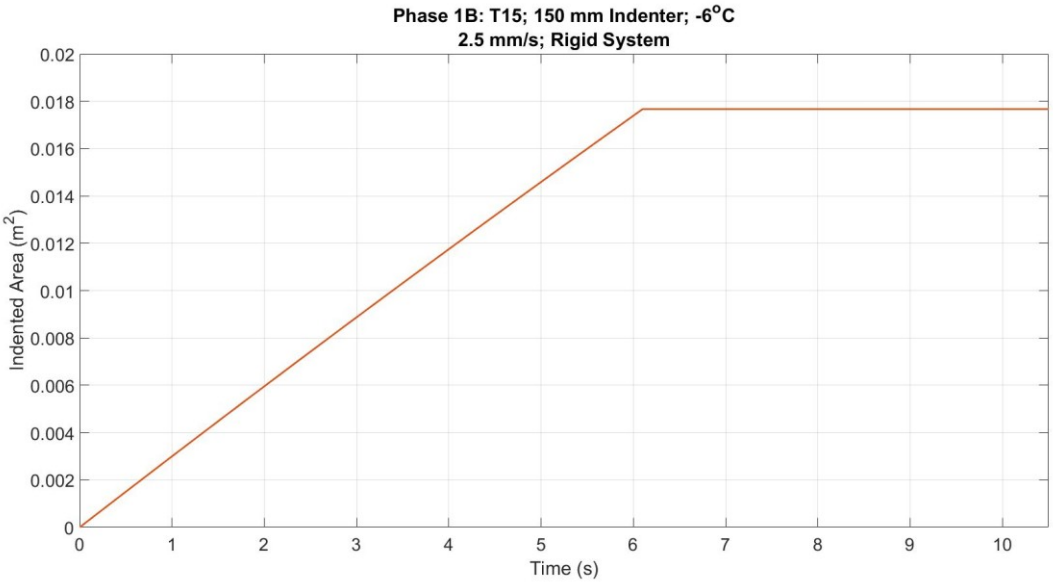

Figure A15.3: Indented area vs. time plot

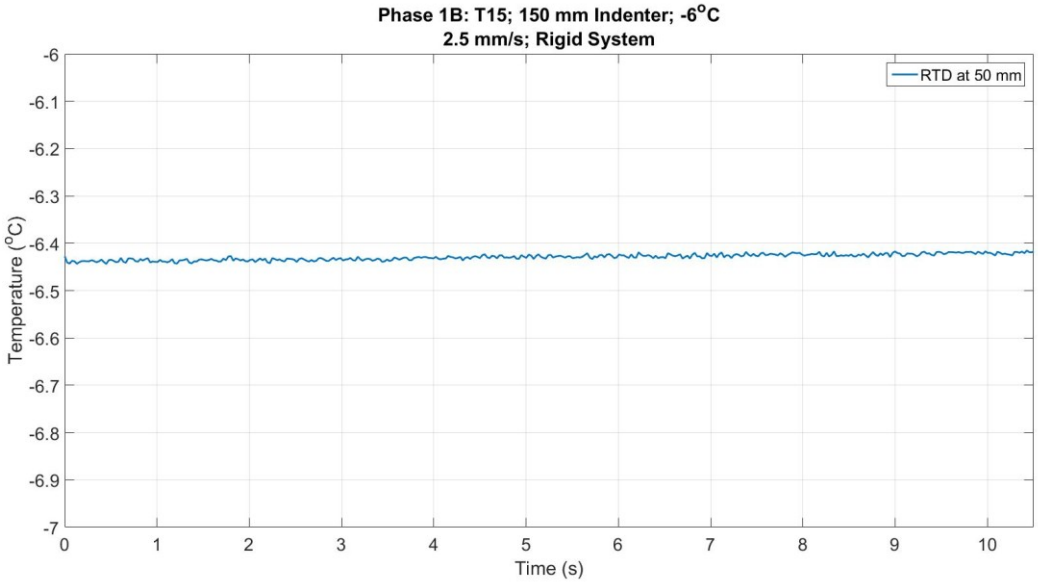

Figure A15.5: Temperature vs. time plot.

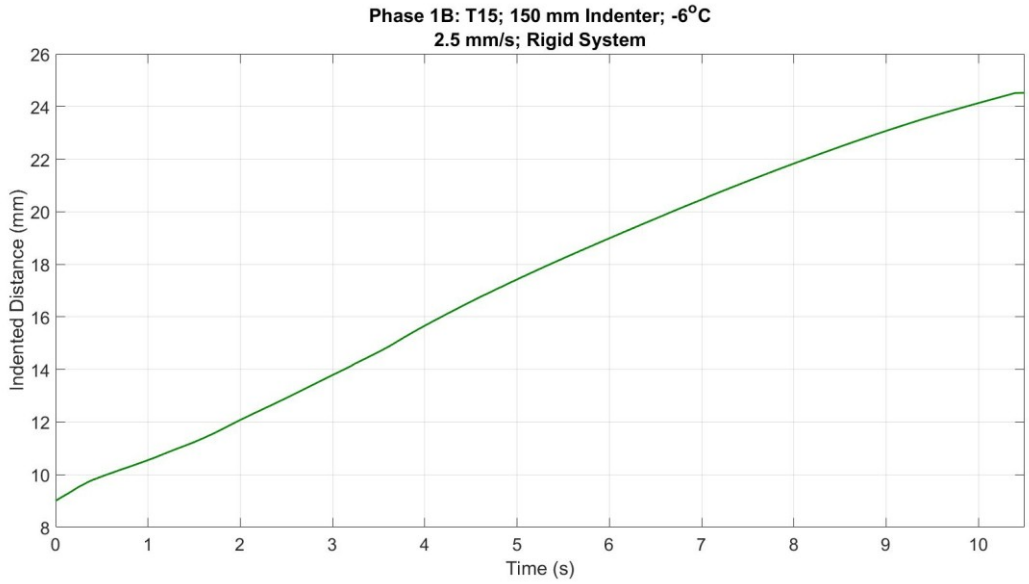

Figure A15.6: Indented distance vs. time plot.

Figure A15.7 (a): Post-test images for test T15_1B_05_150.

Figure A15.7 (b): Post-test images for test T15_1B_05_150.

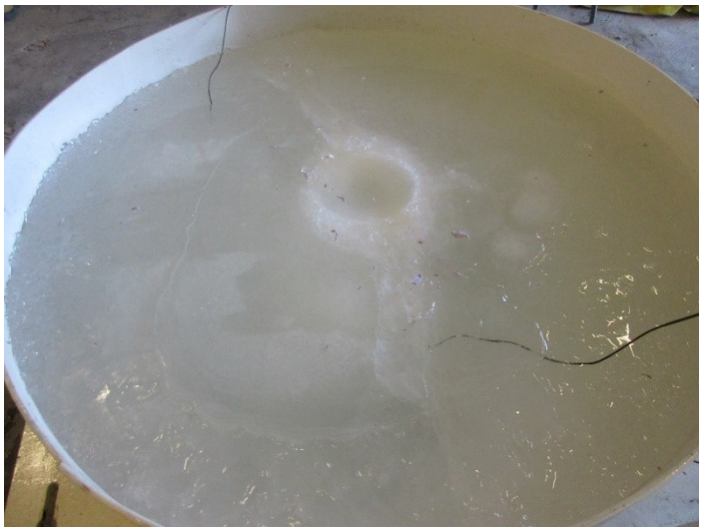

Figure A15.7 (c): Post-test images for test T15_1B_05_150.

APPENDIX B – Calibrations

TRANS-TEK
INCORPORATED

CALIBRATION RECORD

10 Industrial Drive, P.O.Box 338, Ellington, CT 06029 Tel(860)872-8351 Fax(860)872-421

MODEL NUMBER: 0337-0000
SERIAL # 5495

Maximum Nonlinearity: 0.114% F.S.
Calculation Method: Best Fit Straight Line
Calculated Line: Y = 2.5211 X + -0.0058
Working Range: +/- 1 inch(es)
Sensitivity: 0.5032 VAC / inch(es) / Volt Input
Tested at: 5.009772 VAC RMS Input at 6.944283 kHz

If the core is not permanently attached to the extension rod, then the transducer was calibrated with the core's marked end towards the transducer's lead end.

CALIBRATION DATA

POSITION	OUTPUT VAC		ERROR
inch(es)	DATA	ZERO ADJUSTED	% F.S.
-1.0000	2.5326	NA	0.113
-0.8000	2.0243	NA	0.033
-0.6000	1.5213	NA	0.057
-0.4000	1.0113	NA	-0.058
-0.2000	0.5043	NA	-0.114
0.0000	0.0017	* Not Applicable	
0.2000	0.5034	NA	0.099
0.4000	1.0027	NA	0.001
0.6000	1.5037	NA	-0.062
0.8000	2.0053	NA	-0.114
1.0000	2.5154	NA	0.002

* Data point not used in calculating line or error: Voltage at this point is the out-of-phase component removed by demodulation.

Calibrated by: _____ Date: 06-12-2014
Per S022-0198 Rev. # 3

Note: Please refer to attached bulletin for additional information.
BATCH CODE #140612F100607 REF. #: 5

Figure B1: Calibration Sheet for the Series 330 LVDT

measurement SPECIALTIES

FINAL TEST LVDT MHR 500 ASSY

02560411-000
RANGE +/-.5 Inches
INDEPENDENT LINEARITY DATA LEAST SQUARES LINE

S/N J67753
2015-5-4

MEASURED Inches	MEASURED Volts RMS	CALC. Volts RMS	CALC. DEVIATION
-0.5000	-2.4259	-2.4335	+0.0076
-0.4000	-1.9397	-1.9423	+0.0025
-0.3000	-1.4531	-1.4510	-0.0021
-0.2000	-0.9651	-0.9597	-0.0054
-0.1000	-0.4754	-0.4685	-0.0069
+0.1000	+0.5109	+0.5139	-0.0030
+0.2000	+1.0052	+1.0052	+0.0000
+0.3000	+1.4985	+1.4964	+0.0021
+0.4000	+1.9929	+1.9877	+0.0052
+0.5000	+2.4789	+2.4789	-0.0001

Linearity = 0.15%
Sensitivity =1.6375 mv/Volts RMS/.001 Inches
NULL (actual) =0.0077 Volts RMS

Tested by Yingquan Feng Inspected by

Measurement Specialties,Inc
MEAS Global Headquarters
1000 Lucas Way
Hampton, VA 23666
United States
757-766-1500
757-766-4297 fax
www.meas-spec.com

Measurement Specialties (China) Ltd.
No. 26 Langshan Road
Shenzhen High-Tech Park (North)
Nanshan District, Shenzhen 518057
China
+86 755 33305088
+86 755 33305099 fax
www.meas-spec.com

MEAS Deutschland GmbH
Hauert 13
D-44227 Dortmund
Germany
+49 231 97400
+ 49 231 974050 fax
www.meas-spec.com

Figure B2: Calibration Sheet for the MHR series LVDT (J67753).

measurement SPECIALTIES

FINAL TEST LVDT MHR 500 ASSY

02560411-000
RANGE +/-.5 Inches
INDEPENDENT LINEARITY DATA LEAST SQUARES LINE

S/N J67783
2015-5-4

MEASURED Inches	MEASURED Volts RMS	CALC. Volts RMS	CALC. DEVIATION
-0.5000	-2.4510	-2.4602	+0.0093
-0.4000	-1.9645	-1.9664	+0.0019
-0.3000	-1.4757	-1.4726	-0.0032
-0.2000	-0.9834	-0.9787	-0.0046
-0.1000	-0.4905	-0.4849	-0.0056
+0.1000	+0.4969	+0.5027	-0.0057
+0.2000	+0.9942	+0.9965	-0.0023
+0.3000	+1.4933	+1.4903	+0.0030
+0.4000	+1.9897	+1.9842	+0.0055
+0.5000	+2.4798	+2.4780	+0.0018

Linearity = 0.19%
Sensitivity =1.6461 mv/Volts RMS/.001 Inches
NULL (actual) =0.0024 Volts RMS

Tested by Yingquan Feng Inspected by 胡景林

Measurement Specialties,Inc
MEAS Global Headquarters
1000 Lucas Way
Hampton, VA 23666
United States
757-766-1500
757-766-4297 fax
www.meas-spec.com

Measurement Specialties (China) Ltd.
No. 26 Langshan Road
Shenzhen High-Tech Park (North)
Nanshan Distnct, Shenzhen 518057
China
+86 755 33305088
+86 755 33305099 fax
www.meas-spec.com

MEAS Deutschland GmbH
Hauert 13
D-44227 Dortmund
Germany
+49 231 97400
+ 49 231 974050 fax
www.meas-spec.com

Figure B3: Calibration Sheet for the MHR series LVDT (J67783).

measurement SPECIALTIES

FINAL TEST LVDT MHR 500 ASSY

02560411-000
RANGE +/-.5 Inches
INDEPENDENT LINEARITY DATA LEAST SQUARES LINE

S/N J67798
2015-5-4

MEASURED Inches	MEASURED Volts RMS	CALC. Volts RMS	CALC. DEVIATION
-0.5000	-2.4594	-2.4671	+0.0077
-0.4000	-1.9702	-1.9710	+0.0008
-0.3000	-1.4772	-1.4749	-0.0023
-0.2000	-0.9824	-0.9788	-0.0036
-0.1000	-0.4898	-0.4828	-0.0070
+0.1000	+0.5046	+0.5093	-0.0047
+0.2000	+1.0071	+1.0054	+0.0017
+0.3000	+1.5065	+1.5015	+0.0050
+0.4000	+2.0017	+1.9976	+0.0041
+0.5000	+2.4918	+2.4937	-0.0019

Linearity = 0.15%
Sensitivity = 1.6536 mv/Volts RMS/.001 Inches
NULL (actual) = 0.0050 Volts RMS

Tested by Yingquan Feng Inspected by

Measurement Specialties Inc
MEAS Global Headquarters
1000 Lucas Way
Hampton, VA 23666
United States
757-766-1500
757-766-4297 fax
www.meas-spec.com

Measurement Specialties (China) Ltd.
No. 26 Langshan Road
Shenzhen High-Tech Park (North)
Nanshan District, Shenzhen 518057
China
+86 755 33305088
+86 755 33305099 fax
www.meas-spec.com

MEAS Deutschland GmbH
Hauert 13
D-44227 Dortmund
Germany
+49 231 97400
+ 49 231 974050 fax
www.meas-spec.com

Figure B4: Calibration Sheet for the MHR series LVDT (J67798).

C-CORE — **Calibration Sheet** — Page 1 of 1

Description:	Load Cells - DIRKS	Performed by:	Jing Xu
Manufacturer:	Cooper Instruments & Systems	Approved by:	Karl Tuff
Model Number:	LGP 312-2C-HW60-T5C-100K	Date:	27/11/2012
Serial Number:	32120	Excitation (volts):	5
Factory Calibration:	0-5 Volts; 0 - 100,000 lbs	Notes:	ADD
Factory Calibration Date	ADD		

Equipment Used / Source Details: TINIUS OLSEN (Materials Testing Machines), BK PRECISION 5491A (Count Bench Multimeter)

Engr Units 1	Voltage 1	Engr Units 2	Voltage 2	Engr Units 3	Voltage 3	Results			
Klbs	volts	Klbs	volts	Klbs	volts	Slope 1	20.295	Klbs /	volts
0	0.001	0	0.004	0	0.004	Slope 2	20.216	Klbs /	volts
20	1.041	20	1.024	20	1.058	Slope 3	20.222	Klbs /	volts
40	2.08	40	2.043	40	2.053	Average Slope	**20.244**	**Klbs /**	**volts**
60	3.061	60	3.041	60	3.068	R-square 1	0.999		
80	4.006	80	3.969	80	3.992	R-square 2	1.000		
100	4.919	100	4.961	100	4.961	R-square 3	1.000		
						Average	1.000		
						Slope	**0.049**	**volts /**	**Klbs**
							0.010	**volts /**	**v / Klbs**

Cal Note:
ADD

Complete/Update ALL red cells ONLY

Rename file with serial number in name

Sheet Version 1, 7 May 2009

Figure B4: Calibration Sheet for the LGP 312 - Pancake Load Cell.

APPENDIX C – Mean Nominal Stress

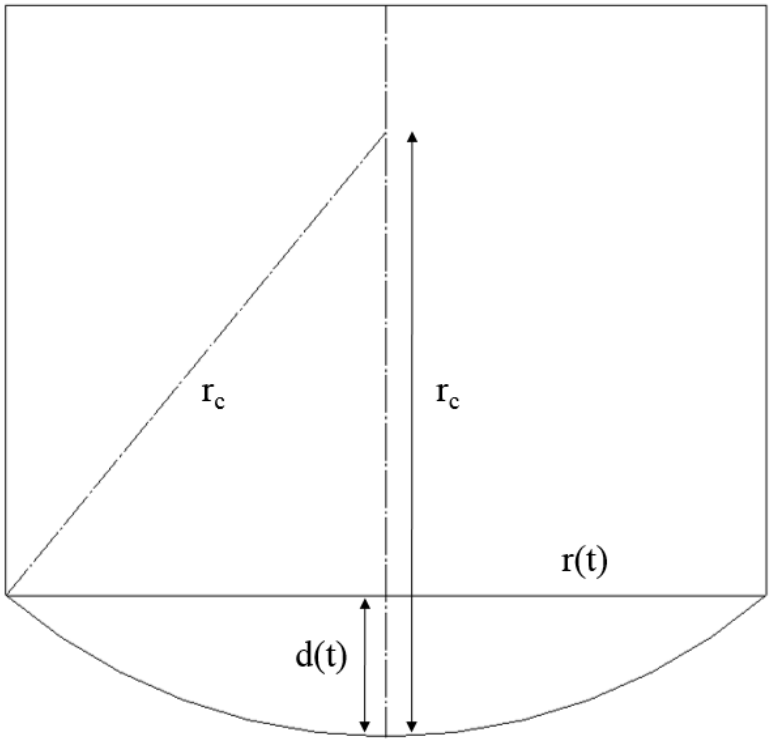

Figure C1: Nominal / projected area of the spherical indenter.

r(t) is the radius of the indenter

r_c is the radius of curvature

d(t) is the depth of penetration

v_p is the velocity of penetration

Since the depth of penetration changes with time:

$$d(t) = v_p t$$

and from geometry:

$$r_c = r(t)^2 + [r_c - d(t)]^2$$

$$r(t)^2 = r_c - (r_c - d(t))^2$$

$$r(t)^2 = r_c - (r_c - v_p t)^2$$

Therefore, mean nominal area (A_n):

$$A_n = \pi[r_c - (r_c - vt)^2]$$

APPENDIX D – Frequency Tests for the Compliant and Rigid Beams

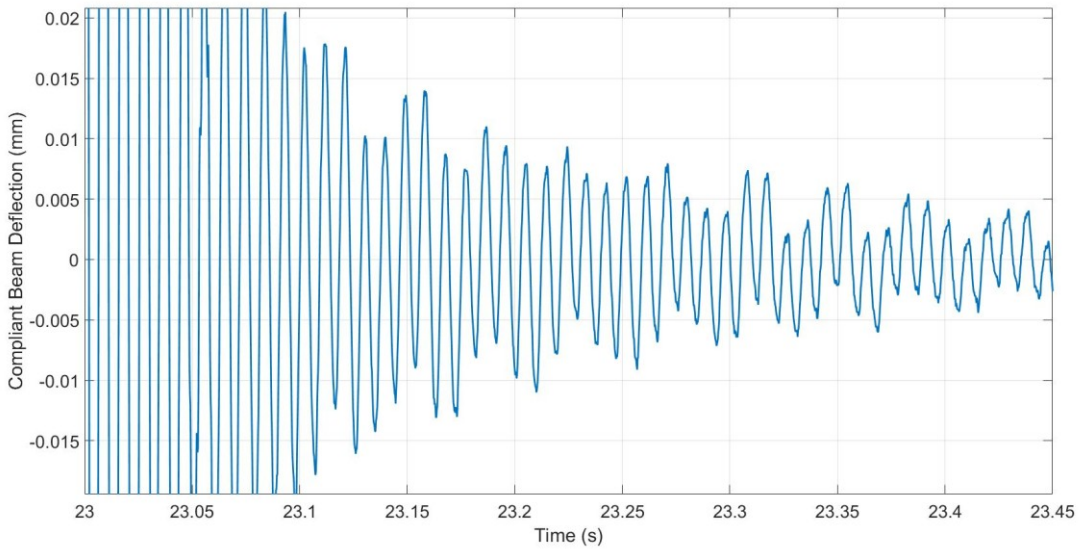

Figure D1: Natural Frequency Test for the Compliant Indentation System.

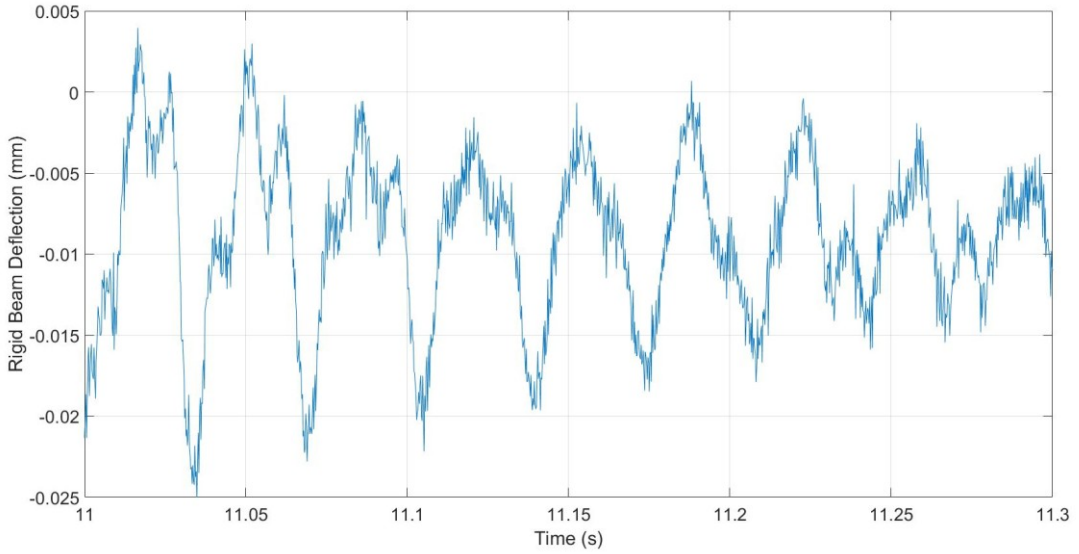

Figure D2: Natural Frequency Test for the Rigid Indentation System.